Model Predictive Control for Multi-Terminal HVDC Grid with Enhanced Fault Management

Shetgaonkar, A.D.

DOI
10.4233/uuid:b606fcc6-9c8d-4dff-ae05-39d07c7b6456

Publication date
2024

Document Version
Final published version

Citation (APA)
Shetgaonkar, A. D. (2024). *Model Predictive Control for Multi-Terminal HVDC Grid with Enhanced Fault Management*. [Dissertation (TU Delft), Delft University of Technology].
https://doi.org/10.4233/uuid:b606fcc6-9c8d-4dff-ae05-39d07c7b6456

Important note
To cite this publication, please use the final published version (if applicable).
Please check the document version above.

Model Predictive Control for Multi-terminal HVDC Grid with Enhanced Fault Management

MODEL PREDICTIVE CONTROL FOR MULTI-TERMINAL HVDC GRID WITH ENHANCED FAULT MANAGEMENT

Proefschrift

ter verkrijging van de graad van doctor
aan de Technische Universiteit Delft,
op gezag van de Rector Magnificus Prof. dr. ir. T. H. J. J. van der Hagen,
voorzitter van het College voor Promoties,
in het openbaar te verdedigen op Maandag 21 oktober 2024 at 15:00 uur

door

Ajay Digamber SHETGAONKAR

Master of Science in Electrical Engineering,
Technische Univesiteit Delft,
geboren te Margao, Goa, Indië.

Dit proefschrift is goedgekeurd door de promotoren

Samenstelling promotiecommissie:

Rector Magnificus,	voorzitter
Prof.dr. P. Palensky,	Technische Universiteit Delft, promotor
Prof.dr.ir. M. Popov,	Technische Universiteit Delft, promotor
Dr . A. Lekić,	Technische Universiteit Delft, copromotor
Onafhankelijke leden:	
Prof.dr.ir. P. Bauer	Technische Universiteit Delft
Prof.dr.ir. O. Isabella	Technische Universiteit Delft
Prof.dr.ir. J.W. Van Wingerden	Technische Universiteit Delft
Dr.-Ing. W. Winter	TenneT, Germany
Prof.dr.ir. A.W. Weeber,	Technische Universiteit Delft, reservelid

Keywords: VSC-HVDC, Model Predictive Control, Renewable Energy Integration, Real-Time Simulation, Fault Current Suppression, DC Fault Ride Through Control, Offshore Grids.

Printed by: ProefschriftMaken

Front & Back: Ron Zijlmans

ISBN 978-94-6510-264-1

An electronic version of this dissertation is available at
http://repository.tudelft.nl/.

Never stop fighting until you arrive at your destined place — that is, the unique you. Have an aim in life, continuously acquire knowledge, work hard, and have perseverance to realize the great life.

Dr APJ Abdul Kalam

NOMENCLATURE

AC CB AC Circuit Breaker

CCSC Circulating Current Suppression Control

CIG Converter Interfaced Generation

CLR Current Limiting Resistor

DC CB Direct Current Circuit Breaker

DC-FRTC DC-Fault Ride Through Controller

DLQR Discrete Linear Quadratic Regulator

DMR Dedicated Metallic Return

DSO Distribution System Operators

DT Digital Twin

DVC Direct Voltage Control

EMT Electromagnetic Transients

FCS Fault Current Suppression

FLD Fault-current Limiting Devices

FPGA Field Programmable Gate Array

GSC Grid-side Converter

GTFPGA Gigabit Transceiver FPGA

HB-SM Half-Bridge Sub-module

HiL Hardware-in-Loop

HVAC High Voltage Alternating Current

HVDC High Voltage Direct Current

ICC Inner Current Control

IGBT Insulated Gate Bipolar Transistor

LCC Line Commutated Converter

LLC Lower-level Control

LL Line-to-line

LTI Linear Time-Invariant

MMC Modular Multilevel Converter

MOG Meshed Offshore Grid

MPC Model Predictive Control

MPP Model Predictive Planner

MSC Machine-side Converter

MT-HVDC Multi-Terminal HVDC

NLC Nearest Level Control

OHL Over-head Line

OVC Outer Voltage Control

PED Power Electronic-Driven

PG Pole-to-Ground

PLL Phase Lock Loop

PoC Point of Common coupling

PP Pole-to-pole

RMS Root Mean Square

RTO Regional Transmission Organization

RTS Real-Time Simulator

SCR Short Circuit Ratio

SiL Software-in-Loop

SLG Single-Phase-to-Ground

TSO Transmission System Operator

VARC VSC Assisted Resonant Current

VSC Voltage Source Converter

WPP Wind Power Plant

Contents

SUMMARY

A secure, equitable, and environmentally sustainable energy system is a critical global challenge in pursuing a sustainable future. As dependence on fossil fuels wanes and the integration of renewable energy sources escalates, traditional power grids are confronted with unprecedented challenges, particularly in system inertia. This situation necessitates a substantial upgrade in energy transmission infrastructure. Such infrastructure must evolve to bridge the expanding geographical gap between renewable generation sites and consumption centres, all while maintaining power system stability. The solution to this complex puzzle may well reside in developing the 'Express Energy Highway'—a concept that envisions a trans-national High Voltage Direct Current (HVDC) grid as the backbone of a modern, digital-era energy network. HVDC grids are at the forefront of this transformation, providing an efficient solution for long-distance power transmission and capable of integrating a diverse range of energy sources with lower losses compared to traditional HVAC power systems. The expansion of HVDC technology, especially within Europe's ambitious energy targets and the phased decommissioning of nuclear power plants, underscores the pressing need for advanced control systems and real-time simulation models to navigate the complexities of these next-generation energy highways.

This thesis delves into modern HVDC technologies, focusing on Voltage Source Converter (VSC) technology. VSC-HVDC grids are renowned for their flexibility, functionality, and efficiency—essential for reducing carbon footprints and integrating massive renewable energy sources. Additionally, the thesis explores the operational dynamics of Multi-Terminal HVDC (MT-HVDC) systems. It develops a comprehensive framework for large offshore multi-terminal HVDC grids, concentrating on three focus areas: Advanced Control Algorithms, Fault Management, and Real-Time Simulation. At its core, the thesis emphasizes Advanced Control Algorithms, especially Model Predictive Control (MPC). This technique optimizes control actions by minimizing an objective function under dynamic system constraints, which includes enhancements like Grid Forming Control for integrating fluctuating energy sources into systems with low inertia and Control Interoperability to ensure stable operations under varying conditions. The second focal area, Fault Management, is critical for ensuring the reliability of HVDC grids. It includes strategies like Fault Current Suppression to assist DC circuit breakers and minimize damage during DC faults, alongside DC Fault Ride Through Control, which maintains system operation during DC cable faults and facilitates rapid recovery, eliminating any resonance in the MT-HVDC grid. The third area, Real-Time Simulation, offers a testing platform for these control strategies through standalone and integrated simulations, including Hardware-in-Loop, Control-in-Loop, and Software-in-Loop setups. These simulations validate the effectiveness of the controls in real-time scenarios, ensuring robust performance under different operating conditions. The convergence of these areas underpins the thesis's goal to Design and

implement robust, stable, and rapid control systems for large offshore MT-HVDC grids.

The findings from this thesis confirm significant advancements in HVDC technology, mainly through implementing MPC strategies within the MT-HVDC grid. The research demonstrates that MPC enhances operational stability, efficiency, and responsiveness to system disturbances and fluctuations in renewable energy inputs—crucial in settings with low system inertia where traditional methods are less effective. Moreover, the thesis highlights the critical role of real-time simulation platforms in validating advanced control strategies, ensuring their robust performance under real-world operational scenarios. In fault management, strategies such as Fault Current Suppression and DC Fault Ride Through Control prove essential in mitigating the impacts of faults, thereby enhancing system resilience and reliability. Overall, these findings underscore the critical role of sophisticated control technologies and real-time simulations in mastering the complexities of modern HVDC grids, supporting the transition toward a sustainable and dependable global energy infrastructure.

SAMENVATTING

Een veilig, eerlijk en milieuvriendelijk energiesysteem is een cruciale wereldwijde uitdaging in de zoektocht naar een duurzame toekomst. Nu de afhankelijkheid van fossiele brandstoffen afneemt en de integratie van hernieuwbare energiebronnen toeneemt, worden traditionele elektriciteitsnetten geconfronteerd met ongekende uitdagingen, met name op het gebied van systeeminertie. Deze situatie vereist een aanzienlijke upgrade van de energie-infrastructuur. Deze infrastructuur moet evolueren om de groeiende geografische kloof tussen hernieuwbare opwekkingslocaties en consumptiecentra te overbruggen, terwijl de stabiliteit van het elektriciteitssysteem behouden blijft. De oplossing voor dit complexe vraagstuk zou wel eens kunnen liggen in de ontwikkeling van de 'Express Energy Highway'—een concept dat een transnationaal Hoogspannings-Gelijkstroomnet (HVDC-net) voorziet als de ruggengraat van een modern, digitaal tijdperk energie netwerk. HVDC-netwerken staan vooraan in deze transformatie, waarbij ze een efficiënte oplossing bieden voor langeafstands-energieoverdracht en in staat zijn om een breed scala aan energiebronnen te integreren met lagere verliezen in vergelijking met traditionele HVAC-energiesystemen. De uitbreiding van HVDC-technologie, vooral binnen Europa's ambitieuze energiedoelstellingen en de gefaseerde buitengebruikstelling van kerncentrales, benadrukt de dringende behoefte aan geavanceerde controlesystemen en real-time simulatiemodellen om de complexiteit van deze nieuwe generatie energie snelwegen te beheersen.

Dit proefschrift verdiept zich in moderne HVDC-technologieën, met de nadruk op Voltage Source Converter (VSC) technologie. VSC-HVDC-netten staan bekend om hun flexibiliteit, functionaliteit en efficiëntie—essentieel voor het verminderen van de koolstofvoetafdruk en het integreren van enorme hoeveelheden hernieuwbare energiebronnen. Daarnaast onderzoekt het proefschrift de operationele dynamiek van Multi-Terminal HVDC (MT-HVDC) systemen. Het ontwikkelt een uitgebreid raamwerk voor grote offshore multi-terminal HVDC-netten, waarbij het zich richt op drie aandachtsgebieden: Geavanceerde Controle-Algoritmen, Storingsbeheer, en Real-Time Simulatie. Centraal in het proefschrift staan Geavanceerde Controle-Algoritmen, met name Model Predictive Control (MPC). Deze techniek optimaliseert controleacties door een doelstelling te minimaliseren onder dynamische systeembeperkingen, waaronder verbeteringen zoals Grid Forming Control voor het integreren van fluctuerende energiebronnen in systemen met lage inertie en Control Interoperability om stabiele operaties te waarborgen onder wisselende omstandigheden. Het tweede focusgebied, Storingsbeheer, is cruciaal voor het waarborgen van de betrouwbaarheid van HVDC-netwerken. Dit omvat strategieën zoals Fault Current Suppression om DC-schakelaars te ondersteunen en schade tijdens DC-storingen te minimaliseren, naast DC Fault Ride Through Control, dat de systeemwerking handhaaft tijdens DC-kabelstoringen en een snelle herstel mogelijk maakt, waarbij elke resonantie

in het MT-HVDC-net wordt geëlimineerd. Het derde gebied, Real-Time Simulatie, biedt een testplatform voor deze controle strategieën door middel van op zichzelf staande en geïntegreerde simulaties, waaronder Hardware-in-Loop, Control-in-Loop, en Software-in-Loop setups. Deze simulaties valideren de effectiviteit van de controles in real-time scenario's, waardoor robuuste prestaties onder verschillende operationele omstandigheden worden gegarandeerd. De samenkomst van deze gebieden ondersteunt het doel van het proefschrift om robuuste, stabiele en snelle controlesystemen voor grote offshore MT-HVDC-netten te ontwerpen en te implementeren.

De bevindingen van dit proefschrift bevestigen significante vooruitgangen in HVDC-technologie, voornamelijk door de implementatie van MPC-strategieën binnen het MT-HVDC-net. Het onderzoek toont aan dat MPC de operationele stabiliteit, efficiëntie en responsiviteit op systeemstoringen en schommelingen in hernieuwbare energie-verbetert—cruciaal in omgevingen met lage systeeminertie, waar traditionele methoden minder effectief zijn. Bovendien benadrukt het proefschrift de cruciale rol van real-time simulatieplatforms bij het valideren van geavanceerde controle strategieën, waardoor hun robuuste prestaties in operationele scenario's in de echte wereld worden gewaarborgd. Op het gebied van storingsbeheer blijken strategieën zoals Fault Current Suppression en DC Fault Ride Through Control essentieel te zijn bij het verminderen van de impact van storingen, waardoor de veerkracht en betrouwbaarheid van het systeem worden verbeterd. Over het geheel genomen onderstrepen deze bevindingen de cruciale rol van geavanceerde controle technologieën en real-time simulaties in het beheersen van de complexiteit van moderne HVDC-netten, ter ondersteuning van de overgang naar een duurzame en betrouwbare wereldwijde energie-infrastructuur.

1

INTRODUCTION

This chapter introduces the critical need for a diversified, resilient energy mix and infrastructure that will support it to address the energy trilemma. The chapter further discusses the challenges of inadequate grid infrastructure and the geographical separation of renewable sources from demand centers, emphasizing the importance of developing an Express Energy Highway — a trans-national power grid integrating diverse energy resources through advanced technologies like High Voltage Direct Current (HVDC) transmission as it will form the backbone of the digital era. This chapter will highlight the significance of advanced control and real-time simulation models to ensure stable and efficient energy transmission that connects large-scale offshore wind farms through HVDC grids. Presented research questions and methods provide answers to the advanced control strategies that can be used for offshore MT-HVDC systems.

1

1.1. IMPERATIVE FOR 21st CENTURY EXPRESS ENERGY HIGHWAY

As the 21st century progresses, the global push towards '*energy trilemma*' [1] – an attempt to balance energy security and accessibility. Therefore, an affordable and sustainable future is becoming an imperative and not an option. However, recent geopolitical shifts [2] have spotted energy security as the bottleneck in *energy trilemma*. Apart from decarbonization policies such as EU's green Deal [3], RePowerEU [4], US Inflation Reduction Act [5] and India's Green Energy Corridor [6], there is urgent need for diversified, resilient energy mix and infrastructure to achieve a predicted 20 % increase in non-fossil energy sources by 2050 [1].

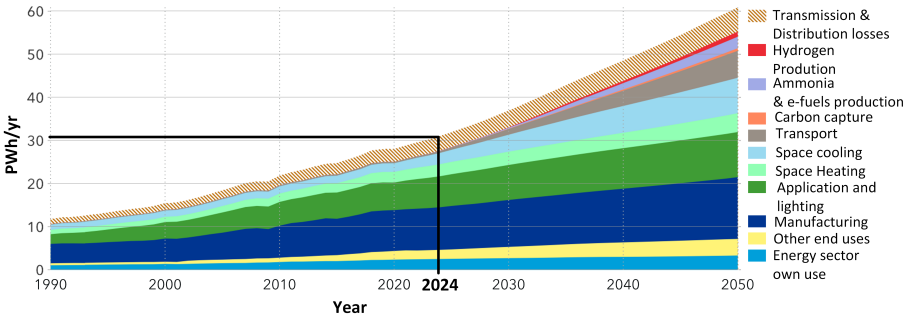

(a) Global electricity demand

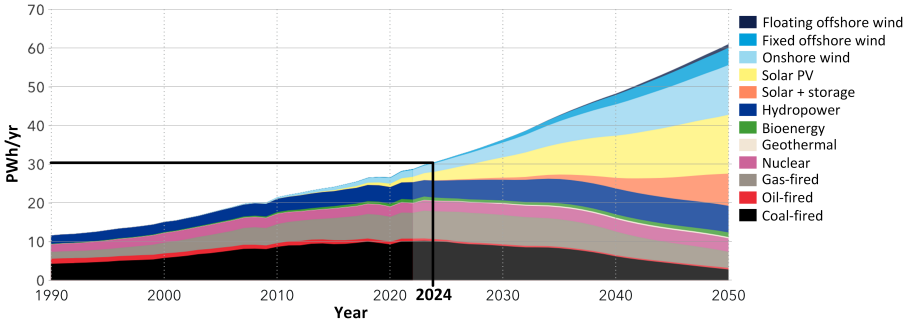

(b) Global electricity generation

Figure 1.1: Global electricity demand and supply [1]

It is expected that both electrification demand and generation will be almost doubled by 2050 (as seen in Figure 1.1a), with a thirteen-fold increase in solar and wind electricity production (as seen in Figure 1.1b), heading toward cleaner and more efficient energy systems. This will bring a net renewable share of 80% [1], [7]. However, challenges like inadequate grid infrastructure and the geographical separation of renewable sources and demand centers pose hurdles to a smooth energy transition. The current trajectory suggests a potential global temperature rise of 2.2°C by the century's end, exceeding the 1.5°C target of the Paris Agreement.

In Europe, in the next decades, electricity demand is expected to be driven by sectors like buildings, transport, and manufacturing [8]. By the late 2030s, grid-connected hydrogen production will be a major electricity consumer. At present, each European region focuses on renewable energy share to meet future demand. The Iberian Peninsula harnesses wind and solar energy and is set to be Europe's renewable powerhouse [9]. In contrast, the North Sea region will provide a high share of offshore wind energy, becoming a 'Green PowerPlant of Europe'. It is also expected that by 2050, the amount of offshore wind energy will reach a value of 300 GW [4]. This will lead to a diverse decarbonized European Power landscape.

To meet these challenges, Europe needs to develop the Express Energy Highway — an interconnected, intelligent, and flexible trans-national power grid, capable of transmitting and distributing electricity efficiently and resiliently. It should accommodate the rapidly increasing demand and integrate diverse energy sources, especially variable renewable energy sources (VRES) like wind, solar, and other conventional power sources. This system will require advanced digitized control strategies, interoperability, and auxiliary support for overall grid stability. High Voltage Direct Current (HVDC) transmission is a suitable candidate for this Express Energy Highway. The HVDC transmission is considered as a 'superhighway' for a high-capacity efficient energy pipeline over long distances [10]. The HVDC technology, combined with hydrogen and other derivatives (like e-methanol, e-methane, liquid e-hydrocarbons, e-formic acid, and e-ammonia), is capable of enhancing energy storage and flexibility [11].

The journey towards a net-zero carbon future involves clean technologies scaling and expanding the global grid. The EU's integrated climate and energy policy aims to limit the global temperature increase to 2°C above pre-industrial levels, with efforts to limit the increase to 1.5°C [12], [13]. The EU's long-term target is to achieve zero carbon emissions by 2050, and significant reductions are underway. To support these goals, substantial infrastructure of solar and wind energy capacities is required, targeting a 42.5 % renewable share by 2030 [14], [15]. The inherent advantages of HVDC technologies, especially when using long cable interconnections, are crucial for the expansion of the energy grid [16]–[20].

1.2. HVDC GRIDS: THE ARTERIES OF DIGITAL ERA

As the integration of intermittent renewable energy sources increases, and the demand for high-capacity, long-distance power transmission grows accordingly, HVDC technologies emerge as a pivotal component in the digital era's energy infrastructure. HVDC grids, known for their flexibility, functionality, and high power density, offer significant advantages over traditional High Voltage Alternating Current (HVAC) grids [19]. One of the advantages is large power transmission over longer distances with minimal transmission losses. The typical distance limits for which HVDC transmission is more efficient than that of HVAC one are longer than 600-800 km for an overhead line, 50-95 km for a land cable, and 24-50 km for a submarine cable [21]. These distance limits are determined according to the generated reactive power amount which for HVAC lines increases for longer distances, and is absent in the case of DC transmission lines [22]. For DC electricity grids, electric power is transmitted at zero frequency and as such

1

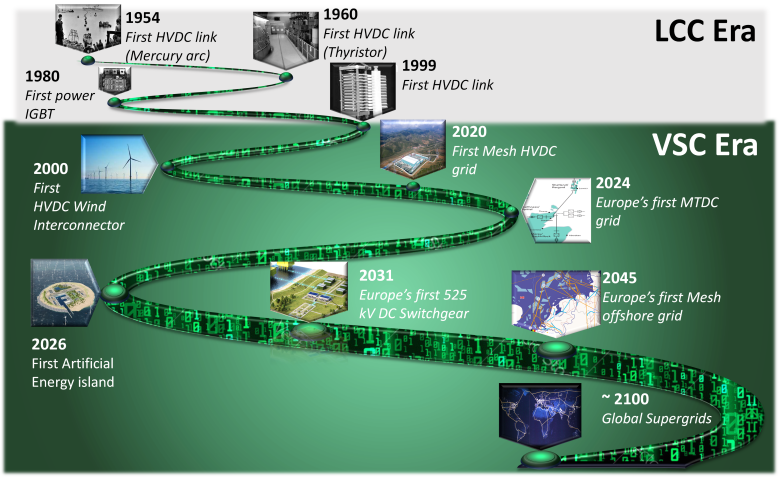

(a) History and projectile future of HVDC

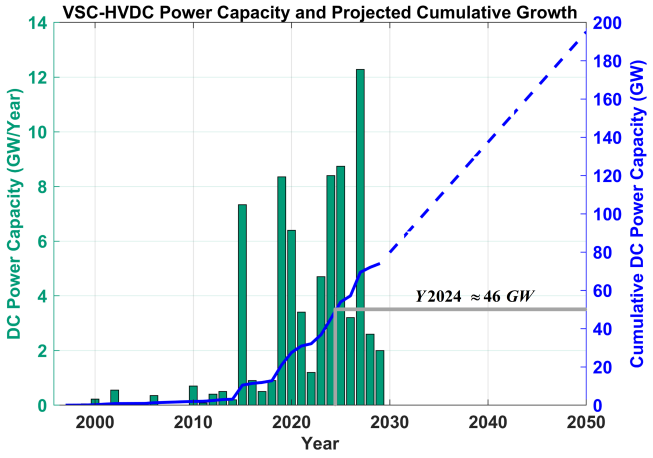

(b) VSC-HVDC Power Capacity and Projected Cumulative Growth

Figure 1.2: Overview of HVDC and VSC-HVDC Trends: (a) shows the historical development and future projections of HVDC technology, (b) presents the current capacity and projected growth of VSC-HVDC technologies.

there are no frequency-related losses, namely, due to the corona [23] and skin effect [24]. Since these losses exist in each conductor in the HVAC grid, the losses are three times higher due to the required three conductors. HVAC transmission lines are equipped with bundled conductors to minimize corona discharge losses. This design increases the conductors' overall diameter, effectively reducing the corona effect's intensity, which results in increased costs for the HVAC grid. In contrast, the cabling costs for HVDC transmission are significantly lower due to 1-2 conductors per connection[25]. A thicker cable is used for AC power transmission to minimize the skin effect in the cable. In

contrast, HVDC cables use lower conducting thinner cable [26]. Also, the HVDC can interconnect two systems operating at different frequencies and unsynchronised remote systems. Its fault-blocking capability does not exacerbate AC fault levels, and in this way, system resilience can be enhanced. HVDC's power quality support functionality is particularly beneficial for AC grids with lower inertia, making it a preferred choice for modern energy grids [27].

The journey of HVDC technology began in 1954 with the commissioning of the world's first mercury-arc valve-based system in Sweden, marking the advent of what later became known as Line Commutated Converter (LCC) technology (Figure 1.2a). This technology heralded rapid advancements in valve technology, catalyzing numerous projects in the following years. However, LCC technology started facing limitations for high-power transmission, primarily due to its high reactive power requirement, the absence of black start capability, large station footprint, and the necessity for a non-standard transformer. Furthermore, it is suitable only for back-to-back and point-to-point connections, which is insufficient to meet supply requirements nowadays.

The late 20^{th} century brought a significant breakthrough with the invention of the insulated gate bipolar transistor (IGBT), paving the way for a new generation of HVDC technology: the Voltage Source Converter (VSC). VSC technology effectively addresses the shortcomings of LCC, offering enhanced flexibility and efficiency. This technological shift is reflected in the current trends of the global HVDC market, where VSC technology is increasingly preferred, as illustrated in Figure 1.2b. Due to the ability for modulation and scaling, the VSC known as modular multilevel converter (MMC) has shown a breakthrough for high-power applications, especially high-power transmission. The ongoing advancements in MMC technology, including eliminating the need for large capacity filters (like in case of LCCs) resulting in reduced station footprints, make it suitable for large-scale offshore energy integration and integration in urban areas. Besides, due to the constant voltage and flexible power control, the VSC is suitable for interconnecting different HVDC transmissions and constructing mesh grids, similar to conventional HVAC grids [19].

With the on-going energy transition policies in Germany, eight nuclear power plants will be taken out of service, and the shortage of energy will be compensated by utilizing wind energy from the North Sea. Five onshore HVDC transmissions are planned to connect Northern wind and Southern solar energy to industrial clusters. This HVDC transmission will be realized initially as a point-to-point topology with the ability to be multi-terminal via a multi-purpose interconnector [10], [28], [29]. In addition to this, there are two multiterminal energy hubs, HeideHub (with installed power of 2 GW) in Schleswig-Holstein (Dithmarschen district) and NordWestHub (with installed power of 4 GW) in Lower Saxony (Wesermarsch district). In the heart of these two hubs, there is a DC switchgear that connects the DC lines from the North Sea with those on land, and further through a converter with the three-phase grid. In high wind power generation, loads can be connected to this power via HVDC, however, when there is low or no power, nearby AC systems can be connected via a converter and DC switching stations, thereby improving flexibility. Heidehub will also be equipped with an electrolyzer to provide green hydrogen. Furthermore, NordWestHub will consist of a DC circuit breaker (DC

CB), which is needed to isolate the fault and prevent possible damage to the power grid. In Germany's offshore region, nine offshore HVDC connections are planned, meeting the expected requirements of 70 GW until 2045. Some of which will be connected through two onshore multi-terminal energy hubs. Eight offshore HVDC links are planned in the Netherlands, which will meet 75% nation target for offshore wind energy.

To utilize the offshore wind energy in the North Sea, the initial point-to-point connection will be converted into Meshed Offshore Grids (MOGs) by 2045 [13], [30]–[32]. According to a report [33], the creation of meshed offshore grids in Europe's sea basins will likely involve connecting multiple offshore hybrid projects. These projects, also known as multi-terminal interconnectors or multi-purpose interconnectors, aim to integrate various offshore wind farms with multiple markets. As defined by WindEurope [33], offshore hybrid projects combine offshore wind energy generation and transmission assets into a single, versatile infrastructure, connecting multiple wind farms to multiple markets.

These MOGs propose two hub concepts: centralized, exemplified by the North Sea Wind Power Hub (NSWPH) [32], with up to 35 GW capacity through connecting multiple offshore wind farms (OWFs), and decentralized, focusing on smaller interconnected hubs for national and European distribution. Danish plan to erect two energy islands by 2033 reflects these strategies [34]. Furthermore, integrating Power to X conversion, particularly for hydrogen production, is crucial for long-term energy storage and balancing supply-demand disparities, with ongoing research aimed at scaling hydrogen production to the gigawatt power levels [32]. It is expected that in 2024, Europe's first Multiterminal (MT)-HVDC grid to be commissioned in Shetlands. The existing Caithness Moray HVDC Link will be expanded to a three-terminal by commissioning the Shetland Link [35], [36].

In the near future, different *'supergrids'* are proposed that will connect different countries or regions by HVDC connections, such as the US and Pan-European Supergrids [37], Eurasian Supergrid [38], Australian–Asian power grid [39], Europe North American interconnections [40] and China-EU transmission link [41]. In the long run, HVDC will act as a global express energy highway connecting not only regional *'supergrids'* but also connecting continents. Creating a *'global supergrid'* [42] in future.

1.3. ADAPTIVE CRUISE CONTROL ON THE EXPRESS ENERGY HIGHWAY

In the modern power grid, with the increasing integration of power electronic-driven (PED) renewable energy sources and interconnected HVDC grids, a metaphorical parallel can be drawn to an 'Express Energy Highway.' On this highway, the flow of electrical energy should be maintained within the system limits and exhibit adaptive management under contingencies. This demands 'Adaptive Cruise Control' – like features in PEDs to maintain stability, reliability, and flexibility.

According to the recent task force on power system stability [43], the definition of power system stability has been revised by including converter-driven and resonance stability. This revision is based on the high penetration of PEDs at different voltage levels. The control system theory has been used in power systems since 1965 [44], and its time

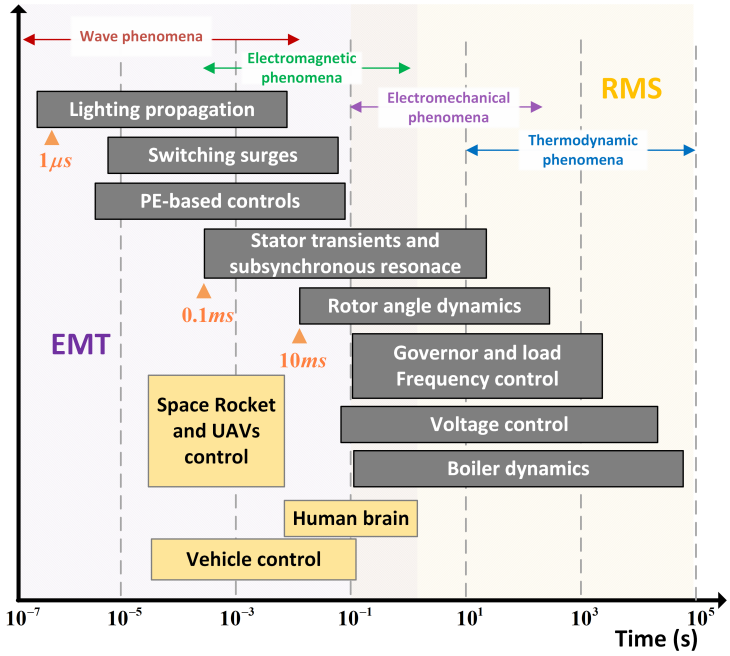

Figure 1.3: Overview of system response time adopted from [43]

scale is shown in Figure 1.3. So far, the existing controls of the converter interfaced generations (CIGs), synchronous machines, and induction machines are based on conventional linear controllers. The effectiveness of linear controllers is significant in the linear time-invariant (LTI) system. In addition, the conventional power system has a pure sinusoidal wave shape, making grid synchronization easier for the small shares of CIGs with the help of a Phase Locked Loop (PLL). Furthermore, the existing power system has high inertia, which provides tolerance to instability in the range of seconds. Thus, slower controls are sufficient.

In contrast to the conventional power system, the modern and future power systems will have a high share of CIGs. Besides, conventional fossil fuel power plants are being decommissioned at an accelerating rate, and this will weaken the power grid. High CIGs and low inertia systems will affect the grid synchronization. In addition, most CIGs are nonlinear, which can trigger control instabilities due to nonlinear functions, such as limits or change of control mode. Thus, there is a need for accurate and robust control during a wide operation range [45]. These systems introduce transient disturbances and require advanced control methods to manage the rapid dynamics effectively [43], [46]–[50].

Like the AC power system, the energy balance in the HVDC grid is defined by the energy extracted from HVDC grids, injected within the HVDC grid, and dissipated in the HVDC grid. Hence energy balance is essential in the HVDC grid operation. This objective needs to be achieved for normal operations and abnormal operations. Unlike

AC power systems, failure to provide energy balance will result in a DC voltage change within milliseconds. Since the DC voltage is a global variable like the frequency in the AC systems, the change of the DC voltage will affect the converters connected to HVDC grids. Thereby, the instability will spread to adjacent AC power systems. Hence, a control law is needed to react to changes in the energy balance within milliseconds and restrict the impact. DC-side fault current interruption in the MT-HVDC grid is challenging due to the high rate of rise of fault current. In addition, fast DC switchgear is proposed and developed to improve the resilience of the HVDC grid. However, the coordination of the DC switchgear operation and converter control strategies must be seamless and faster during and after the disturbance, and thus, interoperable. The control law should be adaptive enough so that a new connection to the HVDC grid will not affect the grid's stability. Furthermore, each converter should be autonomously controlled for large and small disturbances, as the reaction time of the unbalanced events in an HVDC grid is much faster than in an AC grid.

Moreover, as we phase out conventional fossil fuel-based generation, grid's inertia decreases, exacerbating stability issues. This new era of low-inertia, high-renewable integration calls for fast-acting controls that are adaptive to the grid's changing state. This includes transitioning from traditional linear controllers, like proportional-integral (PI) controls, to more sophisticated nonlinear control methods that offer robust performance in the face of the grid's nonlinear behavior due to factors like switching events [45]. Additionally, faster control action leads to lower overvoltage levels over the HVDC grid, thus, prolonging the life of the DC cable, which is considered one of the expensive component in a long HVDC transmission. Faster control is essential to improve the reliability of the power supply. During the AC voltage angle jump, faster control helps to bring the system back to a pre-disturbance state, thereby preventing the minimum impact on AC and DC grids. Faster control can limit the maximum variation of the instantaneous active and reactive power after the phase angle change. In addition to fast control action, the control should also be equipped with/ should have an option for damping functionality in case of power oscillation seen from the connection point [51].

Essentially, the 'Adaptive Cruise Control' for our express energy highway implies a transition to advanced control strategies. These strategies are better suited to address the grid's evolving dynamics, ensuring stability and resilience in the face of rapid changes and disturbances. Just as the cruise control in vehicles maintains steady and controlled motion on an expressway, the adaptive control in power systems ensures a smooth, uninterrupted flow of electricity, safeguarding against disruptions like brownouts or cascading blackouts [44], [45].

1.4. OFFSHORE MT-HVDC DIGITAL TWIN: REAL-TIME EMULATION OF EXPRESS ENERGY HIGHWAYS

Digital Twin (DT) is evolving from aerospace and military to multidisciplinary fields. NASA introduced the first DT during the Apollo 13 program in 1969 [52]. In this program, 15 high-fidelity simulators were used to train astronauts and mission controllers at each mission stage, ultimately avoiding a disaster in both Apollo 11 and 13. Similarly, A

'hardware' twin, the so-called 'Iron Brid,' exists in the aircraft design and engineering cycle [53]. This twin consists of all the aircraft's systems and subsystems mock-ups. It is fully assembled and operational on the hangar floor, replicating the complete plane except for the airframe itself, without being airborne. The DT is defined as (quoted in [54]): " *a description of a process or a system, enhanced with (live) data. The description itself can range from a plain schematic of the system up to a dynamic numerical simulation model, but when we link it to real-world data or a specific application, it becomes a digital twin*".

DT is being explored and trending in the power system sector with evolving computational technologies and digital transformation. General Electric (GE) has unveiled a DT of a wind farm featuring a digital model of wind turbines arranged within the farm and incorporating environmental data [55]. In 2016, Siemens introduced their first Power System Digital Twin called ELVIS for operation management and infrastructure investment planning in Fingrid, Finland. In the following year, AEP Transmission, US collaborated with Siemens to face the mounting challenge of model coordination between different departments. Which led to an open standard, Common Information Model (CIM) [56]. In 2021, Hitachi Energy launched IdentiQ™ – a DT for HVDC and power quality solutions. It provides asset information, analytics, and operational data for optimized operations and smarter decision-making [57]. With the planned development of energy express highways across Europe, DTs are becoming popular due to their ability to enable predictive maintenance, optimize grid performance, ensure system reliability, and facilitate efficient integration with renewable energy sources.

As explained in the previous section, express energy highways will built shortly, and distributed CIGs will dominate the power grid, which brings a new set of instability problems ranging from electromagnetic to electromechanical dynamics [43]. Furthermore, RES's large intermittent power injection challenges conventional stability analysis due to variable equilibrium. Similarly, alone dynamic simulation (root mean simulation (RMS) studies) is not sufficient for Transient stability assessment (TSA) and control stability [58]. In response to this problem, transmission system operators (TSO), regional transmission organizations (RTO), and professional associations such as CIGRE and IEEE are actively investigating detailed electromagnetic transient (EMT) simulations, and CIG models are being developed/ needed and standardized in the electromagnetic domain [59], [60]. The HVDC system owner is responsible for conducting the studies as outlined in Articles 29 and 31 of NC-HVDC [61], unless Member States assign this responsibility to the TSOs. Regardless of who conducts the studies, the TSO must evaluate their results, considering their scope and extent, and may request additional studies if necessary. TSOs also have the authority to review and replicate parts or all of the studies. In such cases, the HVDC system owner must provide the relevant TSO with all necessary models and data to perform the predefined studies. The study required by Article 29 of NC-HVDC must identify any conditions where potential adverse interactions may exist and propose possible mitigation actions. Among these simulation models, EMT models are used to reflect the behavior of the HVDC system in different time domains.

The recent development of machine learning (ML) technologies has made

data-driven solutions for stability issues more attractive. However, a new complex system (like HVDC grids) needs an EMT model-based simulation to train ML-based solutions, making EMT simulation an essential part of the learning process [62]. The EMT-type simulation tool is a circuit-focused method that utilizes highly precise models to analyze a wide frequency range of power system events. This tool provides a more in-depth examination than what is possible with transient stability analysis or phasor-based methods. EMT modeling is adept at depicting transient and sub-cycle frequency phenomena. It is particularly effective in simulating the low-level control systems of CIG. These features are essential in understanding the complexities of today's power grid, which is markedly different from traditional systems predominantly characterized by centralized rotating machines. EMT studies play a vital role from the development phase to the project execution phase during HVDC planning [16]. The growing need for EMT simulation stems from its ability to accurately reflect the dynamic nature of the modern, transformed grid.

Due to high computational burden and inefficiency, offline EMT simulations are not preferred in routine grid operational/ planning [63]. Furthermore, with the increasing integration of CIGs, simulations have become more complex and computationally demanding. In response, advanced hardware-based technologies have been developed to speed up and streamline EMT simulations [64]. As a result, online EMT simulations are now utilized, employing Real-Time Simulators (RTS) – high-performance parallel CPUs or Field-Programmable Gate Arrays (FPGAs) – to handle these demanding simulation tasks effectively. Further online EMT simulations facilitate closed-loop testing, which is infeasible in offline EMT and phasor simulations [63]. As RTS becomes more efficient and offers the capability for Hardware-in-Loop (HiL) testing, it is emerging as a standard tool for replicating the transient dynamic behavior of large power systems, providing a reliable testing environment before implementation in actual scenarios [65]. Commercial company RTDS © technologies have provided FPGA-based support units, which reduce the computational burden on the main processing unit. Switching (detailed) models of the HVDC converter and lower-level controls, which can be implemented on FPGAs, are required for the feasibility study and project execution phase [63]. Furthermore, validating the designed controller provides a dynamical performance test carried out during the factory acceptance test (FAT) by vendors and system operators [66].

The fundamental operation of RTS is to simulate the representation of the real system in the computer environment, ensuring that the time it takes for the simulation to run is equivalent to the actual time elapsed in the real world, often referred to as 'wall clock' time [68]. Based on the definition of DT, among three key features, the model of the real system and simulation tool plays a vital role. A complex DT-like offshore HVDC grid can be constructed by combining the small and validated models. Considering the requirement DT, online EMT simulation and its industrial-validated models bring attractive solutions for Offshore MT-HVDC Digital Twin (as shown in Figure. 1.4). Human errors are rare and hard to model. However, developing such DT in RTS will improve future operator training and standard operation procedures [62]. Due to the HiL capability [69], the offshore MT-HVDC DT can be connected to the real grid or replica of control and protection via standard/experimental communication protocols [70].

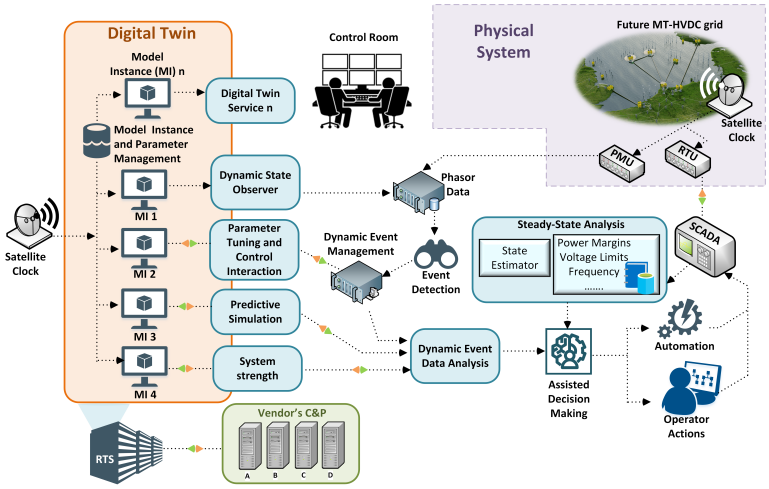

Figure 1.4: Potential Digital Twin setup of offshore MT-HVDC grid, adopted from [67]

With this capability, EU projects like InterOPERA [71], aim to provide interoperability standards, standardized interaction study processes, and interfaces for future European onshore/offshore MT-HVDC grids by testing the control and protection units of different vendors in the Control and Hardware setup using RTS.

1.5. RESEARCH QUESTIONS AND METHODS

Considering the above motivations, this thesis is focused on a framework that investigates three important areas (as shown in Figure 1.5): Advanced Control Algorithms, Fault Management, and Real-Time Simulation. At the heart of this framework are the Advanced Control Algorithms for the MMC-VSC HVDC grid, which consist of Model Predictive Control, an optimized control law in which control actions are derived by minimizing an objective function under dynamic system constraints over a finite receding horizon. This includes an extension to Grid Forming Control, essential for integrating high intermittent energy sources into lower inertia systems, and it is complemented by Control Interoperability, which ensures stable operation of different system controls under normal and abnormal conditions.

The second pillar of this thesis is Fault Management in HVDC grids, which is essential for system reliability. It includes strategies like Fault Current Suppression, which helps DC CB and minimizes damage during faults. Another strategy is DC Fault Ride Through Control, which allows systems to maintain operation during DC line faults, minimize downtime, and restore normal operation by using Fault Detection, Localization, Interruption, and Restoration information.

The third pillar, which is Real-Time Simulation of HVDC grids provides a testing platform for these advanced control strategies. It involves Standalone Control Algorithms that can function independently, as well as HiL, Control-in-Loop, and Software-in-Loop (SiL) simulations. These simulations are designed to validate the

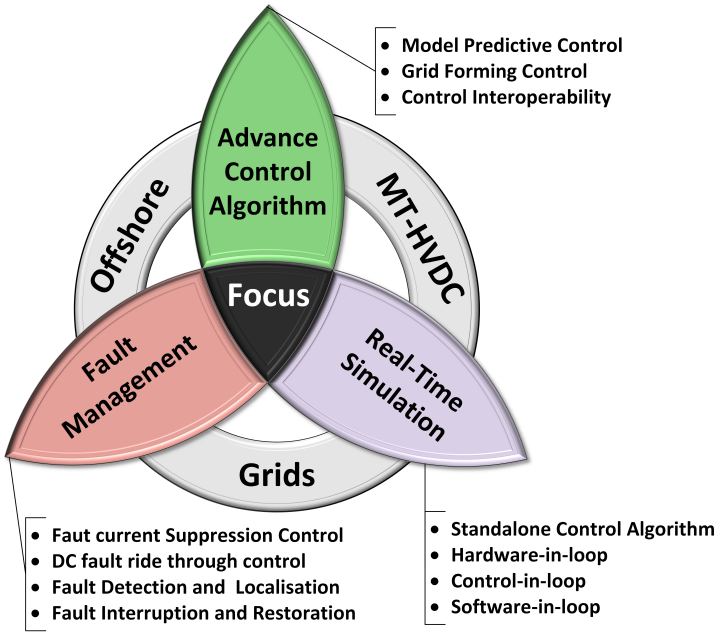

Figure 1.5: Diagram showing this thesis's focus area

performance of control algorithms in real-time, ensuring they can reliably operate in live scenarios.

The convergence of these three components at the center of the diagram formulates the main objective of this Ph.D. work: ***to develop and implement advanced controls to ensure fast, robust, and stable real-time operation of large offshore multi-terminal HVDC grids***.

Furthermore, the main research objectives formulated in this section are approached by answering the following more concrete questions and sub-questions.

RQ1. WHAT INTELLIGENT CONTROL ALGORITHM CAN CONTINUOUSLY ENSURE STABLE AND EFFICIENT ENERGY TRANSMISSION IN LARGE-SCALE OFFSHORE WIND FARMS CONNECTED THROUGH HVDC GRIDS?

The energy conversion in the large offshore MT-HVDC grid is ensured by the PEDs, which are pivotal in AC/DC and DC/AC energy conversion. These devices are governed by fast control loops, which induce predicted and uncertain high-frequency grid interactions, as revealed through EMT simulations [43], [72]. Moreover, PEDs may trigger unstable power system oscillations across a broad frequency spectrum, potentially due to improper control settings, interactions with passive elements, or cross-controller dynamics [73], [74]. Therefore, robust and fast advanced control strategies are needed to control the active/reactive power quickly and effectively

without causing adverse implications on the stability of interconnected power systems. MMC's active/reactive power controls are predominantly implemented as cascaded PI controllers. The time response of these controllers is around 100 ms, which is slow, considering the fast nature of electrical transients in power systems with high RES. Additionally, the PI controllers have limited reach. They can be used to control only one variable at a time—thus the research towards nonlinear control methods, which can control multiple variables within allowable safe boundaries and constraints [75]. However, selecting a non-linear controller has no standard procedure and is application-based. Hence, based on the system requirement, the correct controller choice must be made.

One promising approach for nonlinear control of power electronic converters is the model predictive control (MPC) [75]–[79]. The direct and indirect formulations of the MPC are the most appealing options for systems dominated by power electronic converters [80]. Both variants of MPC have been applied to MMC units for fast mitigation (within a few milliseconds) of frequency excursions due to sudden active power imbalances in low-inertia power systems [47], [48]. Other applications of MPC for VSC units operating in interconnected power systems have been reported in [49]. In addition, the authors in [81], [82] have illustrated the extension of the operating region with active and reactive power control for a single-phase MMC. However, the most challenging part of the MPC is the computational burden during an online optimization [50]. A large combination of input sequences for the next simulation time step for the explicit MPC increases the computation burden. This burden increases when multiple variables are simultaneously controlled. Most of the proposed indirect MPCs or optimization control schemes for the power electronic applications make use of tool support to generate optimal control signals (online or offline) [83], [84]. These tools consist of implicit functions, disabling the MPC algorithm to run on different real-time simulation platforms as they do not support a standalone code.

Accurate MMC control and MT-HVDC operation necessitate reliable component models. MMC is usually characterized only from AC [85], [86] or from the DC [87] side in the spectral domain. However, these models do not allow AC and DC side interactions. Therefore, some methods rely on the Fourier series, such as dynamic phasors [88] and harmonic state-space analysis [89], [90]. These two methods are compared, giving similar results [91]. Even though very accurate, dynamic phasors and harmonic state-space algorithms generate huge system matrices. One more approach is described in [92], where a state-space model of an MMC in dqz-frame employs three harmonics.

Given these considerations, several pertinent questions arise:

- How can we define an analytical model of MMC that gives sufficient complexity with a clearly defined system of nonlinear differential equations?
- What is the most efficient approach to formulate MPC for reference tracking for grid following and grid forming control objectives such that it takes lower computation power?
- Is it possible to design a standalone MPC solution that can operate in environments without an operating system using the V-method as shown in Figure

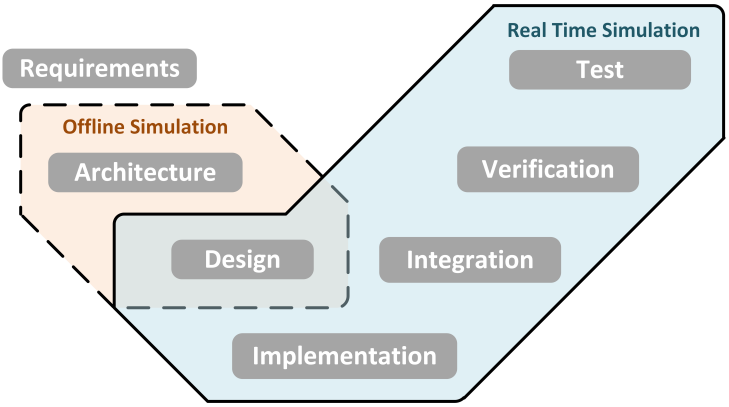

Figure 1.6: Diagram showing V-method for designing, implementing, and testing controller

1.6?

- Is MPC stable and robust under large disturbances in HVDC grids?
- How does the interaction between non-linear control loops and active/passive HVDC network elements influence on the system behavior during different operating scenarios and transient events?
- Can we compare the performance and interaction analysis of an MPC-controlled meshed HVDC grid with a classical PI-control-based meshed HVDC grid to identify interoperable scenarios?

RQ2. HOW CAN RTS BE OPTIMIZED TO MODEL CRITICAL EVENTS IN OFFSHORE MT-HVDC GRIDS, ENSURING COMPUTATIONAL EFFICIENCY AND PRACTICAL ADAPTABILITY?

The integration of DT into the power system sector, inspired by their extensive application in aerospace and military fields, marks a significant advancement in the modeling and simulation of complex systems. Initially developed for mission-critical simulations by NASA, DTs have become essential for addressing the dynamic complexities of offshore MT-HVDC grids, including distributed converters, HVDC cable systems, and the integration of wind power plants (WPPs). The increasing reliance on DTs is driven by their ability to predictively maintain and optimize grid performance, and ensure system reliability as power grids evolve to support express energy highways.

An RTS is pivotal in developing DT models for offshore MT-HVDC grids. RTS has become indispensable by capturing the intricate electromagnetic and electromechanical dynamics that traditional stability analysis methods may overlook, such as those introduced by converters and intermittent power injections from WPPs. The past two decades have seen a surge in the use of EMT software for real-time simulations, particularly for HiL testing. This approach enhances confidence in control-protection schemes and leverages the practical benefits of DTs in system

design, operation, and training. Despite the advantages, the extensive computational demands of RTS necessitate model/sub-system simplification, focusing on detailed modeling of key areas through multi-time step, multi-core, and multi-rack simulation strategies while aggregating the rest of the network to maintain overall system dynamics. Additionally, hardware limitations must be considered, focusing on the areas of interest [93].

RTSs are commonly used for various purposes, including testing new or refurbished HVDC projects, post-disturbance and failure analyses, investigating HVDC and AC system interaction, and studying HVDC special emergence protection schemes. Extensive studies and systematic libraries have been performed and published in that direction. The most recent CIGRE 804 [94] brochure provides RTDS© average value MMC models for 500 kV voltage levels. The benchmark models cover transmission using the overhead DC lines. As a part of the PROMOTioN project, deliverable D9.1 provides a three-terminal grid model with ±320 kV rated DC voltage [95]. The main task of real-time simulations is to perform detailed multi-vendor studies that simulate real-time situations. So far, there have been realized multi-vendor protection studies [96]. Furthermore, Best Paths [97] and PROMOTioN [95] projects provide a reasonable basis for the multi-vendor control and protection studies, which are currently being extended by READY4DC and InterOPERA projects [71], [98].

Offshore wind farms are connected to the converter station, which can be intertwined with the controller's frequency range, and therefore, the control system needs to be modeled in detail. This captures the possible offshore control interaction. To ensure equipment safety and system stability in the offshore HVDC islanded operation, voltage stability studies must be carried out with the coordination of wind farm control and frequency stability. Furthermore, the interaction of the interwind turbine and stability control in HVDC islanded operation requires a detailed representation of offshore wind farms in the RTS. However, for studies on harmonic stability, frequency domain methods can be used iteratively using the script functionality of RTS. Thus, generally, RTS is important to benchmark the control system and model used. Besides, from the system owner's perspective, avoiding the system risk of instability or tripping of the connected AC submarine cable in the case of short circuit faults during offshore HVDC islanded operation is a crucial techno-economical factor. Planned projects in the North Sea focus on ±525 kV DC voltage with a Dedicated Metallic Return (DMR) and a bipolar topology. Hence, the impact of DMR cable on the HVDC grid and vice versa will be crucial during the energization, the transient event, and the post-disturbance state. To investigate these events, a phase domain frequency-dependent model of DMR with realistic data and modeling techniques is required.

To increase the reliability of offshore wind power, North and Baltic Sea TSOs consider the implementation of DC CB in the HVDC grids. However, many technical and economic challenges have been analyzed, and solutions are provided in the PROMOTioN project. The operation of DC CBs on system components like converters and cables should be investigated during the energization and DC fault and breaker re-close period. The time simulation studies during this period will provide input for design and operation studies.

Therefore, the development of real-time simulation models for offshore HVDC grids

demands a focused approach that encompasses the following key aspects:

- Accurate replication of the operational dynamics of offshore HVDC grids.
- Incorporation of validated models, with due consideration for computational requirements.
- Enhanced practical relevance through the ability to connect DT models to real-life or replica control and protection systems using standard or experimental communication protocols.

The envisioned model should include:

- New standard power and voltage ratings for North Sea converter platforms (e.g., 2GW and ±525 kV) with frequency-dependent submarine and land cables.
- Dynamic modeling of wind farms and wind turbines based on real-time wind gusts, utilizing SiL setups.
- Automated perturbation of electrical and control parameters.
- An optimized offshore HVDC grid model that considers RTS constraints.

RQ3. HOW CAN ADVANCED CONTROL STRATEGIES ENSURE ACTIVE FAULT CURRENT SUPPRESSION FOR THE SYSTEM WITH LARGE-SCALE OFFSHORE WIND INTEGRATION?

Based on submodules' (SMs) design and configuration, the MMC technology is classified into half-bridge (HB), full-bridge (FB), and Hybrid MMC [99]. However, HB-MMCs are commissioned due to their lower footprint and cost. This brings up another drawback: the need for DC fault interruption capability. Unlike AC grids, DC grids do not have a natural current zero crossing during a fault period; therefore, a DC CB is needed. Different DC CBs have been proposed, prototyped, and tested in the last decade for the application in the MT-HVDC grids [100], [101]. The DC fault interruption in HB-MMC-based MT-HVDC grids has to be ultra-fast (< 3 ms) due to the high rate of rise of the DC current. In practice, to limit the fault current, Fault Current Limiters, in the form of rectors, are added and used for DC fault detection [102]. However, the high value of the inductance (> 150 mH) impacts the controllability of converters and increases the capital cost of the DC grid [103].

Another method to control the fault current is to regulate the pole-to-pole (PP) voltage near the converter, known as a Fault Current Suppression (FCS) method. In [104], [105], a combination of hybrid-MMC and droop control is applied, which regulates the arm voltage to decrease the fault current. A similar concept for an HB-MMC is used in [45], [106]. Furthermore, the authors also compared different FCS methods. Similarly, [107] provides a soft current suppression control in the outer voltage loop. In [108], a notch filter is applied to extract the DC component and to regulate the fault current only during the fault occurrence. The suppression methods mentioned earlier imply PI-based control action, either in the outer voltage loop or by using a circulating current suppression control (CCSC). In [109], a suppression control was proposed for

the FB-MMC MT-HVDC using CSCC and a protection scheme. These controls are based on a mode selection during the fault; thus, the stability of these controls is not determined [110], [111]. The fault interruption creates temporal instability in the DC grid, propagating into AC grids where renewable energy resources are connected, which are more susceptible to disturbances. Hence, post-fault clearance is crucial.

In the existing literature on suppression control, MT-HVDC grids are simplified for the offshore grid and its control for the offline simulation. Thus, the dynamics of the offshore grid are removed. The existing suppression controls are implemented with PI, which introduces inherent slower performance limitations [112], [113]. An optimization-based control like MPC demands high computation time. Thus, in literature, MPC-involved studies use offline simulation as the dependence on time is removed. In practical application, the controller's action must be in the acceptable time range. Hence, implementing the controller in RTS validates the operability of the control law. In the CCSC, a zero-sequence component of dqz-frame current representation can be viewed as one-third of the DC current. However, in the traditional strategies, this current is either left uncontrolled [94] or used in energy control [114].

The following questions are still open to addressed:

- How can an MPC-based controller (RQ1) be effectively utilized to actively regulate the rate of rise of the fault current in HB-MMC-based MT-HVDC grids (RQ2), thereby reducing the operational stress on DC CBs and enhancing fault recovery mechanisms?
- Can such a controller be seamlessly integrated within existing control loops without compromising the system's stability?
- What empirical pieces of evidence can be provided to substantiate the effectiveness of the proposed control strategy for real-world applications, particularly in the context of large-scale offshore wind integration?

RQ4. HOW CAN A ZONAL DC FAULT RIDE-THROUGH SCHEME BE DEVELOPED FOR OFFSHORE MT-HVDC GRIDS?

FSC strategies, such as those manipulating converter state variables, have effectively managed the rate of rise of the fault currents within MT-HVDC grids. The solution to the RQ3 tacks the challenges of mode-dependent strategies by implementing a continuous setpoint adjustment based on local measurements and converter limits. This approach has shown promising results in handling delayed fault interruptions. Nonetheless, grid reconfiguration following DC CB operations introduces difficulties in achieving a smooth, damped recovery, highlighting the need for refined control strategies [115]–[117]. Research advances have explored various approaches, including voltage re-balancing techniques and rapid recovery methods, to enhance MT-HVDC grid resilience and fault recovery capabilities [118]–[123].

Table 1.1 summarises the recently proposed DC fault ride-through (DC-FRT) strategies for MT-HVDC. Irrespective of the topology and sub-module technology of MMC-HVDC, MT-HVDC goes through 3 stages of DC-FRT. Namely, through fault interruption, system recovery, and system attaining a new steady state as depicted

Table 1.1: Existing DC-FRT for MMC-VSC HVDC grid

Literature	SM topology	Converter control mode	HVDC topology	DC-FRT Method	DC-FRT power operation	DC-Zone based	New steady state time	Fault detection and localization
[118]	FB-MMC	Pac-Q, Vdc-Q	Mesh grid	Separate Vdc control at outer loop	Continuous operation	No-zone	71 ms	No, local protection
[119]	FB-MMC	Vdc-Pdc droop, Pac-Q	Mesh grid	Sequence-based	Temporary P & Q stop	No-zone	600 ms	No, local protection
[120]	FB-MMC	Pac-Q, Vdc-Q	Mesh grid	Sequence-based	Temporary P & Q stop	No-zone	100 ms	No, local protection
[121]	FB-MMC	Pac-Q, Vdc-Q	Mesh grid	Sequence-based	Temporary P & Q stop	No-zone	158 ms	Yes, centralized protection
[124]	HB-MMC	Pac-Q, Vdc-Q	Mesh & Radial grid connected via DC CB	Sequence based	Temporary P & Q stop	Yes, but for DC selection	200-300 ms	No, local protection
[125]	HB-MMC	Pac-Q, Vdc-Q	Radial grid	Sequence-based	Temporary P & Q stop	No-zone	20 s	No, local protection
[126]	HB-MMC	Vdc-Pdc droop, Pac-Q	Mesh grid	Vdc-control and CSCC control	Temporary P & Q stop	No-zone	100 ms	No, local protection
[117]	HB-MMC	Vac-f, Vdc-Q	Radial grid	Diode based control	Continuous operation	No-zone	200 ms	No, local protection
[123]	Hybrid-MMC	Pac-Q, Vdc-Q	Mesh grid	Switch mode & sequence based	Temporary P & Q stop	No-zone	100-200 ms	No, local protection
[122]	Hybrid-MMC	Pac-Q	NA	Energy based control	Temporary P stop	No-zone	500 ms	No, local protection

in Fig. 1.7. In the fault interruption stage, the first occurrence of the DC fault is realized, resulting in local protection operation due to threshold violation of arm current and DC-link voltage [121]. Also, [121] describes a communication-based centralized protection algorithm, which takes input from the local protection of the converters. The flag raised by protection (i.e., centralized and/or local) can be used to *'temporary stop P & Q'*[121] or used as input to trigger an FSC [118]. With *'temporary stop P & Q,'* the converters enter *block* state within 2-3 ms after fault [126]. With the blocking of the converter, the infeed power support to the AC grid is removed temporarily. As a result, the fault current is interrupted. Then, a DC disconnector and/or AC breaker isolate the faulty zone or a converter in the MT-HVDC grid. In the case of FSC, the control attempts to minimize the fault current to zero, and then DC CB interrupts the fault and isolates the faulty zone. With FSC, the AC grid is connected to the DC grid, allowing for control over power, a mode referred to as *'continuous P & Q'* [127].

After the fault current is interrupted, the MT-HVDC grid goes through *system recovery* stage. Depending upon which power mode (i.e. *'continuous P & Q'* or *'temporary stop P & Q'*), extra recovery steps are carried out [119]. In case *temporary stop P & Q*, STATCOM mode is activated to support the AC grid. This is followed by DC voltage control in each converter by connecting the DC disconnector. This control regulates the DC link voltage, eliminating the overvoltage and transient in the DC link [118], [124]. In the case of *'continuous P & Q'*, STATCOM mode is bypassed [118]. Also, [125] provided a delayed re-close of converters to avoid DC voltage transients. Once the DC link voltage is within the accepted system voltage boundaries [118], [126], new droop/ramp characteristics [124] or new setpoint [120] are provided by station control or centralized grid control, which results in *'new steady state'*.

The majority of DC-FRT creates a prolonged loss of power to the AC grid, which might result in frequency deviation. Furthermore, the MT-HVDC grid under investigation

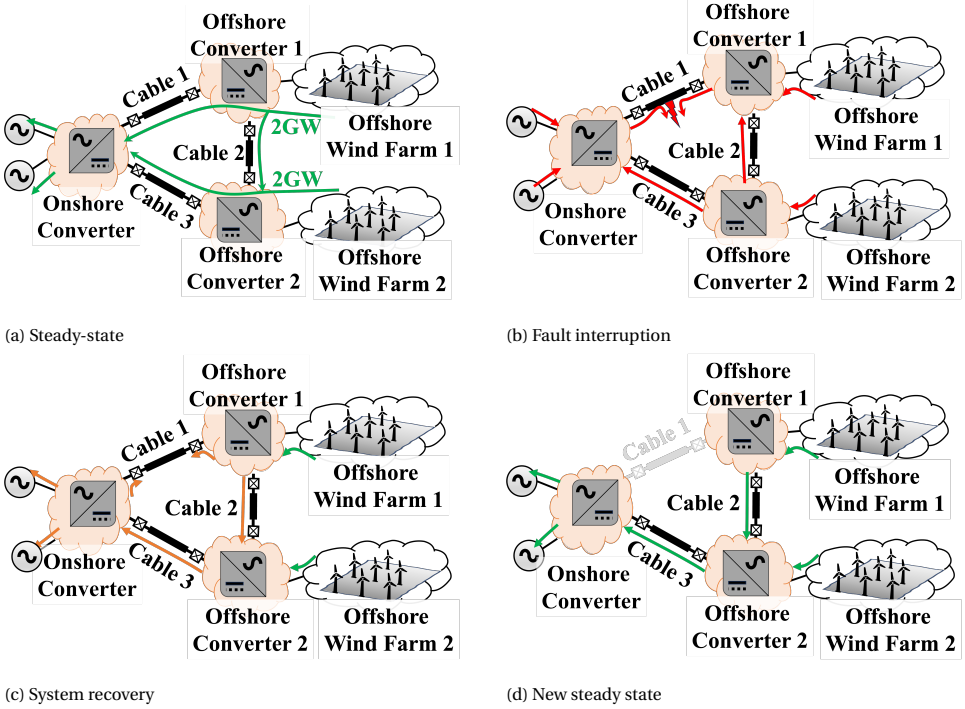

(a) Steady-state

(b) Fault interruption

(c) System recovery

(d) New steady state

Figure 1.7: Pictorial representation of stages involved in DC-FRT

is grid-following and invalid in the current offshore network. Blocking the converter can potentially have adverse effects on the wind power pack. Furthermore, fast DC fault recovery is observed in FB-MMC. However, considering the frequency of fault occurrence v/s operational loss, FB-MMC becomes uneconomical, and current projects focus more on HB-MMC. Similarly, each converter control has only its information during the system recovery. As a result, re-synchronization with other converters leads to current and voltage transients and delayed recovery. In addition, most system recovery cases are not selective and autonomous.

In light of these considerations, the provided solutions of the conducted research results will answer the following question: How can an MPC-based control (RQ1) strategy be developed for offshore MT-HVDC grids (RQ2) to enhance DC fault ride-through capabilities while minimizing the operational and economic impacts of converter blocking and system recovery challenges and reducing reliance on high-speed inter-station communication?

1.6. OUTLINE OF THESIS

The outline of this thesis is as follows :

Chapter 2 introduces currently available HVDC technologies, detailing their structure, components, and control and protection mechanisms at both converter and

system levels. It also presents TenneT's 2GW initiative as a case study for designing and testing advanced MMC control strategies.

Chapter 3 delves into the architecture and operational principles of MMCs within HVDC systems. It outlines traditional control strategies, introduces a detailed analytical model for simulation, and validates this model against online EMT simulations. This chapter answers RQ1 and sets the stage for the advanced MMC control discussions in Chapter 5.

Chapter 4 proposes an improved real-time model for offshore MT-HVDC systems. It covers a network description, computational requirements for real-time applications, and a detailed analysis of core assignments. This chapter aims to address RQ2 and serves as a basis for testing and analyzing advanced control strategies

Chapter 5 explores the application of Model Predictive Control (MPC) in HVDC systems, and highlights its role in enhancing stability and efficiency. It presents the theory, design, and simulation of MPC in MMCs and its practical implementation in MT-HVDC grids. The chapter advocates for MPC's future adoption in HVDC control strategies and answers the RQ1 with the support of Chapter 3.

Chapter 6 presents a novel MPC strategy that applies zero-sequence currents in MMCs to facilitate fault interruption. It includes the control of the fault amplitude by controlling the slope and analysis of the proposed method. The approach assists with fault interruption. It provides an answer to RQ3 and sets a direction for comprehensive future control, optimization, and protection.

Chapter 7 deals with a DC Fault Ride Through Controller (DC-FRTC) for offshore MT-HVDC grids. It validates the controller's effectiveness through an advanced analytical model, demonstrating its ability to dampen oscillations and facilitate rapid recovery after faults, while also being resilient to communication delays. By highlighting its potential to enhance MTDC system reliability and efficiency, the chapter addresses RQ4.

Chapter 8 concludes the thesis, summarizing the findings and contributions of the research.

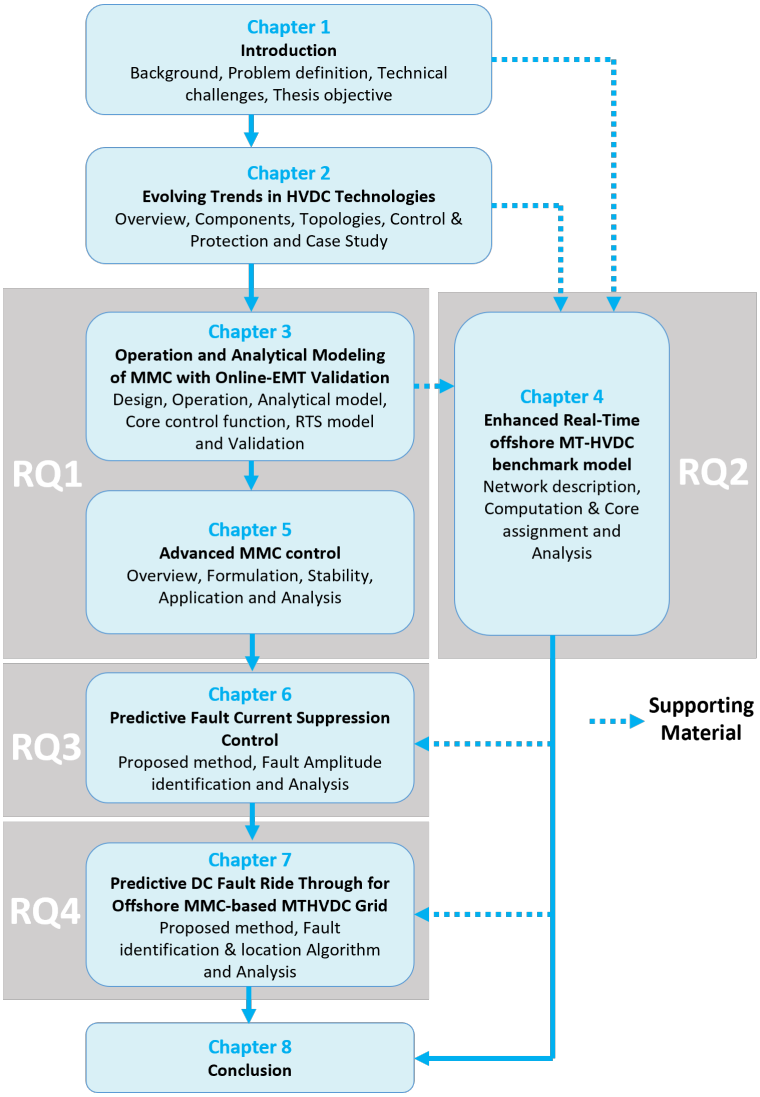

Figure 1.8: Diagram showing the relation between the chapters of this thesis.

2

EVOLVING TRENDS IN HVDC TECHNOLOGIES

This chapter provides an in-depth overview of HVDC technology, emphasizing its flexibility and power density superiority compared to conventional systems. It discusses the evolution of HVDC from LCC to the more advanced VSC, highlighting their operational principles, advantages, and applications in modern power grids. The chapter also delves into the components and topologies of VSC-HVDC systems, covering key elements like AC/DC converters, fault-current limiting devices, and transmission lines. It outlines the evolution of control and protection strategies, focusing on the converter valve protection and offshore MTDC grid as a focus area, particularly within the context of TenneT's expansive 2GW program and Target Grid. The chapter sets the stage for detailed discussions on these technologies in subsequent chapters.

2.1. OVERVIEW OF HVDC TECHNOLOGY

HVDC power system offers superior flexibility, functionality, and higher power density compared to the conventional HVAC system [128]. HVDC's capability to connect networks with different frequencies and unsynchronized grids and its lower cost for long-distance power transmission due to reduced reactive power requirements make it a preferred option. Additionally, HVDC's unique blocking capability prevents the escalation of AC fault levels, and its power quality support function is particularly advantageous for lower inertia AC systems [27].

2.1.1. LINE COMMUTATED CONVERTER

Since its inception in 1954, LCC technology, also known as HVDC classic topology, has been pivotal in power transmission. The advent of thyristor valves enabled significant advancements, facilitating bulk power transfer at system voltages up to 800 kV and potentially up to 1100 kV [27], [129]. LCCs operate primarily in the first quadrant of current-voltage characteristics. They can be turned on by a gate signal, however, they require line commutation (i.e., zero current crossings) for turning off. Consequently, LCCs demand a relatively robust grid connection at the AC point of common coupling (PoC), typically with a short circuit ratio (SCR) greater than 3. In scenarios with approximately 2 to 3 SCR, reactive power compensation devices are often necessary. LCC technologies generally require reactive power up to 60% of the active power rating, irrespective of their operation mode (inverter or rectifier) [130].

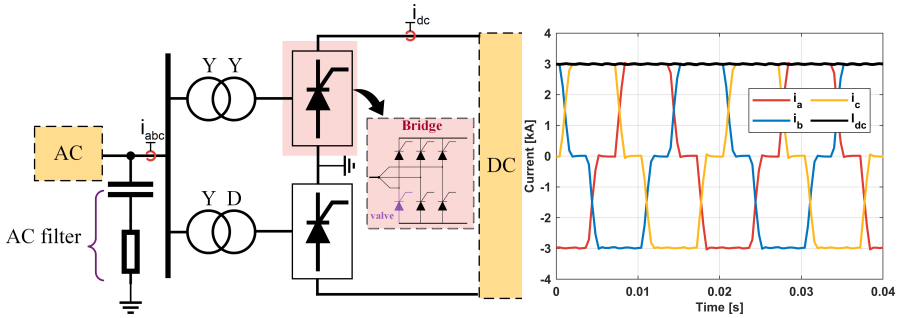

Figure 2.1: (a) Simplified single line diagram of an LCC Converter station; (b) AC and DC measurement at PoC.

An LCC converter station comprises a pair of six-pulse thyristor valves forming a *Graetz bridge*. This configuration involves a series connection on the DC side and a parallel connection on the AC side, optimizing harmonic mitigation on the AC side and voltage level enhancement on the DC side. The AC parallel connection is achieved by linking one six-pulse thyristor valve to a $Y-D$ transformer and another to a $Y-Y$ transformer. Additionally, AC filters are installed to minimize residual low-order harmonics on both AC and DC sides.

2.1.2. VOLTAGE SOURCE CONVERTERS

The introduction of VSCs in the 1980s, leveraging IGBTs, marked a significant leap in high-voltage transmission capabilities, supporting systems of up to 600 kV [27]. A 1997 prototype in central Sweden, spanning 10 km and rated at 3 MW / ±10 kV, showcased the VSC HVDC's feasibility. This technology surpassed LCC limitations, such as high reactive power demands and the absence of black start capabilities, offering a more efficient and compact design suitable for high-power applications.

VSC technology advancements have eliminated the need for extensive filtering, thereby reducing station footprints. This attribute is especially beneficial for offshore energy integration. VSCs also provide consistent voltage output and flexible power control, making them ideal for MTDC grids, which improves the efficiency and robustness of power distribution networks [128], [131].

Semiconductor material innovations have further boosted converter efficiency, curtailing losses to approximately 1-1.5% per converter [132]. Integrated into modern power grids, VSC-HVDC systems, with advanced control and protection, ensure grid stability during power supply or demand fluctuations.

The operational principle of VSCs is to regulate voltage behind impedance, enabling active and reactive power provision. Typically controlled as voltage-controlled current sources (*grid following* converters), VSCs in this role offer a general operational framework. This section primarily considers the 2-level VSC converter, with detailed discussions on other topologies in subsequent chapters.

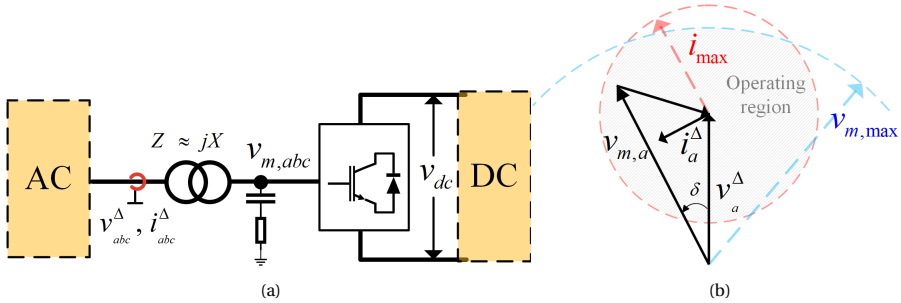

Figure 2.2: (a) Simplified single line diagram of a VSC Converter station; (b) Phasor diagram with converter limits.

The phasor diagram in Figure 2.2 illustrates the fundamental operating philosophy of the VSC. Active and reactive power exchanges over impedance can be expressed as:

$$S = P_{ac} + jQ_{ac} = v_{m,a} i_a^{\Delta *}.$$

Here, $v_{m,k}$ denotes the modulating voltage of phase k, and i_k^{Δ} is the phase k current, where $k \in a, b, c$. The modulating voltage $v_{m,k}$ is a function of the modulation index and pole voltage ($\frac{v_d c}{2}$). Considering only the reactive component (x) in the impedance (z), the equation can be simplified as:

$$P_{ac} = \frac{|v_{m,a}||v_a^{\Delta}|\sin(\delta)}{x}, Q_{ac} = \frac{|v_m||v_a^{\Delta}|\cos(\delta) - |v_a^{\Delta}|^2}{x}. \tag{2.1}$$

In this equation, δ represents the angle between $v_{m,a}$ and v_a^{Δ}. Within the operating region defined by current (i_{max}) and voltage (v_{max}) limits, the modulating voltage can be controlled to provide independent active and reactive power.

As equation (2.1) shows, there is a relation between P_{ac} and $\left|v_a^{\Delta}\right|$ as well as between Q_{ac} and δ. Therefore, a *'vector control'* method is typically employed in onshore converters [133]. This control approach utilizes a rotating dq reference frame, synchronized with the grid voltage, to independently control P_{ac} and Q_{ac} via d and q currents, respectively. The implementation of this control strategy is further explored in Chapter 3.

In offshore or weak-grid-connected VSC converters, a *'direct control'* method is used, which manipulates P_{ac} through δ and Q_{ac} through $\left|v_a^{\Delta}\right|$, also known as *'power synchronization control'* [134].

2.2. VSC-HVDC SYSTEMS: COMPONENTS AND TOPOLOGIES

HVDC is the most economical and efficient high-power transmission medium. Worldwide, there are 198 HVDC systems connections [35], [135]–[137]. It can transfer power over $6GW$ with a voltage rating of $\pm 800kV$. Based on the power level, geographical and social-economical factors, particular specific HVDC system topologies are chosen [138], [139]. Nowadays, VSC-HVDC is planned and commissioned, especially MMC. Hence, the thesis is directed towards the MMC-based HVDC system. The operation of MMC will be discussed in chapter 3. However, the following section will highlight the key elements that exist in the MMC-VSC HVDC System.

2.2.1. KEY ELEMENTS OF VSC-HVDC SYSTEM: AN OVERVIEW

AC/DC CONVERTER UNIT

A converter unit comprises all the equipment that lies within AC- and DC-PoC. This includes a converter transformer, startup insertion resistor, arm reactor, valve, control & protection equipment, and auxiliary devices used in the AC/DC conversion process, as shown in Figure 2.3.

The converter transformer is a two-winding, star-delta configuration. A tertiary winding may provide auxiliary power to the converter station from the AC system. The AC grid side is connected to the transformer's star side, and the DC grid side to the delta side. The delta connection prevents the low-frequency zero-sequence voltage from being injected into the AC system [140]. Furthermore, the leakage inductance of the transformer and the arm rector provide sufficient reactance between the AC-side voltage and the valve required to control the AC grid current. Due to the near-pure sinusoidal waveform of the converter's voltage, a standard AC transformer is adopted. This transformer also provides galvanic isolation between the AC and DC grids.

The pre-insertion resistors are placed between the AC bus and the converter transformer. To limit the inrush current produced by charging the sub-module (SM) capacitors, DC filters, DC line/cable, and the remote station, the resistor is switched on for a few seconds and bypassed after a dedicated set period. The arm reactor is connected in series with a converter valve. The arm reactor is placed on the converter's AC or DC side. The arm reactor limits the circulating current between the converter

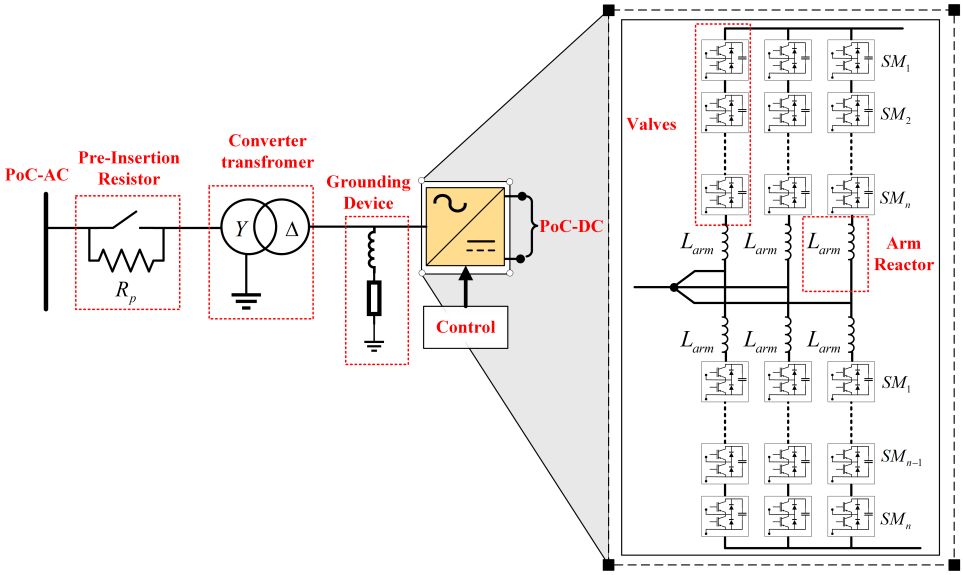

Figure 2.3: Single line diagram example of AC/DC converter unit.

valves. Furthermore, it also limits the rate of rise of the fault current. Each converter valve consists of N_{SM} SMs. The basic structure of SM consists of complementary pair(s) of semiconductor switches in parallel with the capacitor. These are assembled in series to provide the desired voltage.

FAULT-CURRENT LIMITING DEVICES

Fault-current limiting devices (FLD) are used to limit the rate and magnitude of fault current in the HVDC system [101], [141], [142]. This control over fault current provides an extra time window for fault separation devices (FSD) and converter control systems. FLDs are typically placed, at the PoC-DC terminal of the AC/DC converter unit, at the ends of the cable, and at the DC side interconnection points of different HVDC systems as shown in Figure 2.4. Besides, the core function of FLD, FLD should have minimum influence in steady-state operation with lower loss across it. Furthermore, it should provide quick responses during fault periods and should reset after fault isolation. The technologically matured FLD, which is deployed in most HVDC systems, is a dry-type air core coil, also known as *'current limiting reactor (CLR)'* [143]. However, the large capacity of CLR is not recommended as it increases the cost and creates instability in the HVDC system. Besides this, there are also experimental and under R&D FLD [144], [145], namely, solid-state fault current limiter (SSFCL) and superconducting current limiter (SCCL).

SSFCLs use a parallel combination of semiconductor switches, series capacitors and inductors, and metal oxide varistors (MOV). During normal operation, current flows via a semiconductor switch; however, during a fault, the semiconductor switch turns off, resulting in the flow of fault current into the inductor, which results in a decreased rate

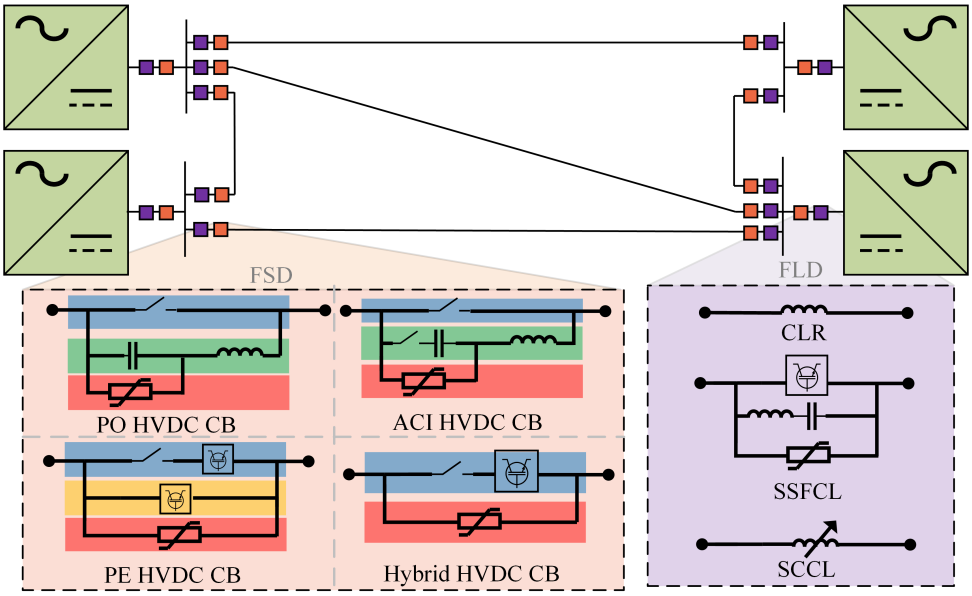

Figure 2.4: A simplified pictorial representation of FLDs and FSDs and their location in mesh HVDC grid.

of rise of fault current. Furthermore, MOV and capacitors are used to limit the magnitude and rate of rise of impulse voltage caused by a change in current through the inductor. In SCCL, the electrical characteristic of the fault current. An expensive cooling system is used to maintain the superconductor's electrical characteristics. This thesis uses only CLR due to its technological readiness level.

FAULT SEPARATION DEVICES

A converter unit, HVDC circuit breaker (HVDC CB), or switches can provide the DC fault separation functionality. The fault separation devices (FSD) are selected based on the type of DC line, adjacent AC/DC intersystem faults, equivalent DC system impedance, consequent fault frequency, recovery attempt, and minimum time between recovery attempts [143]. This thesis focuses on the HVDC CB for DC fault interruption and separation.

The basic functionality of HVDC CB is to provide a counter voltage that is higher than the system voltage and sufficient enough to drive the fault current to the residual current in a fault current suppression time. To generate and maintain the counter voltage, different HVDC CB technologies are classified into four major categories [143]:

- **Passive Oscillation (PO HVDC CB)**: With the opening of the main current circuit, an arc voltage creates an oscillating current due to the LC series circuit in the commutation branch [142]. Rising voltage across the capacitor causes MOV to absorb energy in the energy absorption branch. This HVDC CB is used for lower current commutation due to longer fault cleaning time.

- **Power Electronic (PE HVDC CB)**: In this HVDC CB [146], the main current and commutation branch are fused. During normal operation, current flows through the parallel-series combination of power semiconductor devices comprising the main current and commutation branch. With trip command, power semiconductor devices can operate within a few microseconds, forcing fault current to flow through a high-impedance energy absorption branch. However, due to the large array of parallel-series semiconductor devices, on-state losses are higher for HVDC transmission system applications.

- **Active Current Injection (ACI HVDC CB)**: In a steady state, current flows through the main current branch, which consists of a current-interrupting device [100], [147]. A vacuum interrupter is commonly used due to its high dielectric strength. Furthermore, it has lower on-state loss compared to PE HVDC CB. The current interrupting device opens its closed contacts upon receiving the trip command. After a few milliseconds, the dielectric strength between the contact is sufficient to handle a higher voltage across it. A switch in the commutation branch triggers a current injection source. This source injects the current into the main current branch in the opposite direction to the fault current. This creates an artificial current zero in the main current branch. Resulting in temporary current flow into the commutation branch charging the capacitor and then to the energy absorption branch.

- **Hybrid (Hybrid HVDC CB)**: This HVDC CB is a combination of ACI and PE HVDC CB [148]. The main branch consists of a series-parallel power semiconductor in series with a current interruption device. The operating principle of hybrid HVDC CB is that after the trip command fault current will commute to the commutation branches in the main current branch. Commutation switches are opened after sufficient dielectric strength in the current interruption device. This results in a fault current commute to the commutation branch and then to the energy absorption branch.

This thesis considers VSC-assisted resonate current (VARC) HVDC CB [100]. This DC breaker is an ACI, and the operation is explained in a later chapter.

DC TRANSMISSION LINE

HVDC cables enable bulk power transmission over long distances without charging the transmission line's capacitance with alternating voltage. This makes HVDC a lucrative and highly efficient option for power transfer. The compact transistor-based VSC technology results in the absence of the need to change voltage polarity for reversal of power direction. This has made extruded insulation the preferred choice for HVDC cable systems. Reverse voltage polarity causes superposition of transient stresses on steady-state DC stress, which could be detrimental to the performance of the extruded insulation due to the presence of space charges and consequent localized increase in the electric stress. Extruded insulation makes the cable manufacturing process faster, more cost-effective, and environmentally friendly relative to oil-impregnated paper insulation. Extruded insulation with cross-linked polyethylene (XLPE) has now been serviced at up to 400 kV [149]. The applied voltage level of extruded cables is 640 kV [150].

The present clean energy transition in Europe [4], which aims to integrate maximum offshore wind into the electrical grid [151] along with land-based energy highways that are currently being implemented in Germany [152], all make use of extruded insulation systems, primarily based on XLPE technology at 525 kV.

The performance of the DC cables in service is strongly governed by their electric conductivity, which defines the distribution of the electric field under DC voltage. As the cable carries the load current, joule heating of the conductor creates a temperature gradient over the entire thickness of the cable insulation. This temperature drop is a specified design value for a particular DC extruded insulation. It is verified for the cables in long-term qualification and de-sign-verification tests with its joints and termination. This way, the cables and their electrical interface with associated cable accessories are tested and qualified. Additional insulation heating might result from the leakage current through the insulation due to the electric stress. The leakage current is a characteristic phenomenon that plays a decisive role in demonstrating the electrical integrity of the extruded DC cable insulation system as it quantifies the dielectric loss. The effect is cyclic as the increased temperature of the insulation would increase its losses, which will further increase its electrical conductivity. Such sequential events can lead to thermal runaway if the conductivity exceeds the upper limit's threshold. In DC, the pattern in the electrical field distribution is controlled by temperature-dependent conductivity. The highest electrical stress is encountered near the cable screen at high loads, whereas at no loads, it is near the conductor. In this thesis, these factors have been considered in cable modeling.

2.2.2. HVDC SYSTEM TOPOLOGIES

In a nutshell, the HVDC system topologies can be categorized into two categories. Firstly, how are the AC/DC converters connected in a converter station, and secondly, how these converter stations are connected?

AC/DC CONVERTER TOPOLOGIES

The AC/DC converter topologies can be classified based on the number of poles, station grounding, and neutral return. In converter topology **A**, one converter is connected to two poles (.i.e $+pole$ and $-pole$); hence, it's called as *'Symmetrical Monopole'*. In this topology, there is no return path or conductor present. The converter topologies **B, C** are called *'Asymmetrical Monopole'* because they have one converter with one pole connected to a high voltage (HV) pole, and another pole is connected to the neutral return path. The neutral return path can be a dedicated metallic return conductor (DMR) and earth electrode. As a result, it can be classified as *'Asymmetrical Monopole with DMR'* and *'Asymmetrical Monopole with earth electrode return'*. In addition, based on the type of converter station earthing, it can be sub-classified as *'Direct Earthed'* or *'Impedance Earthed'*. The topology, denoted as **D, E** in Figure 2.5, consists of two converters with one of the converter poles connected to the HV pole, while the other converter pole connected to the neutral return path indicates *'Bipole'* topology. Similar to *'Monopole'*, it can be further categorized corresponding to the neutral return path. If a DMR is used, it is known as *'Bipole with DMR'*. When an HV pole conductor (metallic return) is used during contingency, this special topology is called *'Rigid Bipole'*. In the

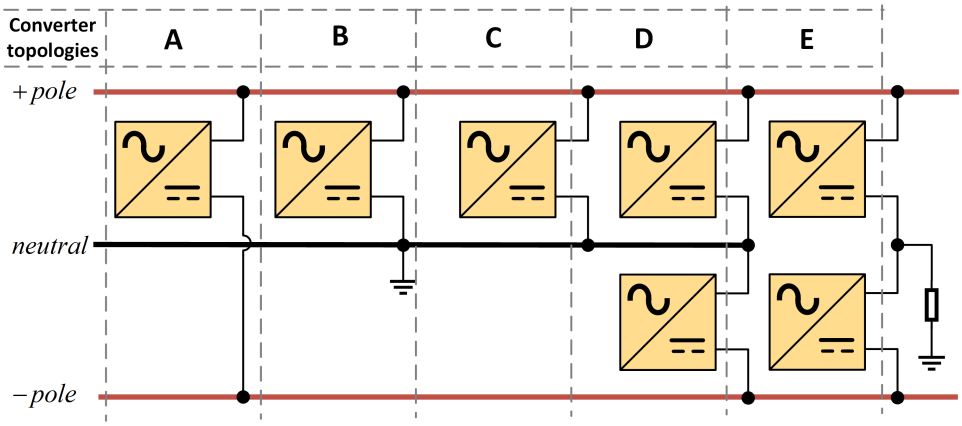

Figure 2.5: Different AC/DC converter station topologies [127].

case of *'Bipole'*, when the station is earthed through impedance, then it is called a *'Bipole with DMR, impedance earthed'* or a *'Rigid Bipole, impedance earthed'*

HVDC SYSTEM CONFIGURATION

Figure 2.6 highlights the most common configuration of the VSC-HVDC grids.

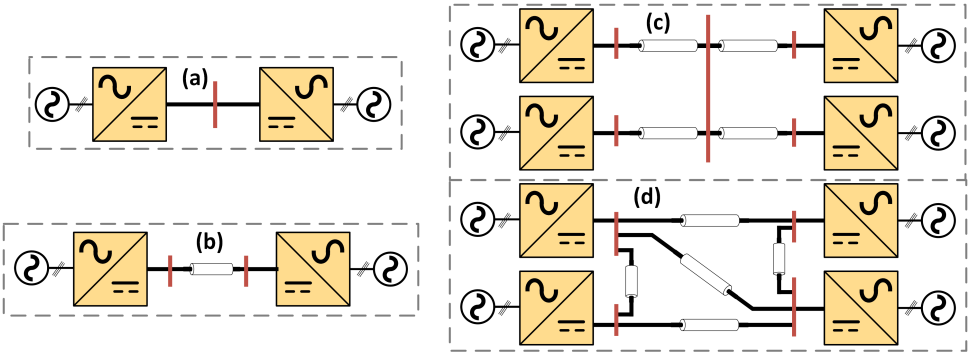

Figure 2.6: Different HVDC grid configurations: (a) back-to-back, (b) point-to-point, (c) Radial, and (d) mesh.

- **back-to-back (b2b) HVDC system**: Typically, this topology is used to interconnect two different asynchronous AC networks near each other [127]. Here, two converters are placed in the same converter station and coupled via a short section of the DC busbar. The DC busbar keeps the DC current high with a lower DC pole voltage ($\leq 150kV$) [130].

- **point-to-point (p2p) HVDC system**: The difference between the previous HVDC system and this is that DC cables or Overhead lines are used to connect two geographically separated areas. This is a common configuration adopted in the

current offshore HVDC system. Based on the type of AC/DC converter topologies, HVDC system can have an $N-1$ contingency for transmitting power over a DC system.

- **Radial HVDC system:** This HVDC system is an extension of p2p, where a common node is created, which acts as a DC switching station. Hence, during contingency, each p2p can operate independently.
- **Mesh HVDC system**: In a mesh topology, more cable/OHLs are connected at the PoC-DC. This configuration provides higher reliability as there are sufficient paths for DC power to flow.

This thesis considers a *Symmetrical Monopole* and *Bipole* Mesh HVDC system for control and protection studies.

2.3. EVOLUTION OF CONTROL AND PROTECTION STRATEGIES IN VSC-HVDC SYSTEMS

Figure 2.7 illustrates the general control hierarchy of the VSC-HVDC. In the VSC-HVDC system, we have two control functions [74], [153]: (1) core control functions and (2) coordinating control functions. The core control functions are restricted to a converter station and perform the control objectives and set points the coordinating controls provide. The core control function primarily focuses on permanently enabling energy balance in the DC grid. It also checks if the operating points are within the device limits. This control function will be explained in chapter 3. The coordinating control function

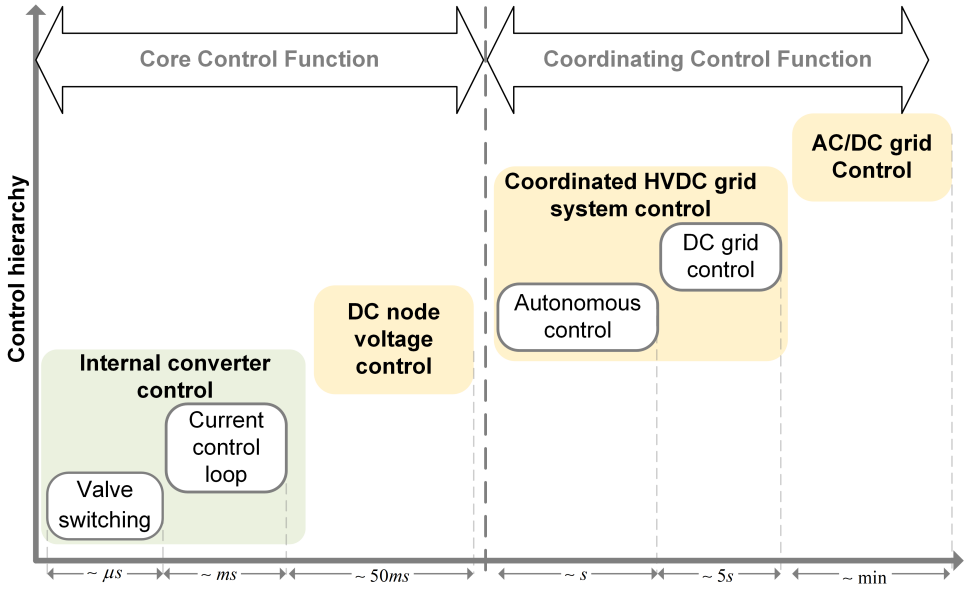

Figure 2.7: Typical control operation time ranges and control hierarchy [127].

provides an optimized and inter-operable control input and controller parameter to core control functions. The objective of the optimization problem is to minimize the power loss in AC and DC grids, to have fast set-point adaptability of the converter station, and to coordinate ancillary services. Due to remote measurements, the coordinating control function is centralized in nature and needs communication. Hence, the response time of the coordinating control function is slower compared to the core control function. The coordinating control function consists of two layers: coordinated HVDC grid system control and AC/DC grid control.

The coordinated HVDC grid system control has a further sub-layer based on autonomous and non-autonomous control. The autonomous control is activated upon a system state change (i.e., alert or emergency state). This control provides a countermeasure to bring the system into a normal or restoration state. The impact of countermeasure categories in terms of priority to avoid any rules conflict. The non-autonomous control, also known as 'DC grid control', maintains the initial converter schedules dispatched by the AC/DC grid control. It supervises the core control function modes of all converters in the HVDC system, such that the system is within pre-described safety limits. The DC grid control acts as the central interface for getting power flow information and has access to all electrical node measurements, equipment status, and command messages of the HVDC system. In addition to its primary objective, this control also has a secondary objective; after an unscheduled event, it optimizes the DC network operation and reacts to changes created by power exchange corresponding to changes in the new converter control mode. It also provides important key sequences in the startup and shutdown of the HVDC system. It also provides post-investigation for DC faults. Furthermore, this control can be distributed into multiple controls for redundancy purposes.

The AC/DC grid control has the highest position in the control hierarchy of the HVDC system. It is a common divisor between TSOs of connected AC grids and connected HVDC systems. The AC/DC grid control's main objective is to provide active and reactive power setpoints for conventional power plants as well as HVDC transmission systems to satisfy the electricity market constraints, mixed AC/DC power flow optimization, local optimization of one or multiple TSOs, renewable energy forecast, security of both systems and ensure the stability of entire AC/DC grid. The AC/DC grid control output is an initial dispatch schedule for all the converter stations and is valid until the next dispatch cycle. This thesis revolves around the core control function and the impact of fast control on system performance.

The protection strategies of the HVDC system can be classified based on the fault location [17], [143]. However, in this thesis two protection strategies are elaborated: DC grid and converter valve. The DC grid protection strategies can be classified based on the philosophy used to detect the fault: traveling wave, DC over-current, current differential, over-/under-voltage protection, and $\frac{dv}{dt}$ based method.

The traveling wave analysis-based protection method uses Fourier transform or wavelet analysis, which requires high sampling measurements (>1 MHz). In this fault detection method, a rapid change in PoC-DC measurements is monitored caused by the traveling wave propagated from the fault location to the line terminals. Due to the high sampling rate, traveling wave protection has limited applicability. DC over-current

protection typically has a DC amplitude threshold, which triggers a trip signal upon violation. Typically, this is considered backup protection for mesh grids. Like AC protection, DC current differential protection comprises the current measurements at the POC-DC, and if the difference and time duration are violated, then the trip command is flagged. Since it is a communication-based protection, it is used as backup protection. The over-/under-voltage protection is also considered backup protection as it waits for the DC voltage to recover. When it is not recovered, it sends a trip command. In $\frac{dv}{dt}$ based method, $\frac{dv}{dt}$ is determined by propagated traveling wave from fault location across the shunt capacitor. When the measured rate exceeds the threshold, the trip signal is raised. Due to its simplicity and adequate detection speed, it is recommended as primary protection for Mesh grids.

Protection strategies for converter valves are crucial for the operational safety of the HVDC systems. While specific methods may vary among vendors, they are broadly classified into the following categories [127]:

- **Valve Over-Current Protection:** It is integrated directly within the valve control unit, and this protection mechanism detects any abnormal current flow or surges in the valve. It is designed to operate swiftly, typically within a few hundred microseconds, to mitigate potential damages or system instability.
- **Submodules Over- and Under-Voltage Protection:** This protection is also situated in the valve control unit and monitors the voltage conditions of each submodule. It ensures that all submodules operate within their specified voltage ranges, reacting quickly to over- or under-voltage events, usually within a few hundred microseconds.

Deploying these protective measures can lead to different operational outcomes, with the most common being the temporary or permanent blocking of the converter. Such actions are essential to prevent damage to the converter components and ensure the overall stability and performance of the power system.

2.4. CASE STUDY: TENNET'S 2GW PROGRAM AND TARGET GRID

TenneT, one of the North Sea TSO, has unveiled an expansive plan for a transnational offshore grid expansion set for 2045, as depicted in Figure 2.8 [10]. This visionary Target Grid is designed to incorporate multi-energy hubs, seamlessly integrating HVAC and HVDC connections to channel North Sea wind power efficiently to the onshore grids of Germany and the Netherlands. Central to this endeavor is the implementation of next-generation 2GW HVDC converter platforms, a cornerstone of the 2GW program [29]. These platforms are envisaged as energy 'superhighways', providing robust, high-capacity channels to supply power to industrial clusters and meet the burgeoning energy demands in the region.

The 2GW program's converter stations aim to facilitate future expansions from point-to-point connections to more complex multi-terminal configurations through MPI. This approach is expected to substantially enhance grid integration, allowing multiple wind farms to connect to each converter platform, thereby augmenting the

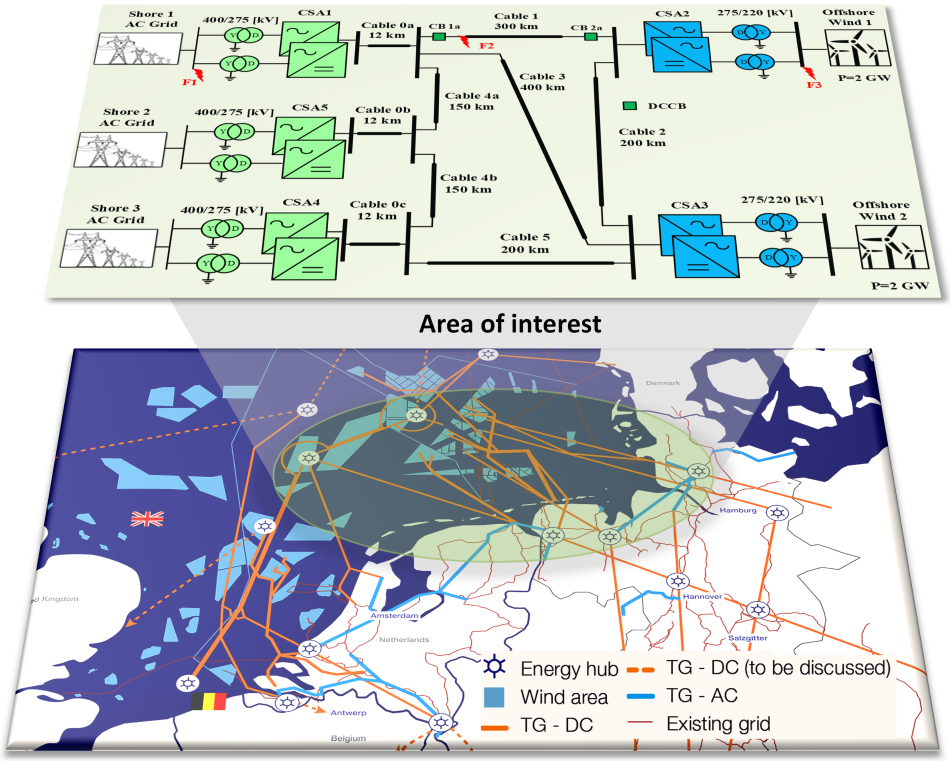

Figure 2.8: TenneT's Target Grid and area of interest for this thesis [10].

overall reliability and efficiency of the energy supply. Such strategic expansions underpin TenneT's commitment to fostering a sustainable, reliable, and future-proof energy infrastructure, leveraging cutting-edge technology to meet the challenges and opportunities of a rapidly evolving energy landscape.

2.4.1. OFFSHORE MTDC GRID: A FOCUS AREA

This thesis focuses on the offshore MTDC grid as an area of interest and is simulated in online EMT environment as highlighted in Figure 2.8. This section of the grid is selected for its intricate interconnection of various subsystems and its crucial role in the overall performance and reliability of TenneT's Target Grid. The offshore MTDC grid, characterized by its ±525 kV DC voltage rating and bipolar DMR configurations, represents a complex yet critical segment of the broader network.

Real-time simulations are indispensable for understanding and optimizing the operational requirements and complex dynamics of the MTDC grid. They provide essential insights for detailed multivendor studies, system testing, validation, and optimization, predicting system behavior under various scenarios. The forthcoming network models, as discussed in later chapters, aim to push existing benchmarks further by incorporating real-time wind gust modeling, HVDC CB, and innovative sea-land DMR cable models. Such enhancements are vital for capturing the grid's dynamic behavior, testing the influence of developed control laws, and ensuring broader range stability.

As the thesis unfolds, it will delve deeper into advanced control laws and their applications, particularly focusing on Grid forming control, Fault Current Suppression, and DC Fault Ride-Through Schemes. The meticulous simulation methodologies and comprehensive results are expected to provide deep insights into the functioning and optimization of the MTDC grid, aligning with the objectives of TenneT's 2GW program. These detailed explorations are crucial for advancing the HVDC technology, catering to the specific needs of large-scale renewable integration projects, and setting a benchmark for developing sophisticated control strategies. This case study effectively demonstrates the contribution of HVDC systems in modern energy infrastructures, emphasizing the importance of continuous innovation in this field.

3

Operation and Analytical Modeling of MMC with Online EMT Validation

This chapter comprehensively explores MMCs in HVDC transmission. It traces the historical evolution of power electronic converters to MMCs, deals with the design and operation of the half-bridge sub-module, presents a detailed analytical model for simulation, dissects the core control function, and explores real-time simulation models using the RTDS©. A comparative analysis between analytical and real-time simulation models highlights the analytical model's suitability for advanced control development. In summary, this chapter provides a holistic understanding of MMCs, contributing to their ongoing development and application in modern HVDC transmission systems.

Parts of this chapter have been published in : A. Shetgaonkar, A. Lekić, J.L. Rueda Torres, P. Palensky, "Microsecond enhanced indirect model predictive control for dynamic power management in MMC units," *Energies*, vol. 14, no. 11, pp. 3318, 2021, MDPI.

3.1. LEAP FROM TWO-LEVEL VSCS TO MULTILEVEL VSCS

Power electronic converters are used for the AC to DC and DC to AC conversions. Until 1970, current source converters (CSCs) were adopted due to their inherent line commutating feature. Due to the presence of high-current devices, like thyristors and mercury arcs, this type of converters were extended to HVDC transmission applications [154], [155]

Apart from the high-current handling capability, one of the drawbacks faced by the CSC was the lack of turn-off capability. In 1990, this drawback was overcome by the introduction of the IGBT, which led to a new category of converters known as voltage source converters [130], [156], [157]. The ability to forcibly commute current and high controllability with improved harmonic performance made VSC the ideal candidate for grid integration with renewable energy resources. Currently, most HVDC transmission projects planned are based on VSC technology. Among the different topologies of the VSC, two-level, three-level diode-clamped, and modular multilevel converter topologies are considered for HVDC applications [18], [158].

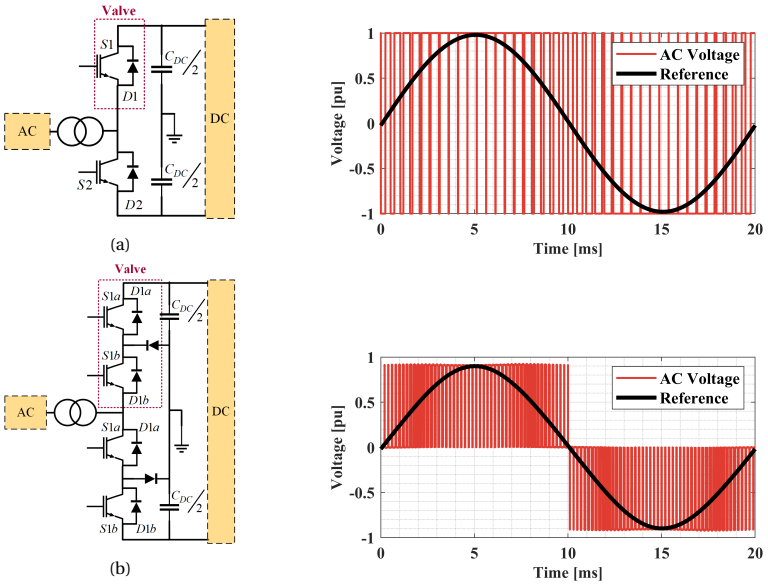

Figure 3.1: Single phase representation of (a) a two-level converter and (b) a three-level diode clamped converter

A single-phase representation of two-level and three-level diode clamped VSCs are shown in Figure 3.1a and 3.1b, respectively. Both converters make use of a series of semiconductor devices (typically IGBTs) in a valve, which are controlled such that a desired power flow is achieved between AC and DC systems. These converters are driven by making use of the Pulse-Width Modulation (PWM) technique, which yields an output AC voltage shown on the right-hand side of Figure 3.1a and 3.1b, respectively. A capacitor C_{dc} is applied to eliminate the DC harmonics.

The series connection of semiconductor devices yields different technical and

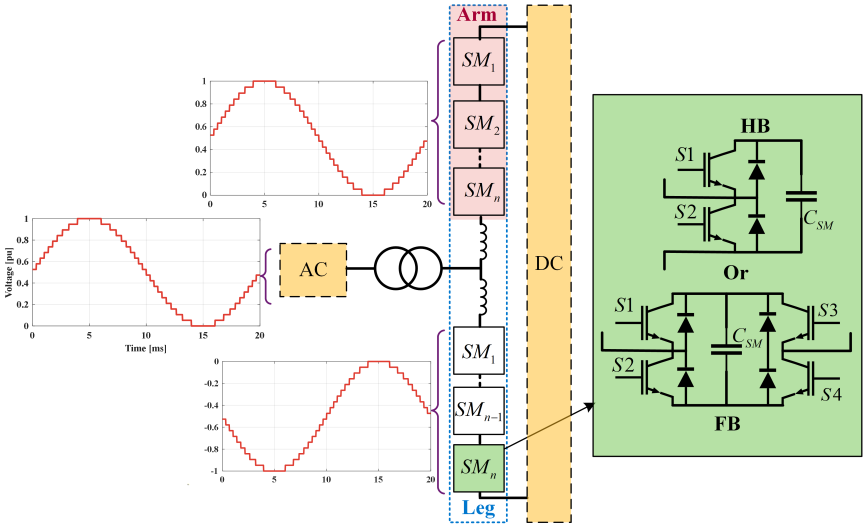

Figure 3.2: Single phase representation of MMC with AC voltage waveform

economic challenges; firstly, a high voltage stress in the valve is experienced due to uneven voltage shared between the series connected semiconductor devices [127], [159]. Secondly, to reduce the harmonics near fundamental frequency, a high switching frequency is embraced, which in return causes higher switching losses. Considering the high-power applications, these losses rise to gigawatts. Thirdly, the size of the AC filters takes a considerable footprint and is costly. By addressing these challenges, two- and three-level converters are not commercially preferred for HVDC applications [130].

Instead, the transition from two- and three-level converters to multilevel converters was motivated due to their high scalability and ability to operate on high power. Besides, the multilevel converter provides a sinusoidal AC voltage waveform with lower switching losses. Among the different multilevel converter topologies, the MMC is commercially recognized for VSC-HVDC transmission [160]. Based on the type of sub-modules (SMs), they are classified as half-bridge (HB) MMC or full-bridge (FB) MMC. Figure 3.2 demonstrates the single-phase representation of MMC with HB and FB SM. HB-MMC is considered the default topology in this thesis due to lower semiconductor switches and ongoing practical projects [29].

3.2. DESIGN AND OPERATION OF HB-MMC

The MMC is a cascaded multilevel converter, where SM is called the *building block* of the converter. An HB-SM can be considered as a two-level converter with a DC capacitor (C_{SM}) parallel to switches ($S1$ and $S2$) as seen in Figure 3.2. External connection to an HB-SM is made at the mid-point of these switches and one of the terminals of C_{SM}. HB-SM has two possible switching states, namely, *'insertion'* and *'bypass'*. During the *'insertion'* state, the S1 is a turn-on and S2 is a turn-off. The voltage across the SM will rise or fall depending on the current direction through the SM. During the *'bypass'* state, the

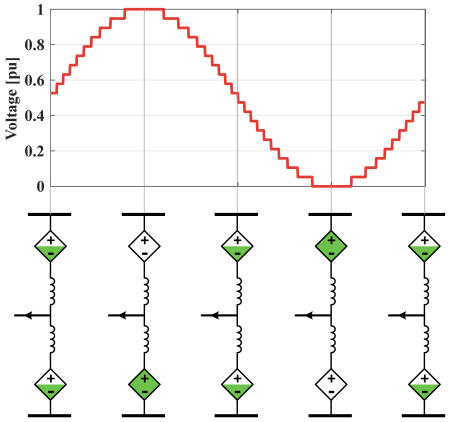

Figure 3.3: Voltages in a leg of an MMC (green colour indicates the percentage of voltage ϵ [0, 1])

S2 is turned on, resulting in a short circuit across the SM terminal. Beside these states, there is another state called a *'blocking'* state, when both switches are turned off. During this state, the SM's current direction derives the voltage across the SM as anti-parallel diodes ($D1$ and $D2$) conduct. This state operates only during specific conditions like energization and certain emergencies.

The structure of the three-phase MMC consists of a *leg* per phase as shown in Figure 3.2. Each *leg* consists of two *arm*s. Each *arm* consists of a series connection of SM strings and a *arm* reactor. The purpose of the *arm* reactor is to avoid any parallel connection of voltage source created by the SM string. The mid-point of both arms creates an AC phase terminal.

In essence, by regulating the voltage of the SM string in the six arms of the converter, the desired DC- and AC-side voltage level can be achieved. A simplified version of MMC operation in a leg is illustrated in Figure 3.3 over a fundamental cycle. The sum of the upper and lower SM string voltages results in a desired PP DC-side voltage, and the difference results in an AC-side voltage.

3.3. ANALYTICAL MODEL OF A THREE-PHASE MMC UNIT

The methodology that is reported in [92] is used as an analytical model of MMC. This MMC model uses multiple dqz-frames, enabling simulation for both balanced and unbalanced operating scenarios. For the analysis it is considered an MMC design as depicted in Fig. 3.4. In Fig. 3.4 with SMs are denoted the H-bridge submodules, L_r, and R_r are reactor's inductance and resistance, L_{arm} and R_{arm} are equivalent arms inductance and resistance. Each arm has N_{SM} number of Sub-modules (SMs) connected in series. The sub-modules are modeled as average equivalent with currents and voltages

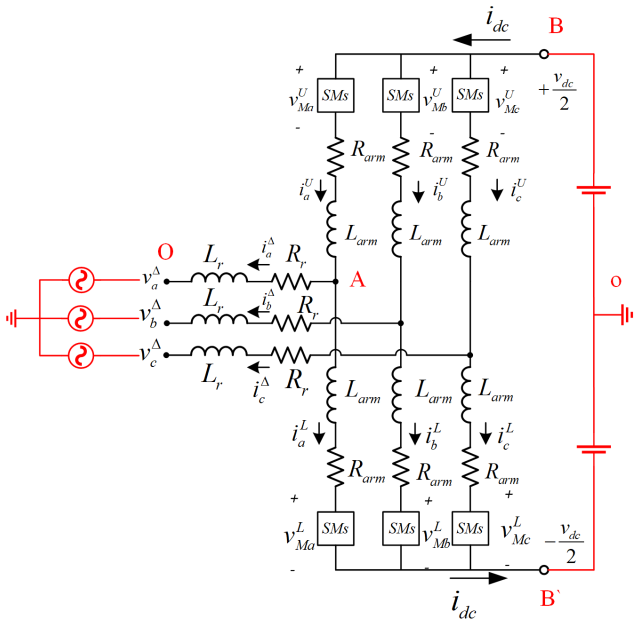

Figure 3.4: Analytic model of three-phase MMC unit

represented by the following equations for the upper and lower arm for each phase:

$$v_a^{U,L} = m_a^{U,L} v_{Ca}^{U,L}, \quad i_a^{U,L} = m_a^{U,L} i_a^{U,L}, \tag{3.1a}$$

$$v_b^{U,L} = m_b^{U,L} v_{Cb}^{U,L}, \quad i_b^{U,L} = m_b^{U,L} i_b^{U,L}, \tag{3.1b}$$

$$v_c^{U,L} = m_c^{U,L} v_{Cc}^{U,L}, \quad i_c^{U,L} = m_c^{U,L} i_c^{U,L}, \tag{3.1c}$$

where $m_a^{U,L}$, $m_b^{U,L}$ and $m_c^{U,L}$ are upper and lower arm insertion indices for 3 phases. Voltages $v_{Cj}^{U,L}$, for phases $j \in \{a,b,c\}$, and upper U and lower L arms, are voltages of equivalent SM's capacitance denoted as C.

The capacitor voltages and inductor currents of the upper and lower arm of MMC are represented using $\Sigma - \Delta$ nomenclature, which can be defined as follows:

$$i_j^\Delta := i_j^U - i_j^L, \quad i_j^\Sigma := \frac{i_j^U + i_j^L}{2}, \tag{3.2a}$$

$$v_{Cj}^\Delta := \frac{-v_{Cj}^U + v_{Cj}^L}{2}, \quad v_{Cj}^\Sigma := \frac{v_{Cj}^U - v_{Cj}^L}{2}, \tag{3.2b}$$

$$m_j^\Delta := m_j^U - m_j^L, \quad m_j^\Sigma := m_j^U + m_j^L, \tag{3.2c}$$

$$v_{Mj}^\Delta := \frac{-v_{Mj}^U + v_{Mj}^L}{2} = \frac{-(m_j^\Delta v_{Cj}^\Sigma + m_j^\Sigma v_{Cj}^\Delta)}{2}, \tag{3.2d}$$

$$v_{Mj}^\Sigma := \frac{v_{Mj}^U + v_{Mj}^L}{2} = \frac{m_j^\Sigma v_{Cj}^\Sigma + m_j^\Delta v_{Cj}^\Delta}{2}, \tag{3.2e}$$

where $j \in \{a,b,c\}$, which represents the three phases. Using the above definition, 12 new state variables in terms of dqz frame can be derived as mentioned in [92], which are defined as follows:

$$\frac{d}{dt}\left(\vec{i}^{\Delta}_{dq}\right) = \frac{\vec{v}^{\Delta}_{Mdq} - \left(\omega L^{ac}_{eq} J_2 + R^{ac}_{eq} I_2\right)\vec{i}^{\Delta}_{dq} - \vec{v}^{G}_{dq}}{L^{ac}_{eq}}, \tag{3.3a}$$

$$\frac{d}{dt}\left(\vec{i}^{\Sigma}_{dq}\right) = -\frac{\vec{v}^{\Sigma}_{Mdq} + (R_{arm} I_2 - 2\omega L_{arm} J_2)\,\vec{i}^{\Sigma}_{dq}}{L_{arm}}, \tag{3.3b}$$

$$\frac{d}{dt}\left(i^{\Sigma}_{z}\right) = \frac{v_{dc}}{2\,L_{arm}} - \frac{v^{\Sigma}_{Mz} + R_{arm}\, i^{\Sigma}_{z}}{L_{arm}}, \tag{3.3c}$$

$$\frac{d}{dt}\left(\vec{v}^{\Delta}_{Cdq}\right) = \frac{N_{SM}}{2C}\vec{i}^{\Delta}_{Mdq} - \omega J_2 \vec{v}^{\Delta}_{Cdq}, \tag{3.3d}$$

$$\frac{d}{dt}\left(\vec{v}^{\Delta}_{CZdq}\right) = -\frac{N_{SM}}{8C}\Psi - 3\omega J_2 \vec{v}^{\Delta}_{CZdq}, \tag{3.3e}$$

$$\frac{d}{dt}\left(\vec{v}^{\Sigma}_{Cdqz}\right) = \frac{N_{SM}}{2C}\vec{i}^{\Sigma}_{Mdqz} + 2\omega J_3 \vec{v}^{\Sigma}_{CZdqz}, \tag{3.3f}$$

where

$$\vec{i}^{\Delta}_{Mdq} = P_{\omega}(t)\,(P^{-1}_{-2\omega}(t)\;\vec{m}^{\Sigma}_{dqz} \circ \frac{P^{-1}_{\omega}(t)\,\vec{i}^{\Delta}_{dqz}}{2} + P^{-1}_{\omega}(t)\;\vec{m}^{\Delta}_{dqz} \circ P^{-1}_{-2\omega}(t)\;\vec{i}^{\Sigma}_{dqz}), \tag{3.4a}$$

$$\vec{i}^{\Sigma}_{Mdqz} = P_{-2\omega}(t)\,(P^{-1}_{-2\omega}(t)\;\vec{m}^{\Sigma}_{dqz} \circ P^{-1}_{-2\omega}(t)\;\vec{i}^{\Sigma}_{dqz} + P^{-1}_{\omega}(t)\;\vec{m}^{\Delta}_{dqz} \circ \frac{P^{-1}_{\omega}(t)\,\vec{i}^{\Delta}_{dqz}}{2}), \tag{3.4b}$$

$$\vec{v}^{\Delta}_{Mdqz} = -\frac{P_{\omega}(t)}{2}\,(P^{-1}_{\omega}(t)\;\vec{m}^{\Delta}_{dqz} \circ P^{-1}_{-2\omega}(t)\;\vec{v}^{\Sigma}_{Cdqz} + P^{-1}_{-2\omega}(t)\;\vec{m}^{\Sigma}_{dqz} \circ P^{-1}_{\omega}(t)\;\vec{v}^{\Delta}_{Cdqz}), \tag{3.4c}$$

$$\vec{v}^{\Sigma}_{Mdq} = -\frac{P_{-2\omega}(t)}{2}(P^{-1}_{\omega}(t)\;\vec{m}^{\Delta}_{dqz} \circ P^{-1}_{\omega}(t)\;\vec{v}^{\Delta}_{Cdqz} + P^{-1}_{-2\omega}(t)\,\vec{m}^{\Sigma}_{dqz} \circ P^{-1}_{-2\omega}(t)\,\vec{v}^{\Sigma}_{Cdqz}), \tag{3.4d}$$

$$\Psi = \begin{bmatrix} i^{\Delta}_{d} m^{\Sigma}_{d} + 2i^{\Sigma}_{d} m^{\Delta}_{d} + i^{\Delta}_{q} m^{\Sigma}_{q} + 2i^{\Sigma}_{q} m^{\Delta}_{q} + 4i^{\Sigma}_{z} m^{\Delta}_{Zd} \\ i^{\Delta}_{q} m^{\Sigma}_{d} + 2i^{\Sigma}_{d} m^{\Delta}_{q} - i^{\Delta}_{d} m^{\Sigma}_{q} - 2i^{\Sigma}_{q} m^{\Delta}_{d} + 4i^{\Sigma}_{z} m^{\Delta}_{Zq} \end{bmatrix}, \tag{3.4e}$$

where $L^{ac}_{eq} = L_r + \frac{L_{arm}}{2}$, $R^{ac}_{eq} = R_r + \frac{R_{arm}}{2}$.

Here, the $P_{\omega_0}(t) = \frac{2}{3}\begin{bmatrix} \cos(\omega_0 t) & \cos\left(\omega_0 t - \frac{2\pi}{3}\right) & \cos\left(\omega_0 t - \frac{4\pi}{3}\right) \\ \sin(\omega_0 t) & \sin\left(\omega_0 t - \frac{2\pi}{3}\right) & \sin\left(\omega_0 t - \frac{4\pi}{3}\right) \\ \frac{1}{2} & \frac{1}{2} & \frac{1}{2} \end{bmatrix}$ and $P^{-1}_{\omega_0}(t) = \frac{3}{2}P^{T}_{\omega_0}(t) + \frac{1}{2}\begin{bmatrix} 0 & 0 & 1 \\ 0 & 0 & 1 \\ 0 & 0 & 1 \end{bmatrix}$ are the Park's transformation and inverse Park's transformation at ω_0 angular frequency and $\omega_0 \in \{-2\omega, \omega, 3\omega\}$. I_n is the identity matrix with an order of $n \times n$, while matrices $J_2 = \begin{bmatrix} 0 & 1 \\ -1 & 0 \end{bmatrix}$, and $J_3 = \begin{bmatrix} 0 & 1 & 0 \\ -1 & 0 & 0 \\ 0 & 0 & 0 \end{bmatrix}$.

A difference of KVL from node OABo and OAB'o in the dq frame yields equation 3.3a, while summation of the KVL provides equations 3.3b and 3.3c. The subtraction of differential equations represents the dynamic AC model of MMC, while the summation of differential equations equation represents the DC model of MMC. The internal dynamics of MMC are given by the equation 3.3d - 3.3f. These ordinary differential equations and control loops are numerically simulated using the ODE45 solver in MATLAB©.

3.4. CORE CONTROL FUNCTION OF A MMC UNIT

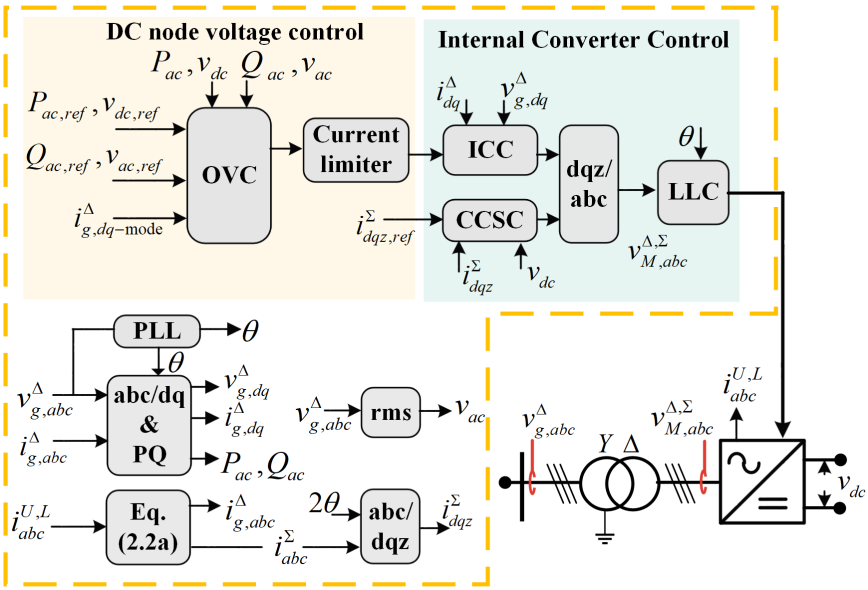

Figure 3.5: Core control function (dark yellow dash line) in a MMC unit

The Core Control Function consists of four major close loop controls, namely, outer voltage control (OVC), inner current control (ICC), circulating current suppression control (CCSC), and lower-level control (LLC) [127], [130], [140]. This function is based on the vector control principle [161]. The ICC, CCSC, and LLC together called internal converter control. This internal converter control is the lower-most control and is unique to each vendor [127]. The function of this control is to regulate the electrical quantities at the PoC. The outer voltage control is also known as DC node voltage control. It regulates the power flow exchange between the AC and DC grid. This control also maintains the DC voltage within its operating limits.

Besides the control loops, the core control function has a PLL, which synchronizes the stationary dqz frame of converter control with the AC voltage at PoC, which yields transformation angle θ. Furthermore, with the help of θ, independent control of active and reactive power is achieved.

3.4.1. Phase Lock Loop (PLL)

The key element of the vector control is the PLL. This loop provides a θ, which is used to synchronize with the AC grid. The simplest form of PLL is discussed in this section.

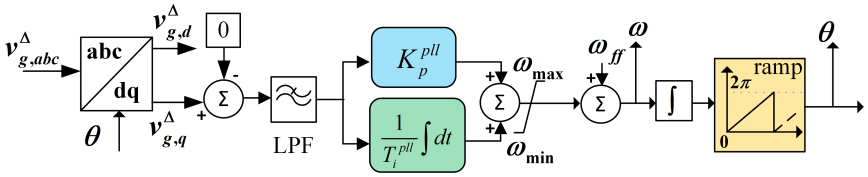

Figure 3.6: Simple block diagram of a Phase-Locked Loop.

As illustrated in Figure 3.6, the PLL is a feedback control system around the dq transformation of $v^{\Delta}_{g,abc}$. Post-transformation, the input signal, $v^{\Delta}_{g,q}$, undergoes processing through a Proportional-Integral (PI) controller coupled with a low-pass filter. This filter effectively eliminates high-frequency components present in the voltage error. The primary objective of the PI controller is to align the magnitude of $v^{\Delta}_{g,abc}$ with $v^{\Delta}_{g,d}$, resulting in a reference value of zero for $v^{\Delta}_{g,q}$. The PI controller's output is constrained within allowable angular frequency limits. To enhance dynamic response, a feedforward term (ω_{ff}) is incorporated.

The combined output of the PI controller and the feedforward term yields the grid angular frequency (ω). To derive θ, an integrator is employed. However, the integrator's output spans from $-\pi$ to $+\pi$. To address this, a modular function is applied, converting the angle to a range from 0 to 2π.

Figure 3.7 shows cases of the PLL's response to alterations in the amplitude of $v^{\Delta}_{g,abc}$ at 0.05s and a system frequency change of 1 Hz at 0.15s. Notably, as the amplitude of grid voltages fluctuates, the d-axis voltage adjusts proportionately. Simultaneously, when a frequency change occurs at 0.15s, the PLL adeptly tracks the system frequency without affecting the d-axis amplitude.

3.4.2. Outer Voltage Control

In this control strategy, local variables are continuously monitored against desired control set-points provided by the final converter schedule (dispatch control) [140]. The output of this control serves as input to the internal converter control. Depending on the control objectives at the Point of PoC, the converter can operate in different control modes, as illustrated in the block diagram in Figure 3.8.

In the following text, some of the equations are written in the Laplace domain, with $s = -\sigma + j\omega$ representing the Laplace operator. The dependence of s is then clearly stated. In other cases, the time dependence is assumed.

- **Active Power Control Mode** (P-control): Due to the synchronization of the converter to the external grid via PLL, the d-axis component aligns with the AC voltage at PoC-AC, while the q-axis component is set to zero. The active power can be expressed as:

$$P_{ac} = v^{\Delta}_{g,d} i^{\Delta}_{g,d}. \tag{3.5}$$

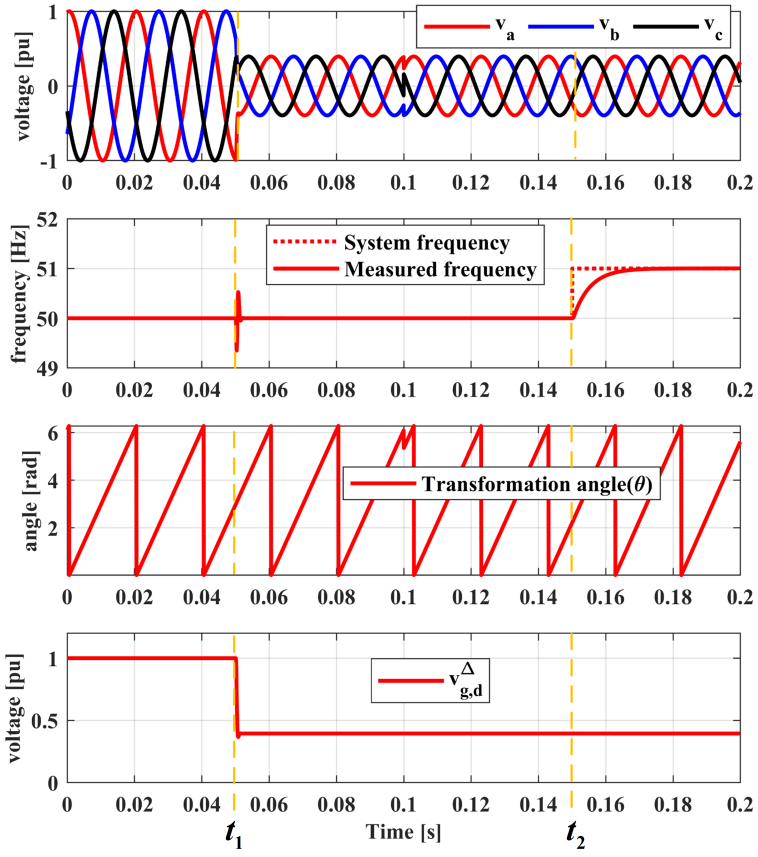

Figure 3.7: Response of the PLL to changes in the amplitude of $v^{\Delta}_{g,abc}$ at $t_1 = 0.05s$ and a 1 Hz system frequency change at $t_1 = 0.15s$.

In this control mode, the converter provides a reference active power $P_{ac,ref}$, and traditional PI control can be defined as:

$$i^{\Delta}_{d,ref*}(t) = \frac{1}{v^{\Delta}_{g,d}} \left[K_p^{ap}(P_{ac,ref} - P_{ac}) + \frac{1}{T_i^{ap}} \int (P_{ac,ref} - P_{ac}) dt \right], \tag{3.6}$$

where K_p^{ap} and T_i^{ap} are proportional gain and time constant of the integral element.

- **Fixed DC Voltage Control Mode** (v_{dc}-control): The capacitance offered by the sub-modules can be expressed as an equivalent capacitance ($\frac{6C}{N_{sm}}$). A relation can

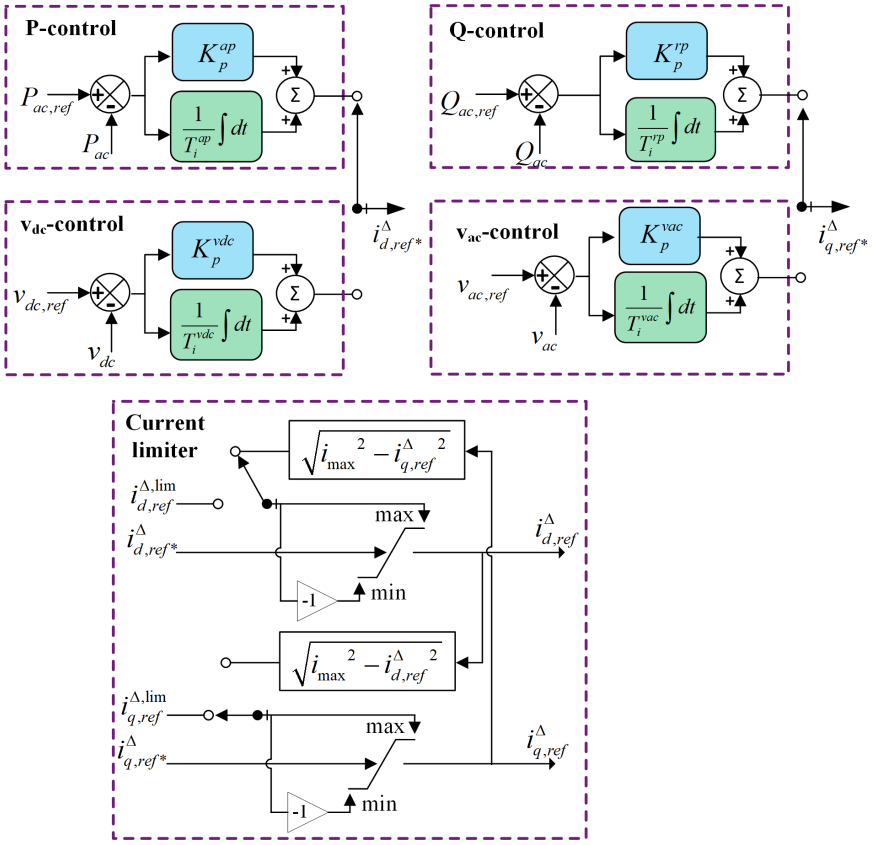

Figure 3.8: Block diagram of Outer Voltage Control with reactive power priority

be formulated that shares similarities with a traditional 2- or 3-level VSC converter:

$$\frac{6C}{N_{sm}}\frac{dv_{dc}}{dt} = i^{\Delta}_{g,d} - i_{dc}. \tag{3.7}$$

Neglecting the feed-forward term i_{dc} in Equation 3.7, PI control can be defined as:

$$i^{\Delta}_{d,ref*}(t) = K_p^{vdc}(v_{dc,ref} - v_{dc}) + \frac{1}{T_i^{vdc}}\int (v_{dc,ref} - v_{dc})dt, \tag{3.8}$$

where K_p^{vdc} and T_i^{vdc} are proportional gain and time constant of the integral element.

- **Reactive Power Control Mode** (Q-control): Synchronization at PoC-AC aligns the d-axis component with the AC voltage, while the q-axis component becomes zero. Reactive power can be expressed as:

$$Q_{ac} = -v^{\Delta}_{g,d} i^{\Delta}_{g,q}. \tag{3.9}$$

The corresponding PI control is defined as:

$$i^{\Delta}_{q,ref*} = \frac{1}{v^{\Delta}_{g,d}} \left[K_p^{rp}(Q_{ac,ref} - Q_{ac}) + \frac{1}{T_i^{rp}} \int (Q_{ac,ref} - Q_{ac}) dt \right], \tag{3.10}$$

where K_p^{rp} and T_i^{rp} are proportional gain and time constant of integral element.

- **PoC-AC Support Control Mode** (v_{ac}-control): The estimated voltage drop across the converter transformer and grid impedance can be expressed as a set of equations:

$$\Delta v_{ac} \approx \frac{\omega L^{ac}_{eq} Q_{ac}}{v_{ac}}, \tag{3.11a}$$

$$\Delta v_{ac} \approx \omega L^{ac}_{eq} i^{\Delta}_{g,q}. \tag{3.11b}$$

Based on these equations, a PI control can be formulated as:

$$i^{\Delta}_{q,ref*} = K_p^{vac}(v_{ac,ref} - v_{ac}) + \frac{1}{T_i^{vac}} \int (v_{ac,ref} - v_{ac}) dt, \tag{3.12}$$

where K_p^{vac} and T_i^{vac} are proportional gain and time constant of the integral element. Furthermore, a $Q_{ac} - v_{ac}$ droop-based strategy can be applied with this control, where the droop coefficient is determined by the Transmission System Operator (TSO) [162]. However, this strategy is omitted in this thesis as the area of interest of the thesis is on the impact of advance control and protection in the DC grid with a centralised voltage control [74].

To protect the semiconductor components within the converter unit from potential damage caused by high current transients, a current limiting mechanism is integrated into the outer voltage control [140]. This current limiter monitors the computed reference currents (denoted as $i^{\Delta}_{d,q,ref}$) and compares them to the converter's current rating (i_{max}). If these limits are exceeded, the values of $i^{\Delta}_{d,q,ref}$ are restricted.

This thesis focuses on two priorities: active power and reactive power. The active power priority is determined by the formula $i^{\Delta,lim}_{q,ref} = \sqrt{i^2_{max} - {i^{\Delta}_{d,ref}}^2}$, while the reactive power priority is represented by $i^{\Delta,lim}_{d,ref} = \sqrt{i^2_{max} - {i^{\Delta}_{q,ref}}^2}$. The choice between these priorities depends on the specific application.

3.4.3. INTERNAL CONVERTER CONTROL

Based on the converter control mode in outer voltage control, the dq-axis current references are chosen. These references are applied to the inner current control loop to regulate the active and reactive power. The ICC has a similar structure with a 2,3-level VSC converter which is described by the equation (3.3 a) and illustrated by a PI control shown in Figure 3.9. The independent control of active and reactive power is achieved by regulating the converter output voltage ($v^{\Delta,\Sigma}_{M,abc}$) by tracking reference currents.

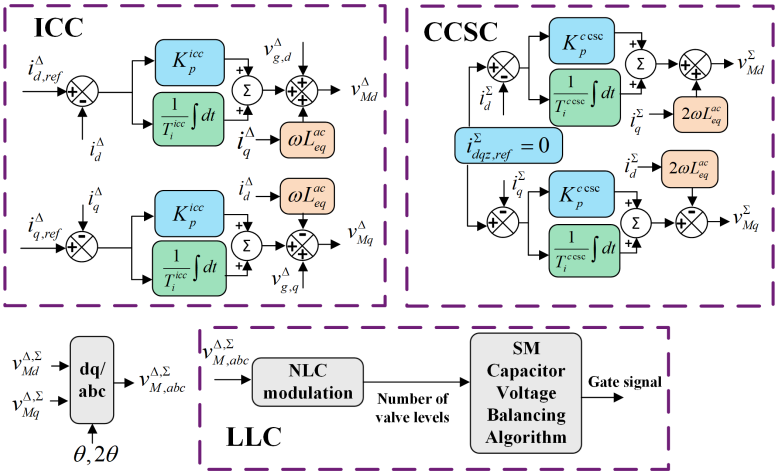

Figure 3.9: Block representation of Internal Converter Control

The series connection of the SM capacitor per converter arm and parallel connection of the same to the DC grid creates a voltage imbalance between each phase [163], [164]. This results in current circulation between phases, known as "circulating current." Due to its presence within phases, it does not affect the AC and DC current. However, it impacts the converter's performance by conducting increased arm current and oversizes the SM semiconductor's current rating. To minimize the circulating current, a dynamic control approach is preferred as oversizing of the rector is prevented, and has been implemented in this thesis.

The circulating current is dominated by second-order harmonic [81]. Hence, the dq axis currents are transformed via twice the transformation angle and can be represented by equation(3.3 b). To suppress these currents, PI controls can be used for each current with a current reference of zero, as shown in Figure 3.9.

Gate signals are generated by the lower-level control after transforming converter voltages corresponding to active-reactive power and voltage needed to suppress circulating current (as seen in the Figure 3.9). The lower level control consists of the nearest level control (NLC) modulation and SM capacitor voltage balancing algorithm. The NLC is one of the modulation techniques for determining the number of SM levels in each arm [165]. With a high SM level in MMC, the other techniques become cumbersome. Furthermore, the number of levels is determined by comparing the converter voltage amplitude with the number of sub-modules. The output of the NLC provides a staircase waveform as a function of inserted SM for each arm. However, without any control over the charge management of the SM capacitor, it will damage the SM and create a convergence issue of the SM capacitor voltage of MMC. To overcome this problem, a capacitor voltage balancing controller is typically designed. In a capacitor voltage balancing algorithm, based on the arm current direction, capacitors with different energy are inserted or bypassed first, as shown in table 3.1.

Table 3.1: Half-bridge capacitor voltage balancing algorithm criteria

status	$-\mathbf{i}_{\mathbf{abc}}^{\mathbf{U,L}}$	$+\mathbf{i}_{\mathbf{abc}}^{\mathbf{U,L}}$
Insert SM	Insert SM with highest SM voltage	Insert SM with lowest SM voltage
Bypass SM	Bypass SM with lowest SM voltage	Bypass SM with highest SM voltage

3.5. REAL-TIME SIMULATION MODELS OF MMC UNIT

In this thesis, RTDS© is used for real-time modeling and simulation studies. RTDS© is a particular purpose computer designed to study Electromagnetic Transient Phenomena in realtime [68]. Due to its advanced parallel processing techniques, it can perform continuous real-time operations. The network solution offered by RTDS© is based on nodal analysis and solved using Dommel's solution algorithm [166]. The Dommel algorithm uses the trapezoidal rule for numerical integration of the system of differential equations which are expressed as algebraic equations. All the power components are represented by current sources ($\vec{I}$) and resistors, and described by the following equation:

$$\vec{V} = \mathbf{G}^{-1}\vec{I}, \tag{3.13}$$

where, with the given current sources values $\vec{I}$ and conductance matrix $\mathbf{G}$, the voltage vector $\vec{V}$ is determined. The inverse of the conductance matrix is determined by LU decomposition [167].

At each discrete time step (which is called a simulation time step (Δt)), the state of the power system model is computed by solving equation (3.13) in the digital simulator. Depending on the frequency of interest, a wide range of simulation time steps is chosen and categorized in subsystem environments [168]. A specific network portion is decoupled and solved independently in a specified simulation time in a particular subsystem environment. Thus, it is possible to run it in parallel with other subsystem environments which are running in different simulation time-steps. Table 3.2 summarises these subsystem environments that exist in RTDS©. Amongst these subsystem environments, small time-step and sub-steps are used for modeling MMC units.

In [140], different VSC model types are described. Each of them is classified based on the intended study and application. Table 3.3 summarises the MMC model. Type-4 and Type-5 are implemented in CPU and FPGA for real-time simulator, respectively. In a nutshell, the MMC arm is modeled using a surrogate network as illustrated in figure 3.10. A surrogate network consists of a series connection of three sections [169]: (1) the reactor section, (2) the blocking SM section, and (3) the insertion SM section. The calculation of SMs in the blocking and insertion states is performed for each simulation time-step before the calculation of the new history term of the Dommel algorithm representation.

The SMs are selected by an internal or external control input at each Δt before the new Dommel history term. There is also a 'Bypass state,' where the SMs are not connected to the network and are discharged by *RC* time constant for each bypassed

Table 3.2: Different subsystem environment in the RTDS© [168]

Subsystem environments	Small Time-step	GPES	Substep	Mainstep	Superstep	Distribution mode
Purpose	Simulate PE networks with small time-steps to capture high-frequency dynamics	Specifically designed for large custom PE converter topologies	Enhanced environment to simulate PE networks with small time-steps to capture high-frequency dynamics.	Simulating the majority of the power system	developing large networks without using equivalent sources	accommodating the implementation of distribution feeder models that include several hundred to over a thousand nodes.
Simulation time-step	1.4 μ s– 3.75μs	1.4μs	~2μs	30μs – 60μs	2-5 times Mainstep	150μs – 200μs
Cutoff Frequency	<3kHz (L/C-ADC switch models) <10kHz (tline decoupled resistive switch 2-level converter models)	<3kHz	<200kHz	<8kHz	<6kHz	<3kHz
Solution process	Pre-calculated conductance matrix	Pre-calculated conductance matrix	Full decomposition of Network Solution	Full decomposition of Network Solution	Full decomposition of Network Solution	Full decomposition of Network Solution
Hardware platform	Processor based	Processor based or FPGA	Processor based	Processor based	Processor based	Processor based

Table 3.3: VSC computational model types [140]

Type of Model	Type of simulation tools	Type of studies
Type 1	Circuit simulation tools	Suitable for component level studies
Type 2	EMT	Validation of simplified models through in-depth submodule fault analyses
Type 3		Validation of simplified models through in-depth submodule fault analyses
Type 4		In-depth examination of AC and DC faults in close proximity to the converter.
Type 5		Analysis of AC and DC transients, informing high-level control system design and conducting harmonic studies
Type 6	RMS	Exploration of remote AC and DC transients for comprehensive system analysis and resilience assessment.
Type 7	Load-flow tools	Power flow

SM. An SM in a surrogated network consists of a parallel connection of a freewheeling diode, capacitor, and discharge resistor. This is represented as the Thevenin branch by considering the history of the capacitor voltage and diode voltage drop, which is further transformed into a Dommel algorithm representation. The surrogated network representation of the MMC arm is simulated on a processor or FPGA, which are classified as Type-4 and Type-5 computational MMC arm models.

3.5.1. TYPE 4-DETAILED EQUIVALENT CIRCUIT MODEL

The Type-4 model uses a surrogated network and a Bergeron transmission line model running on FPGA [169], [170]. The Bergeron transmission line model isolates the MMC arm and provides flexibility with connection in the subnetwork environment. In this model, the network end of the transmission line model is carried out in a subnetwork environment, and the MMC arm end of the transmission line model is performed on FPGA. The information between these ends is carried out over optical fiber. This fiber also carries the internal fault commands from the processor to the MMC arm model. Furthermore, this fiber also communicates information on SM capacitor voltage levels.

The FPGA-based MMC arm can simulate up to 512 SMs in a simulation time step. The FPGA-based MMC model consists of two consolidated branches, namely, the block section and de-block section, as shown in Figure 3.10. The operation process flow of the FPGA-based model is summarized in algorithm 1.

The external control consists of a voltage-balancing algorithm described in the previous section. This voltage-balancing algorithm sends firing control input to each SM in the valve model over an optical fiber.

3.5.2. TYPE 5-AVERAGE VALUE MODEL

A high-level function of the MMC control is sufficient for system-level operation and performance studies. For such studies, no firing control is generated for individual SMs

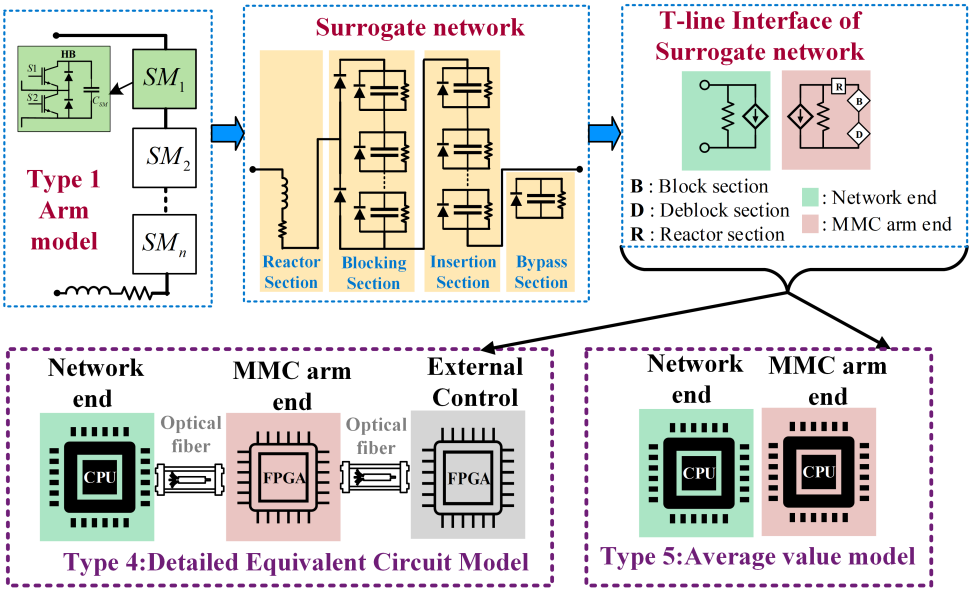

Figure 3.10: Computational arm model representation of MMC in RTDS© [170]

[170]. Thus, Type-5 is preferred. The control signal generated by external or simulator control units includes a block/insertion signal and information on the number of SMs placed within the MMC arm path corresponding to the reference current direction. Type-5 uses the simplified surrogate network described in the previous section with algorithm 2.

This model consists of the automatic SM capacitance-voltage balance algorithm due to equal voltage across each SM capacitor. Unlike the FPGA-based model, this model cannot simulate internal arm faults. However, it can be run on the processor due to a lower computational footprint.

3.6. Comparison between Analytical and Real-Time Simulation Model of the MMC

To benchmark the analytical model for advanced control strategies in forthcoming sections, it needs to be compared with the real-time library model developed by RTDS©. For comparison, a small time-step simulation environment is considered because the switching frequency of MMC is much lower than the cutoff frequency of the simulation environment as described in Table 3.2. An MMC unit is constructed with three legs connected in parallel. Each leg comprises two RTDS© arm models (.i.e., Type-4 or Type-5). Each leg's midpoint has an interface for AC connection. The remote end of the legs, i.e., upper and lower ends, are connected in series, which provides a DC interface. The converter transformer, and the AC and DC source are adopted from the small time-step simulation environment of the RTDS© database, which is reported in

Algorithm 1 Detailed Equivalent Circuit model Computation in FPGA [170]

Input: Previous control input, Old state of SM (V_{hc})
Output: New SM capacitor voltage V_c
if Old state is "blocking" or "insertion" **then**
    Determine chain current for calculation
else
    No current used for voltage calculation
end if
Divide 512 SMs into 8 groups of 64
for Each group **do**
    Calculate new V_c via parallel computing based on selected current and V_{hc}
end for
Apply lower limit of 0 to V_c (accounting for diode presence)
Send new capacitor voltages to controls
    state Determine the new state of each SM based on control input
for Each group of 64 SMs **do**
    Accumulate resistance and history voltage for assigned chain
end for
Combine resistance and history voltage sums for "blocking SM" and "insertion SM" chains in each group
Insert consolidated Thevenin branches into the network
Convert MMC network into a single conductance and current source
Continue circuit computations
Send capacitor voltages and MMC branch currents using the communication protocol

Algorithm 2 Average Value Model Computation in Processor [171]

Input: Block/unblock signal, number of SMs to be inserted, and history terms.
Output: MMC arm voltage and current.
Initialize: Set all capacitor voltages equal.
Determine the state for an SM ("blocking SM," "insertion SM," or "Bypassed SM").
for A SM in its respective state **do**
    Calculate SM capacitor voltage by selecting state duration based on weightings derived from SM order and the total SMs in the MMC arm.
end for
Find the net voltage change on all SMs by multiplying a single SM's voltage change by the total number of SMs. state Distribute the net voltage change equally among all SMs.

the [171].

Figure 3.11 depicts a single-end symmetrical monopolar MMC. The test system is a 380 kV AC source and represents an infinite bus with a zero phase shift. The AC source is connected to the MMC through a star-delta converter transformer, where the

transformer's star point is solidly grounded. The parameters rating of the transformer and MMC are shown in Table 3.4. To check the performance of an MMC, the DC voltage is kept constant, i.e., it is represented as a DC source with ±200 kV.

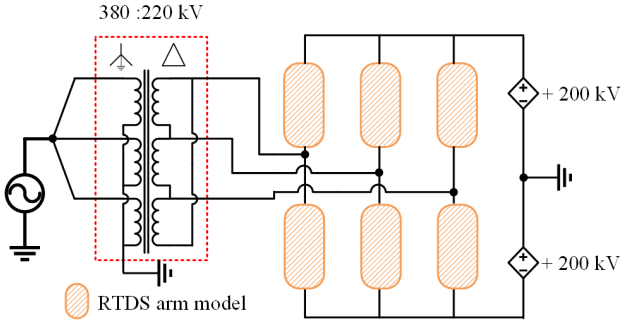

Figure 3.11: A single-end symmetrical monopolar MMC test circuit with constant DC source

Table 3.4: Parameters of the test system from Figure 3.11

Parameter	Symbol	Value	Unit
Base power	P_{base}	800	MVA
Arm resistance	R_{arm}	0	Ω
Equivalent transformer inductance	L_{eq}^{ac}	35	mH
Equivalent transformer resistance	R_{eq}^{ac}	0.363	Ω
Submodule capacitance	C	10	mF
Number of submodules	N_{SM}	400	-
Fundamental grid frequency	f	50	Hz
Rated PP DC voltage	v_{dc}	400	kV
Rated line to line Primary voltage	$v_{ac}pri$	380	kV
Rated line to line secondary voltage	$v_{ac}sec$	220	kV

For both simulation models, RTDS© and analytical, classical PI controlling loops for the MMC unit are implemented for OVC and ICC. Due to the constant DC voltage and delta configuration of the converter's transformer, the zero circulating current and energy control are not implemented. As section 3.4.2 describes, the active and reactive power control modes provide the d and q reference for the inner current (Δ) of the subsequent control loop. The dispatch control sets the set-point for the active and reactive power control.

Without CCSC, the MMC faces a second-order harmonic in the circulating current during steady state. This circulating current increases the net power loss of the MMC [172]. Hence, by implementing the CCSC as shown in Figure 3.9, the power loss is reduced by setting the d and q circulating current components to zero. The simulated proportional and integral gain parameters for each controlling loop are shown in the table 3.5.

Table 3.5: Proportional and Integral gain parameter of the classical CCSC, ICC, and OVC PI controllers from Figure 3.8 and 3.9

Parameter	Value
Active and reactive power controller proportional gain	0.08 [pu]
Active and reactive power controller integral gain	4 [pu]
ICC proportional gain	0.8 [pu]
ICC integral gain	80 [pu]
CCSC proportional gain	0.8 [pu]
CCSC integral gain	80 [pu]

The following subsections compare simulation results of MMC state variables under disturbance and a model error analysis.

3.6.1. SIMULATION RESULTS

The behavior of the MMC during the active power step change is observed by changing the reference $i^{\Delta}_{d,ref*}$ from 1 pu to 0.3 pu at the time instant $t = 0.6$ s. In this paragraph, all diagrams are provided analytically and in RTDS© with blue and red lines, respectively.

For both models, analytical and RTDS©, active power diagrams overlap during the steady-state and transient as seen from Figure 3.12a,c. However, due to the decoupling of reactive and active powers, no change in reactive power and q component of grid current, i^{Δ}_{q}, is observed.

In the simulated results, the circulating currents are set to zero, to achieve a circulating current suppression control effect (see Figure 3.13a). However, it is observed that, in the RTDS© circulating currents, $i^{\Sigma}_{d,q}$ contain the 6th harmonic. This harmonic component is absent in the analytical model, which, for the simplicity of representation, uses only DC values, and harmonic components on 3ω, -2ω and ω, where ω is the system angular frequency. During the change in active power, the circulating current remains zero as observed in Figure 3.13a.

The Σ-components of the arm capacitor voltages, $v^{\Sigma}_{d,q,z}$, are illustrated in Figure 3.13b. It can be observed that the z component of the arm capacitor voltage is equal to the DC-link voltage for both models. As the paragraph above explains, the RTDS© model contains the 6th harmonic, which is absent in the analytical model. With the change in the active power's set point, the amplitude of the d and q components of the arm capacitor voltage reduces as observed in Figure 3.13b. Moreover, with the constant DC voltage, the z component is unaffected by this change.

Figure 3.14 indicates the effect of the change in the active power on the circulating current i^{Σ}_{z}. Due to the difference in the active power reference, the amplitude of the i^{Σ}_{z} reduces. As observed in both models, the current follows the same profile during the steady- and transition state. MMC's DC current will be $i_{dc} = 3i^{\Sigma}_{z}$, which is, in this case, 2 kA at rated power and 0.6 kA at 240 MW.

In the pre-disturbance stage, active power is transferred from the DC source to the AC system. However, with the active power reversal at time instant $t = 0.6$ s, the power direction changes, as shown in Figure 3.15a. For both models, the same response is

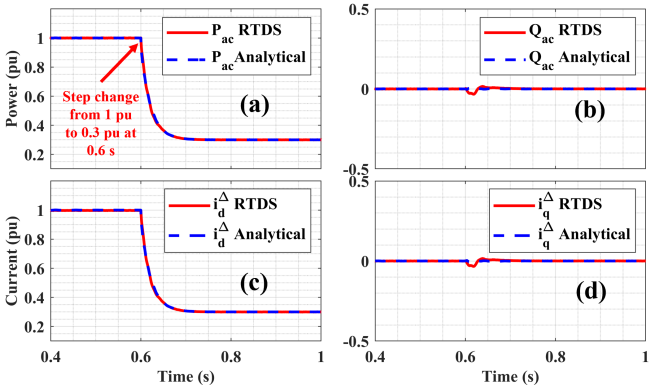

Figure 3.12: Comparison of: (**a**) active power; (**b**) reactive power; (**c**) output current i_d^{Δ}; and (**d**) output current i_q^{Δ}; in analytical (blue) and RTDS© (red) during step change of the active power from 1 pu to 0.3 pu at the time instance $t = 0.6$ s

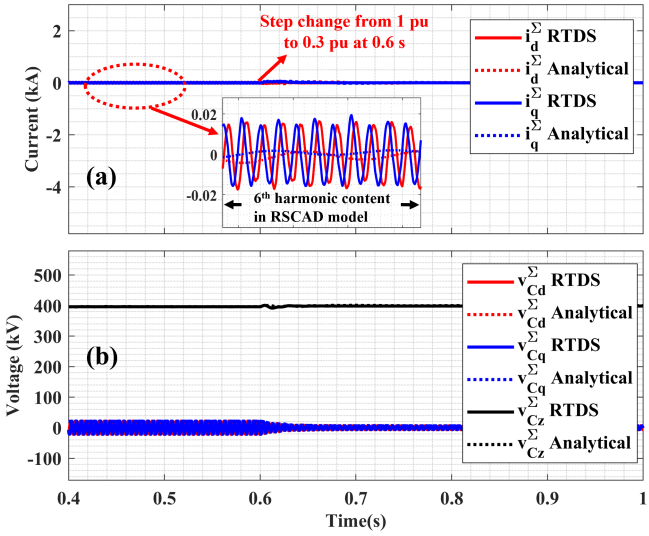

Figure 3.13: Comparison of (**a**) circulating currents (i_d^{Σ} and i_q^{Σ}); (**b**) Σ components of capacitor voltage in dqz reference frame; in analytical (blue) and RTDS© (red) during step change in active power from 1 pu to 0.3 pu at the time instance $t = 0.6$ s

observed. The transition period for both models is approximately 100 ms. It is equal to the time constant of the active power-controlling loop. Even with the decoupling of the active and reactive power components, there is a slight variation in reactive power during this transition. This is due to the uncompensated modulation of an MMC in both models.

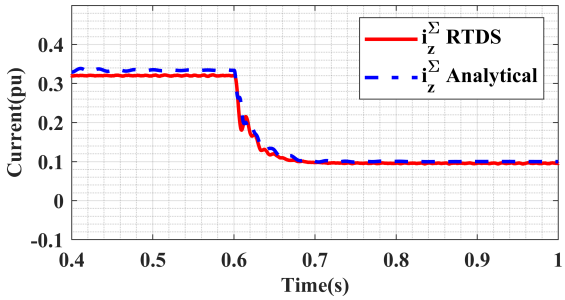

Figure 3.14: Comparison of the zero-sequence circulating current (i_z^{Σ}) in analytical (blue) and RTDS© (red), during step change in active power from 1 pu to 0.3 pu at the time instance $t = 0.6$ s

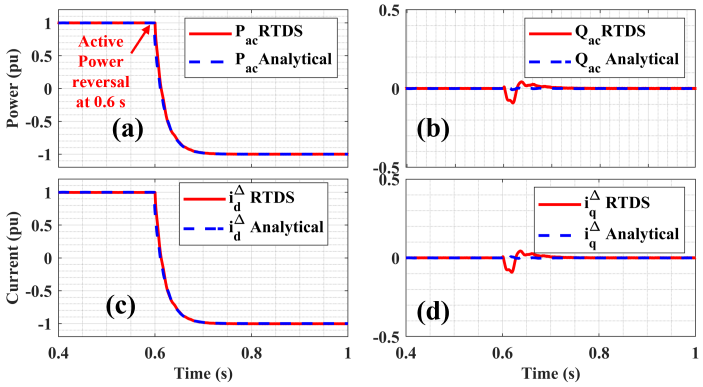

Figure 3.15: Comparison of: (**a**) active power; (**b**) reactive power; (**c**) output current i_d^{Δ}; and (**d**) output current i_q^{Δ}, in analytical (blue) and RTDS© (red) during active power reversal from 1 pu to -1 pu at the time instance $t = 0.6$ s

As discussed in the previous section, both models' circulating currents are nearly zero. Again, the RTDS© model contains the 6th harmonic content as observed in Figure 3.16a. Similarly, dqz components of the arm capacitance voltage remain constant after the reversal because the ideal voltage is on the DC side (see Figure 3.16b). With the active power direction change, the current direction reverses, which is observed in both models as depicted in Figure 3.17.

Further, to validate the analytical models' accuracy with the RTDS© model, the mean absolute error (MAE) is determined for pre-, during, and post-disturbance periods. MAE is a measure of correspondence between the analytical and RTDS© models. MAE is calculated for small signal disturbances as described in the previous subsection: The mean absolute error is determined according to [173],

$$MAE = \frac{\sum_{i=1}^{N} abs\left(yp_i - yo_i\right)}{M}, \tag{3.14}$$

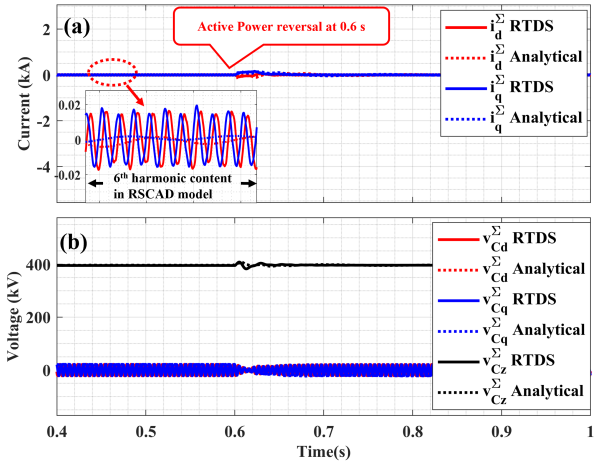

Figure 3.16: Comparison of: (**a**) circulating currents i_d^{Σ} and i_q^{Σ}; (**b**) Σ components of arm capacitor voltage in the dqz reference frame; in analytical (blue) and RTDS© (red) during active power reversal from 1 pu to -1 pu at the time instance $t = 0.6$ s

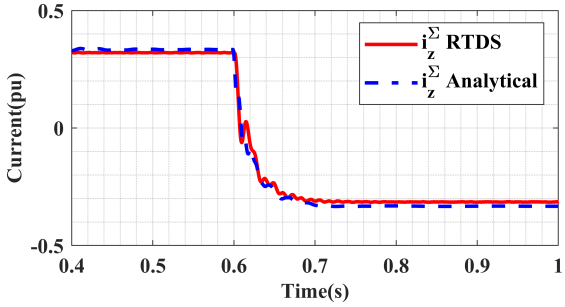

Figure 3.17: Comparison of zero-sequence circulating current i_z^{Σ} in analytical (blue) and RTDS© (red), during active power reversal from 1 pu to -1 pu at the time instance $t = 0.6$ s

where yp_i and yo_i are the predicted and observed values for the ith instance with total M observations.

In case of a step change in the active power, the measured active power in analytical model (P_{ac}) exhibits significantly lower error during the pre- and post-disturbance as shown in Table 3.6. However, this error slightly increases during the disturbance. A similar pattern is observed for the measured reactive power in the analytical model (Q_{ac}). The zero-sequence components' errors (i_d^{Σ} and i_q^{Σ}) are caused by the absence of the 6th harmonic content. Moreover, this error reduces after disturbance; see Figure 3.13 and Table 3.6. The zero-sequence circulating current (i_z^{Σ}) has a considerably higher error rate, which is visible in Figure 3.14 and in Table 3.6. This error arises because, in RTDS©, the analytical model does not consider ohmic losses. In addition, with the reduction in

the active power, this error drops exponentially.

From Table 3.7, with the increase of the reactive power to 200 MVAR at 0.6 s, no significant changes are observed. The MAEs for various signals are much smaller than those determined in the previous case. In the case of an active power reversal, the error during disturbance is higher for most of the signals, as it can be seen in Table 3.8.

Table 3.6: MAE in the analytical model during the step change in Active Power from 1 pu to 0.3 pu at $t = 0.6$ s

Signals	Error in percentage		
	Pre-disturbance	During- disturbance	Post- disturbance
P_{ac}	0.05	0.48	0.02
Q_{ac}	0.04	0.91	0.04
i_z^{Σ}	1.37	0.92	0.43
i_d^{Σ}	1.05	1.78	0.42
i_q^{Σ}	1.00	1.55	0.39
v_{Cz}^{Σ}	0.15	0.74	0.57

Table 3.7: MAE in the analytical model during the step change in Reactive Power from 0 pu to 0.24 pu at $t = 0.6$ s

Signals	Error in percentage		
	Pre-disturbance	During- disturbance	Post- disturbance
P_{ac}	0.04	0.16	0.03
Q_{ac}	0.03	0.22	0.02
i_z^{Σ}	1.50	1.52	1.49
i_d^{Σ}	0.98	1.85	0.95
i_q^{Σ}	0.98	0.79	0.97
v_{Cz}^{Σ}	0.25	0.32	0.24

Table 3.8: MAE in the analytical model during active power reversal at $t = 0.6$ s

Signals	Error in percentage		
	Pre-disturbance	During- disturbance	Post- disturbance
P_{ac}	0.05	1.28	0.05
Q_{ac}	0.06	2.55	0.11
i_z^{Σ}	1.35	2.33	1.79
i_d^{Σ}	1.02	3.74	1.34
i_q^{Σ}	0.99	3.96	1.25
v_{Cz}^{Σ}	0.52	1.41	0.22

3.7. CONCLUSION

In essence, this chapter furnishes a holistic understanding of MMCs, encompassing their historical evolution, design, operation, analytical modeling, control strategies, and real-time simulation. These insights not only contribute to the ongoing development of MMCs but also offer valuable guidance for shaping control strategies in modern HVDC transmission systems.

This chapter meticulously traces the evolution of power converters, highlighting the pivotal shift from current source converters to MMCs in HVDC transmission systems. The limitations of traditional converters pave the way for MMCs, and the in-depth exploration of the HB-SM contributes significantly to the development of a cost-effective high-power solution.

The analysis of the core control function of the MMC unit reveals a sophisticated hierarchy of control loops, ensuring stable operation for diverse scenarios. Real-time simulation models, implemented using RTDS, are investigated, providing valuable tools for accurate and efficient simulations. The comparative analysis between analytical and real-time models demonstrates the analytical model's good performance, with relatively lower error percentages, particularly during transient conditions — periods of critical importance characterized by rapid changes or disturbances within the system.

While the analytical model has simplifications, such as the absence of the 6^{th} harmonic content compared to the RTDS model, the overall error remains below 5%. This implies that the analytical model is well-suited for advanced modern control and controller development.

4

ENHANCED REAL-TIME OFFSHORE MT-HVDC BENCHMARK MODEL

This chapter introduces enhanced real-time network models for HVDC grids, incorporating real-time wind profile feedback to address existing model limitations. Designed to meet North Sea grid operator specifications, these models provide accurate parameters for both sea and land cables, with scripted system and control parameters to facilitate efficient perturbation and sensitivity analyses. Including an aggregated model of wind farms allows for investigation of their dynamic interactions with the HVDC grid. The evaluation of various operational scenarios indicates the models' effectiveness in reducing disturbances during faults and providing critical insights for component design and protection. Additionally, the chapter outlines computational requirements, offering guidance for model selection based on specific study needs. This work lays a foundational framework for future HVDC project lifecycle studies, component design, and operator training, enhancing the efficiency and reliability of HVDC grids.

Parts of this chapter have been published in A. Shetgaonkar, T. Karmokar, M. Popov, A. Lekić, "Enhanced Real-Time Multi-Terminal HVDC Power System Benchmark Models with Performance Evaluation Strategies," *Cigre Science & Engineering*, vol. 32, February 2024, pp. 29, 2024, Cigre.

4.1. BACKGROUND

This chapter provides RTS models for the point-to-point, three-, four- and five-terminal HVDC grids. These models are developed by applying the guidelines established in the recent CIGRE brochures [66], [160] and filling up the gap that needs to be covered by recent CIGRE brochures [174], [175]. These models are available as open software for future users [176]. The ratings of the upcoming ±525 kV, 2 GW offshore aggregated wind farm connections with DC CB have been used in their design as explained in the case study of chapter 2. As per [66], path B is considered in this work, as shown in Figure 4.1, and aims to increase the application of the developed model for academic and industrial projects. Some of the primary key features of the developed network over existing benchmark models are the interfaced aggregated wind turbine model, scripted parameters, simplified VARC DC CB model, DMR cable model, easy expandability, and real-time wind profile. Similarly, this chapter provides insight into the computation requirement for real-time simulations.

The proposed model closes the following modeling gap in the benchmark network:

- Proposed network models consist of ±525 kV submarine and land cables.
- Proposed network models consider wind farm/wind turbine dynamics based on real-time wind gusts using SiL setup.
- Electrical and control parameter perturbation using an automatic script.
- Provides an overview of required Cores per network models.
- Proposed networks consist of an average model of VARC DC CB.

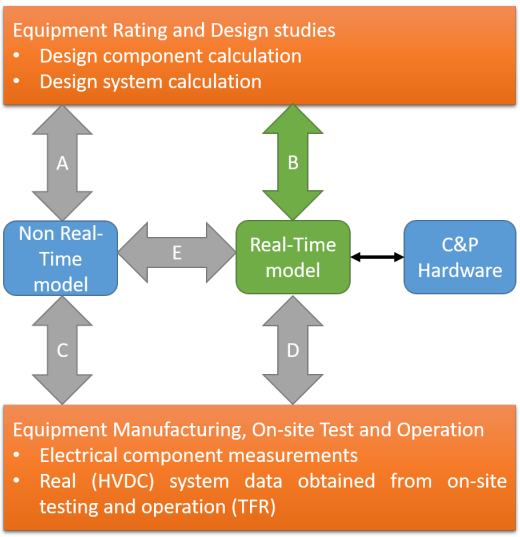

Figure 4.1: Different validation paths overview during the HVDC project phases [66].

4.2. NETWORK DESCRIPTION

For interoperable control and protection studies, the MT-HVDC grid should be designed with the maximum amount of details. In this chapter, different MT-HVDC configurations will be considered depicted in Figure 4.2.

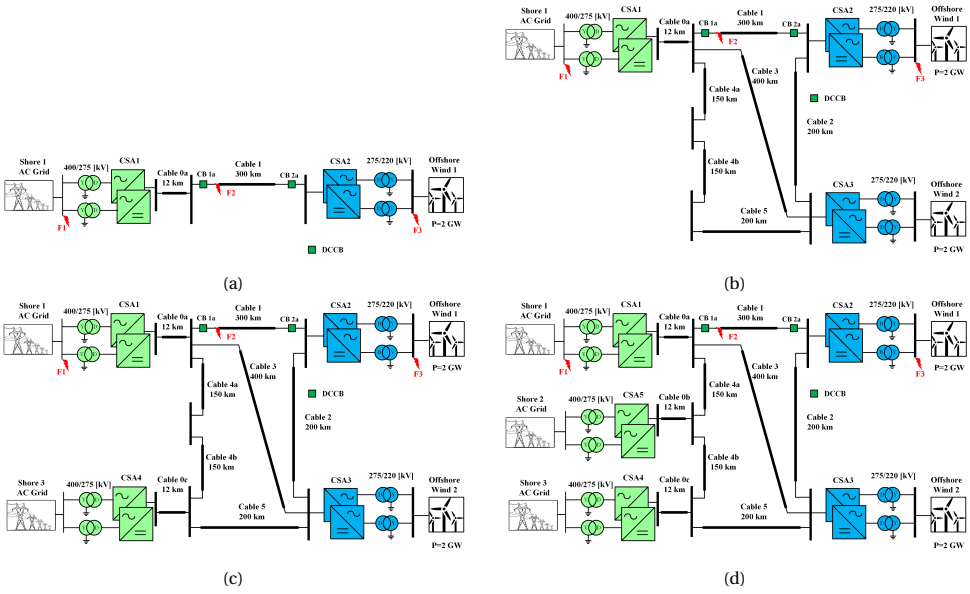

Figure 4.2: MT-HVDC with (a) two-terminals; (b) three-terminals; (c) four-terminals; and (d) five-terminals.

The network topologies have a DC voltage rating of ±525 kV, with bipolar DMR configurations. The converter is a half-bridge topology. The system can be divided into three subsystems: an onshore AC system, a DC system, and an offshore AC system.

The onshore AC system consists of Thevenin's equivalent circuit (static voltage source) of a strong grid; the grid impedance is computed based on the short circuit current level—a series resistor connection of a parallel resistor and inductor models it. By adjusting the values of the inductance and resistance, the short circuit current value and the damping angle at fundamental and N^{th} harmonic are controlled.

The rated line-to-line (LL) voltage is 400 kV. The onshore converter station has two Y-D transformers, with ratings of 2 GVA each. The voltage ratio of this transformer is 400 kV/275 kV. Onshore converters are labeled CSA1, CSA4, and CSA5. However, based on the selected topology, the converters are omitted.

The number of land and submarine DMR cables varies depending on the network topologies. For the five-terminal HVDC system, the number of land DMR cables are cable 0a, 0b, and 0c. The length of these cables is 12 km. The land cables connect the onshore DC hub, which comprises DC breakers; for simplicity and to reduce the computation burden, only one DC breaker is employed. Furthermore, the DC system comprises six submarine cable links: cable 1 (300 km), cable 2 (200 km), cable 3 (400 km), cable 4a (150 km), cable 4b (150 km), and cable 5 (200 km). The cables are modeled

as a Frequency-Dependent (phase) model. Furthermore, the cable link consists of three conductors (i.e., a positive, a negative cable, and metallic return per cable link) due to DMR topology. cable 1 consists of two simplified VARC DC CB placed on the positive pole at either end of the cable, as seen in Figure 4.2.

The offshore AC system consists of converter stations and aggregated average-value model wind farms. In the applied networks, offshore converters are labeled CSA2 and CSA3. However, based on the topologies, the converters are omitted. The offshore converter is connected to the offshore AC system via D-Y transformers. The rating of this transformer is 275 kV/220 kV, 2 GVA. Besides, this converter transformer is connected to a wind turbine transformer. This transformer has a voltage ratio of 220 kV/66 kV and acts as a VA scaled-up transformer. Thus, a power rating of 2 GW can be achieved by choosing the proper scaling factor. The lower voltage end of this transformer is connected to the wind turbine. The wind turbines are Type 4 and have a rating of 2 MW at a wind speed of 15 m/s. In this work, three fault locations are selected. F1 indicates an AC fault at the PoC of the CSA1, F2 indicates a DC fault at the DC terminal near CSA1, and F3 indicates an AC fault at the PoC of CSA2.

4.2.1. CONVERTER STATION

With the high number of SMs, the AC side of the valve provides a smooth AC waveform. The Type 5, i.e., Average Value Models [177] based on switching functions, converter model is used in these networks. To capture the accurate dynamics of the converter station, it is modeled by using small time steps of RTDS©. Table 4.1 lists the converter station parameters with associated values used in this work. Further, to reduce the modeling time, control, electrical parameters, and limits values are scripted using draft variables. These draft variables are controlled via a script at the start of the simulation. This script is written in C++ in an RSCAD© environment.

CONTROL SYSTEM IN CONVERTER STATION

The control hierarchy of the converter station is explained in chapter 3 and summarised in this section. In the MT-HVDC, each onshore converter station consists of three primary control loops, namely, OVC, ICC, and CCSC, as shown in Figure 4.3. Figure 4.3 highlights the PI controls of the onshore and offshore converters. The OVC provides references to the ICC. The dispatch level provides the setpoints to the OVC via TCP/IP communication interface. The setpoint signals include a DC voltage, an AC voltage, an active power, a reactive power, and frequency. The selection of these signals depends on the control mode (i.e., constant DC voltage, grid forming/Islanded mode, active-reactive power control mode). The system operators/DC grid controller typically operate the dispatch controls. The system operators/DC grid controller provide the setpoint based on AC/DC power flow and day-ahead demand. Furthermore, a negative sequence control option is also introduced in the ICC, as shown in Figure 4.3 (b).

The ICC loop generates the modulating voltages ($v^{\Delta}_{M,dq}$) based on the feedforward terms ($v^{\Delta}_{g,dq}$), de-coupled currents ($i^{\Delta}_{g,dq}$), and reference signals provided by OVC. In the case of sequence control, a double synchronous reference frame (DSRF) is used to express voltage and current into a positive (+) and a negative (-) sequence component. Furthermore, to eliminate the $2\omega_0$ frequency component in the DC current and voltage,

Table 4.1: Converter station parameters

Parameter	Onshore converter station per MMC	Offshore converter station per MMC
Rated Power	2000 MVA	2000 MVA
fundamental frequency	50 Hz	50 Hz
AC grid voltage	400kV	220 kV
AC converter bus voltage	275 kV	275 kV
DC-link voltage	525 kV	525 kV
Transformer reactance	0.18 pu	0.15 pu
MMC arm inductance	0.025mH	0.0497mH
MMC arm resistance	0.0785	0.0785
Capacitor energy in each submodule (SM)	30 MJ	30 MJ
Number of submodules per valve	240	200
Rated voltage and current of each submodule (SM)	2.5 kV /2kA	2.5 kV / 2kA
Conduction resistance of each IGBT/diode	5.4410^{-4}	5.4410^{-4}

the reference to the negative current sequence component ($i^{\Delta,-}_{d,dq}$) is set to zero, as shown in Figure 4.3(b). However, according to the ENTSO-E grid codes for specific nations [178], this control might have practical implementation restrictions.

The ICC and OVC are only responsible for the AC grid current's fundamental and odd-harmonic components. The CSCC controls the DC and the even harmonic components of the AC grid current, whose presence is responsible for the generated losses in the converter. Hence, these currents are suppressed by generating modulated voltage ($v^{\Sigma}_{M,dq}$), and as a result, only the DC component is present.

The islanded mode is realized by enabling DVC, which is the simplest form of grid-forming control [177]. Likewise, onshore converters, the offshore converter during the islanded mode of operation receives setpoint commands from the dispatch control. Generated modulated voltages ($v^{\Delta,\Sigma}_{M,dqz}$) are then applied to the LLC, which comprises dq-abc transformation and sort-and-select submodule modulation. Traditionally, these controls are implemented by applying PI controllers to transform AC measurements from the abc-frame into the stationary dq-frame using PLL, except for a grid-forming control using an oscillator [94].

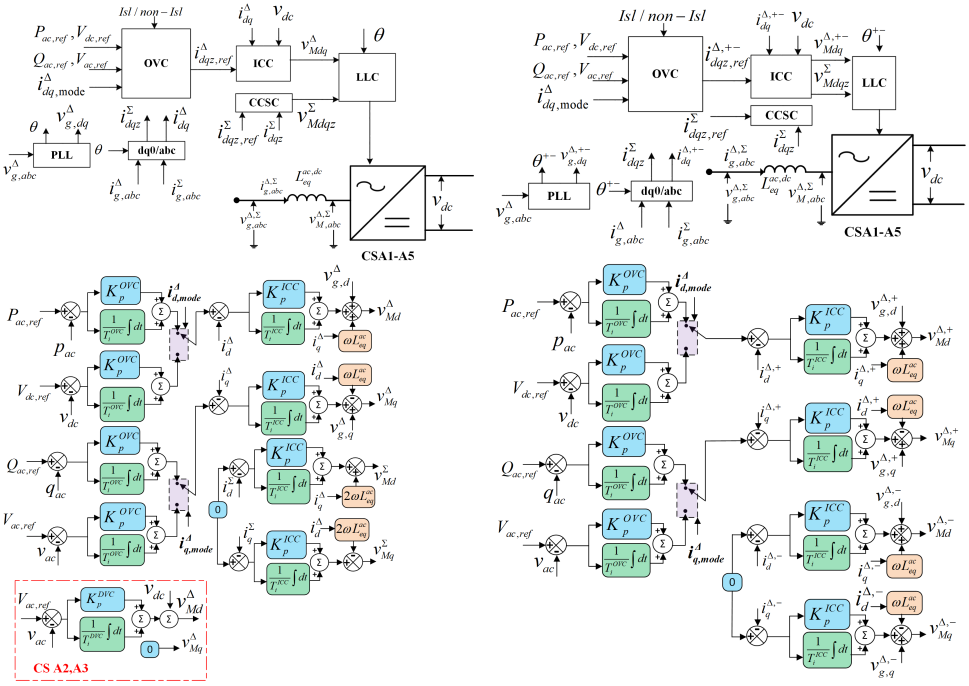

Figure 4.3: Different Control strategies : (a) Traditional PI-based control ; (b) Sequence PI-based control.

4.2.2. DIRECT CURRENT CIRCUIT BREAKER (DC CB)

Among the many different DC CB technologies, VARC DC CB technology is selected for these networks. The VARC DC CB uses a VSC and a series-resonant circuit to generate high-frequency current oscillation, which creates a current zero in the vacuum interrupter. The VARC DC CB consists of three major branches, i.e., a main branch, an energy absorption, and a current injection branch, as shown in Figure 4.4. Furthermore, the working principle, experimental validation, and modularity of the DC CB are explained in [101]. Factors contributing to the selection of load units and limits are

Table 4.2: Parameters of Detailed and Average VARC model for 525 KV system

Parameters	Symbol	Detailed model	Average model
Oscillation Inductor	L_p	$95\mu H$	$0\mu H$
Oscillation Capacitor	C_p	$2.27\mu F$	$0.388\mu F$
Rated / clamping voltage of Surge arrester	V_{rated}/V_{clamp}	$80/120kV$	$525/787.5kV$
Initial voltage across C_p	V_{ini,C_p}	$10kV$	$0\ kV$
Number of modules	N_m	7	1

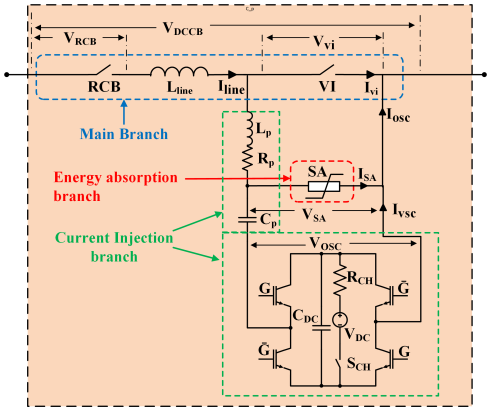

Figure 4.4: An illustration of a 80kV VARC DC CB module [100].

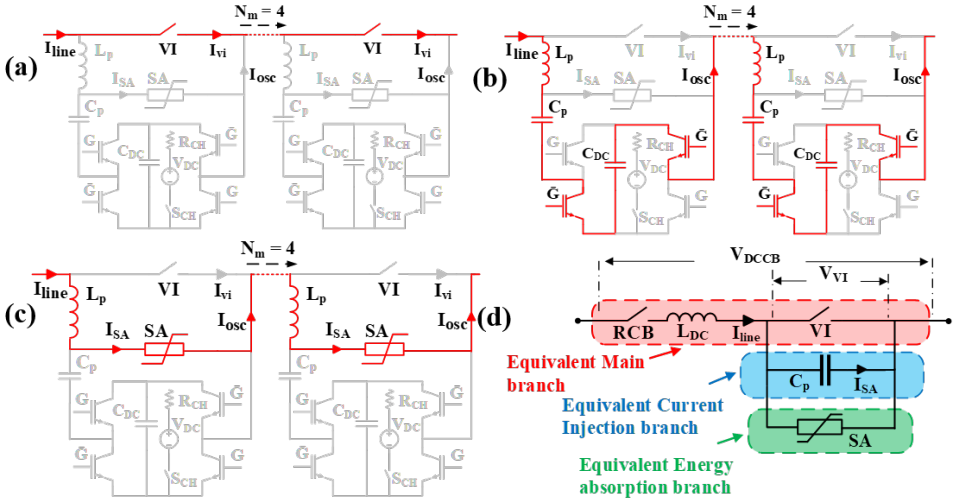

Figure 4.5: Equivalent Average Model of VARC DCCB model.

memory requirements, the number of computations, and execution speed. However, the main goal of the designed model is to keep the time-step at a reasonable size for real-time simulation. Thus, an equivalent average model of VARC DC CB is proposed in [101]. Hence, this work adopts an equivalent average model of a VARC DC CB for system-level dynamic studies. Like the detailed VARC DC CB, the equivalent average model consists of three branches. During the operation of the VARC DC CB, these branches are connected in series for N_m modules, as shown in Figure 4.5(a-c). As a result, an aggregation of the VARC parameter is possible, as shown in Figure 4.5(d). Parameters for each branch are aggregated for the rated DC-link voltage, and aggregated values are shown in Table 4.2. The advantage of this average model is that it can be modeled using power system components of the RSCAD© library with no dedicated Core requirement.

4.2.3. SEA AND LAND HVDC CABLE

The cable is modeled by using the Frequency-Dependent (phase) model. The data for the cable model is based on the experience of 2 GW [179] Offshore Interconnection projects in the North Sea and has been listed in Tables 4.3 and 4.4.

Table 4.3: Relevant Geometrical and Material Data of Generic 525 kV HVDC Land Cable

Main layers	Properties	Unit	Parameter Data (Nominal)
Core Conductor	Metallic cross-sectional area	[mm^2]	3000
	Outer diameter	[mm]	68
	DC resistivity (max.) at 20 °C	[Ωm]	1.724110^{-8}
Main Insulation (XLPE)	Conductor Screen thickness	[mm]	1.8
	Main insulation thickness	[mm]	26.5
	Insulation screen thickness	[mm]	1.5
	Relative permittivity	-	2.4
Metallic Screen	Screen thickness	[mm]	1.2
	Diameter over screen	[mm]	138
	DC resistivity (max.) at 20 °C	[Ωm]	2.826410^{-8}
Outermost Jacket	HDPE Jacket Thickness	[mm]	5.0
	External semiconductive skin thickness	[mm]	0.3
	Relative permittivity	-	2.5
Overall cable	Diameter	[mm]	153

Table 4.4: Relevant Geometrical and Material Data of Generic 525 kV HVDC Subsea Cable

Main layers	Properties	Unit	Parameter Data (Nominal)
Core Conductor	Metallic cross-sectional area	[mm^2]	2500
	Outer diameter	[mm]	60
	DC resistivity (max.) at 20 °C	[Ωm]	1.724110^{-8}
Main Insulation (XLPE)	Conductor Screen thickness	[mm]	2.0
	Main insulation thickness	[mm]	26.0
	Insulation screen thickness	[mm]	1.8
	Relative permittivity	-	2.4
Metallic Sheath	Material	-	Lead
	Thickness	[mm]	3.2
	DC resistivity (max.) at 20 °C	[Ωm]	2.1410^{-7}
Armour	Material of Armour wires	[mm]	galvanized steel
	The thickness of single armor wire	[mm]	6.0
Overall cable	Diameter	[mm]	161

4.2.4. WIND TURBINE/PLANT MODEL

The Wind Turbine model used for this study is a Type-4 full converter model [180], with a single-line diagram shown in Figure 4.6. The Type 4 wind turbine model consists of four main components: the Wind turbine model, a permanent magnet synchronous machine (PMSM), an AC-DC-AC Power electronic converter system, and a scaling transformer.

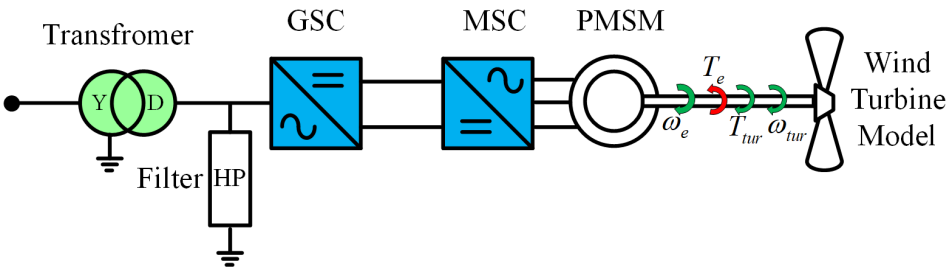

Figure 4.6: Simplified circuit of wind energy system

The AC-DC-AC power electronic converter consists of a back-to-back two-level converter, providing full-scale power to the AC grid. The AC grid-side converter is known as a grid-side converter (GSC) and controls the back-to-back two-level converter's DC-link voltage and AC / reactive power support. Due to the two-level converter, the converter is accompanied by a high pass (HP) filter to filter out higher frequencies. The machine-side converter (MSC) connects PMSM to the back-to-back two-level converter's DC link. This converter acts as a variable-frequency VSC system. The MSC controls the stator voltage and PMSM torque. The control architecture of GSC and MSC will be explained in the following section. A scaling transformer is used to model the wind power plant, which acts as an interface between the lower-power wind turbine and the offshore converter station. Another function of this transformer is to represent an aggregated wind farm by adding a scaling factor to the power produced by the wind farm. The wind speed data is uploaded to RTDS© through co-simulation. The TCP/IP protocol connects RTDS© to the Python script as explained in Appendix A.

The characteristic equations of the GSC at the PoC in a dq rotating frame are given as [181]:

$$v_{md}^G = v_d^G + R^G i_d^G + L_L^G \frac{\mathrm{d}i_d^G}{\mathrm{d}x} - \omega^G L_L^G i_q^G, \tag{4.1a}$$

$$v_{mq}^G = v_q^G + R^G i_q^G + L_L^G \frac{\mathrm{d}i_q^G}{\mathrm{d}x} + \omega^G L_L^G i_d^G, \tag{4.1b}$$

where $v_{md}^G = \frac{1}{2} m_d^G V_{dc}^{bus}$ and $v_{mq}^G = \frac{1}{2} m_q^G V_{dc}^{bus}$ are the dq components of the modulating voltages of GSC, being the product of the modulation index m and DC-bus voltage V_{dc}^{bus}. Furthermore, R^G is the leakage resistance, L_L^G is the leakage inductance, i_d^G and i_q^G are the grid currents in dq-frame and ω^G is the angular grid frequency.

he rated voltage of the PMSM is 4 kV and the power at a wind speed of 12 m/s is 2 MW. An interior magnet machine with a sinusoidally distributed winding is considered during

the modelling of the PMSM. As Clark-Park transformation is used, PMSM is represented in a dq-frame as [181]:

$$v_{md}^P = R^P i_d^P + (L_{Md}^P + L_L^P)\frac{\mathrm{d}i_d^P}{\mathrm{d}x} - \omega_r^P (L_{Md}^P + L_L^P) i_q^P, \tag{4.2a}$$

$$v_{mq}^P = R^P i_q^P + (L_{Mq}^P + L_L^P)\frac{\mathrm{d}i_q^P}{\mathrm{d}x} + \omega_r^P (L_{Mq}^P + L_L^P) i_d^P + \omega_r^P \Psi_f^P, \tag{4.2b}$$

$$T_e^P = \frac{3}{2}\left[\hat{\psi_f^P} i_q^P + (L_{Md}^P - L_{Mq}^P) i_d^P i_q^P\right], \tag{4.2c}$$

where $v_{md}^P = \frac{1}{2} m_d^P V_{dc}^{bus}$ and $v_{mq}^P = \frac{1}{2} m_q^P V_{dc}^{bus}$ are the dq components of the modulating voltages of PMSM, as a product of the modulation index m and the DC-bus voltage V_{dc}^{bus}, R^P is the stator resistance, L_{Md}^P and L_{Mq}^P are the mutual inductances in the dq-frame, L_L^P is the stator leakage inductance, i_d^P and i_q^P are the stator current in dq-frame, ω_r^P is the rotor electrical speed, T_e^P is the developed toque by PMSM and Ψ_f^P is the permanent magnet flux. The model of the wind turbine is derived considering steady-state wind power:

$$P_m^P = c_p(\lambda, \beta)\frac{\rho A}{2} v_{wind}^3, \tag{4.3}$$

where P_m^P is the mechanical power output of the turbine, ρ is the air density, A is the area swept pot by the turbine blade, v_{wind} is the wind velocity, and $c_p(\lambda, \beta)$ is the performance coefficient of the turbine, which is a function of tip speed ratio λ and the blade pitch angle β.

Classical PI controllers are applied to control offshore wind farms. The GSC controls the active and the reactive power exchange between the wind power plant and the offshore AC grid. The dq current decoupling method is used as shown in Figure. 4.7(a). The active power reference is computed in a way that the DC-bus voltage is maintained at a constant value, whereas the reactive reference is computed to support the offshore AC voltage.

For a higher PMSM efficiency, MSC controls maintain the 180-degree phase shift between the stator current and voltage. The quadrature axis component of the stator current maintains the power requested by the wind turbine as shown in Figure. 4.7(b). The rotor speed is a cubic function of power, while the direct component of the stator current controls the reactive power at its minimum level until the rated power is reached. This is carried out by storing the d-axis stator current in a table (formatted as $y = f(x)$), where the output is the function of the rotor electrical speed.

The interface transformer performs two functions. Firstly, it connects the large-time step (i.e., 50 μs) network to the small-time step network. Secondly, it is used to represent an entire wind farm. The scaling increases the MVA power and current ratings. The PWM scheme is used in a way that the switching frequency is 19 times the fundamental frequency. Therefore, the current and the voltage harmonics appear to be around the switching frequency. For this reason, a high-pass filter is implemented at the large time step network side of the interface transformer.

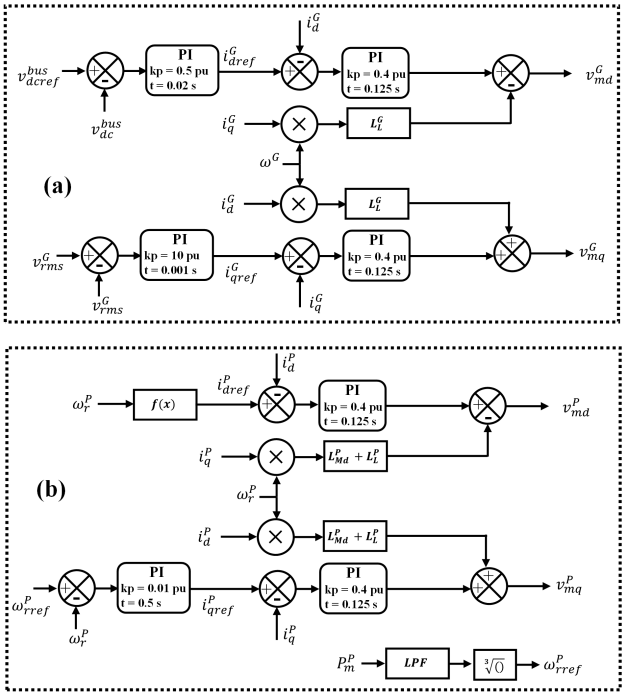

Figure 4.7: Controller scheme for: (a) grid side converter (GSC); (b) machine side converter (MSC).

4.2.5. PROTECTION CRITERIA: CONVERTER AND DC CB

During transient events, protection is essential for component and system safety. The converter is protected from overcurrent during unscheduled events. This work considers full selective fault clearing with a DC CB protection scheme [182]. This scheme uses fault current limiters and DC CB to clear the fault. The primary purpose of this scheme is to keep the grid operating during the DC fault. The protection algorithm blocks the converter when the converter arm currents exceed the threshold value. The IGBT rating determines this value. It is set to be two times the rated IGBT current in this work. Furthermore, the overcurrent protection is not triggered during the energization. The overcurrent protection of the converter also considers an overcurrent period. This protection is in an inactive state for a dormant period. The dormant period is determined by the operating time required by the DC CB to operate. Since VARC DC CB is employed, this dormant period is set to 5 ms. To avoid any complexity, the detection algorithm of the DC CB is based on the rate of rise of the fault current. If the rate is above 4 kA/ms, the trip signal is provided to the DC CBs. Upon receiving a trip command, the breaker operates and interrupts the fault.

4.3. COMPUTATION LOAD AND CORE ASSIGNMENT

RTDS© make use of different Core-based simulation environment as discussed in Chapter 3. To make the model backward compatible (.i.e, older processors), optimal

Core utility, and lower switching frequency of MMC, a small time-step simulation environment is chosen for modeling MMC.

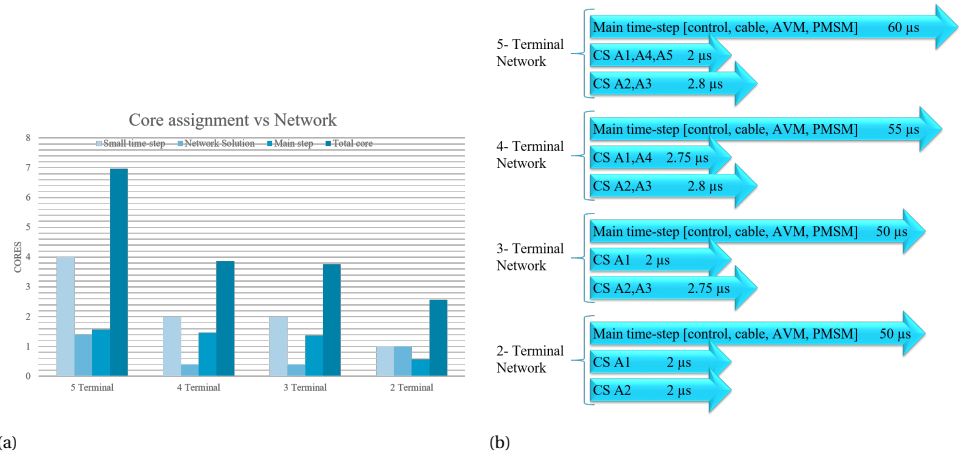

(a) (b)

Figure 4.8: For different networks : (a) Core assignment ; (b) Time-step assignment

Depending on the network, the Core and time steps are shown in Figure 4.8. The offshore converters are placed on a single Core in all networks, as shown in Figure 4.8(b). In the case of a five-terminal network, the minimum number of required Cores is 7. These Cores' distribution can be down based on the simulation environment and element modeled. The converter station is modeled in a small-time step environment. Each onshore converter station requires a dedicated Core, whereas the offshore converter stations run on a single Core. The main reason for this is to reduce the Core requirement. However, placing offshore converters on a single Core increases the computation time. Hence, the requested time step for the small time-step environment consisting of an offshore converter is 2.8 μs. In contrast, the time step for a small time-step environment consisting of an onshore converter is set to 2 μs. Type-4 wind turbines, cables, and control system run in the main time step. Due to the large control signals and measurement, the main time step is about 60 μs.

Figure 4.8(a) displays the computed Core requirements derived from the processor assignment table in RSCAD/RTDS ©, illustrating values that are not whole numbers. For example, a maximum of 300 load units is fitted in one Core. However, for five-terminal networks, the Network solution needs 420 (1.4 Core) load units. Other main step elements require 470 load units (1.5 Cores). These two can share Cores, unlike a small time-step simulation environment. Thus in total, the network occupies 2.9 Cores. In reality, the Core is an integer. Thus the closest maximum value will be 3.

In the four-terminal network, the onshore converters are placed on a single Core, as seen in Figure 8(a); as a result, the time-step requirement is higher than that in other networks. Thus, 2.75 μs is chosen for a small-time step environment. The main simulation time is set to 55 μs as the power and control load is reduced. Since the number of converter stations, cables, and control components is reduced for four-, three-, and two-terminals networks, the net minimum requirement of the number of

Cores is four and three, respectively. With a lower computation load, the main time step of the network is lower for three- and two-terminals.

4.4. NETWORK FEATURES

The network proposed in this work consists of the following feature:

- **Aggregated Wind Turbines model**: The model uses an average value model of the converter to represent the wind farm without losing the dynamics of wind turbines. The aggregation of a wind turbine is done by a scale transformer, where a factor amplifies the current. This avoids high computation load.
- **Scripted Parameter**: The important physical and control parameters are controlled by a script, reducing modeling time. The script controls the draft variables in RSCAD, which is RTDS©'s human-machine interface (HMI).
- **Average Model of VARC DC CB**: The average employed model of the DC CB uses passive and non-linear elements, reducing the computation load without losing the critical feature of breakers.
- **DMR cable model**: Both land and sea cables are modeled using the Frequency-Dependent (Phase) model with data based on the experience of 2GW Offshore Interconnection Projects in the North Sea. This routine accurately models the DMR cables as well.
- **Negative Sequence control**: To have the minimum impact of the AC imbalances, a negative sequence in an onshore converter is introduced in this work.
- **Starting sequence**: The network includes a sequence of DC grid energization. This sequence is written in a script, making the energization process flexible for the user
- **Modular modeling**: The networks enable easy replicability of the converter stations. Hence, the DC grid can be expanded based on user requirements.
- **Converter Protection**: The network provides a converter overcurrent protection, as explained in the previous section.
- **Real-time wind profile**: The network captures wind speed data in real-time from Orkney Islands and Shetland Islands in the North-sea using a SiL setup. The wind data is updated every 100 ms.
- **Different control modes**: This network also comprises different control modes presented in Cigre 604 [177].

4.5. SIMULATION RESULTS

This section investigates unscheduled events like startup and black start sequences for the five-terminal network. Similarly, different steady-state and transient studies can be performed for the selected networks and are omitted in this work due to page limitations. However, these studies are highlighted in the next section.

UNSCHEDULED EVENTS

In the unscheduled events, three scenarios are considered. Namely, Single-Phase-to-Ground (SLG) fault on the offshore AC side, Positive-Pole-to-Ground (PG) fault on the DC side, and SLG fault on the onshore AC side. A temporary SLG fault of 200 ms in the offshore AC grid near CSA2 causes a drop in the AC voltage at PoC, as seen in Figure 4.9 (I-d). This fault causes a decrease in power and second-order fundamental frequency oscillation (Figure 4.9 (I-c)). Further, this oscillation is propagated into the DC grid through DC-link voltage and converter current, as shown in Figure 4.9 (I-a and I-b), which impacts AC grids connected to DC grids. Similarly, the network is tested for a PG fault near the terminal of CSA1, and the simulation results are presented in Figure 4.9 (II). During the fault, net DC-link voltage reduces, as seen in Figure 4.9 (II-a); however, it is interesting that even at fault near the CSA1 terminal, DC-link voltage at the CSA2 terminal reduces. This is due to the uncontrolled power dispatch during the fault between the DC cables. The DC CB completely interrupts the fault current in 5 ms. Once the fault current is interrupted, the DC fault current stops rising due to high impedance by the surge arrester of DC CB. Since there is no increase in the fault current (i.e., after 5 ms from the fault inception), the internal protection of the MMC is not triggered. After the fault interruption, DC grid coverage to a new stable equilibrium point.

Figure 4.9(III) shows the impact of 200 ms SLG onshore fault near CSA1. This figure also compares AC faults with and without negative sequence control. As discussed in the previous section, the onshore converter stations are employed with a negative sequence control; the presence of this control reduces the amplitude of the second-order fundamental frequency component, as seen in Figure 4.9 (III-b,d, and f) compared to the traditional control scheme. This second-order oscillation arises due to an imbalance in the AC voltage (Figure 4.9 (III-g)). Thus by controlling the positive sequence current component and setting the negative sequence current component to zero, the second-order of the fundamental frequency is regulated in the DC grid.

With a temporary three-phase-Fault-to-Ground at the offshore converter (CSA2), the active power injected by wind farms reduces significantly, as seen below in Figure 4.10 I-(c). The CSA1 partially compensates for this loss of power during fault. Rest power is drawn from the DC link causing a drop in the DC-link voltage. With a temporary three-phase-Fault-to-Ground at the onshore converter (CSA1), the active power injected by wind power plants remains the same; however, due to the fault near the converter controlling the DC-link voltage causes overvoltage due to the excess power in the DC link for both type of controls (i.e., traditional and sequence control) as seen in Figure 4.10 II-(a) and (b).

These extreme events were performed to test the network's response. However, these are simulated scenarios, and the occurrence of fault during full load capacity is extreme. However, performing such studies aims to get an overall picture of the transient overvoltage and overcurrent profile, which will help the design and specify the protection equipment's setting and control strategies.

STARTUP AND BLACK START SEQUENCE

Table 4.5 highlights different events carried out during the energization and black start of five-terminal networks. Figure 4.11 illustrates the PP voltage of five converter stations

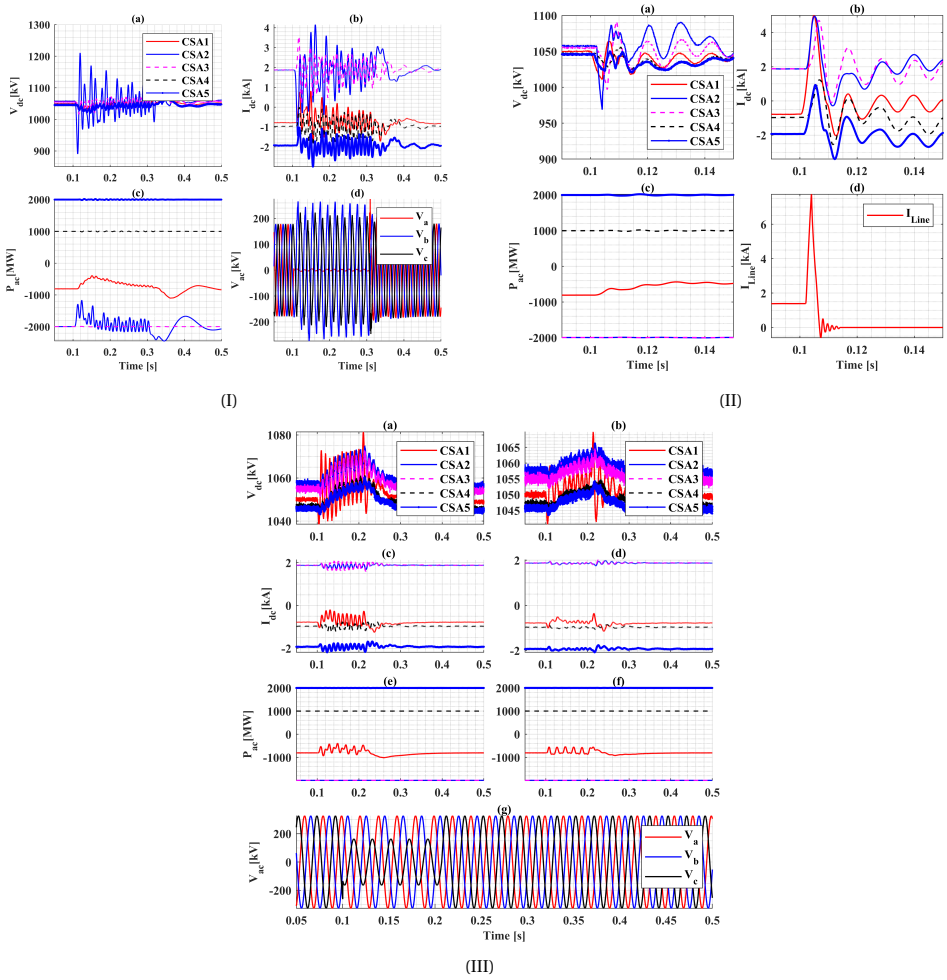

Figure 4.9: [I] SLG fault on the offshore AC side, (a) DC-link voltage, (b) Positive pole DC current of CS, (c) Active Power of CS, and (d) Three-phase offshore voltage at PoC, [II] Positive PG fault on DC-side, where (a) DC-link voltage, (b) Positive pole DC current of CS, (c) Active Power of CS and (d) Positive pole DC current through cable 1 and [III] SLG fault on the onshore AC side, where (a),(c) and (e) are DC link voltage, Positive pole DC current of CS and Active Power of CS without negative sequence control. (b),(d) and (f) are DC link voltage, Positive pole DC current of CS, and Active Power of CS with negative sequence control. (g) The three-phase onshore voltage at PoC

during the startup. This Figure is only high transient due to events being labeled via numerical value. The description of these labels is indicated in Table 4.5.

At the start of simulations, all the converters and cables are de-energized. Hence, the energization occurs by first connecting the converter responsible for regulating DC-link voltage, i.e., CSA1. However, firstly, the pre-insertion resistance is connected to limit the inrush current. Since each converter station has two poles, a sequential connection

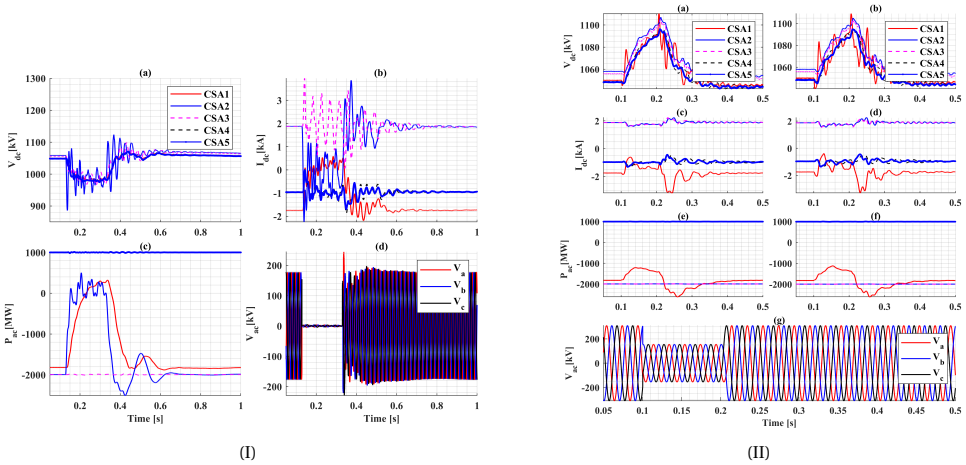

Figure 4.10: [I] The three-phase fault on the offshore AC side, where (a) DC-link voltage, (b) Positive pole DC current of CS, (c) Active Power of CS, and (d) Three phase offshore voltage at PoC and [II] The three-phase fault on the onshore AC side, where (a),(c) and (e) are DC-link voltage, Positive Pole DC current of CS and Active Power of CS without negative sequence control. (b),(d) and (f) are DC-link voltage, Positive pole DC current of CS, and Active Power of CS with negative sequence control. (g) The three-phase onshore voltage at PoC.

of pre-insertion resistance is made. Firstly, the positive pole (CSA1P) pre-insertion resistance is connected, followed by the negative pole (CSA1N) pre-insertion resistance. This leads to the charging of the SM in the positive and negative poles. Once the converters are charged, the next step is to collectively charge the DC cables using a disconnector and pre-insertion resistance. By closing of the disconnector, an extensive DC voltage transient, with a lower peak value of 203 kV, is observed. The pre-insertion resistance is bypassed upon charging the DC cable to eliminate the i^2r losses during the steady-state operation. Similarly, a local impact of DC voltage at CSA2 and CSA3 is observed during closing the disconnectors at CSA2 and CSA3. Like CSA1, the CSA4 converter station is energized and connected to the DC grid.

Firstly, the DC voltage setpoint is kept at 80% of the rated DC voltage, and the converter CSA1 is deblocked. Since there is no offshore grid, CSA2 and CSA3 are deblocked, which creates a transient in the DC voltage, as shown in the zoom plot. Once the offshore voltage is stabilized, the collective black start of the wind farm is carried out. Following this event, the DC voltage is ramped to the rated voltage by changing the setpoints. Once the rated DC grid voltage stabilizes, wind farm 1 and wind farm 2 each inject 1 GW of power into the DC grid. After the deblocking of converter CSA4, the power is ramped to 1 GW into the onshore AC grid.

In this work, an investigation of the performance of the HVDC grid by connecting new HVDC components is also considered. This new connection is converter CSA5. Considering the stable operation, and how the new connection impacts the stability and stress in the DC grid can be investigated. The impact is lower when the new converter station is energized through the onshore AC grid. However, a sharp transient is observed in the PP voltage of converter CSA5 upon re-closing the disconnector. Furthermore, the

Table 4.5: Startup and black start sequence for Five-terminal network

Events	Time (sec)	Events	Time (sec)
Enable pre-insertion resistance at CSA1P (1)	1	Changing the DC-link voltage setpoint to 0.8 pu	41
Enable pre-insertion resistance at CSA1N (2)	3	Deblock CSA1 (8)	43
Close the DC grid disconnector at CSA1 (3)	5	Deblock CSA2 (9)	45
Bypass pre-insertion resistance at CSA1P	7	Close the DC grid disconnector at CSA4 (10)	47
Bypass pre-insertion resistance at CSA1N	9	Deblock both the wind farm	49
Close the DC grid disconnector at CSA2 (4)	11	Deblock CSA3 (11)	51
Enable pre-insertion resistance at CSA2P	13	Changing the DC-link voltage setpoint to 1 pu (12)	53
Enable pre-insertion resistance at CSA2N	15	Increasing wind power to 1GW at WF1 (13)	55
Bypass pre-insertion resistance at CSA2P	17	Increasing wind power to 1GW at WF2 (14)	57
Bypass pre-insertion resistance at CSA2N	19	Deblock CSA4 (15)	59
Close the DC grid disconnector at CSA3 (5)	21	Changing the Active power setpoint to 1000 MW at CSA4 (16)	61
Enable pre-insertion resistance at CSA3P	23	Enable pre-insertion resistance at CSA5P (17)	63
Enable pre-insertion resistance at CSA3N	25	Enable pre-insertion resistance at CSA5N (18)	65
Bypass pre-insertion resistance at CSA3P	27	Bypass pre-insertion resistance at CSA5P	67
Bypass pre-insertion resistance at CSA3N	29	Bypass pre-insertion resistance at CSA5N	69
Close Wind Farm disconnectors	31	Close the DC grid disconnector at CSA5 (19)	71
Enable pre-insertion resistance at CSA4P (6)	33	Deblock CSA5 (20)	73
Enable pre-insertion resistance at CSA4N (7)	35	Changing the Active power setpoint to 1000 MW at CSA5 (21)	75
Bypass pre-insertion resistance at CSA4P	37	Increasing wind power to 2GW at WF1 (22)	77
Bypass pre-insertion resistance at CSA4N	39	Increasing wind power to 2GW at WF2 (23)	79

power setpoint of CSA5 creates an overload in the network, especially in the DC cables and CSA1.

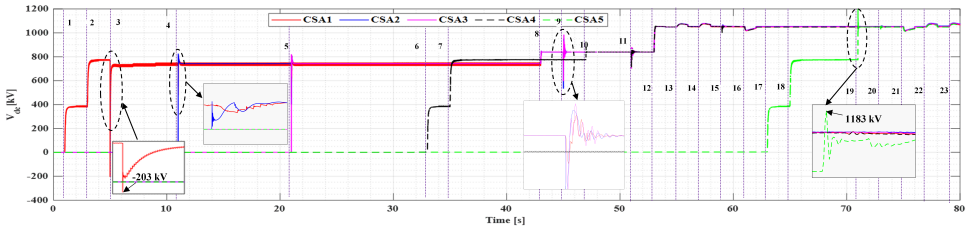

Figure 4.11: PP voltage of different converter stations during startup

Table 4.6: Possible analysis performed on proposed networks

Transients Analysis during normal operation	Setpoint changes and load rejections
	Startup (energisation) sequence
	DC system discharging
	Switching operations
	Black start – sequential and collective energisation.
Grid-side transients analysis	Grid side faults
	Switching operations and abnormal operating conditions
DC-side transient analysis	DC-side faults: Internal and external faults
	DC cable voltage stress: Impact of cable segments
	Failure mode analysis of DC CB
Interaction studies	Parallel VSC-HVDC
	Offshore wind power plant
	Interaction due to DC grid
	Interaction between converters
	Interaction due to non-linear function

4.6. STUDIES AND ANALYSIS PERFORMED ON THE PROPOSED NETWORK

Based on the suggestions provided in Cigre B4-832 [160], the proposed network can be used for different practical studies. During the project's preliminary phase, these networks can be used to determine the DC fault performance and the impact of the new HVDC link. Furthermore, it can also be used for evaluating the effect of DC cable on the transient and dynamic system performance, grid code studies, the impact of the AC system, and different overvoltage investigations. In the bid phase, these networks can be used for the determination of critical measurement locations, transient overvoltages & overcurrents, and dynamic performance studies. During the implementation phase, the studies, as mentioned earlier, can be investigated in detail using these networks via analysis in Table 4.6.

4.7. CONCLUSION

This chapter introduces different models that can be applied to simulate MT-HVDC networks in real-time by using real-time update of wind power data. The models can be used for different actual HVDC topologies. The proposed network models address the shortcomings of existing network models provided in technical brochures and are designed for the system ratings required by the north-sea grid operator. The models use accurate parameters for dedicated metallic returns of sea and land cables, and the system and control parameters are scripted, reducing modeling time for perturbation and sensitivity studies. The proposed models also consider the average value model of wind farms, enabling investigation into the interaction and dynamics caused by wind farms.

The performance of the models is evaluated using unscheduled events, like startup and black start events. It is observed that the presence of the second-order fundamental frequency component is reduced during SLG fault at the onshore PoC due to the use of negative sequence control. However, the SLG fault at offshore PoC causes large disturbances in the offshore grid, which are transmitted into the DC grid. Different stress points are observed in the startup and black start sequence, which are crucial during component design and protection studies.

Additionally, this chapter elaborates on the computational requirement per network model, which helps users select the appropriate model depending on the modeling requirement. Finally, the chapter discusses future studies that can be conducted using the proposed network, which will assist users in defining component design and system calculation. Overall, the proposed real-time network models with wind profile feedback provide a valuable tool for manufacturers and system operators to perform different life-cycle studies of HVDC projects. In this way, it contributes to developing more efficient and reliable HVDC grid systems.

The four proposed networks provide new voltage ratings and cable models for upcoming European projects and can be a starting point for system studies and control system design. Furthermore, these networks can be used for training and developing system operators' skills necessary to acquire knowledge in transient and dynamic studies related to MT HVDC grids.

5

ADVANCED MMC CONTROL

The first part of this chapter introduces advanced controls for HVDC grids, particularly focusing on integrating Model Predictive Control (MPC) with Laguerre's Function to significantly enhance grid stability and operational efficiency. It delves into the theoretical underpinnings of MPC, its formulation, and its application in MMCs, setting a solid foundation for advanced HVDC control. Through rigorous stability analysis and detailed simulations, the effectiveness of MPC in improving grid dynamics and fault management is highlighted, showcasing its advantages over traditional control methods. The second part introduced transitions to the practical application of these advanced control strategies within an MT-HVDC grid. It covers the system's configuration, the implementation of cascaded MPC for DC voltage control, and grid-forming control. This section underscores the superior performance of MPC through simulation results, especially during fault conditions, emphasizing its potential to revolutionize grid reliability and efficiency. Finally, the chapter concludes the widespread application of MPC in future HVDC grid developments, marking a significant leap forward in the power system control approach.

Parts of this chapter have been published in
1. A. Shetgaonkar, A. Lekić, J.L. Rueda Torres, P. Palensky, "Microsecond enhanced indirect model predictive control for dynamic power management in MMC units," *Energies*, vol. 14, no. 11, pp. 3318, 2021, MDPI.
2. A. Shetgaonkar, L. Liu, A. Lekić, M. Popov, P. Palensky, "Model predictive control and protection of MMC-based MTDC power systems," *International Journal of Electrical Power & Energy Systems*, vol. 146, pp. 108710, 2023, Elsevier.

I

Architecture, Design and Implementation of Advanced Control

5.1. BACKGROUND

MPC is an optimization control method that can be applied to linear and non-linear systems [183], [184]. One of the crucial parts of the MPC is the designed objective (cost) function, that can provide a direct solution for the switching signals, thus eliminating the use of a synchronization block. In this way, it improves the dynamic response and controllability of the system. The MPC is simple to design and robust to the variation of system parameters. MPC is flexible, allowing the inclusion of the system constraints and non-linearities, and it easily compensates the control delay. It can handle multiple control objectives using a single objective function. In power electronic applications,

Table 5.1: Overview of the MPC for HVDC application

Literature	MPC problem *	Platform	Online Solver	Circuit
J. Qin *et al.* [185]	$J = \boldsymbol{Q}\left\|y_{ref}(k+1) - y(k+1)\right\|_1$	PSCAD/EMTDC	No	Point to point HVDC
D. Zhou *et al.* [186]	$J = \boldsymbol{Q}\left\|y_{ref}(k+1) - y(k+1)\right\|_1$	dSPACE	No	Grid connected MMC unit.
J. Bocker *et al.* [187]	$J = \boldsymbol{Q}\left\|y_{ref}(k+1) - y(k+1)\right\|_1 + \boldsymbol{R}u\left\|u_(k) - u(k-1)\right\|_1$	Scaled converter test bench.	No	Grid connected MMC unit.
A.Dekka *et al.* [188]	$J = \boldsymbol{Q}\left\|y_{ref}(k+1) - y(k+1)\right\|_1$	MATLAB/Simulink simulations / dSPACE	No	Grid connected MMC unit.
M. Vatani *et al.* [189]	$J = \boldsymbol{Q}\left\|y_{ref}(k+1) - y(k+1)\right\|_1$	PSCAD/EMTDC	No	Grid connected MMC unit.
P. Liu *et al.*[190]	$J = \boldsymbol{Q}\left\|y_{ref}(k+1) - y(k+1)\right\|_1$	MMC Back-to-back dynamic test system	No	Back-to-back MMC-HVDC grid.
J. W. Moon *et al.*[191]	$J = \boldsymbol{Q}\left\|y_{ref}(k+1) - y(k+1)\right\|_1$	PSCAD/EMTDC	No	Grid connected MMC unit.
Y. Wang Yue *et al.* [192]	$J = \boldsymbol{Q}\left\|y_{ref}(k+1) - y(k+1)\right\|_1$	PSCAD/EMTDC	No	Grid connected MMC unit.
J. Huang *et al.* [193]	$J = \boldsymbol{Q}\left\|y_{ref}(k+1) - y(k+1)\right\|_1$	PSCAD/EMTDC & experimental prototype	No	Grid connected MMC unit.
H. Mahmoudi *et al.* [194]	$J = \boldsymbol{Q}\left\|y_{ref}(k+1) - y(k+1)\right\|_1$	DSP/ prototype MMC	No	Grid connected MMC unit.
T. Nowak *et al.* [195]	$J = \boldsymbol{Q}\left\|y_{ref}(k+1) - y(k+1)\right\|_1 + \boldsymbol{R}u\left\|u_(k) - u(k-1)\right\|_1$	PSCAD/EMTDC	No	Multi-terminal HVDC grid
J. Zhang *et al.* [196]	$J = \boldsymbol{Q}\left\|y_{ref}(k+1) - y(k+1)\right\|_1$	PSCAD/EMTDC	No	Point to point HVDC
S. Pirooz Azad *et al.* [197]	$J = \boldsymbol{Q}\left\|y_{ref}(k+1) - y(k+1)\right\|_2 + \boldsymbol{R}u\left\|u_(k) - u(k-1)\right\|_2$	PSCAD/EMTDC	Quadratic	Meshed IEEE 14-bus with HVDC link.
P. Mc Namara *et al.* [198]	$J = \boldsymbol{Q}\left\|y_{ref}(k+1) - y(k+1)\right\|_2 + \boldsymbol{R}u\left\|u_(k) - u(k-1)\right\|_2$	Matlab /Simulink	Quadratic	A multi-terminal DC grid.
S. Fuchs *et al.* [199]	$J = \boldsymbol{Q}\left\|y_{ref}(k+1) - y(k+1)\right\|_2 + \boldsymbol{R}u\left\|u_(k) - u(k-1)\right\|_2$	Matlab/Simulink	Quadratic	Grid-connected MMC unit.
M. M. Belhaouanes *et al.* [200]	$J = \boldsymbol{Q}\left\|y_{ref}(k+1) - y(k+1)\right\|_2 + \boldsymbol{R}u\left\|u_(k) - u(k-1)\right\|_2$	Matlab/Simulink and OPAL-RT	Quadratic	Three-terminal VSC-HVDC

* $\boldsymbol{Q}.\boldsymbol{R}$ are weight matrices for output and control states, $y_{ref}(k+1)$, $y(k+1)$ are reference and predicted output and $u(k)$, $u(k-1)$ are the present and past control inputs.

the MPC has been classified into two major categories: indirect (which is also known as a continuous control set MPC) and direct MPC (which is also known as a finite control

set MPC). The direct MPC creates the firing sequences and has a high degree of control. However, MMC has a few hundred SMs, and creating firing pulses would result in an extremely high computation burden during real-time simulation.

The indirect MPC controls the converter using the modulator, which converts the reference signal into the firing sequences. Furthermore, the indirect MPC is classified into explicit and implicit MPC. Implicit MPC solves the optimization problem online at each time step. In comparison, the explicit MPC makes use of offline optimization techniques. Furthermore, an outline of the MPC implemented in the HVDC application is provided in Table 5.1.

This thesis considers indirect-implicit MPC and will be referred to as MPC in further text.

5.2. MPC WITH LAGUERRE'S FUNCTION

5.2.1. DISCRETE ANALYTICAL MODEL OF MMC

The MMC's operation explained in chapter 3, can be described by using the AC side modeling format [201] with the following differential equation in the discrete form:

$$\dot{\vec{x}} = \boldsymbol{A}\,\vec{x} + \boldsymbol{B}\,\vec{u}, \tag{5.1}$$

where $\vec{x} = [i_d^{\Sigma},\ i_q^{\Sigma},\ i_z^{\Sigma},\ i_d^{\Delta},\ i_q^{\Delta}]^T$ is the state vector of the output current in a dq-frame, and $\vec{u} = [v_{Md}^{\Sigma},\ v_{Mq}^{\Sigma},\ v_{Mz}^{\Sigma} - \frac{v_{dc}}{2},\ v_{Md} - v_d^{\Delta},\ v_{Mq} - v_q^{\Delta}]^T$ is control vector of the modulating voltage in a dq-frame. The matrices $\boldsymbol{A}$ and $\boldsymbol{B}$ are given by

$$\boldsymbol{A} = \begin{bmatrix} -\frac{R_{arm}}{L_{arm}} & 2\omega & 0 & 0 & 0 \\ -2\omega & -\frac{R_{arm}}{L_{arm}} & 0 & 0 & 0 \\ 0 & 0 & -\frac{R_{arm}}{L_{arm}} & 0 & 0 \\ 0 & 0 & 0 & -\frac{R_{eq}^{ac}}{L_{eq}^{ac}} & -\omega \\ 0 & 0 & 0 & \omega & -\frac{R_{eq}^{ac}}{L_{eq}^{ac}} \end{bmatrix},$$
$$\boldsymbol{B} = \operatorname{diag}\left\{ -\frac{1}{L_{arm}}, -\frac{1}{L_{arm}}, -\frac{1}{L_{arm}}, \frac{1}{L_{eq}^{ac}}, \frac{1}{L_{eq}^{ac}} \right\}. \tag{5.2}$$

These matrices are developed from Equations (3.3) and (3.4).

With no approximation of the real model, a zero-order hold method is preferred for discretization. This method is especially suitable for switching power converters since it ensures good harmonic correspondence with the continuous model up to one-half of the converter's switching frequency. It is usually used for the design of controllers for power converters. Hence, zero-order hold is used to represent the continuous state-space model of the MMC in discrete time [201]. Thus, upon discretization, Equation (5.1) can be written as

$$\begin{aligned} \vec{x}(k+1) &= \boldsymbol{F}(T_s)\vec{x}(k) + \boldsymbol{G}(T_s)\vec{u}(k), \\ \vec{y}(k) &= \boldsymbol{H}(T_s)\vec{x}(k), \end{aligned} \tag{5.3}$$

where $k \in \mathbb{N}$ indicates discrete time step. $\boldsymbol{H}(T_s)$ is an identity matrix, whereas $\boldsymbol{F}(T_s)$ and $\boldsymbol{G}(T_s)$ are given by

$$\boldsymbol{F}(T_s) = e^{\boldsymbol{A}\,T_s}, \quad \boldsymbol{G}(T_s) = \boldsymbol{A}^{-1}\left(e^{\boldsymbol{A}\,T_s} - \boldsymbol{I}\right)\boldsymbol{B}.$$

The above model provides the AC/DC model of an MMC for active and reactive power control, circulating current suppression control, and AC support.

By looking at the discrete MMC model from the AC side, it can be considered a five-input and five-output system. In this model, vector $\vec{u}$ represents the control signals, and $\vec{x}_m$ are output signals. To eliminate the steady-state error, an integral is added to the output, hence, the discrete MMC's augmented model is obtained. The standard form of the MMC model is given by Equation (5.3), which is further represented as an augmented model by [202]:

$$\begin{aligned}
\begin{bmatrix} \Delta\vec{x}(k+1) \\ \vec{y}(k+1) \end{bmatrix} &= \overbrace{\begin{bmatrix} \boldsymbol{F}(T_s) & o^T \\ \boldsymbol{H}(T_s)\boldsymbol{F}(T_s) & 1 \end{bmatrix}}^{\boldsymbol{A}_d} \overbrace{\begin{bmatrix} \Delta\vec{x}(k) \\ \vec{y}(k) \end{bmatrix}}^{\vec{x}_m(k)} + \overbrace{\begin{bmatrix} \boldsymbol{G}(T_s) \\ \boldsymbol{H}(T_s)G(T_s) \end{bmatrix}}^{\boldsymbol{B}_d} \Delta\vec{u}(k), \\
\vec{y}_m(k) &= \overbrace{\begin{bmatrix} 0 & I \end{bmatrix}}^{\boldsymbol{C}_d} \vec{x}_m(k),
\end{aligned} \tag{5.4}$$

Here, o is a zero matrix with a size $1 \times n_s$, where n_s is the number of state variables, and T_s is the sampling time. Furthermore, the augmented state is defined as $\Delta\vec{x}(k) = \vec{x}(k) - \vec{x}(k-1)$, where $\vec{x}(k)$ indicates the system state vector at the k^{th} instant and $\vec{x}(k-1)$ indicates vector of past states. Similarly, the augmented input is defined as $\Delta\vec{u}(k) = \vec{u}(k) - \vec{u}(k-1)$, where $\vec{u}(k)$ represents the system inputs at the k^{th} instant and $\vec{u}(k-1)$ indicates the past inputs. Representing the discrete MMC model in Equation (5.4) is the starting point for the formulation of MPC.

5.2.2. MPC FORMULATION AND STABILITY ANALYSIS

As described in table 5.1, the implicit MPC in literature for HVDC application usually uses the difference of the control signal (i.e., Δu). The use of Δu in the cost function with the high sampling rate and stable close-loop performance requires a large number of parameters (i.e., control horizon N_c). This further creates poorly numerically conditioned solutions and high computation power.

Thus, this subsection explains Laguerre network representation, approximating Δu to speed up the MPC. One advantage of the Laguerre function is that it removes the dependency on the control horizon, which is present in the conventional MPC [202]. This is done by representing the $\Delta\vec{u}(k)$ with the Laguerre network. In the Laguerre based MPC design, the $\Delta U = [\Delta u(k_i)\ \Delta u(k_i+1) \cdots \Delta u(k_i+N_c-1)]^T$ can be represented by pulse operator (i.e. $\delta(i)$) in conjunction with ΔU and N_c. As a result, $\Delta u(k_i+1) = [\delta(i)\ \delta(i-1)\ \cdots\ \delta(i-N_c+1)]$, where the pulse operator is defined as

$$\delta(i) = \begin{cases} 1, & i = 0, \\ 0, & i \neq 0. \end{cases}$$

Therefore, the presented MPC results in a lower number of parameters and lower computation burden during online optimization [202].

The discrete augmented system is

$$\vec{x_m}(k+1) = \boldsymbol{A_d}\vec{x_m}(k) + \boldsymbol{B_d}\Delta\vec{u}(k), \tag{5.5}$$

with state variables $\vec{x_m}$, inputs $\vec{u}$, for k^{th} instance. Matrices $\boldsymbol{A}_d$ and $\boldsymbol{B}_d$, with subscript d denoting a discrete system, contain corresponding quantities. Inputs $\Delta\vec{u}(k)$ are represented using orthonormal Laguerre functions [202]. The removal of the dependency of the control horizon gives an advantage for real-time applications, as the number of parameters is reduced. With Laguerre's function, the control parameter changes to $\vec{\eta}$ from $\Delta\vec{u}(k)$:

$$\Delta\vec{u}(k+m|k) = \begin{bmatrix} L_1(m)^T & o_1^T & \cdots & o_M^T \\ o_1^T & L_2(m)^T & \cdots & o_M^T \\ \vdots & \vdots & \ddots & \vdots \\ o_1^T & o_2^T & \cdots & L_M(m)^T \end{bmatrix} \vec{\eta}, \tag{5.6}$$

where o_k^T represents a zero block raw vector with an identical dimension to $L_k(m)^T$. The vector $L(k) = [l_1(k), l_2(k), \cdots, l_N(k)]^T$, and $l_i(k)$ is the discrete Laguerre function determined by the inverse Z-transform of $\Gamma_i(z)$. Function in Z-domain $\Gamma(z)$ is defined as $\Gamma_i(z) = \Gamma_{i-1}(z)\frac{z^{-1}-a}{1-az^{-1}}$, and $\Gamma_1(z) = \frac{\sqrt{1-a^2}}{1-az^{-1}}$. Here, a is called Laguerre's network pole with $0 < a < 1$ for safeguarding the network's stability, $\beta = \sqrt{1-a^2}$, and N is the number of terms required to represent the approximated system response. The notation $\vec{f}(k+m|k)$ is a discrete value of the vector $\vec{f}$ at instant $k+m$ estimated during sampling instant k. Furthermore, it is

$$L(k+1) = \boldsymbol{A}_l L(k), \tag{5.7a}$$

$$\boldsymbol{A}_l = \begin{bmatrix} a & 0 & 0 & 0 \\ \beta & a & 0 & 0 \\ -a\beta & \beta & a & 0 \\ \vdots & \vdots & \vdots & \ddots \end{bmatrix}, \tag{5.7b}$$

$$L(0)^T = \sqrt{\beta}\begin{bmatrix} 1 & -a & a^2 & \cdots & (-1)^{N-1}a^{N-1} \end{bmatrix}, \tag{5.7c}$$

$$\vec{\eta} = \begin{bmatrix} c_1 & c_2 & \cdots & c_N \end{bmatrix}^T, \tag{5.7d}$$

The value of $\vec{\eta}$ is calculated by minimizing the objective function, subject to the equality and inequality constraints. The cost function considers a Linear Quadratic Regulator (LQR) as a base. Hence, the objective function is given by

$$\min_{\vec{\eta}} J = \sum_{i=1}^{N_p} \vec{x_m}(k+i|k)^T \boldsymbol{Q}\vec{x_m}(k+i|k) + \vec{\eta}^T \boldsymbol{R}\vec{\eta}, \tag{5.8a}$$

$$\text{subject to } \boldsymbol{M}\vec{\eta} \leq b, \tag{5.8b}$$

$$\vec{x_m}(k+i|k) = \vec{r}(k) - \vec{y}_m(k|k). \tag{5.8c}$$

Here, $\boldsymbol{Q} \succeq 0$ and $\boldsymbol{R} \succ 0$ are positive (semi-)definite weighting matrices, and N_p is the prediction horizon. For variables $\vec{x_m}(k)$, vector $r(k)$ is a reference signal. The matrix $\boldsymbol{M}$ and the column vector b are related to the constraint information on the rate and amplitude:

$$\boldsymbol{M} = \begin{bmatrix} \boldsymbol{M}_{\Delta U} & o & o & o \\ o & \boldsymbol{M}_{\Delta U} & o & o \\ o & o & -\boldsymbol{M}_U & o \\ o & o & o & -\boldsymbol{M}_U \end{bmatrix},$$

$$b = \begin{bmatrix} \Delta U_{max} \\ -\Delta U_{max} \\ U_{max} - \vec{u}(k-1) \\ -U_{min} + \vec{u}(k-1) \end{bmatrix},$$

$$\boldsymbol{M}_{\Delta U} = \begin{bmatrix} L_1(m)^T & o & \cdots & o \\ o & L_2(m)^T & \cdots & o \\ \vdots & \vdots & \ddots & \vdots \\ o & o & \cdots & L_m(m)^T \end{bmatrix},$$

$$\boldsymbol{M}_U = \begin{bmatrix} \sum_{i=0}^{N-1} L_1(i)^T & o & \cdots & o \\ o & \sum_{i=0}^{N-1} L_2(i)^T & \cdots & o \\ \vdots & \vdots & \ddots & \vdots \\ o & o & \cdots & \sum_{i=0}^{N-1} L_m(i)^T \end{bmatrix},$$

$$\Delta U_{max} = 1 \times \vec{1}, \quad \Delta U_{min} = -1 \times \vec{1},$$
$$U_{max} = 0.8 \times \vec{1}, \quad U_{min} = -0.8 \times \vec{1},$$

where $\vec{1}$ is the vector of all ones with dimensions $N \times 1$, and m indicates the future sampling instant. Since the formulation of MPC is in per unit, the constraint values $\Delta U_{max,min}$ and $U_{max,min}$ are set based on the performance and control energy. In this thesis, control energy of inner and grid forming MPC is set to 80 % of the rated voltage such that the modulation index remains below 1.2 pu. Further, this limit impacts the arm current during the fault. Furthermore, considering the performance, the rate constraints are kept equal to 1 pu.

In the unconstrained case, Equation (5.8b) does not exist, and the optimization problem is only solved using a terminal constraint. The quadratic programming problem (5.8a) is solved by using Hildreth's quadratic programming procedure [202].

The MPC algorithm 3 begins by initializing the augmented model, Laguerre's parameter, and the prediction horizon. Controllers' input $\vec{x}$ is measured at the k sampling instance at step 1. The output is computed by optimizing the quadratic problem given by Equation (5.8a) in step 2. Here, the output is $\vec{\eta}$, which is further used to calculate $\Delta\vec{u}(k)$ in step 3. The computed $\Delta\vec{u}(k)$ consists of N_p terms representing the N_p future control signals for current measured signals. The preceding horizon principle applies only the first term to the system model at a $k+1$ sampling instance, and other terms are neglected in step 4. This entire process continues until the end of the simulations.

Algorithm 3 MPC using Laguerre's function

1: **Initialization** : Augmented model ($\boldsymbol{A}_d, \boldsymbol{B}_d, \boldsymbol{C}_d$ *and* $\boldsymbol{D}_d$), $\boldsymbol{A}_l$, a, $\boldsymbol{M}$, N_p and b.
2: Measure $\Delta\vec{x}$ at k-th instance.
3: Compute optimal $\vec{\eta}$ by minimising the quadratic cost function Equation (5.8a) using Hildreth's Quadratic programming procedure considering the constraints.
4: Compute $\Delta\vec{u}(k)$ using with $\vec{\eta}$ from step 2 to calculate Equations (5.7).
5: Using the receding horizon principle, apply $\Delta\vec{u}(k)$ corresponding to kth instance and neglecting the inputs at other sampling instances.
6: Go to step 2.

MPC shown by Equation (5.8a) is stable, and this can be seen by taking into account the terminal constraint $\vec{x}(k+N_p|k)=0$, as reported in Chapter 3 in [202]. If it is assumed that for every k exists $\vec{\eta}$ which satisfies Equation (5.8a) subjected to terminal constraint, the stability can be expressed by using the Lyapunov function:

$$V(\vec{x}(k),k)=\sum_{i=1}^{N_p}\vec{x}(k+i|k)^T\boldsymbol{Q}\vec{x}(k+i|k)+\sum_{i=1}^{N_p-1}\Delta\vec{u}(k+i)^T\boldsymbol{R}\Delta\vec{u}(k+i).$$

This Lyapunov function equivalents the cost expressed by Equation (5.8a). The equality stems from the fact that $\Delta\vec{u}(k+i)=L(i)^T\vec{\eta}(k)=[l_1(i),\cdots,l_N(i)]^T\vec{\eta}(k)$, and that the convolution between Laguerre functions gives:

$$\sum_{m=0}^{N_p}l_i(m)l_j(m)=\begin{cases}0 & \text{for } i\neq j,\\ 1 & \text{for } i=j.\end{cases}$$

The Lyapunov function for the next sampling instant $k+1$ is:

$$\begin{aligned}V(\vec{x}(k+1),k+1) &= \sum_{i=1}^{N_p}\vec{x}(k+i+1|k+1)^T\boldsymbol{Q}\vec{x}(k+i+1|k+1)\\ &+ \sum_{i=1}^{N_p-1}\Delta\vec{u}(k+i+1)^T\boldsymbol{R}\Delta\vec{u}(k+i+1).\end{aligned}\tag{5.11}$$

Then, because of the optimality of the solution for $\vec{\eta}$, the following inequality holds $V(\vec{x}(k+1),k+1)\leq\overline{V}(\vec{x}(k+1),k+1)$, for $\overline{V}(\vec{x}(k+1),k+1)$ which is similar to $V(\vec{x}(k+$

$1), k+1)$, where the original control sequence (i.e. $L(0)^T\eta^k$, $L(1)^T\eta^k, \ldots, L(N_p-1)^T\eta^k$) is replaced by the sequence
$L(1)^T\eta^k, L(2)^T\eta^k, \ldots, L(N_p-1)^T\eta^k, 0$. Therefore, $\overline{V}(\vec{x}(k+1), k+1)$ shares the same control sequence as $V(\vec{x}(k), k)$ for the sample time $k+1, k+2, \ldots, k+N_p-1$. To prove that the system is stable, it is sufficient to show that the forward difference of the discrete Lyapunov function is negative. In the unconstrained case, this can be shown using terminal constraint [202]:

$$
\begin{aligned}
& V(\vec{x}(k+1), k+1) - V(\vec{x}(k), k) \leq \overline{V}(\vec{x}(k+1), k+1) - V(\vec{x}(k), k) = \\
= \; & \overbrace{0, \text{ terminal constraint}}\, \vec{x}(k+N_p|k)^T \boldsymbol{Q}\vec{x}(k+N_p|k) - \vec{x}(k+1)^T \boldsymbol{Q}\vec{x}(k+1) - \Delta\vec{u}(k)^T \boldsymbol{R}\Delta\vec{u}(k) = \\
= \; & -\vec{x}(k+1)^T \boldsymbol{Q}\vec{x}(k+1) - \Delta\vec{u}(k)^T \boldsymbol{R}\Delta\vec{u}(k) < 0.
\end{aligned}
$$

Clearly, the system is stable. In the constrained case, the stability is proven using Equation (5.8b).

5.3. SIMULATION AND ANALYSIS

5.3.1. OFFLINE SIMULATION PLATFORM

Table 5.2 provides parameter values that are used for the simulation of MMC in this subsection. Active and reactive power setpoints are varied to check the performance

Table 5.2: Parameters of the MMC for MPC validation simulations

Name	Symbol	Value
Arm inductance	L_{arm}	0.15 [p.u.]
Arm resistance	R_{arm}	0.0015 [p.u.]
AC filter inductance	L_r	0.12 [p.u.]
AC filter resistance	R_r	0.003 [p.u.]
Sample time	T_s	2 [ms]

of the MMC using MPC. The test bench in Figure 3.4 is used for the simulation. This variation is directly reflected through the dq-frame output currents. In general, there are two cases: small and large disturbance scenarios. Within each case, we simulated two events at different times. Similarly, each case has two variables, i.e., active and reactive power, and their values are changed at different time instances, as summarised in Table 5.3. First, the unconstrained problem is tackled, i.e., no constraints on any state variables. At the beginning of the simulation, active and reactive power setpoints are kept at zero, as shown in Figure 5.1. For the sake of comparison, the response of MPC is contrasted against the close loop step response of the MMC.

Thus, with the change of reference signal at different time instances, it can be seen that the MPC and close loop step response show similar results. Observed overshoots are less than 2 % in output currents during the small disturbance. Similarly, we have a higher overshoot during large disturbances than with small disturbances. Due

Table 5.3: Cases for the MPC simulation study

Cases	Variables	Value (sampling instance)	Value (sampling instance)
Small	Active power	0.5 [p.u.] (10)	1 [p.u.] (30)
Disturbance	Reactive power	0.2 [p.u.] (20)	1 [p.u.] (30)
Large	Active power reversal	-1 [p.u.] (40)	1 [p.u.] (80)
Disturbance	Reactive power reversal	-1 [p.u.] (50)	0.5 [p.u.] (80)

to the uncompensated MMC model, as discussed in Chapter 3, currents i_d^Δ and i_q^Δ are dependent on each other, which is seen in the change of $u_d = v_{Md} - v_d^\Delta$ and $u_q = v_{Mq} - v_d^\Delta$ control voltages (see Figure 5.1). For example, with the active power reversal from 1 p.u. to -1 p.u. at the 40^{th} sampling instance, there is a dependence of u_d, corresponding to the sharp peak with a maximum amplitude of - 160 and -190 in MPC and step response, respectively. However, at the same time, u_q changes its direction from 0.2 to -0.2 as predicted. The width of this sharp peak is equal to the width of the current reversal transient.

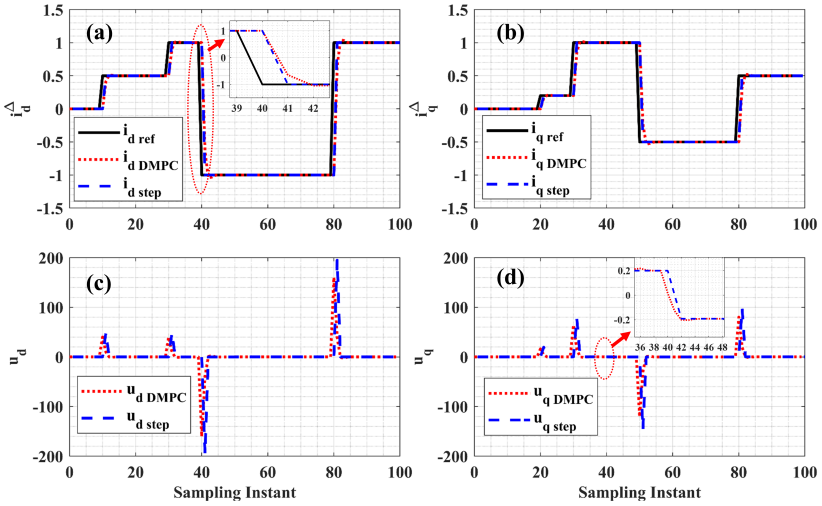

Figure 5.1: Case study with unconstrained scenario: (a) i_d^Δ current; (b) i_q^Δ current; (c) u_d voltage; and (d) u_q voltage.

MPC is designed with parameters turned using a discrete linear quadratic regulator (DLQR). Thus, with an unconstrained condition, the quadratic optimization problem is linear. This means that the underlying response is the same as that of DLQR, which is shown by the lower relative error between eigenvalues of DLQR and MPC in Table 5.4.

Table 5.4: Eigenvalues comparison between DLQR and MPC under the unconstrained condition

MPC	DLQR	Relative Error
$0.121 \pm 0.223\,j$	$0.121 \pm 0.223\,j$	$5.28 \times 10^{-4} - 2.46 \times 10^{-4}\,j$
$0.121 \pm 0.223\,j$	$0.121 \pm 0.223\,j$	$-3.63 \times 10^{-4} + 2.36 \times 10^{-4}\,j$

CONSTRAINT SATISFACTION PROBLEM

The MPC's constraint handling in the online optimization problem draws a line between MPC and DLQR. This section shows the effect of two constraints, i.e. rate constraint and amplitude constraint. However, the constraint on the output is not considered as it is linearly dependent on the rate and amplitude constraints and sometimes causes instability.

Rate Constraint In the case of the MMC control, the control signals are u_d and u_q, which is already discussed in Chapter 3. However, from the unconstrained case, it was observed that the rate of rise of the control voltages is higher. Thus, a limit can be imposed during the online quadratic optimization to limit this high rate. To see the effect of rate constraints, three limits are chosen, which are: $|\Delta u_d| = |\Delta u_q| = 30$, $|\Delta u_d| = |\Delta u_q| = 40$, and $|\Delta u_d| = |\Delta u_q| = 50$. Figure 5.2 illustrates the consequence of the rate constraint on the input and output signals. In Figure 5.2c, we can see that the rate of u_q does not violate the respective constraints. The reduction of the rate constraint directly impacts the dynamic response of the i_d^{Δ} and i_q^{Δ}. With the small disturbance, the rate constraints have a significantly lower impact during the transient response of i_d^{Δ}, as it is below the respective constraint limit. However, during active power reversal, there is a large peak in Δu_d (shown in a small window in Figure 5.2a). However, due to the constraint, the rate saturates to its respective limits and, thus, leads to a slower transient response.

Among all the constraints, the $|\Delta u_d| = |\Delta u_q| = 30$ constraints have a severe impact on the transient response of the i_d^{Δ} and it has a higher undershoot. Since the amplitude of the control signal u_d is unconstrained, it is derived from the rate of the control signal.

Amplitude Constraint To examine the effect of the amplitude constraint on the output response, three amplitude constraints are considered, which are: $|u_d| = |u_q| = 30$, $|u_d| = |u_q| = 60$, and $|u_d| = |u_q| = 80$. Figure 5.3 shows the control and output response with the amplitude constraint on the control signal, i.e., u_d and u_q. There are no constraint violations during the small disturbance, as depicted in Figure 5.3b. However, in the case of large disturbances, we can see that some constraints tend to be violated, but they are well maintained within limits due to online optimization. For example, with constraints corresponding to line 3, the input signal is optimized, which in turn changes the rate of an input signal. Like rate constraints, the dynamic response of the i_d^{Δ} and i_q^{Δ} are affected due to the amplitude constraints as seen in Figure 5.3a. It is also observed that there is no undershoot, as it was present in the previous section.

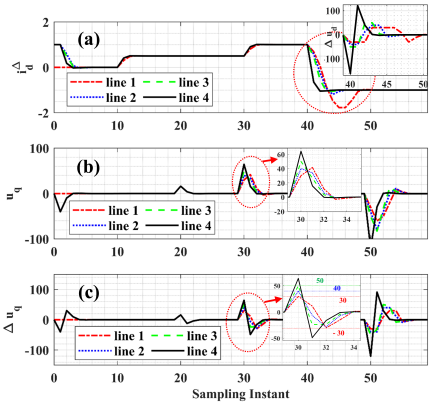

Figure 5.2: Case studies with rate constraint, line 1: $|\Delta u_d| = |\Delta u_q| = 30$, line 2 : $|\Delta u_d| = |\Delta u_q| = 40$, line 3 : $|\Delta u_d| = |\Delta u_q| = 50$, and line 4: unconstrained.

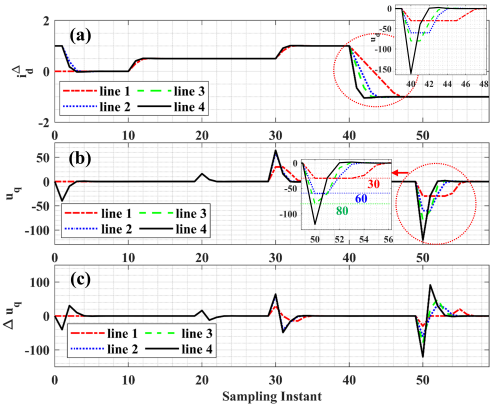

Figure 5.3: Case studies with amplitude constraint:line 1 : $|u_d| = |u_q| = 30$, line 2 : $|u_d| = |u_q| = 60$, line 3 : $|u_d| = |u_q| = 80$ and line 4: Unconstrained.

Another set of constraints can be imposed on the controller, which is the combination of the control signal's rate and amplitude constraints. However, in the application of MMC, the i_d^{Δ} current has a similar response to that of amplitude constraints. Due to the constraints, rate and amplitude remain within their limits, as the predictive controller computes the control signals online considering these limits.

Sensitivity Analysis

Various parameters govern the performance of the MPC. Hence, sensitivity analysis is carried out to check the controller's robustness. The main goal of the sensitivity analysis is to identify the factors that severely affect the controller's performance during transient and steady-state.

Sample Time (T_s) Figure 5.4 shows the effect of the sample time (T_s) on the stability and dynamic response. As Figure 5.4 indicates that with the increase of the sample time from 0.1 ms to 10 ms, the dynamic response is faster, especially during a large disturbance. Furthermore, as we increase the sample time, the underline DLQR response ($\circ$) overlaps the MPC ($*$) without tuning the N and a parameters. However, with a lower sample time (0.1 ms), we see a significant error between the two responses, shown by the bold black $\circ$ and $*$ symbols. Besides, at different sampling instances, we can see overshoots and higher settling times even for the small disturbance (bold black dash line).

Weighting, Predictive Horizon, and Laguerre's Parameter Typically, $\boldsymbol{R}$ and $\boldsymbol{Q}$ are the weighing parameters of objective functions. However, this section will only discuss the effect of $\boldsymbol{R}$ on the control and output response. Similarly, the effect of variation in N and a are studied. With the increase of $\boldsymbol{R}$, the dynamic response of the controller reduces, and the pole moves toward the unit circle, as shown in Figure 5.5. The bold black $\circ$ and

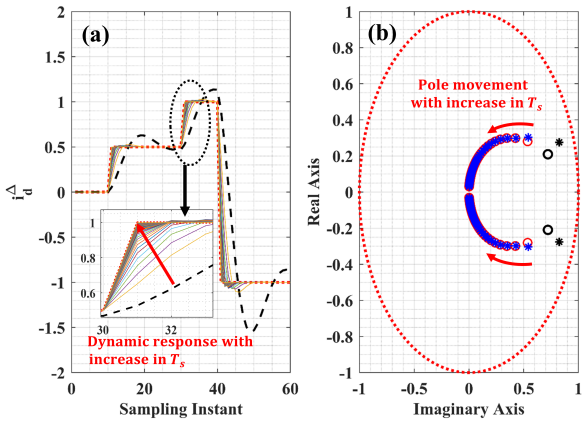

Figure 5.4: Effect of sample time (T_s) on the dynamic response and stability.

$*$ indicate the initial condition. Figure 5.5 illustrates the effect of the sample times on the pole movement with the increase of $\boldsymbol{R}$. For higher T_s = 10 ms, the pole movement is restricted within the circle with a radius of 0.2 as $\boldsymbol{R}$ increases, which indicates a damped and faster response. With the higher sample time and lower $\boldsymbol{R}$, the response of MPC is more similar to the step response, as shown by the dotted red line in Figure 5.4a.

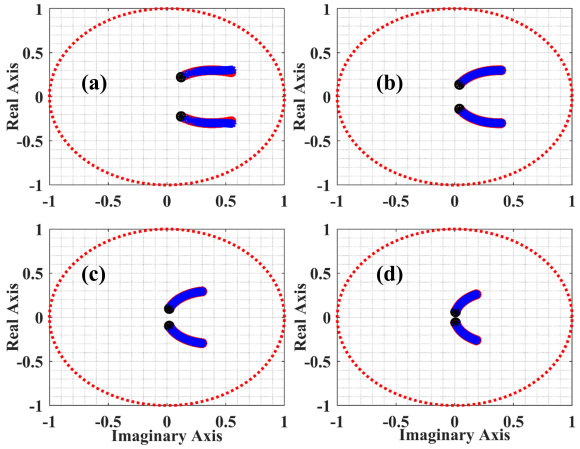

Figure 5.5: Effect of R on the dynamic response and stability with: (a) $T_s = 2 \times 10^{-3}$; (b) $T_s = 4 \times 10^{-3}$; (c) $T_s = 6 \times 10^{-3}$; and (d) $T_s = 10 \times 10^{-3}$.

The effect of the predictive horizon (N_p) and Laguerre's parameter are shown in the Figure 5.6. By looking at the eigenvalues, we see that the effect of the N_p is minimum for fixed N and a at a given sample time (T_s). The system's response with $N_p = 4$ is the same as that of $N_p = 100$, which indicates the independence of the MMC model on the Predictive horizon. However, let's look at the effect of Laguerre's parameter on the output signal. We can see that, at given N_p, both the parameters show alternative behavior, i.e.,

with the increase in the N value, the system pole converges to the underlying DLQR poles. While with the increasing a, the system goes into an unstable state, as a pole on the unit circle (as shown in Figure 5.6b). With $a = 0$, the i_d^{Δ} response is equal to the conventional MPC, i.e., $\Delta\vec{u}$ as the control variable.

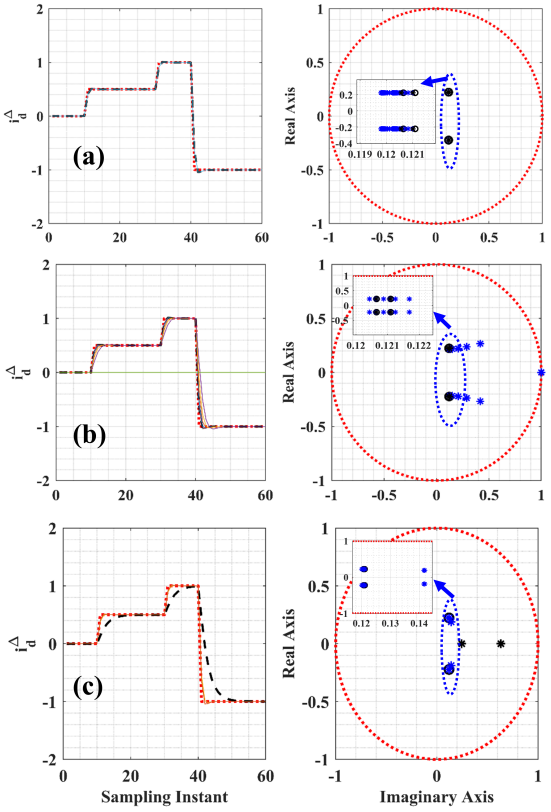

Figure 5.6: Effect of: (a) N_p with $a = [0.237, 0.237]$, $N = [4, 4]$; (b) a with $N_p = 4$, $N = [4, 4]$; and (c) N with $a = [0.237, 0.237]$, $N_p = 4$ on the dynamic response and stability.

5.3.2. Online Simulation Platform

The operation of MPC is validated by real-time simulations in RTDS©. MPC is implemented via C-builder, which runs at the time step of 80 μs. The RISC processor of NovaCor in RTDS© consists of 10 cores, which operate at 3.5 GHz each. A dedicated core is utilized for the MPC. Under steady-state conditions, the MPC with online quadratic optimization takes 6 μs. However, during transient conditions, the computation time rises to 65 μs due to constraint handling. By contrast, without online optimization, the computation time remains 9 μs for both conditions. Thus, the proposed MPC with and without online optimization can theoretically run on real-time applications. A small and large disturbance in active and reactive power is performed to test the performance of

the MPC, as discussed in the previous section. The constraint satisfaction problem is also analyzed in the RTDS©.

SIMULATIONS OF DISTURBANCE IN ACTIVE AND REACTIVE POWER

Figures 5.7 and 5.8 show the small and large disturbances due to the active and reactive power reference change. With the change in the active power reference from 0 to 0.5 p.u. at the time instance $t = 0.5$ s (see Figure 5.7a), MPC provides an optimized modulating voltages values u_d^Δ and u_d^Δ after 80 μs. As a result, the d-component of grid current i_d^Δ tracks the reference within 4 ms as it is shown in the Figure 5.7a. Due to the decoupling of dq components, the change in the active power setpoint did not influence the reactive power component i_q^Δ in the steady state. However, during the transient, some influence is caused by the Type-5 MMC model in RTDS© and the uncompensated modulation.

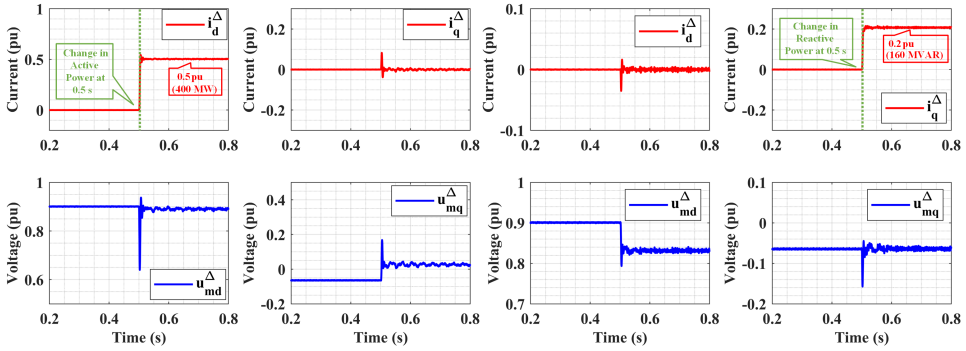

Figure 5.7: change at the time instance $t = 0.5$ s in: (a) active power reference from 0 p.u. to 0.5 p.u.; (b) reactive power reference from 0 p.u. to 0.2 p.u.

Similarly, observation is made when reactive power reference changes from 0 to 0.2 p.u. at the time instance $t = 0.5$ s and depicted in Figure 5.7b.

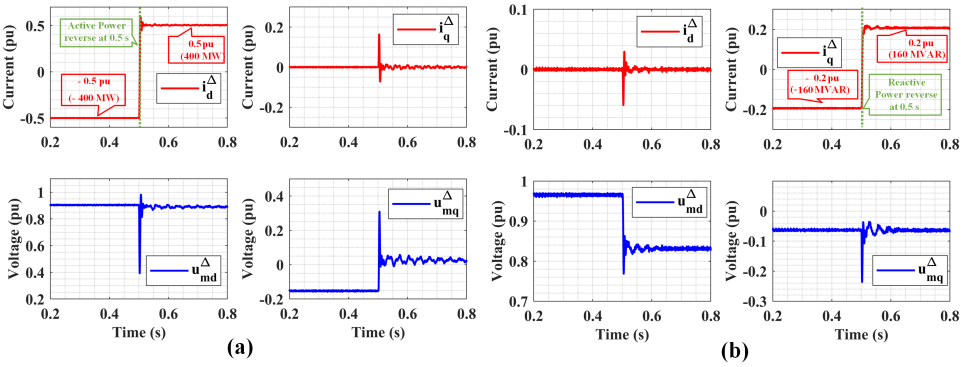

Figure 5.8: change at the time instance $t = 0.5$ s in: (a) active power reference from -0.5 p.u. to 0.5 p.u.; (b) reactive power reference from -0.2 p.u. to 0.2 p.u.

The active and reactive powers' reversal causes small overshoots in both dq components of grid current after $t = 0.5$ s, see Figure 5.8. However, these overshoots last less than 2 ms due to the fast response of the MPC. MPC enables quick damping of the currents and their convergence to desired references. The magnitude of overshoot is less than 5% in the case of rated power.

Constrained Satisfaction Problem in RTDS©

Figure 5.9 illustrates the effect of the constraints on the amplitude and rate of MPC's control variables. The amplitude and rate limit are set to ±0.3 and ±0.1, respectively. With the application of the constraints, the amplitude of $v_{Md} - v_d^{\Delta}$ is limited to the lower limit, and the control signal is recomputed to avoid the violation. This is not the case for the unconstrained scenario at the time of disturbance, as seen in Figure 5.9b. However, due to the amplitude, the rise of the control signal is affected as it is directly dependent on the amplitude (see Figure 5.9b). With the reduced rate of a control signal, the response of the MPC is delayed, as seen in Figure 5.9a. Which further leads to a reduction of the current overshoot. This delay is minimal, as seen in a small window in Figure 5.9a. However, reducing the limit can cause significant delay or instability.

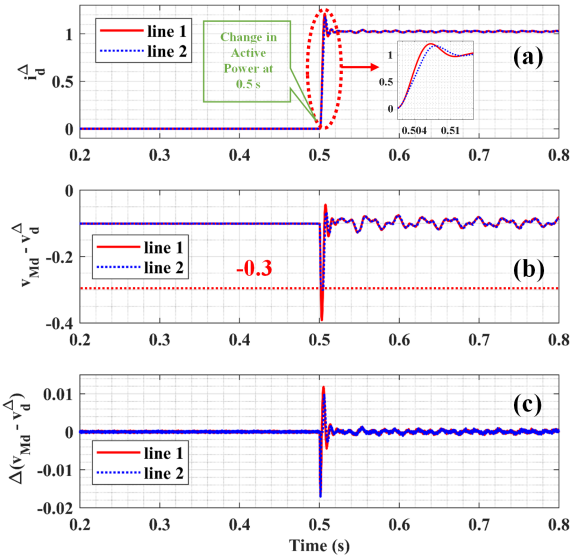

Figure 5.9: Effect of contains on (a) i_d^{Δ} (b) $v_{Md} - v_d^{\Delta}$ (c) rate of change of $v_{Md} - v_d^{\Delta}$, where line 1 : Unconstrained , line 2: Constrained

Comparison of PI and MPC Controls for the MMC in RTDS©

Three control loops are considered to compare the performance of MPC with PI. The parameters of PI controllers are given in Table 3.5.

Figure 5.10a compares MPC and PI controllers during an active power reversal. In both cases, the active power reference is initially set to the rated power (i.e., -800 MW). At time instant $t = 0.5$ s, a reversal command is given, which changes the reference to

1 p.u. (800 MW), as shown in Figure 5.10a. During the power reversal, the MPC tracks the reference within 10 ms with an overshoot of 20%. Furthermore, the overshoot lasts for 5 ms. For PI-controlled MMC, i_d^{Δ} current tracks reference point from $t = 0.6$ s. This delayed response is due to cascaded PI controllers in PI-controlled MMC, as discussed in Chapter 3. In both controllers, active and reactive power controls are decoupled in the steady state. Due to uncompensated modulation, dq components are interdependent during a transient.

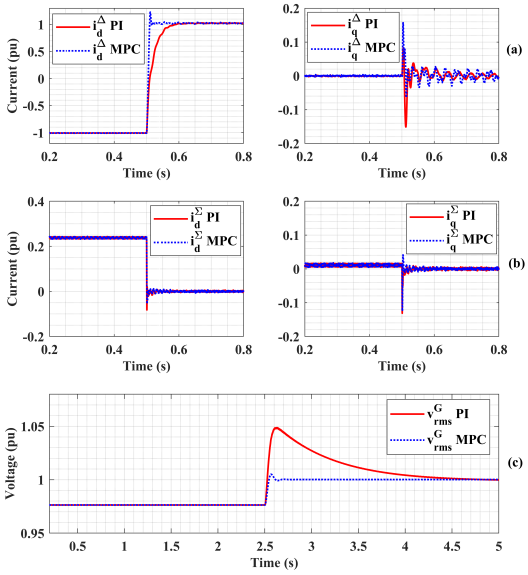

Figure 5.10: Comparison of PI and MPC controller during: (a) active power reversal; (b) circulating current suppression; and (c) AC voltage support.

Figure 5.10b shows the effect of the circulating current suppression control for both controllers. Initially, the system operates at rated power (800 MW). The CCSC is activated at 0.5 s for both controllers. As seen from Figure 5.10b, dq components of circulating current drop to zero, indicating activation of CCSC. Due to the lower time constants in the PI, the response of PI and MPC overlaps.

Figure 5.10c illustrates reactive power support for both controllers. At rated active power, the RMS value of the AC bus voltage drops to 0.97 p.u. With the activation of the reactive support, bus voltage restores to 1 p.u. (380 kV) in both controllers. The response of the MPC is faster than that of the PI and has a much smaller overshoot. The MPC restores the AC bus voltage within 100 ms, which is not the case for the PI-controlled MMC. The PI controller needs 2 s to reach the reference value (1 p.u.). This higher time is due to the slower outer controlling PI loop.

II

INTEGRATION AND VERIFICATION IN MT-HVDC GRID

5.4. CASCADED MPC FOR DC VOLTAGE CONTROL

The MPC is designed using two cascaded controllers: inner and outer MPC. The inner MPC controls the MMC's currents, whilst the output sets the DC voltage, as depicted in Figure 5.11. This control architecture is similar to conventional PI control as given in [203]. The inner and outer MPC controllers control the discretized augmented system defined by the difference Equations (5.5).

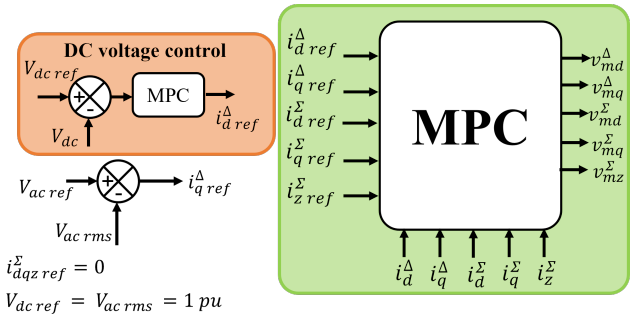

Figure 5.11: Graphical representation of the cascaded MPC DC voltage controller: left - outer MPC and right - inner MPC controller.

The dynamics of the DC voltage are closely linked to the behavior of the power grid, which can be complex and challenging to be modeled accurately. In that case, it is possible to use the model mismatch factor.

The mismatch between the model and plant can be handled by a factor called model mismatch factor. This factor considers the effect of any difference in the plant and model into the optimisation problem. This mismatch factor is formulated as:

$$\begin{aligned} x(k+m|k) &= C_d A_d^m x(k) + C_d \sum_{i=0}^{m-1} A^{m-i-1} B_d L(i)^T \eta + I_m e(k) \\ &= F(m)x(k) + \phi(m)^T \eta + I_m e(k), \end{aligned} \tag{5.12}$$

where $F(m) = C_d A_d^m$, $\phi(m)^T = C_d \sum_{i=0}^{m-1} A^{m-i-1} B_d L(i)^T$ and $m \in \{1,2,\ldots,N_p\}$. The new term in the above formulation is the $I_m e(k)$ for I_m being an identity matrix of order (5,5) and $e(k)$ is error between the model output signal and plant output at time step k. Considering the cost function, J given equation (5.8a) and substituting the equation 5.12 in J and re-arranging terms we get:

$$H = \phi^T Q \phi + R, \tag{5.13a}$$

$$f = \phi^T Q[\overline{R(k)} - I_p e(k) - Fx(k)], \tag{5.13b}$$

where H and f matrices are the input to the QP optimization solver. The $\overline{R(k)} = \vec{1}_{1\times N_p} \otimes \vec{r}$, where $\vec{r}$ is the reference signal column matrix of order 5 at k instance and $\otimes$ is Kronecker Tensor Product. F and ϕ are evolution of $F(m)$ and $\phi(m)$ matrix over N_p with given system dynamics. The $I_p = [I_1, I_2, \ldots, I_{N_p}]^T$ and I_i, for $i \in \{1,2,\ldots,N_p\}$, is an identity matrix of order (5,5), which acts like weight factor for the error mismatch.

Inner MPC Loop

The inner MPC loop is formulated in a discretized augmented version as shown in Equation (5.4), featuring the state matrix $\boldsymbol{A}_d$, the input matrix $\boldsymbol{B}_d$, and the output matrix $\boldsymbol{C}_d$. The matrices $\boldsymbol{A}$ and $\boldsymbol{B}$ originate from a continuous averaged model of the MMC, as outlined by Equation (3.3), and are expressed in a state-space form by Equation (5.2).

Upon discretization and augmentation (Equation (5.4)), $\vec{x_m} = [\Delta\vec{x}, i^{\Sigma}_{d\ ref} - i^{\Sigma}_{d}, i^{\Sigma}_{q\ ref} - i^{\Sigma}_{q}, i^{\Sigma}_{z\ ref} - i^{\Sigma}_{z}, i^{\Delta}_{d\ ref} - i^{\Delta}_{d}, i^{\Delta}_{q\ ref} - i^{\Delta}_{q}]^T$ is vector representing the state variables. Here, the output variables are the same as the state variables.

This MPC loop controls the circulating and output currents, as shown in Figure 5.11 right. To minimise the circulating currents, the references of Σ-currents ($\vec{i}^{\Sigma}_{dqz\ ref}$) are set to zero. The references of Δ-currents ($\vec{i}^{\Delta}_{dq\ ref}$) are provided by the outer MPC loop and the reactive power or AC voltage support control.

Outer MPC Loop

This MPC loop is used to control the DC voltage. It is designed as the outer loop to ensure that the rated DC voltage is maintained dynamically, i.e., without linearization. Thus, the outer loop is added to consider other system variables indirectly derived by the inner MPC loop state variables. The continuous state space matrices are:

$$\boldsymbol{A} = \left[\frac{-1}{k_{dc} \times T_{dc}}\right], \quad \boldsymbol{B} = \left[\frac{1}{k_{dc}}\right]. \tag{5.14}$$

The vector $\vec{x} = [v_{dc\ ref} - v_{dc}]$ represents the state variables, while $\vec{u} = \left[i^{\Delta}_{d,ref}\right]$ represents system inputs. The k_{dc} and T_{dc} are 6.5 and 0.0035, respectively. This is further discretized and augmented to form Equation (5.4). Upon discretization and augmentation, $\vec{x_m} = [\Delta\vec{x}, v_{dc\ ref} - v_{dc}]^T$ represents state variables. Here, the output variables are the same as the state variables. The cost function minimizes the control signal to eliminate deviation from the rated DC link voltage. The rate constraint is responsible for damping, and damping is better when the rate constraint is larger. Thus, the input rate and amplitude constraints are set to 5 and 0.8, respectively.

5.5. Grid Forming MPC

The GFM is based on the direct voltage ($V_{ac} - f$) control [204]. Matrices represent the state Equation for the grid forming MPC:

$$\boldsymbol{A} = \begin{bmatrix} \frac{-1}{k_{GF} \times T_{GF}} & 0 & 0 & 0 \\ 0 & -\frac{R_{arm}}{L_{arm}} & 2\omega & 0 \\ 0 & -2\omega & -\frac{R_{arm}}{L_{arm}} & 0 \\ 0 & 0 & 0 & -\frac{R_{arm}}{L_{arm}} \end{bmatrix}, \tag{5.15a}$$

$$\boldsymbol{B} = \text{diag}\left\{\frac{1}{k_{GF}}, -\frac{1}{L_{arm}}, -\frac{1}{L_{arm}}, -\frac{1}{L_{arm}}\right\}, \tag{5.15b}$$

and vector $\vec{x} = [v_{ac\ ref} - v_{ac}, i^{\Sigma}_{d}, i^{\Sigma}_{q}, i^{\Sigma}_{z}]^T$ represents the state variables,
while $\vec{u} = [v^{\Delta}_{Md}, v^{\Sigma}_{Md}, v^{\Sigma}_{Mq}, v^{\Sigma}_{Mz} - \frac{v_{dc}}{2}]$ represents system inputs. The k_{GF} and T_{GF}

are 6.5 and 0.008, respectively. Upon discretization and augmentation as shown in Equation (5.4), $\vec{x}_m = [\Delta\vec{x},\ v_{ac\,ref} - v_{ac},\ i^{\Sigma}_{d\,ref} - i^{\Sigma}_{d},\ i^{\Sigma}_{q\,ref} - i^{\Sigma}_{q},\ i^{\Sigma}_{z\,ref} - i^{\Sigma}_{z},\ ]^T$ represents state variables. Here, the output variables are the same as the state variables. The cost function minimizes the control signal to eliminate any deviation from the rated AC voltage at the offshore AC grid's PoC and minimize the circulating current in the converter.

5.6. SYSTEM CONFIGURATION OF THE FOUR-TERMINAL HVDC GRID

For every simulation, three components exist in RTDS ©, namely, the *Network solution*, *Control*, and *Power system*. Among these components, the *Power system* changes with the type of simulation time step model (i.e., super step, main step, etc.). The *control* works in the main step. Thus, the execution of all *control* units has to be done within 80 μs. The *control* can be split into several parallel paths for a large system. However, this parallel path is restricted to the number of available cores in RTDS ©. Considering all these requirements, in this thesis, MPC's execution time must be within a time frame of 80μs to run successfully in the real-time simulator.

Figure 5.12 depicts a ±200 kV monopole meshed four-terminal MMC-based HVDC power system with a digital twin model of a 2 GW offshore wind farm. This power system is applied to test the accuracy of the proposed control and protection algorithms. In the system of Figure 5.12, two offshore wind farms operate at different wind speeds. The Type-4 wind turbine is used in the aggregated wind farm model. Chapter 4 has discussed wind power plants' operation, structure, and control system. The wind speed data is taken directly from the actual measurement in the North Sea. The wind speed measurements are updated into the RTDS © every two seconds using the SiL setup (explained in Appendix A). Three Type-4 MMC models (MMCs 1, 2, and 4) are implemented using GTFPGAs, and one Type 5 MMC model (MMC3) is implemented in the RTDS © core. In the Type-4 MMC model, a GTFPGA unit represents one leg of the MMC. Thus, three GTFPGA units are required to represent one MMC unit. Additionally, the sub-module capacitor voltage balancing controller is required. Due to the high number of submodules, this controller is implemented using two GTFPGA units. The connections between RTDS © and GTFPGAs and between GTFPGAs are realized using the Aurora protocol by two full-duplex fibre optic cables. To represent three detailed MMCs (MMCs 1, 2, and 4), nine GTFPGAs are used for the legs of MMC units. Furthermore, six GTFPGAs are used to represent the submodule capacitor voltage balancing controllers for respective MMC units. In total, fifteen GTFPGAs are used. The connection outline of these GTFPGA is provided in Appendix A.

Furthermore, MMC1 is connected to a strong grid and is modeled as a Thevenin grid equivalent. MMC3 is connected to a weak grid modeled as a Thevenin grid equivalent with a lower SCR. The offshore MMCs act as grid forming converters. The data of the four-terminal HVDC grid is shown in Table 5.5. The MTDC system has five cables with lengths of 200 km each. The Frequency-Dependent Phase model is used among the two traveling wave cable modeling methods due to its higher accuracy, shown during controller interactions. The cable data for XLPE submarine cables are used. The VARC

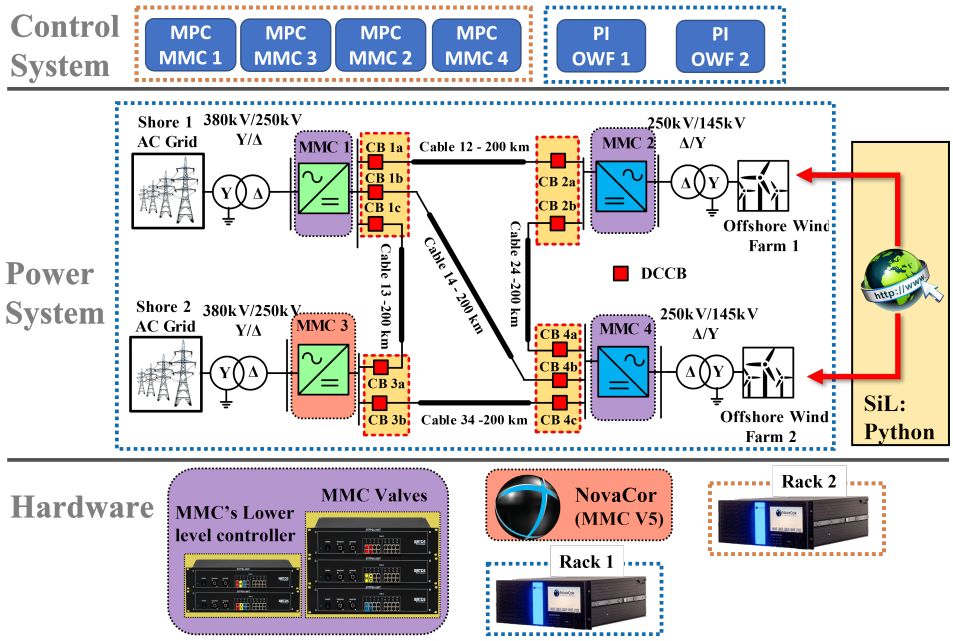

Figure 5.12: The four-terminal MMC-based MTDC system with a HiL and a SiL setup.

DC CB is implemented at both ends of the cable, as shown in Figure 5.12. The detailed model structure, operating principle, and VARC DC CB experimental validation have been discussed in chapter 4 and [100]. In [100], authors have used four 80 kV VARC modules for a 320 kV MTDC system. This is in line with the requirement of high computational power. Since one of this chapter aims to understand the interaction between the advanced control and VARC DC CB, some simplifications are made in the VARC DC CB. The stray capacitance across the vacuum breaker and the surge arrester in the VARC DC CB can be neglected. During fault elimination and fault current suppression time intervals, specific VARC DC CB module branches are connected in series, and the model can be aggregated.

The upper and lower-level controls of MMCs are based on the MPC and PI control published in Cigre B4.57. [205]. The details of the PI control for different control loops are provided in Table 5.6. The MMC1 is DC voltage controlled, whilst MMC3 is active/reactive power controlled. Furthermore, MMC2 and MMC3 have direct voltage ($V_{ac} - f$) control. In this system, a decentralized controlling approach is applied.

Here, the values for $a = 0.65$ and $N = 4$ will be used for the MPC. For the cost function expressed by Equation (5.8a), matrices $\boldsymbol{Q} = 1 \times \boldsymbol{I}$ and $\boldsymbol{R} = 0.2 \times \boldsymbol{I}$ are used, where $\boldsymbol{I}$ is an identity matrix. The prediction horizon (N_p) is set to 30 sampling instances. Furthermore, all the physical quantities, like current and voltages, are normalized. In the simulations, the input amplitude and input rate constraints are implemented in the

Table 5.5: Data of the four-terminal MTDC

Parameter	Converters			
	MMC1	MMC2	MMC3	MMC4
Active power	500 MW	500 MW	500 MW	500 MW
Control mode	Vdc	Vac-f	PQ	Vac-f
Reactive power	0 MVAR	0 MVAR	0 MVAR	0 MVAR
DC link Voltage	±200 kV			
Rated power	800 MW			
Number of Submodules per arm	200			
Arm capacitance C_{arm}	22 μF			
Arm inductance L_{arm}	42 mH			
Arm resistance R_{arm}	0.544 Ω			
AC converter voltage	220 kV			
Transformer leakage reactance	0.18 pu			
Onshore AC grid				
Onshore grid 1		Onshore grid 2		
AC grid voltage	380 kV	AC grid voltage	380 kV	
SCR	37.5	SCR	3	
Offshore AC grid				
AC grid voltage	145 kV			

Table 5.6: Values for PI control

	MMC1	MMC2	MMC3	MMC4
Outer Voltage loop				
Proportional constant (k_p)	8 pu	-	8 pu	-
Integral Time constant (T)	0.2 s	-	0.2 s	-
Inner current loop				
Proportional constant (k_p)	0.48 pu	0.2 pu	0.48 pu	0.2 pu
Integral constant (T)	0.0067 s	0.0333 s	0.0067 s	0.0333 s

inner and outer MPC for the entire prediction horizon. These constraints are given as

$$-0.04 \leq v^{\Sigma}_{Mdqz} \leq 0.04, \tag{5.16a}$$

$$-0.8 \leq v^{\Delta}_{Mdqz} \leq 0.8, \tag{5.16b}$$

$$-1 \leq \Delta v^{\Sigma}_{Mdqz} \leq 1, \tag{5.16c}$$

$$-1 \leq \Delta v^{\Delta}_{Mdqz} \leq 1. \tag{5.16d}$$

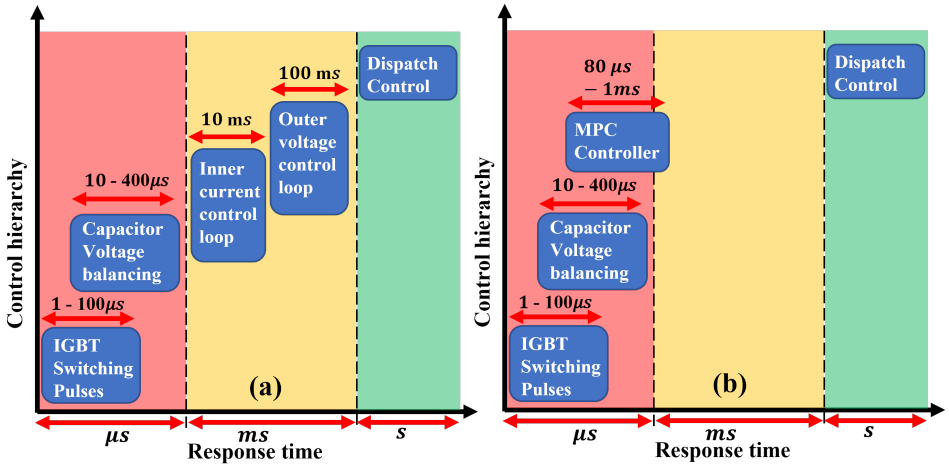

Figure 5.13: Overview of the control hierarchy of MMC: (a) PI-based control hierarchy; (b) MPC-based control hierarchy.

It should be noted that in RSCAD/RTDS ©, the response times of PI and MPC control are different. Figure 5.13(a) depicts how the calculation times of the PI control evolve for different controlling loops. With the MPC, all control values are computed within the shortest control interval of 80 μs, as shown in Figure 5.13(b).

5.7. Simulation Results

Considering the full selective HVDC protection scheme, the blocking of MMCs is disabled. Furthermore, the internal protection of the MMCs is turned off to test the performance of both controllers under the worst operating conditions. In all cases, the disturbance (small and large) occurs at $t = 0.2$ s. In the mentioned case studies, the CCSC is enabled for all the converters. During the steady-state conditions before AC and DC fault occurrence, Figure 5.14 shows the CCSC for MMC2 with a PI and MPC control in the abc and dqz rotating frames. Next, CCSC is enabled at 0.1 s. Likewise, Figure 5.15 shows the first and the last four upper and lower SM capacitor voltages for phase C of MMC2 during the steady-state condition before AC or DC faults occur.

The following case studies are performed to identify the dynamic performance of the control and protection along with its effect on the system. The PI and MPC-controlled MMCs' performances are compared for each case.

5.7.1. Transients during Nominal Operation

To evaluate the controller's performance, an increase of the wind power (case 11), active power injection into the weak grid (case 12), and a reclose of cable 12 (case 13) are conducted in this study.

For case 11, Figure 5.16 shows the performance of the MPC and PI-controlled MMC during the higher wind gusts of OWF 1 and OWF 2. Before the disturbance, OWF 1 and OWF 2 transferred active power of 202 MW and 221 MW, respectively, into the HVDC

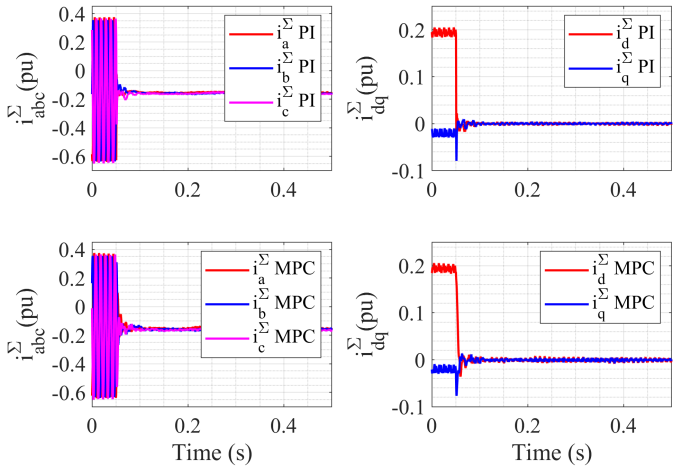

Figure 5.14: Circulating current suppression control in MMC2 with a PI and a MPC control.

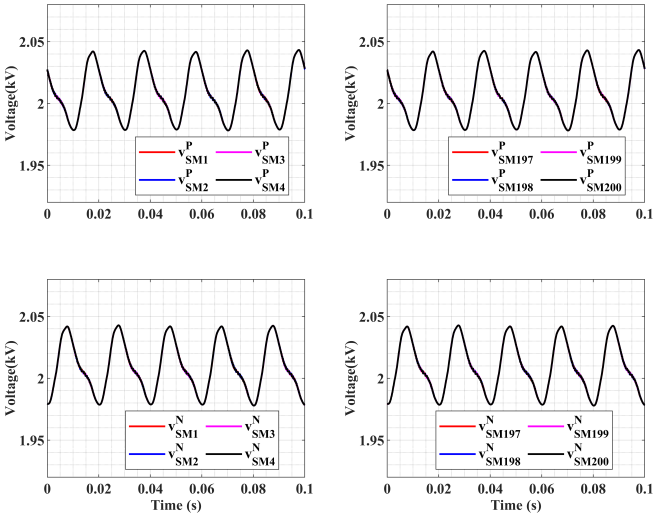

Figure 5.15: The first and the last four upper and lower SM capacitor voltages for the phase C of MMC2.

grid through MMCs 2 and 4. MMC3 absorbs 400 MW from the HVDC grid. The surplus power within the DC grid is injected into a strong AC grid to maintain the DC voltage. At 0.2 s, an extra 201 MW and 218 MW are injected by OWF 1 and OWF 2, respectively. With the same active power by MMC3, the DC voltage increases to a new steady-state value at the MMCs' terminals, except the one near MMC1 (due to DC voltage control), as shown in Figure 5.16(a). However, during the transient period, the MPC-controlled DC grid

regulates the DC voltage at the rated value with an overshoot of 0.1 % and a short settling time of 0.3 s (for 0.125 % of the steady-state value), as shown in Figure 5.16(a). Likewise, an overshoot of 0.825 % in the DC voltage is observed for the PI-controlled MMC with a settling time of 1.48 s (for 0.125 % of steady-state value). Furthermore, MPC-controlled MMC provides higher damping in the offshore and onshore AC voltage grids, as seen in Figure 5.16(c).

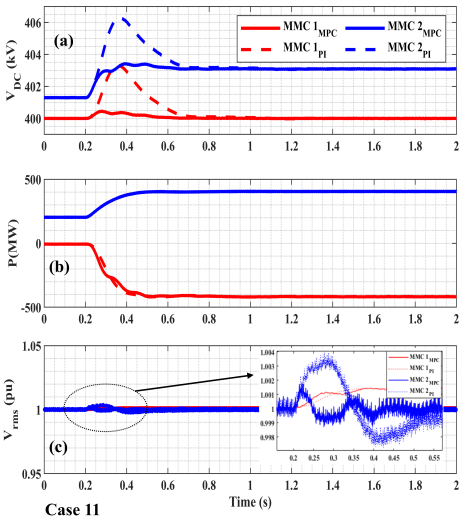

Figure 5.16: Case 11: (a) MMC's voltage [kV], (b) active power [MW], and (c) RMS AC voltages [pu].

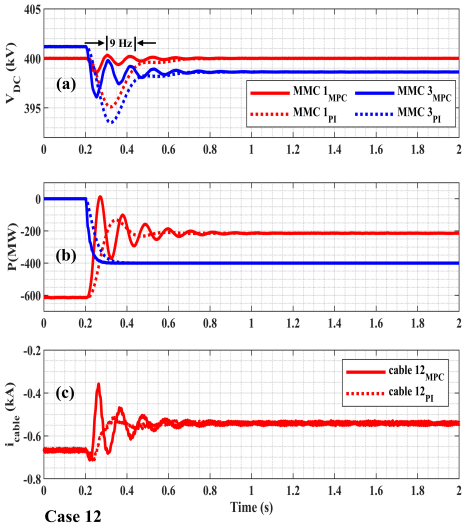

Figure 5.17: Case 12: (a) MMC's voltage [kV], (b) active power [MW], and (c) current of the positive part of cable 12 [kA].

Case 12 demonstrates an active power injection into the weak grid, as depicted in Figure 5.17. It shows the capability of active power regulation. Initially, no active power is injected into the weak grid, as seen in Figure 5.17(b). Then, OWF 1 and OWF 2 provide active power of 304.4 MW and 330.4 MW in the HVDC grid, respectively. To keep the DC voltage fixed to the rated value, more power is injected into the AC grid through MMC1, which behaves as a slack bus. At 0.2 s, 400 MW of power is injected into a weak grid, keeping the AC terminal voltage stable with MMC2's AC voltage support. The active power injection into the weak grid creates a power shortage in the HVDC grid, and the DC voltage drops, as seen in Figure 5.17(b). The DC voltage drop for the MPC-controlled MMCs near MMC2 is 101 V/ms, while for the PI-controlled MMCs is 78 V/ms. The high voltage drop in the case when MPC is used occurs due to the faster response of the MPC at MMC2. However, with the fast power support from MMC1, the DC voltage decreases to 396.1 kV, as seen in Figure 5.17(a) and settles to 398.6 kV. In the case of a PI-controlled DC grid, the DC voltage reaches the negative peak of 393.5 kV. A fast control action of the MPC influences slow transient oscillations. The DC voltage swing is within ±2 kV around the steady-state value with a frequency of 9 Hz and a damping of 0.1 kV per cycle. Furthermore, it is observed that this slower oscillation is reflected in the state variables of the DC and AC grids, which induces slow transient oscillations of 9 Hz and 12 Hz in

offshore and onshore AC grids. The time taken by the MPC to reach the active power reference in MMC3 is 120 ms, while the PI controller takes 260 ms, as shown in Figure 5.17(b).

Figure 5.18 indicates the controllers' effect and performance with reclosing the DC CB and putting cable 12 in service. During the pre-disturbance stage, the active power from OFW 1 is transferred to the onshore grids through four other DC cables. The DC bus voltages near MMCs 1 and 2 are 400 kV and 408 kV, respectively (see Figure 5.18(a)). Upon reclosing cable 12 from both ends at 0.2 s, there is a current surge in the cable with a peak value of 2.73 kA, which oscillates at 112 Hz, as Figure 5.18(c) shows. This oscillation is caused by the charging of the cable's capacitance and the interaction with the line inductance of the DC CB, which is given by Equation $\frac{1}{\sqrt{LC}}$, where $L = 80$ mH and $C = 0.125\,\mu$F/km. However, this oscillation is damped around the steady-state value at the time instant of 0.44 s for the MPC-controlled DC grid, while PI takes 0.5 s to settle. Due to the restoration of cable 12, the DC bus voltage at MMC2 decreases to a new steady-state value. The current surge in the cable produces a larger MMC1's arm current (as shown in Figure 5.19) and MMC2's arm current, which in a realistic system leads to converter blocking.

Furthermore, this surge has a minimum impact on MMCs 3 and 4, and the AC grids they are connected to, as they are not directly connected to cable 12. This current surge suppression can be done by introducing the high inductance value in series with cable 12. The addition of this inductance not only suppresses this surge but will support the current interruption. However, the high inductance value will negatively impact the converter's control. Thus, an appropriate value of inductance needs to be selected. However, the possibility of suppressing this current by control action is out of the scope of this chapter and will be investigated in chapter 6.

5.7.2. AC GRID SIDE FAULT ANALYSIS

The two standard studies, i.e., symmetrical and asymmetrical fault cases, are simulated at two locations: at the PoC of MMC1 and PoC of MMC2. As a result, three cases are considered: a three-phase fault at PoC of MMC1 (case 21), a SLG fault at PoC of MMC1 (Case 22), and a three-phase fault at PoC of MMC2 (Case 23). The pre-fault condition is shown in Figure 5.20.

Figure 5.21 depicts the performance of the MPC and the PI-controlled MMCs during the three-phase fault at the PoC of MMC1. This fault is self-clearing, and the duration is 200 ms. The terminal AC voltage collapses during the fault at PoC of MMC1, as seen in Figure 5.21(c). Since MMC1 controls the DC grid voltage, after an AC fault takes place, MMC1 loses its synchronization. Due to the fault, the power delivered by the MMC1 goes to zero. With the same power infeed from the OWFs and the power extraction by MMC3, the DC grid voltage increases to 468 kV, as seen in Figure 5.21(a). During the fault, the offshore AC grid voltage in case of the PI-controlled DC grid, produces an overvoltage of 3 %, which is absent in the MPC-controlled DC grid (indicated in Figure 5.21(c)). Furthermore, the AC side fault near MMC1 causes a large arm current, as seen in Figure 5.24. For both controllers, the arm current increases during the fault. However, the MPC restricts this rise to a lower level. This restriction is enabled with the MPC constraints in MMC1. However, the MPC takes a longer time to recover after the fault is cleared due to

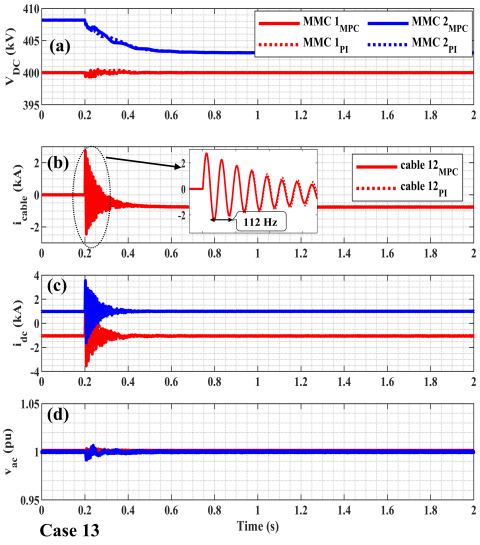

Figure 5.18: Case 13: (a) MMC's voltage [kV], (b) current of the positive part of cable 12 [kA]; (c) positive MMCs' currents [kA], and (d) RMS AC voltages [pu].

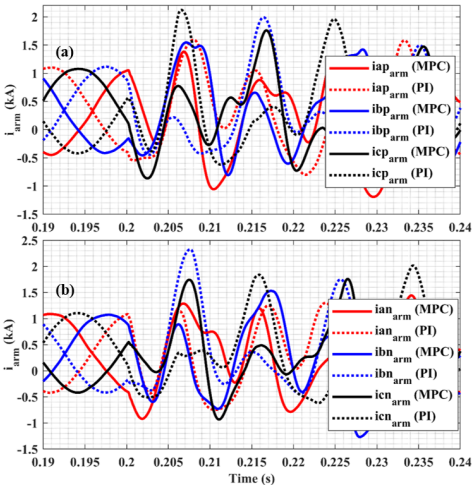

Figure 5.19: Three-phase MMC1's arm currents in: (a) upper arm; and (b) lower arm during reclosing of cable 12.

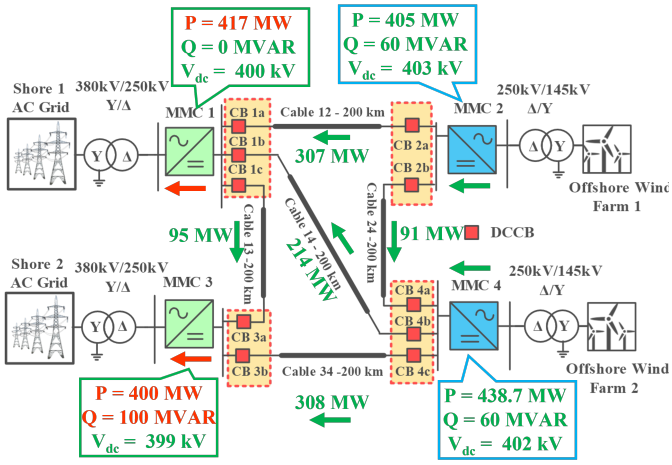

Figure 5.20: Steady-state condition before AC and DC fault.

the input constraints. As a result, a DC over-voltage of 486 kV near MMC1 with a higher settling time than the PI controller. Still, the MPC at MMC1 regulates the arm current and power, as seen in Figure 5.21(b) and 5.21(d). Further, the performance of MPC can be enhanced by introducing the drop-based control strategies at the PQ-controlled converter.

Figure 5.22 shows the impact of a temporary SLG fault at PoC of MMC1 considering

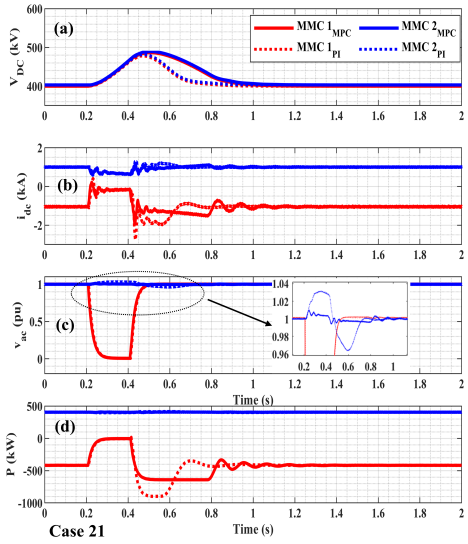

Figure 5.21: Case 21: (a) MMC's voltage [kV], (b) positive MMC's current [kA], (c) RMS AC voltages [pu], and (d) active power [MW].

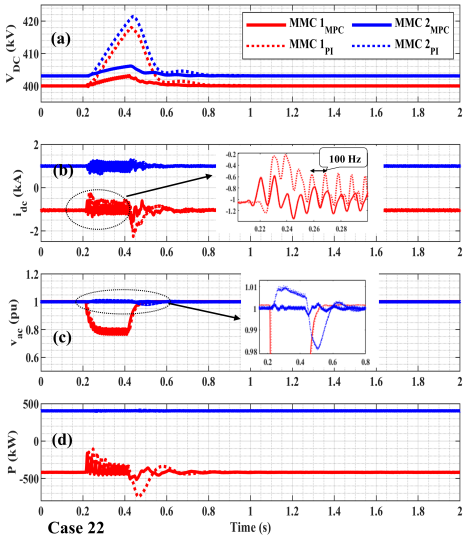

Figure 5.22: Case 22: (a) MMC's voltage [kV], (b) positive MMC's current [kA], (c) RMS AC voltages [pu], and (d) active power [MW].

PI and MPC controllers, with a SLG fault at PoC of MMC1, the AC voltage at PoC drops. However, there is an oscillation of 100 Hz at the PoC during a fault. This onshore oscillation propagates into the DC grid, as seen in Figure 5.21(a). Furthermore, it is also reflected in the offshore AC grid but with a lower amplitude. During the fault, the DC overvoltage observed with MPC-controlled is 0.5 %, while with PI-controlled converter is 4 %. Comparing both controllers, MPC performs better during the fault and post-fault period in terms of response and stability. In case of a phase-to-ground fault at the PoC of MMC1, at $t = 0.2$ s, the AC voltage at PoC drops to 0.78 p.u for both controllers, as seen in Figure 5.21(c). During the fault, the arm current of PI-controlled MMC1 has a peak value of 2.8 kA, whereas the arm current of the MPC-controlled MMC1 has a peak of 1.8 kA, as depicted in Figure 5.25.

Figure 5.23 depicts the performance of the MPC and the PI-controlled MMCs during the temporary three-phase fault at the PoC of MMC2. The AC voltage at MMC2's PoC decreases to zero during the three-phase fault, as observed in Figure 5.23(c). The fault creates a power shortage of 405 MW. MMC1 injects the required power into the DC grid to maintain the rated DC voltage, as indicated by the power reversal in Figure 5.23(d). It is observed that the MPC-controlled MMC1 regulates the DC grid voltage quickly, with a DC voltage drop of 3 % at MMC2 and 2 % at the MMC1 terminal. However, in the PI-control case, the DC grid experiences a DC voltage drop of 7.4 % at MMC2 and 5.75 % at MMC1. Furthermore, the higher voltage drop generates a significant overshoot of 30 % at the PoC of MMC4. Due to the fast control of the MPC over the DC voltage and the offshore AC voltage, the overshoot is 7 %. The MPC-controlled DC grid shows a faster recovery than the PI-controlled DC grid, as seen in Figure 5.23.

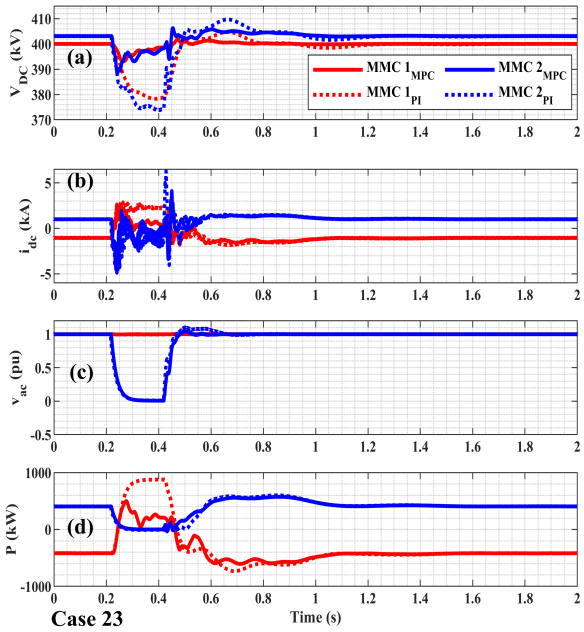

Figure 5.23: Case 23: (a) MMC's voltage [kV], (b) positive MMC's current [kA], (b) RMS AC voltages [pu], and (d) active power [MW].

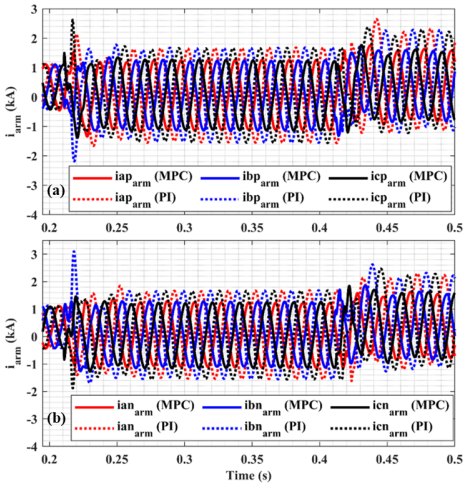

Figure 5.24: Three-phase MMC1's arm currents in: (a) upper arm; and (b) lower arm during three-phase fault.

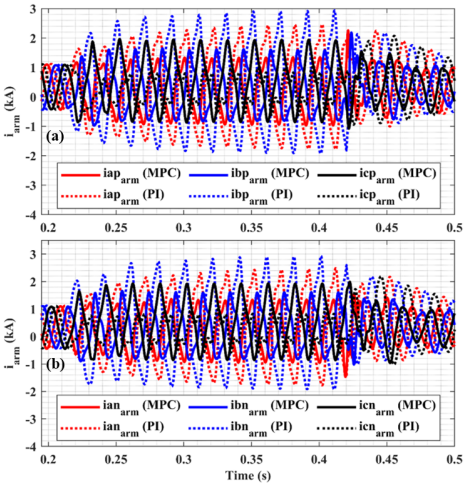

Figure 5.25: Three-phase MMC1 arm currents in: (a) upper arm; and (b) lower arm during single-phase fault at PoC of MMC1.

5.7.3. DC Grid Side Fault Analysis

The steady-state solution (i.e., power flow solution) of the four-terminal HVDC grid is depicted in Figure 5.20. For the DC fault analysis, a PP fault on cable 12 near MMC1

(case 31), a PP fault on cable 34 near MMC3 (case 32), and eight MMC1 sub-module faults (case 33) are performed.

During the PP fault near MMC1 on cable 12 at 0.2 s, the DC voltage of MMC1 drops until the DC CB operates. With the higher potential provided by the surge arrester of the DC CB, the fault current in cable 12 reaches a peak value of 7.2 kA (as shown in Figure 5.26(d)). Due to the fast recovery of the MPC-controlled DC grid, the DC voltage drops near MMC1 and is restricted to 397 kV, as seen in Figure 5.26(a), while in PI-controlled MMC1, the DC voltage decreases to 395 kV. After the fault is cleared, the MPC provides higher damping, resulting in faster post-fault recovery. When cable 12 is disconnected, power redistribution occurs. This redistribution is due to potential differences at the MMC terminals. MMCs 2 and 4 are the grid forming offshore converters, which reduce the impact on the onshore AC grids during and after the fault.

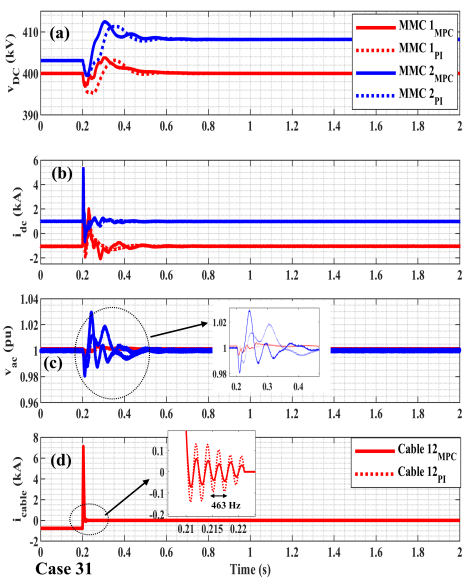

Figure 5.26: Case 31: (a) MMC's voltage [kV], (b) positive MMC's current [kA], (c) RMS AC voltages [pu], and (d) positive cable 12 current [kA].

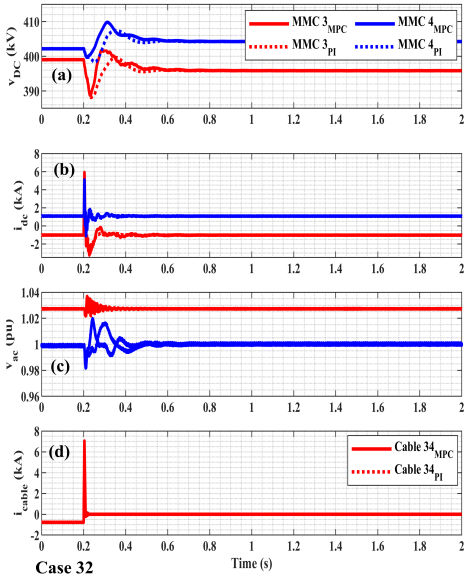

Figure 5.27: Case 32: (a) MMC's voltage [kV], (b) MMC's current [kA], (c) RMS AC voltages [pu], and (d) positive cable 34 current [kA].

With a PP fault near MMC3 at cable 34, the DC voltage near MMC3 decreases to 388 kV. The recovery of the MPC-controlled MMCs DC grid is faster with the decreasing rate of 273.33 V/ms, while for a PI-controlled MMCs DC grid's decreasing rate is 135.34 V/ms, as seen in Figure 5.27(a). The VARC DC CB receives the trip signal after 3 ms, and the maximum fault current rises to 7 kA (as seen in Figure 5.27(d)). Since MMC2 is connected to a weak grid, there is a damped oscillation of 125 Hz after the fault is cleared, as seen in Figure 5.27(c). However, when the AC voltage is controlled, this oscillation is damped.

In the case of eight internal SM faults in the upper and lower leg of phase A of MMC1, a lower-order frequency oscillation is observed in the AC and DC voltages of MMC1. For PI-controlled MMCs, the oscillation frequency is 100 Hz, whilst for MPC-controlled

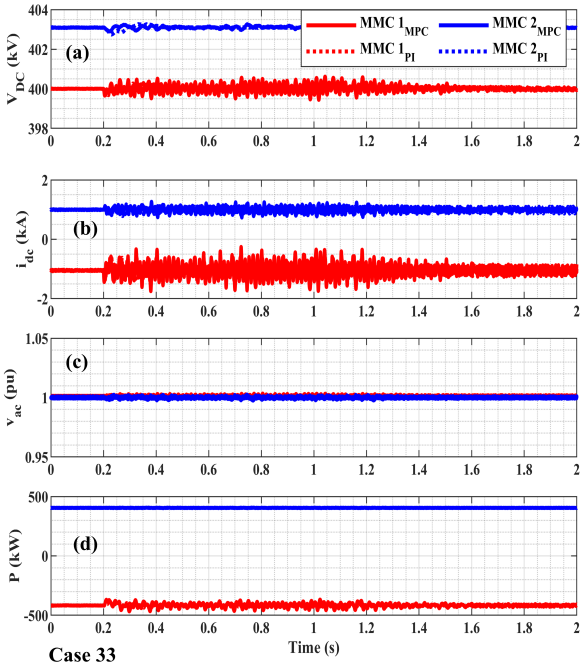

Figure 5.28: Case 33: (a) MMC's voltage [kV], (b) MMC's current [kA], (c) RMS AC voltages [pu], and (d) active power [MW].

MMCs, it is 59 Hz. The oscillation of the DC voltage observed at MMC1's terminal with an MPC control has a peak-to-peak value of 0.6 kV from the pre-disturbance value. However, by using the PI control, the peak-to-peak value is 0.2 kV. Moreover, this oscillation is restricted to only the MMC1's AC and DC terminals, as seen in Figure 5.28(a) and 5.28(b).

5.7.4. Control Interoperability

To understand the controller interaction, the following case studies are performed for MMC1, as they are graphically illustrated in Figure 5.29:

- **Case 1** - all PI controllers - In this case, the inner current, the outer voltage, and the circulating current suppression controls of MMC1 are realized using classical PI controllers. The proportion gains and the integral time constants for different loops are summarised in Table 5.6 and taken from [205].

- **Case 2** - PI controller in cascade with the inner MPC controller - In this case, the DC voltage control of MMC1 is realized as a PI controller. The output of this controller provides the reference to the MPC controller.

- **Case 3** - all MPC controllers - In this case, all control loops of MMC1 are designed using the MPC.

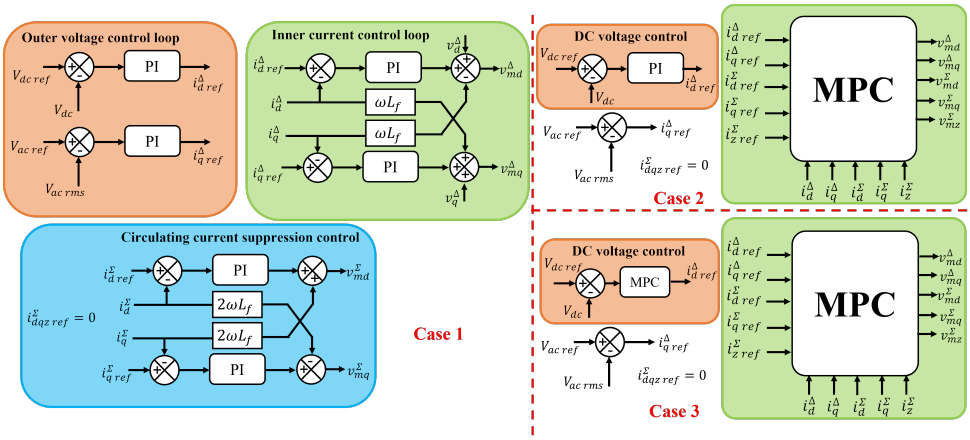

Figure 5.29: Graphical representation of different cases implemented in MMC1 control for interoperability studies.

For this operating scenario, the system is analyzed before and after the change of the wind power. Before the disturbance, the wind farm near MMC2 provides active power of 10 MW. Similarly, the active power of 100 MW is produced by the wind farm near MMC3. At $t = 0.5$ s, there is a sudden rise in the wind power with a time constant of 5 ms near MMC2. Thus, the active power rises from 10 MW to 500 MW. A different controller combination shows a different reaction to this sudden change, as shown in Figure 5.30. In the case of a classical PI controller (case 1), this rise in power stimulates the increase of the DC link voltages (Figure 5.30(a)). The maximum percentage rise of the DC bus voltage varies with the bus location. Due to the DC voltage control at MMC1, this voltage rise is restricted to 6 %, whereas the DC link voltage at MMC2 and MMC3 rises by 7.82 % and 8 %, respectively. Furthermore, the converging time to the new steady-state is 1 s. For case 2, even with the MPC, a similar pattern is observed during the wind power increase at MMC2. However, due to the MPC-based DC voltage controller in case 3, the maximum DC voltage rise of MMC2 and MMC3 is less than 4 %, which is less than the standard DC voltage margin [74]. Also, the settling time of the DC-link voltage is 100 ms.

The active power injected into MMCs and the cable currents are shown in Figure 5.30(b) and (c), respectively. Case 3 yields a faster and more stable response compared to other cases. Furthermore, the interaction with other MMCs' controllers can be seen in Figure 5.31. The fast control action in case 3 provides a good reference for the PI controllers of MMC2 and MMC3 to achieve a new steady-state with a minimum deviation.

The dynamic change of power causes an increase in the DC voltage for a few seconds in the case when a classical PI controller is applied(case 1). This sudden and longer duration of the DC overvoltage can create protection anomalies. Besides, the effect of this overvoltage is propagated in the offshore grids. In this case, fast control action will play a crucial role, leading to optimal coordination between advanced control and protection. In this scenario, combining the advanced and classical controllers does not improve the performance compared to case 1. This poor performance arises due to the

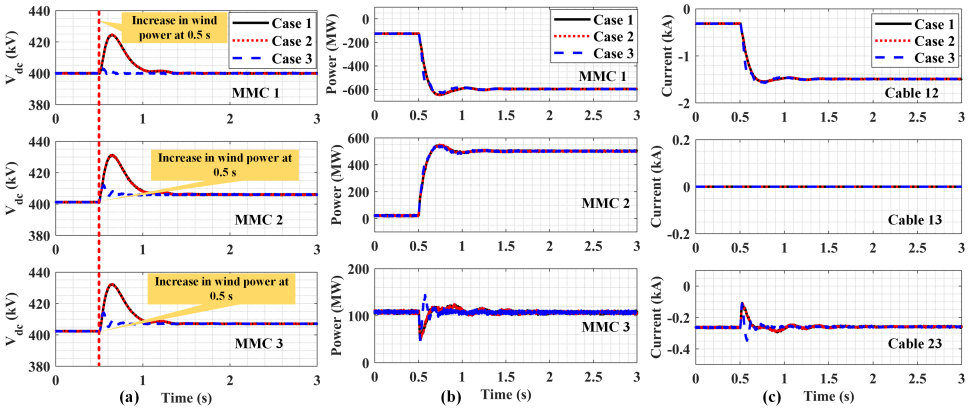

Figure 5.30: Effect of the increase in the wind power (speed): (a) bus voltages of the MMCs; (b) active power at PoC of MMCs; (c) DC cable current.

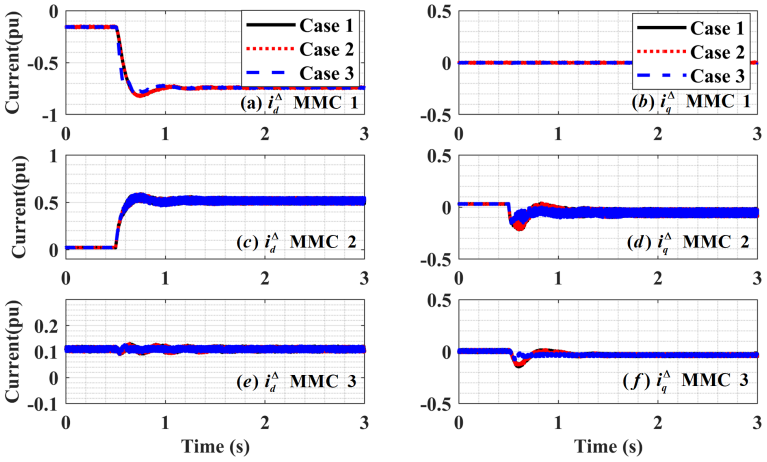

Figure 5.31: Effect of the increase in the wind power (speed) on i_d^Δ and i_q^Δ grid current of MMCs.

slower DC voltage control. Thus, re-tuning of the PI is required. In the future, faster power control will be needed to connect intermittent energy sources. Adaptive tuning of the PI or controllers like the MPC will be required at the converter and system operator levels.

5.8. CONCLUSION

Part I of this chapter presents a variant of MPC using Laguerre's function for the discretized MMC with the exact solution of the differential equations. The MPC is designed as an indirect implicit control. Both constrained and unconstrained scenarios are analyzed and compared, considering active and reactive power setpoint changes. With the constraints on the states, the dynamic response is generally affected. However,

there is no effect on the steady-state response. With the amplitude-constrained control signals, the overshoot is reduced with recomputation during an online optimization. It is shown that the transient response is largely dependent on the sample time (T_s). Thus, with the increase in the T_s, a highly damped model is obtained, with a response equivalent to the step response of the model. The designed control is computationally efficient, with a small prediction horizon, which does not influence pole placement. Thus, it can be considered a potential candidate for real-time simulation and testing. The pole movement with the change in the weighting factor $\boldsymbol{R}$ gets concentrated below the unity circle with an increase in the T_s, which makes the model stable. Similarly, the pole movement due to an increase in N gets saturated after a certain value, whereas the pole movement with a change in Laguerre's pole varies. Furthermore, the implementation of the proposed variant of MPC is validated by RTDS. The comparison between PI and proposed MPC during different operating scenarios indicates MPC's stable and faster response, which is essential during transient events. The proposed MPC has a clear advantage over classical controlling methods.

Part II of this chapter investigates the performance of the MPC in a four-terminal, monopolar, MMC-based HVDC grid connecting two offshore wind power plants, a weak grid, and a strong grid, under fast transient like AC, DC faults, and submodule internal faults. The chapter also highlights the expansion of the control scheme from a single MMC terminal to a multi-terminal, indicating the MPC control's minimum tuning. The chapter highlights the use of a switching model of an MMC by applying a GTFPGA in a HiL and its interaction with the average MMC model. Furthermore, SiL is used for an online update of the wind profile. The studies are conducted using real-time simulations. The performance of the MPC is investigated against the traditional PI control.

The performance results show:

- The MPC-controlled MMC-based HVDC grid enables the converter to provide faster and more reliable controlled power support during the nominal operation with the minimum effect on the AC and DC terminal voltages than the PI-controlled MMC-based HVDC grid.

- The lower arm current and DC voltage droops are observed with the MPC-controlled MMCs during AC-side disturbances. Furthermore, the MPC-controlled MMC's post-recovery is faster than the PI-controlled ones.

- During a DC fault, the MPC provides rigid terminal DC voltage support with a fast and damped recovery.

- The propagation of AC and DC side disturbances (faults) is smaller when the control is an MPC rather than a PI-controlled MMCs. Furthermore, the MPC-based grid forming converter provides better voltage stability compared to the one with PI control. During the interoperability studies, the slower response of the PI controller creates a bottleneck in the system recovery. Thus, the parameter of the PI controller needs to be re-calibrated. In contrast, the MPC provides a faster and more stable response.

Nevertheless, both controllers show similar performance during internal MMC faults. The reason for this is the internal implementation of the lower-level controlling strategies for the SM capacitor voltage balancing in RTDS© and GTFPGAs.

6

PREDICTIVE FAULT CURRENT SUPPRESSION CONTROL

This chapter deals with a novel MPC approach for zero-sequence current in MMCs, aimed at improving DC link voltage stability in MT-HVDC systems. The strategy extends the fault detection and DC CB operation window by 3 ms, optimizing energy dissipation during faults and maintaining voltage regulation. It highlights the potential integration with existing PI-controlled converters, despite their slower response, by balancing DC voltage and fault current management. This MPC method enhances DC CB reaction time, offering a cost-effective, improved fault management solution. Future research will focus on the control's adaptability to system changes and optimization of protection strategies.

Parts of this chapter have been published in A. Shetgaonkar, M. Popov, P. Palensky, A. Lekić, "Zero-sequence current suppression control for fault current damper based on model predictive control," *Electric Power Systems Research*, vol. 223, pp. 109592, 2023, Elsevier.

6.1. MPC-BASED ZERO-SEQUENCE CURRENT CONTROL

As the name indicates, the MPC's prediction and accuracy are determined purely by the system's behaviour. A decade of development in the modelling of MMCs has led to an accurate MMC non-linear model [113]. The dynamics of the MMC can be formulated by using two components, Σ and Δ, which represent the DC and AC characteristics of the converter, respectively. By applying the Clarke-Park transformation, the Σ and Δ AC components are translated into the stationary $dq-$frame given by Equation (3.3). Zero-sequence component current is defined by Equation (3.3c). Its physical importance is in its influence on the DC current since $i_{dc} = 3i_z^{\Sigma}$. Furthermore, the discrete form of this MMC model is discussed in Chapter 5.

The same like in section 5.2.1, the vector $\vec{x} = [i_d^{\Sigma},\ i_q^{\Sigma},\ i_z^{\Sigma},\ i_d^{\Delta},\ i_q^{\Delta}]^T$ represents state variables, while $\vec{u} = [v_{Md}^{\Sigma},\ v_{Mq}^{\Sigma},\ v_{Mz}^{\Sigma} - \frac{v_{dc}}{2},\ v_{Md} - v_d^{\Delta},\ v_{Mq} - v_q^{\Delta}]^T$, $\vec{u} \in \mathbb{U} = [-1,1]^5 \subset \mathbb{R}$, represents system inputs. Similarly to Chapter 5, the future control sequence is represented by the discrete Laguerre network, $\vec{\eta} \in [-1,1]^5 \subset \mathbb{R}$, which is determined by solving the optimal control problem, and minimizing the objective (cost) function based on the equality and inequality constraints:

$$\min_{\vec{\eta}} J = \sum_{i=1}^{N_p} \|\vec{x}_m(k+i|k)\|_{\mathbf{Q}}^2 + \left\|\vec{\eta}\right\|_{\mathbf{R}}^2 + I_m e(k), \tag{6.1a}$$

$$\text{subject to } \mathbf{M}\vec{\eta} \leq \vec{b}, \tag{6.1b}$$

$$\vec{x}_m(k+i|k) = \vec{r}(k) - \vec{y}_m(k|k). \tag{6.1c}$$

Here, $\mathbf{Q} \succeq 0$ and $\mathbf{R} \succ 0$ are weighting matrices, and $N_p = 20 \in \mathbb{I}^+$ is the prediction horizon. For variables $\vec{x}_m(k)$, vector $r(k) \in \mathbb{R}^5$ is a reference signal. Matrix $\mathbf{M}$ and column vector $\vec{b}$ are related to the constraint information of the rate, and amplitude [112]. In reality, there will be an error due to the modelling or signal noise. However, these disturbances can be considered in the optimal control problem, which is represented by $e(k)$. $e(k)$ denotes the error between the system's measured signal and plant's predicted signal at k^{th} instance. $I_m \succ 0$ is the weight matrix. The reference determination of the differential-current components (denoted as $i_{d,q}^{\Delta}$) remains the same as the traditional control hierarchy as explained in Chapter 3. The CCSC mainly suppresses additive currents in the traditional control. However, the zero-sequence current component (i_z^{Σ}) reference is left uncontrolled. As previously explained, the MMC current on the DC side can be represented by the zero-sequence current component. This work calculates the zero-sequence current reference using the active power injected/absorbed in the AC system and DC voltage as shown in Figure 6.1.

One method to reduce the DC fault current is to reduce the voltage across the DC CB line inductance (l_{line}). The DC link voltage at the MMC terminals must be reduced to reduce the voltage across the DC CB line inductance. This decrease in the DC link voltage will further decrease the fault current rate of rise. During the steady state operation, the active power and DC link voltages are inside the prescribed limits (i.e., ± 1.2 p.u, and 0.8 p.u $-$ 1 p.u, respectively). Hence, the calculated zero-sequence current component (i.e $i_{z,ref}^{\Sigma} = \frac{p_{ac}}{3v_{dc}}$) remains the same as the measured zero-sequence current (i_z^{Σ}). Thus, no control action is provided by the zero-sequence current control. However, during the

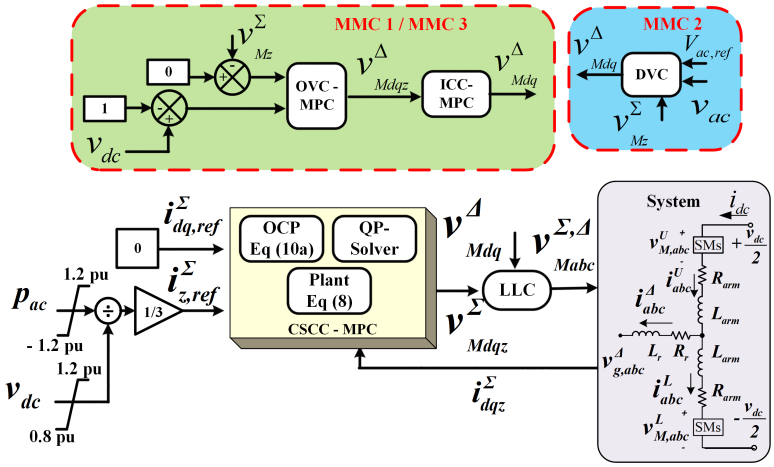

Figure 6.1: Block diagram of implemented zero-sequence current control.

DC fault period, the active power P_{ac} increases, and the DC link voltage v_{dc} decreases leading to saturation of the calculated zero-sequence current. Hence, the zero-sequence current control provides the control action, that temporally reduces the DC link voltage. With the reduction of the DC link voltage, the rate of rise of the fault current is reduced. Further, this control action is added to the outer voltage loop and direct voltage control in the case of grid-forming converters (as shown in Figure 6.1) to ensure that both AC and DC component values remain within the operating limits.

6.2. EXPERIMENTAL STUDIES

Figure 6.2 shows the simulated three-terminal ±525 kV metal-return bipolar MT-HVDC system programmed for the real-time simulation in the RTDS©. This model is a modified version of the model developed in Chapter 4 and summarised in this section. The system is divided into two zones (i.e., onshore and offshore). The onshore system consists of two converters (i.e., MMC1 and MMC3). Each platform is connected to two 1 GW MMC converters. The onshore platforms are connected to a strong grid, with a short circuit ratio of $SCR = 44$, by two converter transformers with a rating of 400/275 kV, 1250 MVA. Similarly, the offshore platform has two 1GW MMC converters connected to a wind farm via 275/66kV, 1250MVA. This transformer also acts as a scaling transformer. The offshore platform is connected to the wind park by a 66 kV AC cable with a distance of 7 km. The grounding for the MT-HVDC is provided at the onshore platform with a resistance value of 0.01 Ω. Type-4 converter model (detailed equivalent model, implemented on FPGA) is used for MMC 1 and MMC 2, whereas MMC 3 is modelled as Type-5 (averaged RTDS model) [177]. The setup is comprehensively described in [112].

The onshore zone is connected to the offshore zone by three 2 GW, 525 kV HVDC cables with the ratings shown in Figure 6.2. Cable 12 has two VARC DC CBs at each cable's end. This VARC DC CB is scaled to 525 kV with a fault interruption capability of 20 kA [206]. The wind park has nine Type-4 wind turbines, each with a rating of 2 MW at 16 m/s. Since this work investigates DC system-level dynamics, the averaged model

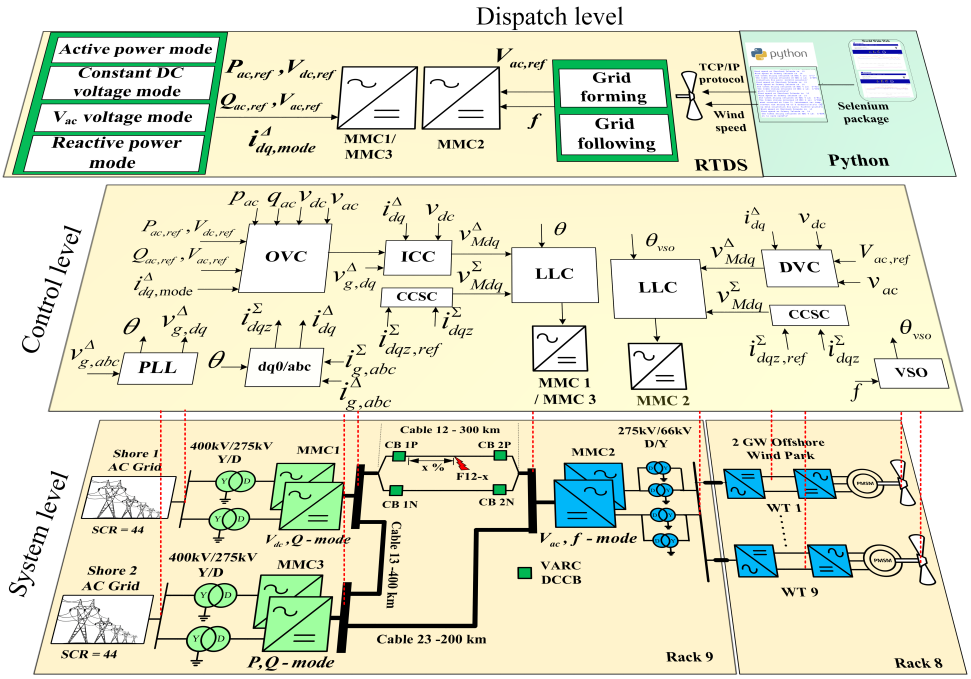

Figure 6.2: Circuit and control hierarchy of Three terminal ±525 kV bipolar MT-HVDC simulated systems (The red dotted line indicates the ac-DC measurement).

of a back-to-back converter of a Type-4 wind turbine is considered. This back-to-back converter is modelled using the Descriptor State-Space (DSS) modelling approach [63]. The grid-side converter controls the DC link voltage of the Type-4 wind turbine and provides reactive power support at the point of common coupling. In contrast, the machine-side converter controls the torque and stator terminal voltage of the PMSM. The wind speed data is updated in real time through a North Sea sensor by using a Python script.

Table 6.1 highlights the circuit parameters for the converters given in Figure 6.2. The proposed controls are located in both offshore and onshore converters. In the onshore grid-tie converter station, MMC1 controls DC voltage (V_{dc},Q-mode), whilst MMC3 controls active power (P,Q-mode). The offshore converter MMC2 is grid-forming (v_{ac},f-mode). The data for the cable are adopted from the ongoing project [29].

In a steady state, MMC2 injects an active power of 2 GW into the DC grid generated by the wind power plant. MMC3 injects an active power of 1 GW into the onshore AC grid. To keep the DC-link voltage constant, the remaining power is absorbed by MMC1 and injected into the onshore AC grid. Due to a full selective protection scheme being introduced, the internal protection of converters is disabled. The rated fault current interruption capability of the VARC DC CB is set to 20 kA, and the operating time of the DC CB is 5 ms. Furthermore, the DC fault detection is not instantaneous, so a 1 ms delay is introduced. Due to the multi-timestep simulation in the real-time simulator, the

Table 6.1: Circuit parameter for the simulated system

Parameter		Values
Rated capacity		2000 MVA
Control Mode	MMC1	V_{dc}, Q
	MMC2	V_{ac}, Q
	MMC3	P, Q
DC link voltage (v_{dc})		± 525 kV
Number of Submodules per arm (N_{sm})		240
Arm capacitance (C_{arm})		22 μF
Arm inductance (L_{arm})		42 mH
Arm resistance (R_{arm})		0.544 Ω
Transformer leakage reactance (l_r)		0.18 p.u
AC converter voltage (onshore)		275 kV
AC system voltage (onshore/offshore)		400 kV/66 kV
DC CB line inductance (l_{line})		120 mH
cable resistance per km (R_{cable})		9 $m\Omega$
AC frequency (f)		50 Hz

interested areas are modelled in small timesteps ($2-3\mu s$) using processors and FPGAs. As a result, the accuracy is maintained at an acceptable level. Since we investigate the control action by the proposed controller, this modelling accuracy is sufficient.

6.2.1. FAULT AMPLITUDE IDENTIFICATION

To identify the current hotspot in the MT-HVDC during the fault, two different types of faults at two different cable locations are simulated. In this work, a positive PG DC fault and a PP DC fault is studied. These faults are located at MMC1's terminal (0 %) and near the opposite terminal (100 %). The syntax, $PG-0-12$ in Figure 6.3 indicates the PG DC fault at the terminal in cable 12. Similarly, $PG-100-12$ indicates the PG DC fault at the opposite terminal of cable 12. Furthermore, I^{+}_{linexy} indicates the current measured in cable xy from x terminal of the cable.

Figure 6.3 shows the fault current measured at $t = 6$ ms without any fault current limiting scenario at different locations during different faults. The analysis shows that, for a given MT-HVDC system at rated power, the PG and PP fault near the MMC1 create fault currents with amplitudes 41.73 kA and 42.44 kA, respectively. Similarly, the fault near MMC2, on cable 23 produces the second highest fault current. The converters' pre-fault condition and the operating mode determine the fault current amplitude. Since MMC1 regulates the DC-link voltage to a constant value, the fault near this

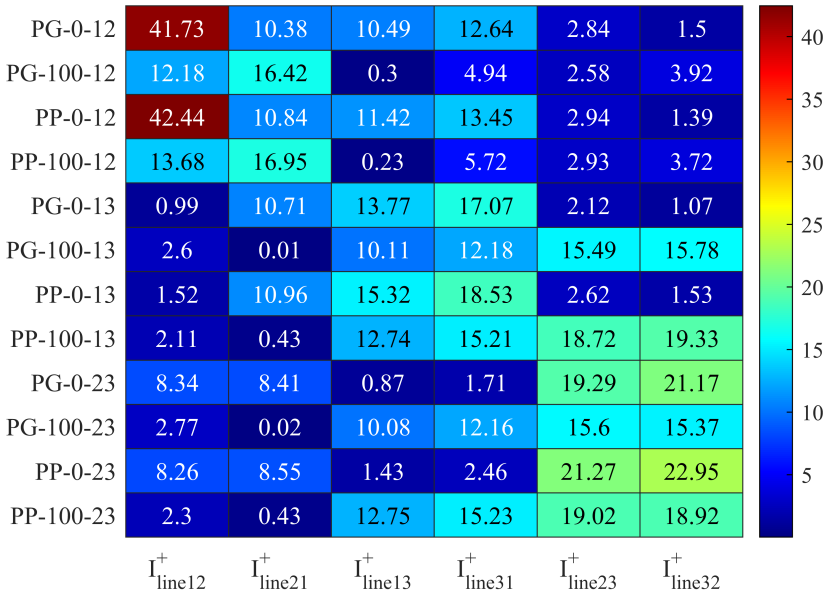

Figure 6.3: Fault amplitude in kA at 6 ms for different fault types and locations in MT-HVDC.

terminal results in a high fault current. Similarly, the fault near MMC2 produces a high fault current due to the AC power infeed. Hence, the subsequent study considers the fault near MMC1 and MMC2 on cable 12.

To understand the impact of the proposed control strategies, the following cases are investigated:

C1 Traditional PI control without zero-sequence current control.

C2 MPC control without zero-sequence current control.

C3 Traditional PI control with zero-sequence current control.

C4 MPC control with zero-sequence current control.

6.2.2. DC FAULT AT MMC1'S TERMINAL

In this scenario, the PG and PP faults are applied at the terminal of MMC1. Furthermore, the impact of protection delay (i.e delay in fault detection or DC CB operation) (t_d) is investigated for all cases and summarised in Table 6.2 and 6.3. From these tables, it can be seen that the fault is interrupted by the DC CB with both traditional PI controls and MPC for t_d = 1 ms. Compared to PI control, during PG fault with MPC, the peak fault current in CB1P DC CB and MMC1 is lower by 0.7 kA and 1.26 kA, respectively. These lower values result from the MPC's fast control action on the state variables of MMC. However, this results in decreasing of DC-link voltage at MMC1 ($v_{dc,MMC1}$) by

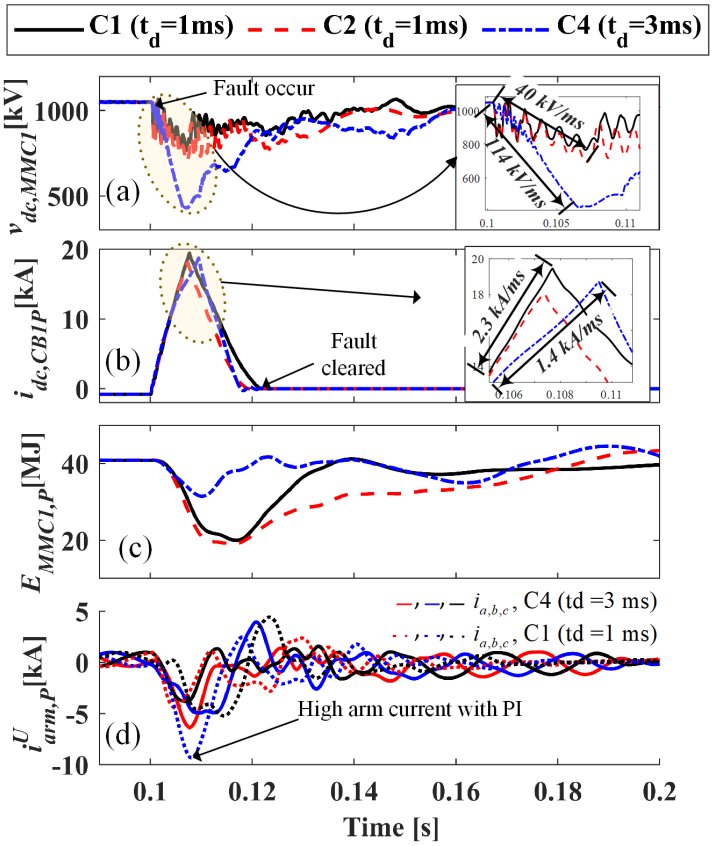

Figure 6.4: Impact of proposed control during PP fault at MMC1 terminal: (a) MMC1's terminal voltage [kV]; (b) Line Current [kA] in CB1P DC CB; (c) Total Energy stored in the MMC1 [MJ]; and (d) Upper arm current of MMC1 [kA].

16% compared with the rated voltage, which is referred to as undershoot in this and subsequent sections. Furthermore, the settling time is increased by 50 ms. However, the fast control action helps the DC CB to absorb less energy. As the t_d increases, the peak amplitude of the fault current increases, and as a result, DC CB in the PI controlled system fails to interrupt. However, the MPC during the PG fault only adds up a surplus of 0.5 ms delay before the DC CB fails to interrupt the fault. A similar trend is observed with a higher fault current and undershoot in DC-link voltage from rated voltage during the PP fault as shown in Table 6.3.

With the proposed control over i_z^{Σ} current, in PI's and MPC's CCSC, the sensitivity of the t_d is minimised to a greater extent. The system can withstand a higher delay, with a lower fault current in the converter and in the DC CB. This results in lower energy absorption in the DC CB's surge arrester during DC fault. The energy absorbed by the traditional PI-controlled MMC is 30% (PG) and 40% (PP) higher than that of the MPC-controlled MMC with the proposed control over i_z^{Σ} current for t_d = 3 ms during the PG and the PP fault, respectively. Furthermore, the settling time is shortened due to

the active power feedback in the proposed control. However, a significant undershoot in $v_{dc,MMC1}$ from rated DC link voltage is observed with the proposed control. It is also interesting to observe that the energy absorbed during the PG and PP fault interruption remains the same, indicating reduced stress on the surge arrester during the PP fault. As a result, the increase in t_d does not influence the increase of the absorbed energy drastically. Figure 6.4 highlights the significance of the proposed control compared to

Table 6.2: Performance of different cases under the PG fault at the MMC1 terminal.

PG fault		Peak in $i_{dc,CB1P}$	Peak in $i_{dc,MMC1}$	Undershoot in $V_{dc,MMC1}$	settling time of $V_{dc,MMC1}$	Energy SA	Status
PI without i_z^{Σ} control	$t_d = 1ms$	17.70 kA	15.30 kA	916.31 kV (-12.73 %)	0.13 s	69.25 MJ	Interrupts
	$t_d = 1.5ms$	37.01 kA	24.36 kA	533.87 kV (-49.15 %)	Inf	0.00 MJ	Fails
	$t_d = 2ms$	36.93 kA	24.46 kA	534.68 kV (-49.07%)	Inf	0.00 MJ	Fails
	$t_d = 2.5ms$	36.84 kA	24.51 kA	532.94 kV (-49.24 %)	Inf	0.00 MJ	Fails
	$t_d = 3ms$	36.78 kA	24.57 kA	533.79 kV (-49.16 %)	Inf	0.00 MJ	Fails
MPC without i_z^{Σ} control	$t_d = 1ms$	17.00 kA	14.04 kA	881.92 kV (-16.00 %)	0.18 s	55.38 MJ	Interrupts
	$t_d = 1.5ms$	18.77 kA	15.18 kA	867.75 kV (-17.35 %)	0.19 s	62.27 MJ	Interrupts
	$t_d = 2ms$	32.63 kA	22.14 kA	538.90 kV(-48.67 %)	Inf	0.00 MJ	Fails
	$t_d = 2.5ms$	32.55 kA	22.18 kA	539.94 kV (-48.57 %)	Inf	0.00 MJ	Fails
	$t_d = 3ms$	32.47 kA	22.14 kA	540.47 kV (-48.52 %)	Inf	0.00 MJ	Fails
PI with i_z^{Σ} control	$t_d = 1ms$	15.59 kA	11.52 kA	789.86 (-24.78%)	0.18 s	42.5 MJ	Interrupts
	$t_d = 1.5ms$	16.53 kA	12.49 kA	790.77 (-24.69%)	0.18 s	47.96 MJ	Interrupts
	$t_d = 2ms$	17.57 kA	13.36 kA	789.43 (-24.82%)	0.29 s	53.51 MJ	Interrupts
	$t_d = 2.5ms$	18.8 kA	13.88 kA	790.13 (-24.75%)	0.29 s	59.83 MJ	Interrupts
	$t_d = 3ms$	47.1 kA	29.51 kA	517.49 (-50.72%)	Inf	0 MJ	Fails
MPC with i_z^{Σ} control	$t_d = 1ms$	15.03 kA	9.5 kA	739.02 (-29.62%)	0.16 s	32.33 MJ	Interrupts
	$t_d = 1.5ms$	15.76 kA	10.71 kA	739.51 (-29.57%)	0.17 s	36.55 MJ	Interrupts
	$t_d = 2ms$	16.5 kA	11.5 kA	738.56 (-29.66%)	0.17 s	40.4 MJ	Interrupts
	$t_d = 2.5ms$	17.34 kA	11.95 kA	736.82 (-29.83%)	0.16 s	44.05 MJ	Interrupts
	$t_d = 3ms$	18.53 kA	12.53 kA	735.28 (-29.97%)	0.16 s	48.78 MJ	Interrupts

the PI and MPC in the time domain for PP fault. During the fault period, the MMC with the proposed control has $\frac{dv}{dt}$ of -114 kV/ms, while PI and MPC controlled MMC1 has $\frac{dv_{dc,MMC1}}{dt}$ of -40 kV/ms. The high value of $\frac{dv_{dc,MMC1}}{dt}$ creates a reduction in $\frac{di_{dc,CB1P}}{dt}$ of fault current as seen Figure 6.4(b). Furthermore, the proposed control prevents a large drop in converters' energy. Hence, it protects the sub-modules during fast transients. The arm currents of the converts are smaller compared to traditional PI-controlled MMC, as seen in Figure 6.4(d).

Table 6.3: Performance of different cases under the PP fault at the MMC1 terminal.

PP fault		Peak in $i_{dc,CB1P}$	Peak in $i_{dc,MMC1}$	Undershoot in $V_{dc,MMC1}$	settling time of $V_{dc,MMC1}$	Energy SA	Status
PI without i_z^{Σ} control	$t_d = 1ms$	19.46 kA	16.4 kA	767.07 kV (-26.95 %)	0.19 s	84.32 MJ	Interrupts
	$t_d = 1.5ms$	43.24 kA	24.94 kA	-14.22 kV (-101.35 %)	Inf	0 MJ	Fails
	$t_d = 2ms$	43.16 kA	25.13 kA	-13.62 kV (-101.3 %)	Inf	0 MJ	Fails
	$t_d = 2.5ms$	43.08 kA	25.18 kA	-13.88 kV (-101.32 %)	Inf	0 MJ	Fails
	$t_d = 3ms$	43 kA	25.25 kA	-13.98 kV (-101.33 %)	Inf	0 MJ	Fails
MPC without i_z^{Σ} control	$t_d = 1ms$	18.06 kA	14.7 kA	691.54 kV(-34.14 %)	0.19 s	63.95 MJ	Interrupts
	$t_d = 1.5ms$	37.88 kA	22.69 kA	-10.72 kV(-101.02 %)	Inf	0 MJ	Fails
	$t_d = 2ms$	37.67 kA	22.76 kA	-15.06 kV(-101.43 %)	Inf	0 MJ	Fails
	$t_d = 2.5ms$	37.57 kA	22.79 kA	-14.02 kV(-101.34 %)	Inf	0 MJ	Fails
	$t_d = 3ms$	37.44 kA	22.87 kA	-13.36 kV(-101.27 %)	Inf	0 MJ	Fails
PI with i_z^{Σ} control	$t_d = 1ms$	15.71 kA	11.34 kA	535.32 kV (-49.02%)	0.25 s	44.57 MJ	Interrupts
	$t_d = 1.5ms$	16.63 kA	12.4 kA	530.33 kV (-49.49%)	0.26 s	50.27 MJ	Interrupts
	$t_d = 2ms$	17.71 kA	13.12 kA	520 kV (-50.48%)	0.27 s	56.11 MJ	Interrupts
	$t_d = 2.5ms$	19.13 kA	13.61 kA	535.75 kV (-48.98%)	0.26 s	64.22 MJ	Interrupts
	$t_d = 3ms$	49.91 kA	28.1 kA	-16.5 kV (-101.57%)	Inf	0 MJ	Fails
MPC with i_z^{Σ} control	$t_d = 1ms$	15.15 kA	9.27 kA	417.64 kV (-60.22%)	0.18 s	33.31 MJ	Interrupts
	$t_d = 1.5ms$	15.87 kA	10.49 kA	418.39 kV (-60.15%)	0.18 s	37.55 MJ	Interrupts
	$t_d = 2ms$	16.65 kA	11.36 kA	418.08 kV (-60.18%)	0.18 s	41.61 MJ	Interrupts
	$t_d = 2.5ms$	17.52 kA	11.87 kA	422.06 kV (-59.8%)	0.18 s	45.39 MJ	Interrupts
	$t_d = 3ms$	18.71 kA	12.21 kA	421.38 kV (-59.87%)	0.17 s	50.34 MJ	Interrupts

Table 6.5: Performance of different cases under the PP fault at the MMC2 terminal.

PP fault		Peak in $i_{dc,CB2P}$	Peak in $i_{dc,MMC2}$	Undershoot in $V_{dc,MMC2}$	settling time of $V_{dc,MMC2}$	Energy SA	Status
PI without i_z^{Σ} control	$t_d = 1ms$	39.26 kA	14.71 kA	-20.01 kV (101.91%)	Inf	0 MJ	Fails
	$t_d = 1.5ms$	39.14 kA	14.66 kA	-19.1 kV (-101.82%)	Inf	0 MJ	Fails
	$t_d = 2ms$	39.09 kA	14.61 kA	-20.47 kV (-101.95%)	Inf	0 MJ	Fails
	$t_d = 2.5ms$	39.09 kA	14.64 kA	-20.16 kV (-101.92%)	Inf	0 MJ	Fails
	$t_d = 3ms$	39.19 kA	14.67 kA	-19.53 kV (-101.86%)	Inf	0 MJ	Fails
MPC without i_z^{Σ} control	$t_d = 1ms$	35.42 kA	16.22 kA	-44.7 kV (-104.26%)	Inf	0 MJ	Fails
	$t_d = 1.5ms$	35.31 kA	16.08 kA	-40.77 kV (-103.88%)	Inf	0 MJ	Fails
	$t_d = 2ms$	35.15 kA	15.85 kA	-33.77 kV (-103.22%)	Inf	0 MJ	Fails
	$t_d = 2.5ms$	35.11 kA	15.46 kA	-29.99 kV (-102.86%)	Inf	0 MJ	Fails
	$t_d = 3ms$	34.94 kA	15.25 kA	-19.57 kV (-101.86%)	Inf	0 MJ	Fails
PI with i_z^{Σ} control	$t_d = 1ms$	15.25 kA	4.98 kA	324 kV (-69.14%)	0.27 s	39.34 MJ	Interrupts
	$t_d = 1.5ms$	16 kA	5 kA	324.31 kV (-69.11%)	0.27 s	42.87 MJ	Interrupts
	$t_d = 2ms$	16.75 kA	4.98 kA	323.68 kV (-69.17%)	0.25 s	46.39 MJ	Interrupts
	$t_d = 2.5ms$	17.56 kA	5.01 kA	324.28 kV (-69.12%)	0.24 s	49.49 MJ	Interrupts
	$t_d = 3ms$	18.63 kA	4.98 kA	324.24 kV (-69.12%)	0.22 s	53.77 MJ	Interrupts
MPC with i_z^{Σ} control	$t_d = 1ms$	15.15 kA	4.97 kA	307.95 kV (-70.67%)	0.23 s	32.88 MJ	Interrupts
	$t_d = 1.5ms$	15.89 kA	5.04 kA	307.74 kV (-70.69%)	0.18 s	35.64 MJ	Interrupts
	$t_d = 2ms$	16.57 kA	5.04 kA	307.95 kV (-70.67%)	0.18 s	38.52 MJ	Interrupts
	$t_d = 2.5ms$	17.26 kA	5.04 kA	307.61 kV (-70.7%)	0.18 s	40.45 MJ	Interrupts
	$t_d = 3ms$	17.99 kA	5.11 kA	308.5 kV (-70.62%)	0.18 s	42.86 MJ	Interrupts

Table 6.4: Performance of different cases under the PG fault at the MMC2 terminal.

PG fault		Peak in $i_{dc,CB1P}$	Peak in $i_{dc,MMC2}$	Undershoot in $V_{dc,MMC2}$	settling time of $V_{dc,MMC2}$	Energy SA	Status
PI without i_z^{Σ} control	$t_d = 1ms$	36.33 kA	14.77 kA	572.04 kV(-45.52%)	Inf	0 MJ	Fails
	$t_d = 1.5ms$	36.41 kA	14.46 kA	568.81 kV(-45.83%)	Inf	0 MJ	Fails
	$t_d = 2ms$	36.36 kA	14.49 kA	570.08 kV(-45.71%)	Inf	0 MJ	Fails
	$t_d = 2.5ms$	36.37 kA	14.43 kA	568.81 kV(-45.83%)	Inf	0 MJ	Fails
	$t_d = 3ms$	36.4 kA	14.43 kA	569.14 kV(-45.8%)	Inf	0 MJ	Fails
MPC without i_z^{Σ} control	$t_d = 1ms$	30.12 kA	15.97 kA	606.88 kV(-42.2%)	Inf	0 MJ	Fails
	$t_d = 1.5ms$	29.99 kA	15.74 kA	605.47 kV(-42.34%)	Inf	0 MJ	Fails
	$t_d = 2ms$	29.85 kA	15.49 kA	604.13 kV(-42.46%)	Inf	0 MJ	Fails
	$t_d = 2.5ms$	29.84 kA	15.1 kA	607.27 kV(-42.16%)	Inf	0 MJ	Fails
	$t_d = 3ms$	29.75 kA	14.85 kA	605.14 kV(-42.37%)	Inf	0 MJ	Fails
PI with i_z^{Σ} control	$t_d = 1ms$	14.73 kA	5.51 kA	723.09 kV(-31.13%)	0.26 s	32.98 MJ	Interrupts
	$t_d = 1.5ms$	15.41 kA	5.56 kA	719.83 kV(-31.44%)	0.27 s	36.07 MJ	Interrupts
	$t_d = 2ms$	15.99 kA	5.56 kA	716 kV(-31.81%)	0.27 s	38.39 MJ	Interrupts
	$t_d = 2.5ms$	16.62 kA	5.51 kA	715.35 kV(-31.87%)	0.26 s	40.63 MJ	Interrupts
	$t_d = 3ms$	17.48 kA	5.56 kA	719.83 kV(-31.44%)	0.25 s	43.04 MJ	Interrupts
MPC with i_z^{Σ} control	$t_d = 1ms$	14.51 kA	5.06 kA	701.06 kV(-33.23%)	0.16 s	27.69 MJ	Interrupts
	$t_d = 1.5ms$	15 kA	5.06 kA	700.16 kV(-33.32%)	0.17 s	29.15 MJ	Interrupts
	$t_d = 2ms$	15.59 kA	5.07 kA	701.49 kV(-33.19%)	0.17 s	30.84 MJ	Interrupts
	$t_d = 2.5ms$	16.01 kA	5.05 kA	700.58 kV(-33.28%)	0.17 s	31.85 MJ	Interrupts
	$t_d = 3ms$	16.6 kA	5.05 kA	700.8 kV(-33.26%)	0.18 s	33.18 MJ	Interrupts

6.2.3. DC FAULT AT MMC2'S TERMINAL

In this case, a PG and a PP fault are applied at the MMC2 terminal. The effect of protection delay is investigated for all cases and is summarised in Table 6.4 and 6.5, respectively. The DC fault near MMC2 creates a high rate of rise of fault current, which results in current interruption failure. The high value of $\frac{\mathrm{d}v_{dc,MMC2}}{\mathrm{d}t}$ is caused by the wind park's power infeed. Hence, MMC2 is very sensitive to the delay of the operation of the DC CB, and the DC CB line inductance.

However, with the application of the proposed zero-sequence current PI and MPC control, the delay sensitivity is removed for both types of faults as illustrated in Table 6.4 and 6.5 for PP and PG faults. The energy absorption and the peak fault current through CB2P and MMC2 for both controls differ by less than 1%. This is caused by the constant current source behaviour of the grid-forming converters. Moreover, on average, the settling time is improved by 100 ms in the MPC-controlled system. Furthermore, the undershoot in DC-link voltage at MMC2 $v_{dc,MMC2}$ from rated DC-link voltage during the PP fault is higher compared to the undershoot during the PG fault.

6.3. CONCLUSION

In this chapter, a new MPC zero-sequence current control for the MMC converter is proposed, which influences the DC-link voltage control. The proposed control method controls the additive zero-sequence current component, and it can provide an extra window of 3 ms for fault detection or DC CB operation. This control is especially beneficial for a converter that directly influences the DC grid. The proposed control ensures the same energy absorption in the surge arrester during terminal PP and PG faults at the converter, which regulates the DC voltage of MT-HVDC. The proposed controller can also be added to the existing PI-controlled converter. However, the slower nature of the existing PI-control strategies causes a larger settling time of the DC-link voltage.

There is a trade-off between the DC-link voltage and the fault current. Based on the priority, suitable control constraints need to be set up. However, the implementation of this control reduces the time dependence on the protection algorithm, breaker operation, and fault current limiters by increasing the reaction time window. Hence, it provides more time for the proper reaction of the DC CB during the DC fault. Furthermore, the energy absorption during the fault is reduced. Therefore, the footprint of the DC CB is reduced, and thus, it provides a low-cost solution.

7

PREDICTIVE DC FAULT RIDE THROUGH FOR OFFSHORE MMC-BASED MT-HVDC GRID

This chapter presents a novel DC-FRTC for offshore MMC-based MT-HVDC grids, emphasizing its effectiveness in enhancing system stability during wind power ramp-ups. By developing a precise $3\,\mu s$ *time-step MTDC grid analytical model, the study validates the controller's reliability for predictive control strategies. The DC-FRTC significantly dampens frequency oscillations during PP faults, facilitates quicker recovery, and reduces the stress on DC circuit breakers. The analysis also demonstrates the controller's resilience to inter-station communication delays, underscoring its adaptability. Through comprehensive simulation results, the controller's potential to improve the reliability and efficiency of MTDC systems is demonstrated.*

7.1. BACKGROUND

As Europe confronts the increased level of energy demand and the need for carbon neutrality, TSOs are pivotal in transitioning towards sustainable energy infrastructures. The offshore MT-HVDC grids, favored for their efficient long-distance power transmission and superior control, represent a key technology in this shift. Central to MT-HVDC systems are HB-MMCs, which offer various configurations to optimize performance and cost. Despite their advantages, HB-MMC-based systems face challenges, particularly in managing DC faults effectively. Approaches like DC CBs require enhancements to address rapid fault detection and interruption.

Innovative solutions, such as FSC, have emerged, focusing on adjusting converter state variables to improve fault management. However, ensuring system stability during faults necessitates careful consideration of control strategies. The last chapter has addressed some of these challenges by implementing a setpoint-based strategy for fault current suppression, highlighting the need for advanced control methods to handle system reconfiguration post-fault. Thus, this chapter answers this challenge.

7.2. PROPOSED DC-FRT CONTROLLER

Figure 7.1 illustrates the proposed DC-FRT control strategy. The DC-FRT controller consists of four key elements:

- **A** - pre-fault interruption reference generator;
- **B** - fault suppression period reference generator;
- **C** - model predictive planner (MPP);
- **D** - circulating current suppression control.

The primary function of **A** is to monitor current and voltage measurements from both local and inter-station systems, providing a reference for **C**. Under normal conditions, the converter's current corresponds proportionally to the power injected or absorbed in the DC grid, maintaining an amplitude bound for operational transients. Upon exceeding this bound, indicating a fault, the reference generator in **A** freezes the last power (P_{ac} and Q_{ac}) set-point values. Consequently, **C** adjusts the converter currents back to pre-fault conditions utilizing **D** for FSC. The role of **B** is to project a new steady state for the system after the fault. **B** calculates when the internal converter protection is raised and DC protection information is communicated. The calculated value of **B** is applied to **C** when an acknowledged signal from the DC CB is available.

Central to the DC-FRT control is **C**, which processes the information from the reference generator and DC protection to compute a controlled signal for **D**. The aim is to mitigate the fault impact and bring efficiently the system to a new steady state. **D**, acting as a traditional CSCC, regulates the z-component of the summation current in the dqz frame based on references from **C**, with the output influencing the modulator. The detailed control strategy is outlined in algorithm 4 and visually represented in Figure 7.2, illustrating the controller's sequential actions.

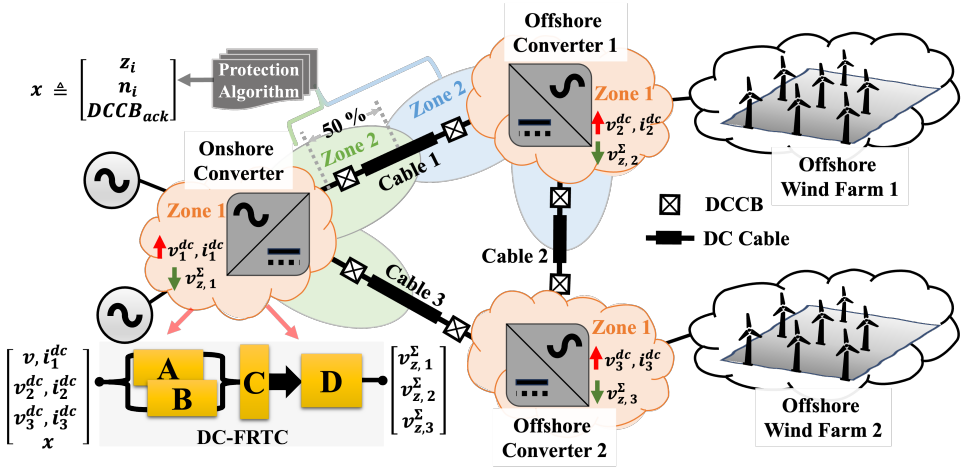

Figure 7.1: Proposed zone-based protection informed DC Fault Ride Through strategy, where **A**, and **B** are pre-fault interruption and fault suppression period reference generators, respectively. The **C** is a model predictive planner, and **D** is the dq frame circulating current suppression control (CCSC).

Algorithm 4 Zone-based protection informed DC Fault Ride Through strategy

INPUT: DC measurement point (v_i^{dc}, i_i^{dc}), fault zone (z_i), fault location (l_i), DC CB acknowledgement ($DCCB_{ack}$)
OUTPUT: Control actions and deblock signals

1: Detect fault by internal arm protection
2: Activate FCS via MPP with pre-fault interruption reference generator (**A**)
3: **while** Acknowledgement of fault interruption not received from DC CB **do**
4: Wait for acknowledgment
5: **if** No acknowledgement received **then**
6: Block the converter
7: **end if**
8: **end while**
9: **while** Information on fault location and distance is updated from the protection algorithm **do**
10: Generate a new reference using the fault suppression period reference generator(**B**)
11: **end while**
12: Receive an acknowledgement signal from the DC CB
13: Apply the newly generated references from the reference generator **B** to the MPP

7.2.1. DC EQUIVALENT MTDC GRID AND REFERENCE GENERATOR

The reference generator, **A, B**, can be modeled as a simplified distributed system model. A simplified model of the distributed system is considered to reduce the computation in

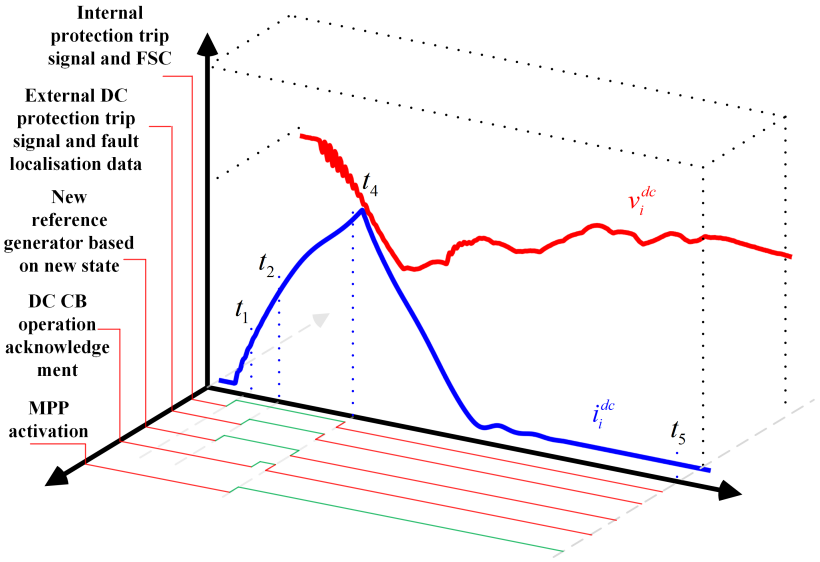

Figure 7.2: Graphical Illustration of the proposed DC fault ride through control.

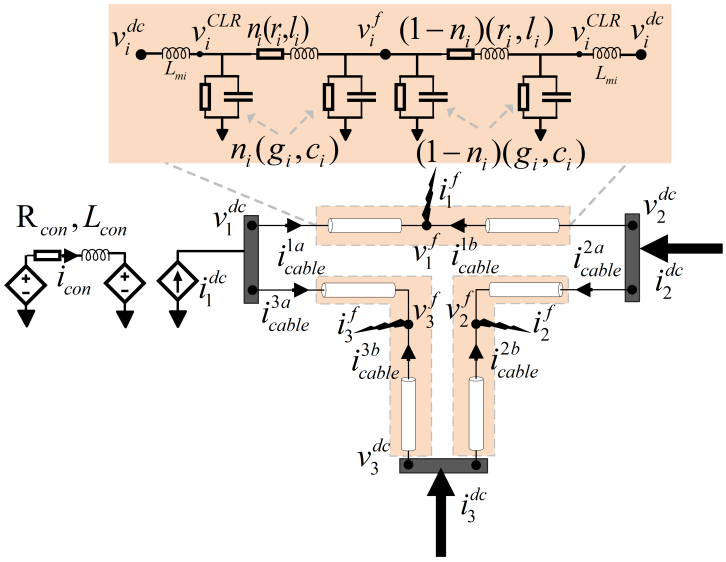

Figure 7.3: Simplified model of test network with π cable model and simplified converter model connected to node v_1^{dc}.

real-time simulation as described in [207]. Considering the three-terminal mesh grids

and applying KVL and KCL, we obtain the following:

$$\begin{aligned}\dot{\vec{V}}_{dc,f} &= \boldsymbol{C}^{-1}\vec{I}_{dc,f} - \boldsymbol{C}^{-1}\boldsymbol{I_m}^{T}\vec{I}_{cable} - \boldsymbol{C}^{-1}\boldsymbol{G}\vec{V}_{dc,f}\\ \dot{\vec{I}}_{dc,f} &= \boldsymbol{L}^{-1}\boldsymbol{I_m}\vec{V}_{dc,f} - \boldsymbol{L}^{-1}\boldsymbol{R}\vec{I}_{cable}\end{aligned} \tag{7.1}$$

$$\boldsymbol{R} = \text{diag}\{n_1 r_1,\ n_2 r_2,\ n_3 r_3,\ (1-n_1)r_1,\ (1-n_2)r_2,\ (1-n_3)r_3\} \tag{7.2}$$

$$\boldsymbol{L} = \text{diag}\{n_1 l_1,\ n_2 l_2,\ n_3 l_3,\ (1-n_1)\,l_1,\ (1-n_2)\,l_2,\ (1-n_3)\,l_3)\} \tag{7.3}$$

$$\boldsymbol{C} = \frac{1}{2}\,\text{diag}\left\{\begin{bmatrix} n_1c_1+(1-n_3)c_3 & 0 & 0\\ 0 & n_2c_2+(1-n_1)c_1 & 0\\ 0 & 0 & n_3c_3+(1-n_2)c_2\end{bmatrix}, \begin{bmatrix} c_1 & 0 & 0\\ 0 & c_2 & 0\\ 0 & 0 & c_3\end{bmatrix}\right\} \tag{7.4}$$

$$\boldsymbol{G} = \frac{1}{2}\,\text{diag}\left\{\begin{bmatrix} n_1g_1+(1-n_3)g_3 & 0 & 0\\ 0 & n_2g_2+(1-n_1)g_1 & 0\\ 0 & 0 & n_3g_3+(1-n_2)g_2\end{bmatrix}, \begin{bmatrix} g_1 & 0 & 0\\ 0 & g_2 & 0\\ 0 & 0 & g_3\end{bmatrix}\right\} \tag{7.5}$$

where, $\vec{I}_{cable} = [i^{1a}_{cable}, i^{2a}_{cable}, i^{3a}_{cable}, i^{1b}_{cable}, i^{2b}_{cable}, i^{3b}_{cable}]^T$, $\vec{V}_{dc,f} = [v_1^{dc}, v_2^{dc}, v_3^{dc}, v_1^f, v_2^f, v_3^f]^T$, and $\vec{I}_{dc,f} = [i_1^{dc}, i_2^{dc}, i_3^{dc}, i_1^f, i_2^f, i_3^f]^T$.

To provide fault information into the state-space representation of the MT-HVDC grid, a virtual node is set up, $v_i^f, \forall i \in 1,2,3$. Furthermore, i_i^{dc} and v_i^{dc} denote converter current and voltage at i node. The distance between the virtual node and the actual node (v_i^{dc}) is determined by the fault location algorithm described in section 7.3. This distance is defined by $n_i = [0,1]$. Considering the π-model of cable, the diagonal matrix is derived by Equation (7.5), where r_i, l_i, c_i and g_i are total resistance, inductance, shunt capacitance, and shunt conductance for cable. In this work, the mutual coupling between conductors is neglected for simplicity purposes.

The following case argument defines the incidence matrix,

$$\boldsymbol{I_m}(ix,n) = \begin{cases} 1, & \text{if } i^{ix}_{cable} \text{ is flowing from node } n\\ -1, & \text{if } i^{ix}_{cable} \text{ is flowing in node } n\end{cases} \quad \text{where, } n \in [1,\ 6] \text{ and } x \in a, b$$

By applying the above case argument to the above MT-HVDC with the assumed current direction, we can formulate the following incidence matrix:

$$\boldsymbol{I_m} = \begin{bmatrix} 1 & 0 & 0 & -1 & 0 & 0\\ 0 & 1 & 0 & 0 & -1 & 0\\ 0 & 0 & 1 & 0 & 0 & -1\\ 0 & 1 & 0 & -1 & 0 & 0\\ 0 & 0 & 1 & 0 & -1 & 0\\ 1 & 0 & 0 & 0 & 0 & -1\end{bmatrix}. \tag{7.6}$$

Rewriting Equation (7.1), a state-space representation of MT-HVDC grid is derived in the following classical form: $\dot{\vec{x}}_{net} = \boldsymbol{A_{net}}\vec{x}_{net} + \boldsymbol{C_{net}}\vec{u}_{net}$, $\vec{y}_{net} = \boldsymbol{B_{net}}\vec{x}_{net} + \boldsymbol{D_{net}}\vec{u}_{net}$, The $\boldsymbol{A_{net}}$, $\boldsymbol{B_{net}}$, $\boldsymbol{C_{net}}$, and $\boldsymbol{D_{net}}$ matrices can be formulated using (7.1) and given by: $\boldsymbol{A_{net}} = \begin{bmatrix} -\boldsymbol{C}^{-1}\boldsymbol{G} & -\boldsymbol{C}^{-1}\boldsymbol{I_m^T} \\ \boldsymbol{L}^{-1}\boldsymbol{I_m} & -\boldsymbol{L}^{-1}\boldsymbol{R} \end{bmatrix}$, $\boldsymbol{B_{net}} = \begin{bmatrix} \boldsymbol{C}^{-1} \\ \boldsymbol{\emptyset} \end{bmatrix}$, $\boldsymbol{C_{net}} = \boldsymbol{I}$, and $\boldsymbol{D_{net}} = \boldsymbol{\emptyset}$, where $\emptyset$ indicates the empty matrix and $\boldsymbol{I}$ indicates the identity matrix. The state variables are $\vec{x}_{net} = \begin{bmatrix} \vec{V}_{dc,f} & \vec{I}_{cable} \end{bmatrix}^T$, and control vector is $\vec{u}_{net} = \begin{bmatrix} \vec{I}_{dc,f} \end{bmatrix}$.

Considering the $v_{dc} - Q$ operation mode of the converter at v_1^{dc} terminal, while the other converters operate in power mode, the first element of input vector $\vec{u}_{net}$, can be written in terms of v_1^{dc}. Considering a steady-state condition, with converter dynamics described in [207], the state-space system equation can be written as $\dot{\vec{x}}_{sys} = \boldsymbol{A_{sys}}\vec{x}_{sys} + \boldsymbol{B_{sys}}\vec{u}_{sys}$ and $\vec{y}_{sys} = \boldsymbol{C_{sys}}\vec{x}_{sys}$, where $\vec{x}_{sys} = \begin{bmatrix} \vec{x}_{net} & i_{con} & \alpha & \beta \end{bmatrix}^T$, $\vec{u}_{sys} = \begin{bmatrix} v_1^{dc} & i_2^{dc} & i_3^{dc} & i_1^f & i_2^f & i_3^f \end{bmatrix}^T$, and

$$\boldsymbol{A_{sys}} = \begin{bmatrix} \boldsymbol{A_{net}} & \boldsymbol{A_{12}} \\ \boldsymbol{A_{21}} & \boldsymbol{A_{22}} \end{bmatrix}, \boldsymbol{B_{sys}} = \begin{bmatrix} \boldsymbol{B_{net}} \\ \boldsymbol{B_{21}} \end{bmatrix}, \boldsymbol{C_{sys}} = \boldsymbol{I},$$

$$\boldsymbol{A_{12}} = \begin{bmatrix} k_{con} & 0 & 0 \\ 0 & 0 & 0 \\ \vdots & \vdots & \vdots \\ 0 & 0 & 0 \end{bmatrix}_{12\times 3}, \boldsymbol{B_{21}} = \begin{bmatrix} k_{con} & 0 & 0 \\ \frac{(k_{p1}k_{p2})}{L_{con}} & 0 & 0 \\ k_{i2} & 0 & 0 \end{bmatrix}_{3\times 3}$$

$$\boldsymbol{A_{21}} = \begin{bmatrix} \frac{-(k_{p1}k_{p2})}{L_{con}} & 0 & \cdots & 0 \\ -k_{i1}k_{p2} & 0 & \cdots & 0 \\ -k_{i2} & 0 & \cdots & 0 \end{bmatrix}_{3\times 12}$$

$$\boldsymbol{A_{22}} = \begin{bmatrix} \frac{-(R_{con}+k_{p1})}{L_{con}} & \frac{1}{L_{con}} & \frac{k_{p1}}{L_{con}} \\ -k_{i1} & 0 & k_{i1} \\ 0 & 0 & 0 \end{bmatrix}_{3\times 3}.$$

The i_{con}, α, β are currents flowing in the inductance (L_{con}) and resistance (R_{con}) of the converter transformer, current and voltage controller state variables, receptively. The k_{p1} and k_{p2} are proportional gains of the inner and outer loops, respectively, whereas k_{i1} and k_{i2} are integral gains of the inner and outer loops, respectively. The $k_{con} = \frac{k}{C_{con}}$, k is linearlisation factor and equivalent capacitor, $C_{con} = \frac{6C_{sm}}{N_{sm}}$, where C_{sm} is the capacitance of the sub-modules and N_{sm} is the number of sub-modules of the converter.
The pre-fault interruption and fault suppression period reference generator is defined by $\vec{x}_{sys}$ and $\vec{y}_{sys}$, and the corresponding fault distance and location. This set of equations is solved using the forward Euler numerical integration method to reduce the computational complexity in the real-time simulator. Furthermore, the $DCCB_{ack}$ determines the selection between the reference generators.

7.2.2. MODEL PREDICTIVE PLANNER (MPP)

MPP is a model predictive control providing an optimized reference path to the internal state of each converter based on the fault occurrence. As the name indicates, the system's behavior determines the MPC's prediction and accuracy. The mathematical model of the network is represented by the state-space model and is rewritten in an augmented matrix discrete form for $\vec{x}_m(k) = \begin{bmatrix}\Delta\vec{x}_{net}(k) & \vec{y}_{net}(k)\end{bmatrix}^T$ as given in section 5.2.1:

$$\begin{aligned}\vec{x}_m(k+1) &= \begin{bmatrix}\mathbf{F}(T_s) & o^T\\ \mathbf{F}(T_s) & 1\end{bmatrix}\vec{x}_m(k) + \begin{bmatrix}\mathbf{G}(T_s)\\ \mathbf{G}(T_s)\end{bmatrix}\Delta\vec{u}(k),\\ \vec{y}_m(k) &= \begin{bmatrix}0 & \mathbf{I}\end{bmatrix}\vec{x}_m(k),\end{aligned} \tag{7.8}$$

where $k \in \mathbb{N}$ indicates discrete time step, whereas $\mathbf{F}(T_s) = e^{\mathbf{A_{net}}\,T_s}$ and $\mathbf{G}(T_s) = \mathbf{A_{net}}^{-1}\left(e^{\mathbf{A_{net}}\,T_s} - \mathbf{I}\right)\mathbf{B_{net}}$.

The future control sequence, $\Delta\vec{u} \in [-1,1]^3 \subset \mathbb{R}$, which is determined by solving the optimal control problem and minimizing the objective (cost) function, such that, change in network energy remains low at any given time. Which is then subjected to the equality and inequality constraints:

$$\begin{aligned}\min_{\Delta\vec{u}} J = \sum_{j=1}^{N_p-1} \left\|\vec{x}_m(k+j|k)\right\|^2_{\mathbf{Q}} + \left\|\Delta\vec{u}\right\|^2_{\mathbf{R}} + I_d e(k) + \left\|\vec{x}_m(k+N_p|k)\right\|^2_{\mathbf{Q_{LQR}}},\\ \text{subject to } \mathbf{M}\Delta\vec{u} \le \vec{b},\\ \vec{x}_m(k+j|k) = \vec{r}(k) - \vec{y}_m(k|k).\end{aligned} \tag{7.9}$$

where $\mathbf{Q}$ and $\mathbf{R}$ are given in Equation (7.11). Here, $l_i \in \{0.25, 0.5, 1\}$ and $z_i \in \{0.25, 0.5, 1\}$ are the arbitrary weighting factor that indicates the priority and control efford depending upon fault location and zone. These weight coefficients of the quadratic stage cost are given by the following algorithm 5. The influence of regions on the weight coefficients is depicted in Figure 7.4. Q_{LQR} is a weighing factor calculated using an implicit solver for discrete-time Riccati equations. The $N_p = 20 \in \mathbb{I}^+$ is the prediction horizon. For variables $\vec{x}_m(k)$, vector $r(k) \in \mathbb{R}^6$ is a reference signal provided by the reference generator. Matrix $\mathbf{M}$ and column vector $\vec{b}$ are related to the control rate and amplitude constraint information. In reality, there will be an error due to the modeling or signal noise. However, these disturbances can be considered in the optimal control problem, represented by $e(k)$. $e(k)$ denotes the error between the system's measured signal and the plant's predicted signal at k^{th} instance. $I_d > 0$ is the weight matrix.

7.3. FAULT IDENTIFICATION AND LOCATION ALGORITHM

In the presence of a fault, the proposed control architecture uses a fault distance, n_i to define the cable parameters, $\boldsymbol{R}$, $\boldsymbol{L}$, $\boldsymbol{C}$, and $\boldsymbol{G}$ (see Equation (7.5)). The calculated distance is also used for the weight selection criteria in MPC. The weight coefficients of the quadratic stage cost are defined with zones of fault location (see figure **??**). Therefore, it is essential to know the instant of the fault occurrence, its behavior, and its location.

Algorithm 5 Algorithm for weight coefficients of the quadratic stage cost

Require: $cable_i,\ n_i | i \in \{1,2,3\}$
Ensure: $z_i,\ l_i | i \in \{1,2,3\}$
Initialize $z_i, l_i = 0.25$ for all $i \in \{1,2,3\}$
for $i \in \{1,2,3\}$ **do**
  if $cable_i == 1$ **then**
    if $n_i < 0.4$ **then**
      $z_i = 1,\ l_i = 1,\ l_{(i \mod 3)+1} = 0.5$
    else if $0.4 \leq n_i \leq 0.6$ **then**
      $z_i = 0.5,\ z_{(i \mod 3)+1} = 0.5,\ l_i = 1,$
      $l_{(i \mod 3)+1} = 0.5,\ l_{((i+1) \mod 3)+1} = 0.5$
    else
      $z_{(i \mod 3)+1} = 1,\ l_i = 1,\ l_{(i \mod 3)+1} = 0.5$
    end if
  end if
end for

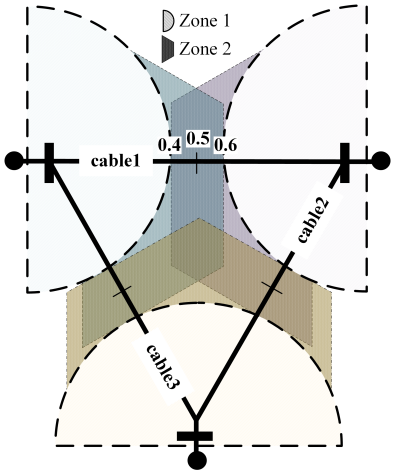

Figure 7.4: Illustration of control zones around three cables, indicating the varying influence regions for the weight coefficients in the quadratic stage cost function.

7.3.1. FAULT IDENTIFICATION

The externally placed CLRs act as impeccable fault differentiators, accumulating a large amount of energy upon the fault's inception. When the voltages across them at the positive and negative poles are measured in real-time and compared to a threshold, U_{oset} (specific to the system configuration and rating), then the fault occurrence is determined almost instantaneously [208].

$$\begin{cases} |v_{1p}^{dc}(t) - v_{1p}^{CLR}(t)| = |u_{1p}(t)| & (7.12) \\ |v_{1n}^{dc}(t) - v_{1n}^{CLR}(t)| = |u_{1n}(t)| & (7.13) \end{cases}$$

- PP fault: both Equation (7.12) & Equation (7.13) violate threshold, U_{oset};
- positive PG fault: only Equation (7.12) violates threshold, U_{oset};

$$\boldsymbol{Q} = \text{diag}\left\{ \begin{bmatrix} l_1 r_1 & 0 & 0 \\ 0 & l_2 r_2 & 0 \\ 0 & 0 & l_3 r_3 \end{bmatrix}, 0.1\boldsymbol{I}_{3\times 3}, \begin{bmatrix} l_1 c_1 & 0 & 0 \\ 0 & l_2 c_2 & 0 \\ 0 & 0 & l_3 c_3 \end{bmatrix}, 0.1\boldsymbol{I}_{3\times 3} \right\}, \quad (7.10)$$

$$\boldsymbol{R} = \text{diag}\left\{ \begin{bmatrix} z_1 r_1 & 0 & 0 \\ 0 & z_2 r_2 & 0 \\ 0 & 0 & z_3 r_3 \end{bmatrix}, 0.1\boldsymbol{I}_{3\times 3} \right\} \quad (7.11)$$

- negative PG fault: only Equation (7.13) violates threshold, U_{oset}.

7.3.2. FAULT LOCATION

The subsection explains the time-domain-based evaluation of the fault distance for a PP fault between terminals 1 and 2 (see Figure 7.3). Here $v_1^{dc}(t)$ and $v_2^{dc}(t)$ are the terminal DC bus voltages, $i_{cable}^{1a}(t)$ and $i_{cable}^{1b}(t)$ are the currents from terminals 1 and 2 respectively. In contrast, $v_1^{CLR}(t)$ and $v_2^{CLR}(t)$ are the voltages after CLRs, L_{m1} and L_{m2}. $v_1^f(t)$ is defined as the voltage across the fault resistance whereas n_1 is defined as the percentage fault location for cable 1 with unit length. Using simplified R-L representation, r_1 is the resistance per unit length, whereas l_1 is the inductance per unit length of cable 1. For a PP fault, Equation (7.14)- (7.15) are obtained with the application of Kirchoff Voltage Law (KVL) from terminals 1 and 2.

$$2r_1 n_1 i_{cable}^{1a}(t) + 2l_1 x_1 \frac{di_{cable}^{1a}(t)}{dt} + v_1^f = v_1^{CLR}(t) \tag{7.14}$$

$$2r_1(1-n_1) i_{cable}^{1b}(t) + 2l_1(1-n_1) \frac{di_{cable}^{1b}(t)}{dt} + v_1^f = v_2^{CLR}(t) \tag{7.15}$$

The current derivative terms can be obtained using the voltage drop across the CLR, avoiding additional WGN due to differential calculations. These terms are $\frac{di_{cable}^{1a}(t)}{dt} = \frac{v_1^{dc}(t) - v_1^{CLR}(t)}{2L_{m1}} = \frac{u_1(t)}{2L_{m1}}; \frac{di_{cable}^{1b}(t)}{dt} = \frac{v_2^{dc}(t) - v_2^{CLR}(t)}{2L_{m2}} = \frac{u_2(t)}{2L_{m2}}$. Subtracting Equations (8) and (9) negates the dependence of fault location on fault resistance. Further, substituting and rearranging them give n_1 as

$$n_1 = \frac{\left[v_1^{CLR}(t) - v_2^{CLR}(t)\right] + 2r_1 i_{cable}^{1b}(t) + \frac{l_1}{L_{m2}} u_2(t)}{2r_1\left[i_{cable}^{1a}(t) + i_{cable}^{1b}(t)\right] + \frac{l_1 u_1(t)}{L_{m1}} + \frac{l_1 u_2(t)}{L_{m2}}} \tag{7.16}$$

Similar expressions can be derived for n_2, $n_3 \ldots n_i$ [209]. The implemented time-domain fault location reduces the computation burden. It complements the nature of the MPC, which uses an optimized reference path to the internal state of each converter based on the fault location information.

7.4. TEST MESH OFFSHORE MMC-MTDC GRID

A three-terminal bipolar metallic return MMC-HVDC network is used to test the proposed control strategies, utilizing the RTDS© simulator. The system parameters and operating mode are detailed in table 7.1, with the setup explained in Chapter 4. The control loop framework of the converters is depicted in Figure 7.5 and has been explained in Chapter 3, 4.

The DC-FRTC is implemented on a separate RTDS© NovaCor chassis, simulating an external controller's role in the setup. This setup provides a comprehensive environment to validate and refine various DC-FRT strategies, ensuring robust and efficient performance of the HVDC system under test conditions.

Table 7.1: Control mode and parameter of test HVDC system

Parameter	Converters		
	CSA 1	CSA2	CSA3
Active power [MW]	2000	2000	2000
Control mode	Vdc-Vac	Vac-f	Vac-f
Reactive power [MVAR]	-	-	-
Number of Submodules per arm	240	200	200
MMC arm inductance [mH]	25	49.7	49.7
Transformer leakage reactance [pu]	0.18	0.15	0.15
AC Point of couple voltage [kV]	400	220	220
DC-link Voltage [kV]	±525		
Rated power [MVA]	2000		
Capacitor energy in a submodule (SM) [MJ]	30		
MMC arm resistance [Ω]	0.544		
Rated voltage/current of each SM [kV/kA]	2.5/2		
AC converter bus voltage [kV]	275		
Wind farm AC Point of couple voltage [kV]	66		

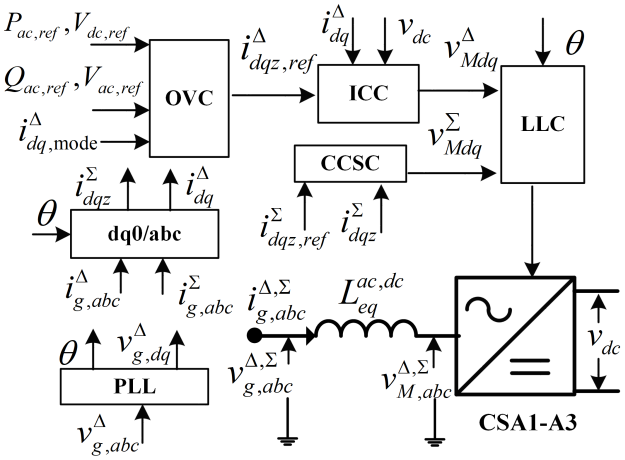

Figure 7.5: Generic block diagram representation of MMC converter control loops.

7.5. SIMULATION RESULTS

7.5.1. VALIDATION OF DC-SIDE EQUIVALENT CIRCUIT

To anticipate the DC grid's behavior accurately, the analytical model employed in the MPP must exhibit precise performance under steady-state conditions and during

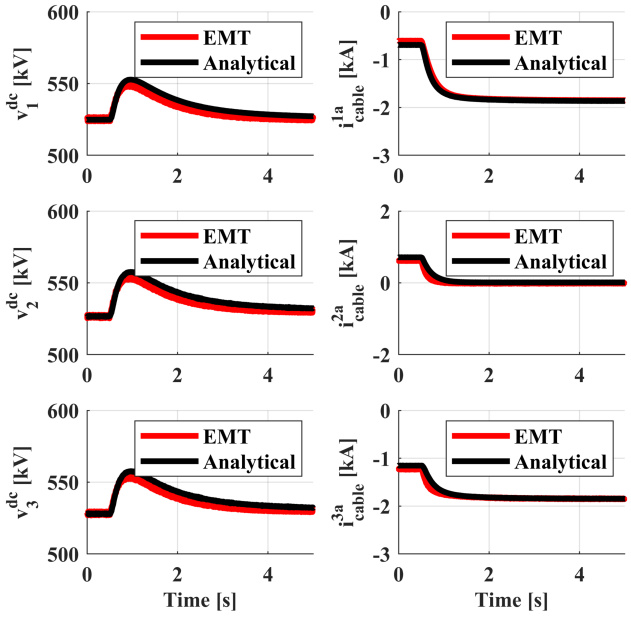

Figure 7.6: Comparison of EMT DC grid and DC side equivalent circuit model under wind power changed from 100 MW to 2000 MW.

significant disturbances. Figure 7.6 illustrates the performance of the analytical model derived from Ordinary Differential Equation (4), validated by detailed Electromagnetic Transient (EMT) simulations during a wind power variation from 100 MW to 2000 MW. The analytical model, implemented through C-builder [168] with a time step of $3\mu s$, clearly shows the system's dynamics. Notably, the wind power alteration initiates at 0.5 s, leading to a change in the DC cable currents according to the new power flow in the DC grid. The analytical model exhibits high conformity with the EMT models across various phases - before, during, and after the disturbance. This alignment underscores the analytical model's performance in predicting the dynamic behavior of the DC grid, establishing its credibility for advanced control law design.

7.5.2. DC CABLE FAULT

Figure 7.7 illustrates the performance of cable 1 under a PP fault in the middle of cable 1, both with and without integrating a proposed controller. Without the controller, the terminal voltages and currents exhibit a dominant frequency oscillation of 100 Hz after the fault clearance by DC CBs 1a and 1b. This persistent oscillation lasts for more than 100 ms, as evident in Figure 7.7 (a)-(f). The recovery process is expedited by introducing a fast-acting DC CB. Similar can be achieved following the method outlined in [126], where converters are blocked, and an AC breaker, necessitating DC grid re-energization, accomplishes fault clearance.

Upon fault removal by the DC CB, a substantial current swing occurs with a reversal at offshore converters, resulting in a higher rate of rise of converter current during the interruption period. This stresses the DC CB at the terminal's end, and is observed

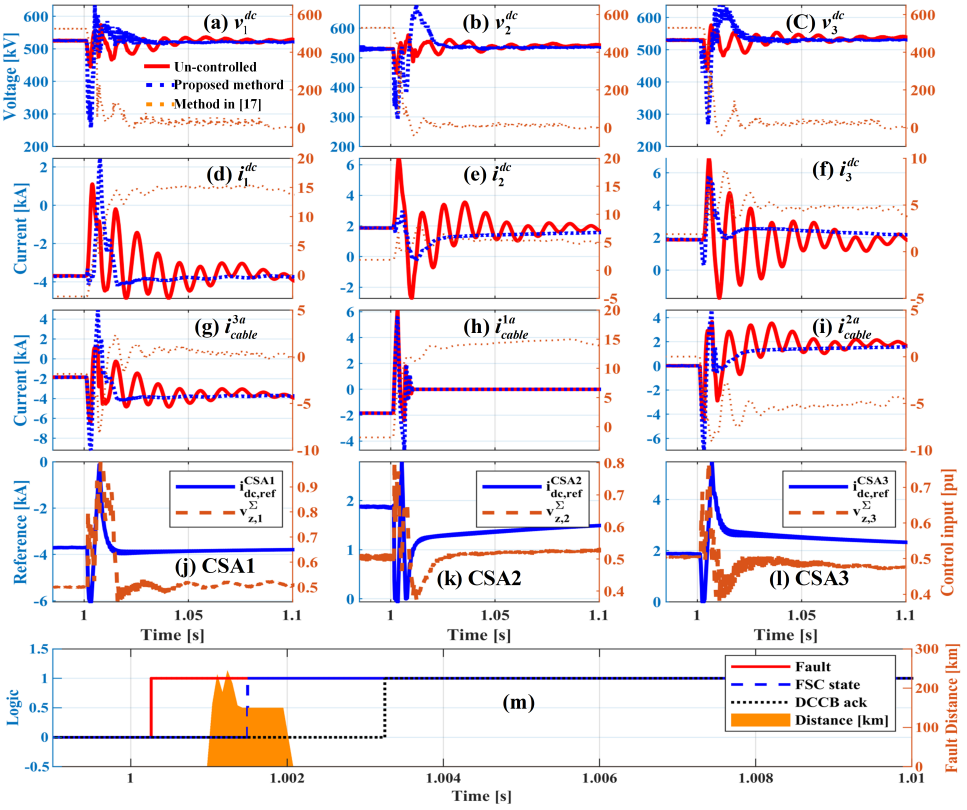

Figure 7.7: PP fault with a fault resistance of 0.01 Ω at the middle of the cable 1. (a)-(c) and (d)-(f) shows converter voltages and currents, (j) - (l) are reference currents generated by MPP and corresponding control actions and (m) is the internal and external protection operation.

through the elevated energy stored in DC CB surge arresters, detailed in Table 7.2a.
The implementation of the DC-FRTC yields a notable improvement. The dominant frequency oscillations in voltage and current are effectively suppressed. Upon triggering the internal protection of the converter, FSC is activated at 1.0015 s. This activation prompts a reference change at CCSC via MPP, as depicted in Figure 7.7 (j)-(l). The primary goal of this reference adjustment is to minimize the converter current rate, subsequently reducing the rate of rise of fault current, as shown in Figure 7.7 (h). The regulation of the DC-link voltage at each converter terminal achieves this control, as illustrated in Figure 7.7 (a)-(c).
Simultaneously, as FSC is activated, the protection algorithm calculates the fault distance and provides a trip command to the DC CBs, as seen in Figure 7.7 (m). The computed distance and localization information are relayed to the reference generator (**B**) and MPP. Following a successful fault interruption by the DC CB, a confirmation signal triggers changes in the weight matrices of the MPC, leading to the use of a new reference (**B**). Consequently, the converter current follows a non-oscillatory optimal

Table 7.2: Comparison with and without DC FRT controller during a PP fault

(a) PP-0-cable1

PP-0-cable1	Converter Current	Dominated frequency [Hz]	$\frac{di}{dt}$ at t= 1.004 s [kA/ms]	Settling Time [ms]	Peak value [kA]	Energy absorbed in DC CB 1a [MJ]	Energy absorbed in DC CB 1b [MJ]
Without DCFRT	i_1^{dc}	100	0.407	118	3.697	5.87	9.69
	i_2^{dc}	100	0.525	145	4.198		
	i_3^{dc}	100	0.337	133	5.77		
With DCFRT	$i^d c_1$	-	0.133	15	3.627	3.5	7.708
	$i^d c_2$	-	0.111	12	2.975		
	$i^d c_3$	-	0.005	15	5.615		

(b) PP-50-cable1

PP-50-cable1	Converter Current	Dominated frequency [Hz]	$\frac{di}{dt}$ at t= 1.004 s [kA/ms]	Settling Time [ms]	Peak value [kA]	Energy absorbed in DC CB 1a [MJ]	Energy absorbed in DC CB 1b [MJ]
Without DCFRT	i_1^{dc}	100	0.650	118	4.467	3.3	11.69
	i_2^{dc}	100	1.133	144	6.359		
	i_3^{dc}	100	0.294	164	6.86		
With DCFRT	i_1^{dc}	-	0.038	16	4.859	2.27	7.90
	i_2^{dc}	-	0.071	15	2.930		
	i_3^{dc}	-	0.001	20	5.800		

(c) PP-100-cable1

PP-100-cable1	Converter Current	Dominated frequency [Hz]	$\frac{di}{dt}$ at t= 1.004 s [kA/ms]	Settling Time [ms]	Peak value [kA]	Energy absorbed in DC CB 1a [MJ]	Energy absorbed in DC CB 1b [MJ]
Without DCFRT	i_1^{dc}	100	0.545	118	4.984	1.47	15.06
	i_2^{dc}	100	1.372	145	7.365		
	i_3^{dc}	100	0.337	165	5.873		
With DCFRT	i_1^{dc}	-	0.190	16	4.626	1.16	10.39
	i_2^{dc}	-	0.111	12	2.585		
	i_3^{dc}	-	0.067	10	5.665		

trajectory, exhibiting a faster settling time than scenarios without a controller, as shown in table 7.2a.

Moreover, the MPP enforces control amplitude constraints of [-6 kA +6 kA] on

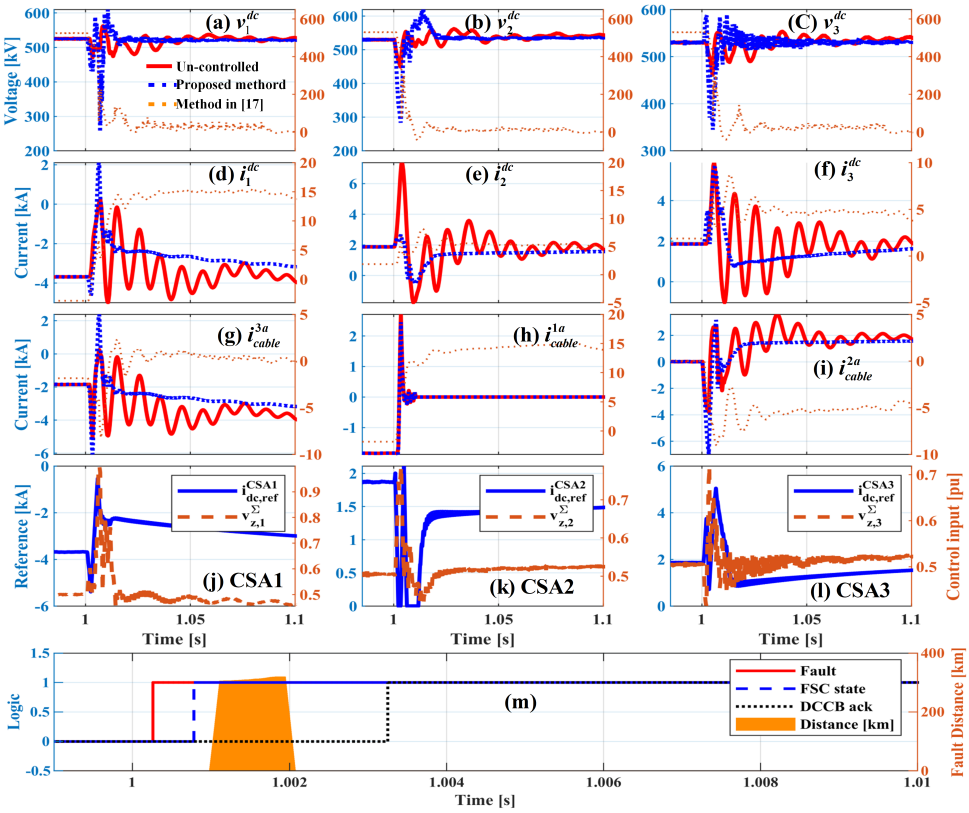

Figure 7.8: PP fault with 0.01 Ω fault resistance near CSA2 terminal. (a)-(c) and (d)-(f) show converter voltages and currents, (j) - (l) are reference currents generated by MPP and corresponding control actions, and (m) is the internal and external protection actions.

the onshore converter and [0 kA 6 kA] on the offshore converter. All converters maintain a controlled rate amplitude of 0.2 kA/ms, preventing offshore converters from experiencing current reversal. Despite observing overvoltage during the recovery process, it remains within the acceptable limit of the cable overvoltage profile [210], [211]. During FSC activation, a significant current amplitude is noted, attributed to the redistribution of energy from the faulty segment, resulting in less energy absorption in the DC CB and safeguarding its energy absorption element, as mentioned in Table 7.2b. Similarly, for a PP fault at the DC terminal of converter CSA2, the DC-FRTC provides a damped and controlled response. The early activation of FSC, as shown in Figure 7.8, holds for PP faults at the DC terminal of converter CSA1.

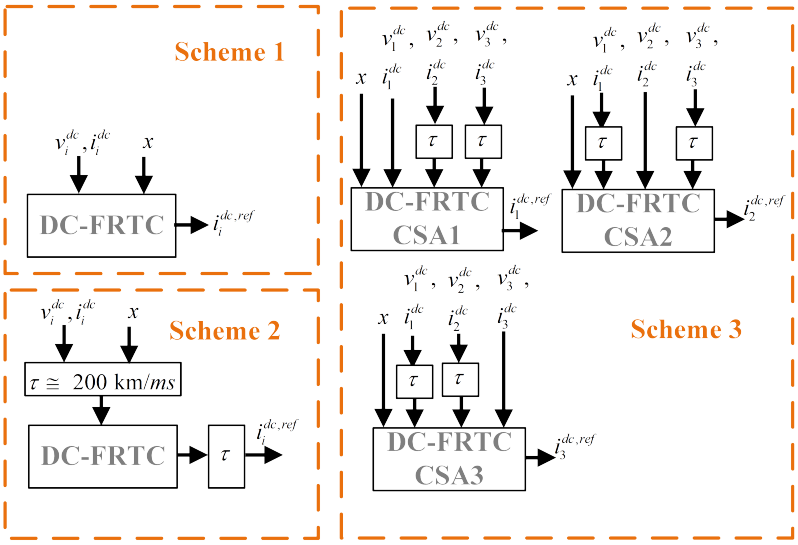

Figure 7.9: Different DC-FRTC Schemes

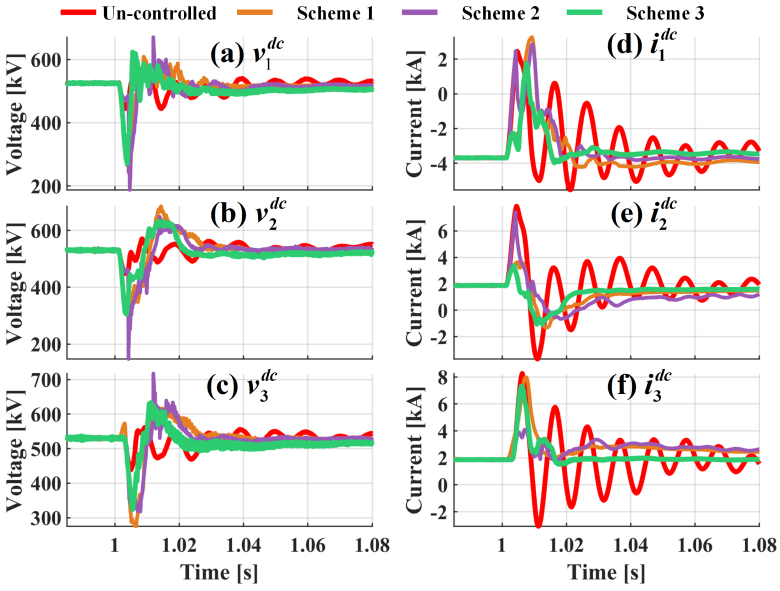

Figure 7.10: DC fault recovery for different Schemes.

7.5.3. DIFFERENT DC-FRTC SCHEME

Three distinct schemes have been scrutinized to assess the impact of communication delay (τ) on system performance, as illustrated in Figure 7.10. So far DC -FRTC does not include the influence of communication delay caused by intra-station measurement signals and external protection signals. This DC-FRTC is denoted as scheme 1 in Figure

7.10. However, real-world conditions introduce a communication delay, set at 200 ms/km in this study [127].

In response to this delay, two additional schemes have been proposed. Scheme 2 involves a centralized configuration with communication delays affecting both input and output signals, while Scheme 3 employs a decentralized approach with delays particularly dedicated on external signals.
In Scheme 1, the DC-FRTC is centrally located, receiving converter voltages and currents from stations 400 km away, resulting in a 2 ms delay. This delay also applied to information provided by the DC protection algorithm. Consequently, a delayed response by the controller is depicted in Figure 7.10. During the initial 2 ms delay, all converters follow an uncontrolled trajectory. However, upon data reception, the MPP algorithm implements corrective measures, regulating converter currents and restoring the system to its optimal course of operation. Despite the introduced delay, Scheme 1 exhibits a robust response compared to an uncontrolled system.

Scheme 2 represents a scenario where DC-FRTC is embedded at each converter station, receiving measurements from other converters with delays corresponding to the inter-station distances. Leveraging local measurements, DC-FRTC can swiftly react to internal protection events, activating the FSC. The DFRTC, based on historical measurements and protection information, provides a trajectory for each converter, facilitating a rapid system recovery, as illustrated in Figure 7.10. Moreover, this scheme furnishes a backup control signal for the converters in the DC grid, ensuring an N-1 contingency. This feature is proved to be pivotal in multi-vendor scenarios, enhancing overall system reliability.

7

7.6. CONCLUSION

This chapter proposed a protection zone-informed predictive DC Fault Ride Through Controller (DC-FRTC). The results highlight that the modified DC side equivalent circuit model can accurately represent the MTDC grid's dynamics, especially during wind power ramping, validating its utility for advanced control algorithms. The key findings of this chapter include:

- A $3\mu s$ time-step MTDC grid-analytical model in C-builder closely matching the real-time simulation model, confirming its credibility for control law formulation.
- DC-FRTC enhances system stability under PP faults by damping dominating frequency oscillations in DC-side voltage and current, facilitating faster-guided recovery.
- DC-FRTC effectively reduces stress on DC circuit breakers by suppressing converter current peaks and improving system reliability.
- Different DC-FRTC schemes, both centralized and decentralized, demonstrate resilience against inter-station communication delays, proving the controller's adaptability and fidelity.

8

CONCLUSION

8.1. MAIN CONCLUSION

In the 21^{st} century, different new technologies like HVDC ones will make part of the future power grids. HVDC technology becomes a backbone for the integration of large intermittent renewable energy resources in geographically separated areas. A global shift toward 100 % renewable energy to tackle the Paris Climate Agreement conclusions requires the integration of power electronic-based renewable sources. The decommissioning of conventional power generation is and will create system-wide inertia problems. This makes HVDC technologies more welcome due to their fast response to inertia decay matters. In any HVDC technology, at the heart is the control system; faster, intelligent, and interoperable control algorithms, together with protection, will play a vital role in future power systems. Following this, the thesis focuses on, and answers the main research question "***how to develop and implement advanced controls to ensure fast, robust, and stable near real-time operation of large offshore multi-terminal HVDC grids***."

Addressing the main research question requires a detailed look into several key factors of HVDC technology. These factors include the design of intelligent advanced control algorithms, the development of real-time simulation models and control strategies for fault management. Each of the following sub-research questions has explored these areas, aiming to uncover solutions that contribute to the fast, robust, and stable operation of large offshore multi-terminal HVDC grids essential for the future of renewable energy integration.

RQ1. WHAT KIND OF INTELLIGENT CONTROL ALGORITHM CAN ENSURE CONTINUOUS STABLE AND EFFICIENT ENERGY TRANSMISSION IN LARGE-SCALE OFFSHORE WIND FARMS CONNECTED THROUGH HVDC GRIDS?

Chapter 3 and 5 explore the development of MMCs and their control strategies, mainly through a perspective of MPC offering substantial advancements in the response, robustness, and operational stability of HVDC transmission systems. The journey from traditional power converters (i.e., LCC and 2-Level) to MMCs marks a significant leap toward addressing the inherent limitations of previous technologies. With a focused analysis of the HB-SM, this thesis underscores the evolution of MMCs as a cost-effective solution for high-power applications.

An in-depth investigation of the core control functions of MMC units shows a complex hierarchy of control loops essential for maintaining stable operations during scheduled and unscheduled events between analytical and real-time MMC models shows the excellent performance of analytical models, especially during transient conditions where rapid system changes pose significant challenges. Despite simplifications, such as omitting the 6^{th} harmonic content in analytical models, the error margins remain below 5%, affirming the analytical approach's validity for advanced control and development purposes.

With the input from Chapter 3, Chapter 5 introduces a detailed examination of a variant of MPC, utilizing Laguerre's function for discretizing MMC, signifying a low computation in control strategy formulation. This approach optimizes active and

reactive power setpoints. It demonstrates reduced overshoot and enhanced stability through online optimization by achieving an exact solution to differential equations and considering both constrained and unconstrained scenarios.

The computational efficiency, minimal prediction horizon, model stability, sample time selection, weighting factor, and Laguerre's pole highlight the MPC's potential as a suitable candidate for real-time simulation and testing. Furthermore, implementing MPC in a complex system like an MT-HVDC grid connecting intermittent power sources and grid strengths showcases its superior performance in managing fast transients, such as AC and DC faults, with minimal impact on terminal voltages. The comparative analysis with traditional PI-control methods reveals MPC's advantages in providing faster, more reliable power support and enhanced voltage stability during nominal and disturbed conditions. The scalability of MPC from single to multi-terminal configurations with minimal tuning underscores its adaptability and efficiency in diverse operating scenarios.

In conclusion, integrating advanced control strategies, particularly MPC, into the design and operation of MMC-based HVDC systems signifies a vital advancement in addressing the dynamic challenges of future power transmission. The findings from this comprehensive study not only validate the theoretical and practical superiority of MPC over conventional control methods but also pave the way for future research and development in enhancing the resilience and efficiency of power systems. The ability of MPC to ensure rapid, stable, and efficient response under a wide array of disturbances and operating conditions heralds a new era in optimizing HVDC transmission systems, promising significant improvements in the integration of renewable energy sources and the overall reliability of the power grid.

RQ2. HOW CAN RTS BE OPTIMIZED TO MODEL CRITICAL EVENTS IN OFFSHORE MT-HVDC GRIDS, ENSURING COMPUTATIONAL EFFICIENCY AND PRACTICAL ADAPTABILITY?

Chapter 4 introduces and evaluates comprehensive real-time MT-HVDC models that integrate real-time wind profile feedback, marking a crucial step towards understanding and improving the lifecycle management of HVDC projects. These models are tailored to meet the specific system ratings the North Sea grid operators require, ensuring their relevance and applicability to current and future offshore HVDC grids.

By overcoming the limitations of existing network models, the chapter provides detailed parameters for DMR for both sea and land cables, thereby enhancing the accuracy of the simulations. The models' ability to script system and control parameters for quick perturbation and sensitivity studies significantly reduces the modeling time, making the simulation process more efficient and effective. Including average value models for wind farms allows for a nuanced exploration of the complex dynamics and interactions between wind farms and the HVDC grid, a critical aspect for ensuring grid stability and reliability. This model also incorporates the high-voltage DC circuit breaker, and its interaction with the converter and cable.

The performance evaluation of these models through scenarios such as unscheduled events, startup, and black start events has revealed their robustness in managing disturbances and ensuring stable grid operations. This demonstrates the models'

capability to support HVDC components' design and protection studies by identifying potential stress points and areas susceptible to disturbances, especially during critical operations like black start sequences.

Furthermore, Chapter 4 highlights the computational requirements of each network model, guiding users to select the most appropriate model based on their specific needs. This aspect is particularly beneficial for manufacturers and system operators, enabling them to balance between computational demands and the depth of simulation required for accurate studies. The chapter also outlines the potential future studies and applications of the proposed real-time network models, emphasizing their role in aiding component design, system calculations, and operator training. These models provide a solid foundation for technical studies and control system design and serve as a valuable resource for developing the skills and knowledge necessary for managing future HVDC grids.

In answering the research question, this chapter concludes that the development of real-time simulation models for offshore MT-HVDC grids, as presented, significantly enhances the interoperability of control and protection strategies. By providing a detailed, accurate, and computationally efficient modeling approach, these models facilitate a better understanding and management of the complex interactions within offshore HVDC grids. Consequently, they contribute to the advancement of more efficient, reliable, and resilient HVDC grids, capable of supporting the integration of renewable energy sources and meeting the dynamic demands of the energy sector.

RQ3. How can advanced control strategies ensure active fault current suppression for the system with large-scale offshore wind integration?

Integrating large-scale offshore wind power into the MT-HVDC grid presents unique challenges, particularly in managing DC-side fault current in a grid equipped with HB-MMCs. The question of how advanced control strategies can ensure active fault current suppression in such grids has been comprehensively explored in Chapter 6, focusing on the potential of MPC-based strategies.

The investigation reveals that MPC-based control (proposed in Chapter 5), specifically the novel MPC zero-sequence current control strategy proposed for HB-MMC converters, effectively solves the challenge of fault current suppression in MT-HVDC grids. This approach directly influences the DC-link voltage control, enhancing the system's ability to manage DC-side fault currents efficiently. By controlling the additive zero-sequence current component, the proposed strategy offers an additional window of 3 ms for fault detection or DC CB operation, significantly improving the system's responsiveness to faults. The effectiveness of this control strategy is in the active control of the rate of rise of the fault current in HB-MMC-based MT-HVDC grids, thereby reducing the operational stress on DC CBs and enhancing fault recovery mechanisms. It seamlessly integrates with existing control loops, ensuring system stability without compromising performance. Furthermore, implementation and analysis of these control strategies in real-time simulations provide empirical evidence of their effectiveness for real-world applications.

In conclusion, the MPC-based control strategy addresses the open questions

regarding active fault current suppression in the MT-HVDC grid with large-scale offshore wind integration. It marks a significant advancement in the field.

RQ4. HOW CAN A ZONAL DC FAULT RIDE-THROUGH SCHEME BE DEVELOPED FOR OFFSHORE MT-HVDC GRIDS?

Chapter 7 proposes a Zonal DC Fault Ride-Through (DC-FRT) scheme to enhance the resilience and reliability of offshore MT-HVDC grids during DC faults. Introducing a protection zone-informed predictive DC-FRTC represents a significant advancement towards achieving this goal. The proposed scheme effectively addresses the challenges outlined in the research question, particularly focusing on reducing the operational and economic impacts of converter blocking and system recovery and diminishing the reliance on high-speed inter-station communication.

The key achievements of this research comprises:

- The development of a 3 μs time-step MTDC grid analytical model, implemented in C-builder, that closely matches real-time simulation models. This model validates the feasibility of formulating advanced control laws based on the precise dynamics of MTDC grids, especially under conditions of wind power ramping.

- Demonstrate system stability enhancement under PP faults through the DC-FRTC's ability to damp dominating frequency oscillations of DC-side voltage and current. This facilitates a faster and more guided recovery process, directly addressing the need for improved fault ride-through capabilities.

- By incorporating the concept presented in Chapter 6 in DC-FRTC, there is a significant reduction in stress on DC circuit breakers by suppressing converter current peaks. This improvement in system reliability is critical for minimizing economic and operational impacts during fault conditions.

- Evaluating different DC-FRTC schemes, both centralized and decentralized, showcases the controller's resilience against inter-station communication delays. This controller attribute proves its adaptability and fidelity, ensuring reliable fault management despite communication challenges.

The proposed Zonal DC-FRT scheme, underpinned by the predictive DC-FRTC, marks a paradigm shift in managing DC faults within offshore MT-HVDC grids. By leveraging local measurements and converter limits for continuous setpoint adjustment, this research tackles the immediate challenges of fault interruption and system recovery. It paves the way for smoother and damped post-fault recovery. The predictive nature of the DC-FRTC, coupled with its demonstrated resilience against communication delays, offers a robust solution that minimizes the reliance on high-speed inter-station communication, thereby enhancing the overall reliability and stability of the offshore MT-HVDC grids. Furthermore, the proposed Zonal DC-FRT scheme can also be extended to onshore MT-HVDC as it uses information about network topology and operating control models to determine power flow. However, the constraints used for optimization can be adjusted based on the location of the converter.

In conclusion, the research question has been addressed by developing a protection zone-informed predictive DC-FRTC, significantly enhancing offshore MT-HVDC grids' DC fault ride-through capabilities. This scheme effectively mitigates the operational and economic challenges associated with DC faults, ensuring a resilient and reliable power supply from offshore wind sources.

ACKNOWLEDGEMENTS

It feels like just yesterday that I completed my master's defense and embarked on the journey of research. It's true what they say—time flies when you're having fun. I must confess that I thoroughly enjoyed the scientific research and activities throughout my PhD. The past four years have been a cycle of excitement and setbacks, but they have also been transformative. This PhD journey not only shaped me as a researcher but also offered significant opportunities for personal growth. Along this adventure, I was fortunate to have the support of incredible people who guided and inspired me.

My curiosity about electricity began early, sparked when I accidentally shorted an AC power plug. My cousin, Anant, explained why that happened, introducing me to concepts like KCL and KVL in circuit theory. He guided me on how to simplify and solve complex electrical circuits. This experience planted a seed in me—the desire to find simple solutions to complex problems. I want to thank him for guiding me during my high school and engineering years. I also want to thank my big brother and friend, Dr. Abhijit, who has been a role model and a guide throughout both my personal and PhD journey. It's easy to get lost in the PhD process, but talking with him always renewed my motivation.

Moving to the Netherlands meant leaving friends behind, but distance is just a number when you're close to someone in spirit. That's exactly how I feel about my two friends in Goa, Rohit and Tanay. Thank you for being true friends. Whenever we meet, it's as if I never left Goa. They say people change with time, but not these two. They have always made me feel at home. I also want to thank my friends in Delft, with whom I shared so many memorable experiences and travels. A special thanks goes to my (ex-) roommates in Delft, Shashank and Aron, who witnessed the peaks and valleys of my PhD and personal life. Your support and companionship were invaluable throughout this journey. Thank you, guys, for being there.

First and foremost, I would like to express my deep gratitude and respect to my supervisor, Dr. Aleksandra Lekić. The first time we met was virtually during my PhD interview. The pandemic was a challenging period, especially when you lack face-to-face interaction, but Aleksandra's constant support ensured that my research remained on track, allowing me to complete my work in a timely manner. Although the control area was new to me, Aleksandra helped me focus on the most relevant topics and guided me throughout my PhD journey. She also provided me with unique opportunities to collaborate with others and share my ideas with a wider audience. I'm grateful for the freedom she gave me to conduct my own research within a well-defined framework. Thank you, Dr. Aleksandra Lekić, for being both a supervisor and a colleague. I am confident that our paths will cross again, and I look forward to future collaborations.

I would also like to express my deepest gratitude to my promotor, Prof. Dr. Ir. Marjan Popov. I first encountered Marjan during a master's course in 2018. His energetic and motivating teaching style led me to enroll in three more of his courses. At a certain point,

I was uncertain about which area to pursue, so I expressed my interests in 'breakers,' 'power electronics,' and 'simulation' to Marjan. He suggested, 'Gent, I have an EU project called PROMOTioN; it involves state-of-the-art DC breakers and would be a fantastic opportunity for you.' This conversation sparked my deep interest in HVDC, which eventually became the focus of my master's thesis. The COVID period was particularly difficult, but with Marjan as my supervisor, I was able to complete my thesis on time, with an iconic COVID handshake. I'm fortunate to have had him as my promotor during my PhD as well. Not only did he provide critical support in my research, but he also cared about my mental well-being and overall success. I always appreciated our encounters in the 3rd-floor corridor, where he would ask, 'Gent, how are you doing?'—even on rough days, his words had a calming effect and helped me persevere. Thank you, Marjan, for all the life hacks and great moments we've shared over the years. I am certain that this is just the beginning of our long-term collaboration and friendship.

Finally, I would like to thank my promotor, Prof. Dr. Ir. Peter Palensky, for his excellent support and for shaping my research. Peter consistently supported my work and motivated me to focus on finding significant scientific contributions, particularly in the early stages of my research. I have always admired his attention to detail and his forward-thinking vision for the power systems field. I would also like to thank my external thesis committee for their invaluable feedback, which significantly improved the quality of my thesis.

A big shoutout to my friends and colleagues in the IEPG section. Nisdarshan and Zameer, thank you for demonstrating the power of real-time simulation and for our coffee breaks that were always a highlight. To my office mates—Enshia, Neda, and Dimitri—thank you for the great company, positive energy, and countless memorable conversations. Special thanks to Nanda for being such a helpful friend and for organizing fun activities both in the Netherlands and during our USA trip. I would also like to extend my gratitude to Haiwei, Vetri, Shengren, Mert, Kutay, Ali, Farzad Dehghan Marvasti, Reza, Farzad Nasirpour, Milan, Ties, Wouter, Zeynab, Behzad, Ioannis, Aleksandar, Dong, and Nikolina. Your contributions have greatly enriched my academic and personal experiences. Furthermore, many thanks to my other numerous TU Delft and IEPG colleagues and friends who made my time at the university enjoyable.

I want to acknowledge my co-authors—Le, Vaibhav, Jelena, and Morteza—whose insights and collaboration have significantly enhanced the quality of my research. I am deeply grateful for the stimulating discussions and your invaluable contributions.

My master's students Rohan and Jane made the Ph.D. journey even more memorable. It was an absolute pleasure to guide you both, and I am confident that you have great potential for the future. Additionally, I extend my thanks to Tanumay for providing your industrial experience and expertise.

In every research project, there is always one person who ensures that the equipment and lab are running smoothly 24/7. For me, that person is Mr. Remko, the great lab technician. Remko is an excellent technician, a great friend, and a colleague. I always enjoyed our coffee break discussions and practising my poor Dutch language skills with him. Thank you, Remko, for supporting my research and offering wise advice about life. Your presence made a significant difference in my PhD journey and personal life. Furthermore, I would like to thank our section secretaries, Carl and Sharmila, for their

support and help during this journey.

Last but not least, I would like to thank my parents and family . I want to say something in my mother tongue:

मम्मी आनी डॅडी, आयज हांव म्हज्या पांयार उबो आसां हें फकत तुमचेच कृपेन. ल्हान आसतना साकून हांव हुशार नासलो, पूण तुमी म्हाका ताची केन्नाच याद करून दिली ना. तुमी सदांच सांगताले, किदेंय करप शक्य आसा, तितलोच अभ्यास कर. जिवितांत हांवें केन्नाच सरळ शिडीचो दावो केलो ना, हांव सदांच एक दोन फावटी पडलों. सगळें किदें घडटा तें एका कारणा खातीरूच घडटा अशें तुमी सांगताले. म्हाका हाची खबर आसा. धाकटो आसून लेगीत, तुमी खूब कश्ट घेतले आनी म्हाका आनी भय्याक मागता तें तुमी दिलां. 'ना' हो शब्द तुमी केन्नाच वापरलो ना. म्हाका इतली इश्टागत आनी आदार दिवपी आवय-बापूय मेळ्ळ्यात हाची म्हाका खोस भोगता. परिस्थिती कितली कठीण आशिल्ली, तुमी सदांच म्हणटालीं - आशा सोडची न्हय आनी कश्ट करपाचो यत्न चालूच दवरचो. तशेंच म्हज्या फाटल्यान उबे रावून म्हज्या पुराय जिविता खातीर जाय आशिल्लो आदार दिल्ले खातीर म्हज्या पुराय कुटुंबाचे हांव उपकार मानतां.

Ajay Digamber SHETGAONKAR
Delft, August 2024

A

SIMULATION TOOL CONFIGURATION

A.1. NOVACOR RACK AND GTFPGA CONFIGURATION

In RTDS/RSCAD, two MMCs can be programmed on one GTFPGA, namely, *'rtds_vsc_FPGA_U5'* and *'rtds_vsc_FPGA_GM'* models [171]. The later MMC model can simulate IGBT faults within the SM(s). However, this requires extra computation burden, and as a result, one GTFPGA unit can be used to simulate one leg. Hence, to represent an MMC unit, three GTFPGA units are required. The GTFPGA unit is connected to the GTIO port of RTDS via a full-duplex optical fiber using the Aurora protocol. The *'rtds_vsc_FPGA_GM'* model uses 2 additional GTFPGA units for capacitor voltage balancing of MMC's sub-modules known as "MMC's lower level controller". Each leg sends SM capacitor voltage values and receives a Firing sequence over two full-duplex optical fibers from MMC's lower-level controller, as shown in Figure A.1. Using this configuration, 5 GTFPGA units are used to represent one MMC.

Due to a large number of system nodes, the meshed HVDC system is programmed on one RTDS rack. The MPC is programmed on another rack, as shown in Figure. 5.12. Hence, this rack can be considered an external cubical control. The cross-rack communication is performed by a global bus hub and an IRC switch.

A.2. SOFTWARE-IN-THE-LOOP SETUP

A wind gust data expressed in meter per second (m/s), measured near the Orkney Islands (58.9809° N, 2.9605° W) and Shetland Islands (60.5297° N, 1.2659° W) are adopted from [212], represents OWF 1 and OWF 2 wind profiles, respectively. A *Selenium* tool is used to extract the wind speeds from the web using Python. These wind data are communicated through a TCP/IP connection to RSCAD with a communication delay of 100 ms, and the update rate is every 2 s. An illustrated overview of the software-in-the-loop is shown in Figure. A.2.

A

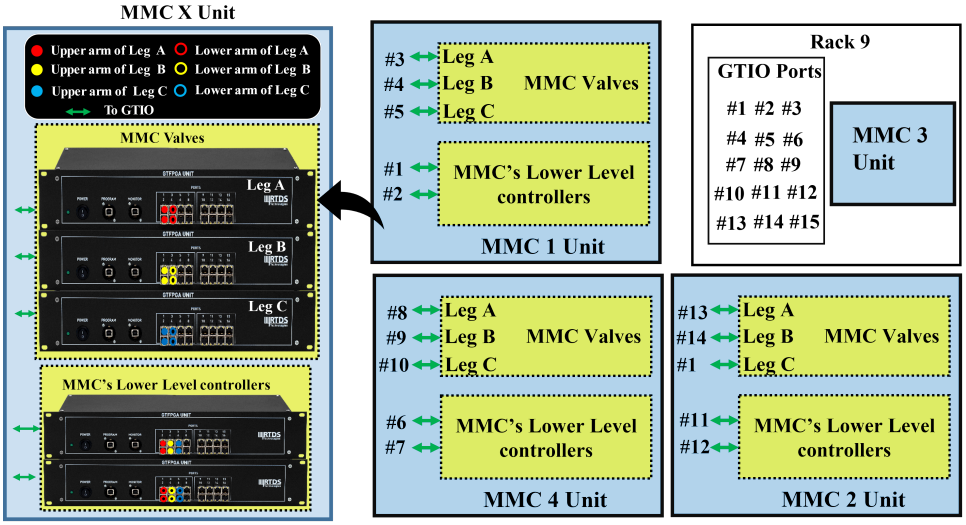

Figure A.1: Overview of the GTIO port connections between GTFPGA and RTDS.

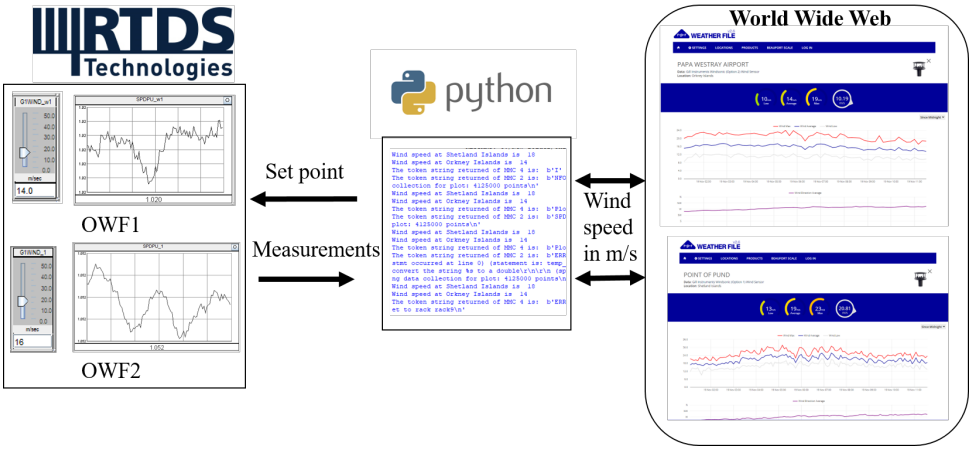

Figure A.2: Overview of software-in-the-loop setup.

BIBLIOGRAPHY

[1] DNV, "Energy Transition Outlook 2023", Tech. Rep., 2023, p. 211.

[2] D. Harrison, S. Fall, and I. McCan, *Ukraine Fights To Build More Resilient, Renewable Energy System in Midst of War*, 2023. [Online]. Available: https://www.nrel.gov/news/features/2023/ukraine-fights-to-build-a-more-resilient-renewable-energy-system-in-the-midst-of-war.html.

[3] European Council and Council of the EU, *European Green Deal and Fit for 55*, 2023. [Online]. Available: https://www.consilium.europa.eu/en/policies/green-deal/timeline-european-green-deal-and-fit-for-55/.

[4] European Commission, *REPowerEU: affordable, secure and sustainable energy for Europe*, 2022.

[5] The White House, "Building a clean energy economy: a guidebook to the inflation reduction act's investments in clean energy and climate action", no. January, pp. 1–183, 2023. [Online]. Available: https://www.whitehouse.gov/wp-content/uploads/2022/12/Inflation-Reduction-Act-Guidebook.pdf.

[6] Ministry of New and Renewable Energy, *Green Energy Corridor*, 2019. [Online]. Available: https://mnre.gov.in/green-energy-corridor.

[7] IEA, "World Energy Outlook 2023", Tech. Rep., 2023, p. 355. [Online]. Available: https://www.iea.org/reports/world-energy-outlook-2023.

[8] "Electricity Market Report", *Electricity Market Report*, 2020. DOI: 10.1787/f0aed4e6-en.

[9] *Iberia: New emerging European energy powerhouse*. [Online]. Available: https://www.rystadenergy.com/news/iberia-a-new-european-energy-powerhouse-emerges.

[10] *TenneT presents Target Grid, its vision for the electricity grid of 2045*. [Online]. Available: https://www.tennet.eu/news/tennet-presents-target-grid-its-vision-electricity-grid-2045.

[11] A. Patonia, V. Lenivova, R. Poudineh, and C. Nolden, "Hydrogen pipelines vs . HVDC lines : Should we transfer green molecules or electrons ?", no. November, p. 35, 2023. [Online]. Available: https://www.oxfordenergy.org/publications/hydrogen-pipelines-vs-hvdc-lines-should-we-transfer-green-molecules-or-electrons/.

[12] Comisión Europea, *2020 climate & energy package | Climate Action*, 2009. [Online]. Available: https://ec.europa.eu/clima/policies/strategies/2020_en#tab-0-0.

[13] J. N. M. Moore and A. Wagner, "D12.4 - Final Deployment Plan", no. 691714, 2020.

[14] Solar Power Europe (SPE), "Global Market Outlook for Solar Power: 2019-2023", *Global Market Outlook*, p. 92, 2019.

[15] European Wind Energy Association, "Wind energy scenarios for 2030", Tech. Rep. August, 2015, pp. 1–16. [Online]. Available: http://www.ewea.org/fileadmin/files/library/publications/reports/EWEA-Wind-energy-scenarios-2030.pdf.

[16] IEEE Task Force, "Studies for Planning HVDC PES-TR86", Tech. Rep., 2021, p. 102.

[17] CIGRE WG B4/B5.59, "Protection and local control of HVDC-grids", Tech. Rep. 300, 2018, p. 3.

[18] CIGRE WG B4.63, "Commissioning of VSC HVDC systems", Tech. Rep. 294, 2017.

[19] D. Lindley, "Smart grids: The energy storage problem", *Nature*, vol. 463, no. 7277, pp. 18–20, 2010, ISSN: 00280836. DOI: 10.1038/463018a. [Online]. Available: https://library.e.abb.com/public/aff841e25d8986b5c1257d380045703f/140818%20ABB%20SR%2060%20years%20of.

[20] M. Barnes, D. Van Hertem, S. P. Teeuwsen, and M. Callavik, "HVDC Systems in Smart Grids", *Proceedings of the IEEE*, vol. 105, no. 11, pp. 2082–2098, 2017, ISSN: 15582256. DOI: 10.1109/JPROC.2017.2672879.

[21] L. Reed, M. G. Morgan, P. Vaishnav, and D. Erian Armanios, "Converting existing transmission corridors to HVDC is an overlooked option for increasing transmission capacity", *Proceedings of the National Academy of Sciences*, vol. 116, no. 28, pp. 13 879–13 884, Jul. 2019, ISSN: 0027-8424. DOI: 10.1073/pnas.1905656116. [Online]. Available: https://pnas.org/doi/full/10.1073/pnas.1905656116.

[22] A. Alassi, S. Bañales, O. Ellabban, G. Adam, and C. MacIver, "HVDC Transmission: Technology Review, Market Trends and Future Outlook", *Renewable and Sustainable Energy Reviews*, vol. 112, pp. 530–554, Sep. 2019, ISSN: 13640321. DOI: 10.1016/j.rser.2019.04.062. [Online]. Available: https://linkinghub.elsevier.com/retrieve/pii/S1364032119302837.

[23] D. Committee, "IEEE Standard Definitions of Terms Relating to Corona and Field Effects of Overhead Power Lines", *IEEE Std 539-2020 (Revision of IEEE Std 539-2005)*, vol. 1990, pp. 1–54, 1991. DOI: 10.1109/IEEESTD.2021.9513501.

[24] J. Martinez, B. Gustavsen, and D. Durbak, "Parameter Determination for Modeling System Transients—Part I: Overhead Lines IEEE PES Task Force on Data for Modeling System Transients of IEEE PES Working Group on Modeling and Analysis of System Transients Using Digital Simulation (General Systems Subc", *IEEE Transactions on Power Delivery*, vol. 20, no. 3, pp. 2038–2044, Jul. 2005, ISSN: 0885-8977. DOI: 10.1109/TPWRD.2005.848678. [Online]. Available: http://ieeexplore.ieee.org/document/1458877/.

[25] nationalgrid, "High voltage direct current electricity - technical information", Tech. Rep., pp. 1–8. [Online]. Available: https://en.wikipedia.org/wiki/High-voltage_direct_current.

[26] M. Ardelean and P. Minnebo, "HVDC Submarine Power Cables in the World", Tech. Rep., 2015, p. 79.

[27] A. Nami, J. Liang, F. Dijkhuizen, and G. D. Demetriades, "Modular Multilevel Converters for HVDC Applications: Review on Converter Cells and Functionalities", *IEEE Transactions on Power Electronics*, vol. 30, no. 1, pp. 18–36, Jan. 2015, ISSN: 0885-8993. DOI: 10.1109/TPEL.2014.2327641. [Online]. Available: http://ieeexplore.ieee.org/document/6824228/.

[28] TenneT, *Multiterminal hubs*, 2024. [Online]. Available: https://www.tennet.eu/de/projekte/multiterminal-hubs.

[29] TenneT, *The 2GW Program | TenneT*, 2023. [Online]. Available: https://www.tennet.eu/about-tennet/innovations/2gw-program.

[30] J. Moore, "D12.1 Preliminary analysis of key technical, financial, economic, legal, regulatory and market barriers and related portfolio of solutions", no. 691714, p. 82, 2018.

[31] J. M. Johnmooretenneteu and J. N. M. Moore, "D12 . 4 Deployment Plan for Future European offshore Grid Development . Short Term Project – Bornholm Island CleanStream Energy Hub .", no. 691714, 2020.

[32] NSWPH, "Hubs and spokes – viable beyond theory, Sharing of feasibility Results", 2022.

[33] Wind Europe and Hitachi Energy, "Offshore Grids: the next frontier", Tech. Rep., 2023. [Online]. Available: https://windeurope.org/intelligence-platform/product/offshore-grids-the-next-frontier/.

[34] *ENERGY ISLANDS IN DENMARK*. [Online]. Available: https://en.energinet.dk/infrastructure-projects/energy-islands/.

[35] Hitachi Energy, "HVDC Light Reference list", Tech. Rep., 2023, p. 20.

[36] P. FAIRLEY, "HVDC NETWORKS COME TO EUROPE", *IEEE Spectrum*, 2024. [Online]. Available: https://spectrum.ieee.org/multiterminal-hvdc-networks.

[37] G. Zarazua de Rubens and L. Noel, "The non-technical barriers to large scale electricity networks: Analysing the case for the US and EU supergrids", *Energy Policy*, vol. 135, p. 111 018, Dec. 2019, ISSN: 03014215. DOI: 10.1016/j.enpol.2019.111018. [Online]. Available: https://linkinghub.elsevier.com/retrieve/pii/S0301421519306056.

[38] D. Bogdanov and C. Breyer, "Eurasian Super Grid for 100% Renewable Energy Power Supply: Generation and Storage Technologies in the Cost Optimal Mix", in *Proceedings of the ISES Solar World Congress 2015*, Freiburg, Germany: International Solar Energy Society, 2016, pp. 1–15, ISBN: 978-3-9814659-5-2. DOI: 10.18086/swc.2015.06.01. [Online]. Available: http://proceedings.ises.org/citation?doi=swc.2015.06.01.

[39] E. Halawa, G. James, X. Shi, N. Sari, and R. Nepal, "The Prospect for an Australian–Asian Power Grid: A Critical Appraisal", *Energies*, vol. 11, no. 1, p. 200, Jan. 2018, ISSN: 1996-1073. DOI: 10.3390/en11010200. [Online]. Available: http://www.mdpi.com/1996-1073/11/1/200.

[40] A. Purvins, L. Sereno, M. Ardelean, C.-F. Covrig, T. Efthimiadis, and P. Minnebo, "Submarine power cable between Europe and North America: A techno-economic analysis", *Journal of Cleaner Production*, vol. 186, pp. 131–145, Jun. 2018, ISSN: 09596526. DOI: 10.1016/j.jclepro.2018.03.095. [Online]. Available: https://linkinghub.elsevier.com/retrieve/pii/S0959652618307522.

[41] Ardelean M and Minnebo P, *A China-EU electricity transmission link Assessment of potential connecting countries and routes*. 2017, pp. 1–99, ISBN: 9789279793585. DOI: 10.2760/67516. [Online]. Available: https://ec.europa.eu/jrc.

[42] K. Hojckova, H. Ahlborg, and B. A. Sandén, "A global super-grid: sociotechnical drivers and barriers", *Energy, Sustainability and Society*, vol. 12, no. 1, p. 42, Oct. 2022, ISSN: 2192-0567. DOI: 10.1186/s13705-022-00368-y. [Online]. Available: https://energsustainsoc.biomedcentral.com/articles/10.1186/s13705-022-00368-y.

[43] IEEE, "Stability definitions and characterization of dynamic behavior in systems with high penetration of power electronic interfaced technologies", Tech. Rep. April, 2020, pp. 1–42.

[44] F. F. Wu, K. Moslehi, and A. Bose, "Power system control centers: Past, present, and future", *Proceedings of the IEEE*, vol. 93, no. 11, pp. 1890–1908, Nov. 2005, ISSN: 00189219. DOI: 10.1109/JPROC.2005.857499. [Online]. Available: http://ieeexplore.ieee.org/document/1519722/.

[45] L. Wu, M. Mao, Y. Shi, and Y. Liu, "Evaluation on Fault Current Suppression Ability of Current Limiting Control Algorithms for MMC-HVDC-Grid", *PEAS 2021 - 2021 IEEE 1st International Power Electronics and Application Symposium, Conference Proceedings*, 2021. DOI: 10.1109/PEAS53589.2021.9628400.

[46] Y. Toghani Holari, S. A. Taher, and M. Mehrasa, "Power management using robust control strategy in hybrid microgrid for both grid-connected and islanding modes", *Journal of Energy Storage*, vol. 39, p. 102 600, 2021, ISSN: 2352-152X. DOI: https://doi.org/10.1016/j.est.2021.102600. [Online]. Available: https://www.sciencedirect.com/science/article/pii/S2352152X2100342X.

[47] O. Stanojev, U. Markovic, E. Vrettos, P. Aristidou, D. Callaway, and G. Hug, "Enhanced MPC for Fast Frequency Control in Inverter-Dominated Power Systems", in *2020 International Conference on Smart Energy Systems and Technologies (SEST)*, 2020, pp. 1–6. DOI: 10.1109/SEST48500.2020.9203035.

[48] O. Stanojev, U. Markovic, P. Aristidou, G. Hug, D. S. Callaway, and E. Vrettos, "MPC-Based Fast Frequency Control of Voltage Source Converters in Low-Inertia Power Systems", *IEEE Transactions on Power Systems*, p. 1, 2020. DOI: 10.1109/TPWRS.2020.2999652.

[49] C. Zheng, T. Dragicevic, and F. Blaabjerg, "Model Predictive Control Based Virtual Inertia Emulator for an Islanded AC Microgrid", *IEEE Transactions on Industrial Electronics*, p. 1, 2020. DOI: 10.1109/TIE.2020.3007105.

[50] S. D. Tavakoli, S. Fekriasl, E. Prieto-Araujo, J. Beerten, and O. Gomis-Bellmunt, "Optimal H Infinity Control Design for MMC-based HVDC Links", *IEEE Transactions on Power Delivery*, 2021.

[51] R. Preece and J. V. Milanović, "Power Oscillation Damping using VSC-based Multi-terminal HVDC Grids", *IFAC Proceedings Volumes*, vol. 45, no. 21, pp. 20–25, 2012, ISSN: 14746670. DOI: 10.3182/20120902-4-FR-2032.00006. [Online]. Available: https://linkinghub.elsevier.com/retrieve/pii/S1474667016319383.

[52] J. McLeod, "Introduction to Special Apollo Issue", *SIMULATION*, vol. 15, no. 1, pp. 5–11, Jul. 1970, ISSN: 0037-5497. DOI: 10.1177/003754977001500104.

[53] K. SZALAI, P. FELLEMAN, J. GERA, and R. GLOVER, "Design and test experience with a triply redundant digital fly-by-wire control system", in *Guidance and Control Conference*, Reston, Virigina: American Institute of Aeronautics and Astronautics, Aug. 1976, p. 1911. DOI: 10.2514/6.1976-1911. [Online]. Available: https://arc.aiaa.org/doi/10.2514/6.1976-1911.

[54] P. Palensky, M. Cvetkovic, D. Gusain, and A. Joseph, "Digital twins and their use in future power systems", *Digital Twin*, vol. 1, p. 4, Aug. 2022, ISSN: 2752-5783. DOI: 10.12688/digitaltwin.17435.2. [Online]. Available: https://digitaltwin1.org/articles/1-4/v2.

[55] A. M. Lund, K. Mochel, J.-W. Lin, *et al.*, *Digital twin interface for operating wind farms*, Jun. 2018. [Online]. Available: https://patents.google.com/patent/US9995278B2/en.

[56] Siemens, "Electrical Digital Twin Brochure", Tech. Rep., 2018, pp. 1–12.

[57] Hitachi Energy, *Hitachi Energy launches IdentiQ™ digital twin for sustainable, flexible and secure power grids*, Nov. 2021. [Online]. Available: https://www.hitachienergy.com/news/press-releases/2021/11/hitachi-energy-launches-identiqtm-digital-twin-for-sustainable-flexible-and-secure-power-grids.

[58] B. Badrzadeh, N. Modi, J. Lindley, A. Jalali, and J. Lu, "Power System Operation With a High Share of Inverter-Based Resources: The Australian Experience", *IEEE Power and Energy Magazine*, vol. 19, no. 5, pp. 46–55, Sep. 2021, ISSN: 1540-7977. DOI: 10.1109/MPE.2021.3088744. [Online]. Available: https://ieeexplore.ieee.org/document/9520155/.

[59] B. Badrzadeh, S. Goyal, J. Lu, *et al.*, "WG C4.56 Electromagnetic Transient Simulation Models for Large-Scale System Impac Studies in Power Systems Having a High Penetration of Inverter-Connected Generation", CIGRE, Tech. Rep., 2022, pp. 435–479.

[60] M. Ndreko, T. Geraerds, M. Martín Almenta, *et al.*, "Expert Group Interaction Studies and Simulation Models (EG ISSM)", Tech. Rep., 2021, pp. 3–73.

[61] European Commission, "COMMISSION REGULATION (EU) 2016/1447 of 26 August 2016. Establishing a network code on requirements for grid connection of high voltage direct current systems and direct current-connected power park modules", Tech. Rep. L 241, 2016, pp. 1–65.

[62] T. Liu, Y. Song, L. Zhu, and D. J. Hill, "Stability and Control of Power Grids", *Annual Review of Control, Robotics, and Autonomous Systems*, vol. 5, no. 1, pp. 689–716, May 2022, ISSN: 2573-5144. DOI: 10.1146/annurev-control-042820-011148. [Online]. Available: https://www.annualreviews.org/doi/10.1146/annurev-control-042820-011148.

[63] K. Sidwall and P. Forsyth, "A Review of Recent Best Practices in the Development of Real-Time Power System Simulators from a Simulator Manufacturer's Perspective", *Energies*, vol. 15, no. 3, p. 1111, Feb. 2022, ISSN: 1996-1073. DOI: 10.3390/en15031111. [Online]. Available: https://www.mdpi.com/1996-1073/15/3/1111.

[64] J. Beerten, O. Gomis-Bellmunt, X. Guillaud, J. Rimez, A. van der Meer, and D. Van Hertem, "Modeling and control of HVDC grids: A key challenge for the future power system", in *2014 Power Systems Computation Conference*, IEEE, Aug. 2014, pp. 1–21, ISBN: 978-83-935801-3-2. DOI: 10.1109/PSCC.2014.7038505. [Online]. Available: http://ieeexplore.ieee.org/document/7038505/.

[65] T. Duan and V. Dinavahi, "Adaptive Time-Stepping Universal Line and Machine Models for Real Time and Faster-Than-Real-Time Hardware Emulation", *IEEE Transactions on Industrial Electronics*, vol. 67, no. 8, pp. 6173–6182, Aug. 2020, ISSN: 0278-0046. DOI: 10.1109/TIE.2019.2935930. [Online]. Available: https://ieeexplore.ieee.org/document/8818631/.

[66] Cigre WG B4.74, "Guide to Develop Real-Time Simulation Models for HVDC Operational Studies", *Technical Brochure 864*, vol. 864, no. February, 2022.

[67] OPAL-RT, *Digital Twins for Modern Power Systems*, 2023. [Online]. Available: https://www.opal-rt.com/digital-twins/.

[68] M. D. Omar Faruque, T. Strasser, G. Lauss, *et al.*, "Real-Time Simulation Technologies for Power Systems Design, Testing, and Analysis", *IEEE Power and Energy Technology Systems Journal*, vol. 2, no. 2, pp. 63–73, Jun. 2015, ISSN: 2332-7707. DOI: 10.1109/JPETS.2015.2427370. [Online]. Available: http://ieeexplore.ieee.org/document/7138557/.

[69] K. Sidwall, "The Closed-Loop Revolution", *IEEE Power and Energy Magazine*, vol. 18, no. 2, pp. 38–46, Mar. 2020, ISSN: 1540-7977. DOI: 10.1109/MPE.2020.2974595. [Online]. Available: https://ieeexplore.ieee.org/document/9011507/.

[70] J. Bélanger, P. Venne, J.-N. Paquin, *et al.*, "The what, where and why of real-time simulation", *Planet Rt*, vol. 1, no. 1, pp. 25–29, 2010.

[71] *InterOPERA:Enabling multi-vendor HVDC grids*. [Online]. Available: https://interopera.eu.

[72] A. J. Agbemuko, J. L. Domínguez-García, E. Prieto-Araujo, and O. Gomis-Bellmunt, "Dynamic modelling and interaction analysis of multi-terminal VSC-HVDC grids through an impedance-based approach", *International Journal of Electrical Power & Energy Systems*, vol. 113, pp. 874–887, Dec. 2019, ISSN: 01420615. DOI: 10.1016/j.ijepes.2019.06.029. [Online]. Available: https://linkinghub.elsevier.com/retrieve/pii/S0142061519300195.

[73] O. (Despouys, A. (Petit, P. (Rault, *et al.*, "BEST PATHS D4.3: First recommendations to enhance interoperability in HVDC-VSC multi- vendor schemes", Tech. Rep., 2016, p. 54. [Online]. Available: http://www.bestpaths-project.eu/contents/publications/d43-vfinal-20161025_logo.pdf.

[74] K. Lindén, J. Beerten, A. Alvarez, *et al.*, "Control methodologies for direct voltage and power flow in a meshed HVDC Grid", Tech. Rep. 294, 2017, pp. 72–75. [Online]. Available: https://lirias.kuleuven.be/1731467%0Afiles/12399/1731467.html.

[75] R. P. Aguilera, P. Acuna, X. Su, P. Lezana, and B. McGrath, "Sequential Phase-Shifted Model Predictive Control for multicell power converters", in *2017 IEEE Southern Power Electronics Conference (SPEC)*, 2017, pp. 1–6. DOI: 10.1109/SPEC.2017.8333644.

[76] S. Martin, H. Li, and O. Anubi, "Modulated MPC for Arm Inductor-Less MVDC MMC With Reduced Computational Burden", *IEEE Transactions on Energy Conversion*, vol. 36, no. 3, pp. 1776–1786, Sep. 2021, ISSN: 0885-8969. DOI: 10.1109/TEC.2021.3069150. [Online]. Available: https://ieeexplore.ieee.org/document/9387585/.

[77] S. Wang, T. Dragicevic, Y. Gao, and R. Teodorescu, "Neural Network Based Model Predictive Controllers for Modular Multilevel Converters", *IEEE Transactions on Energy Conversion*, vol. 36, no. 2, pp. 1562–1571, Jun. 2021, ISSN: 0885-8969. DOI: 10.1109/TEC.2020.3021022. [Online]. Available: https://ieeexplore.ieee.org/document/9183974/.

[78] X. Kong, X. Wang, M. A. Abdelbaky, X. Liu, and K. Y. Lee, "Nonlinear MPC for DFIG-based wind power generation under unbalanced grid conditions", *International Journal of Electrical Power & Energy Systems*, vol. 134, p. 107 416, Jan. 2022, ISSN: 01420615. DOI: 10.1016/j.ijepes.2021.107416. [Online]. Available: https://linkinghub.elsevier.com/retrieve/pii/S0142061521006554.

[79] H. Tao, T. Peng, C. Yang, *et al.*, "An FCS-MPC-based open-circuit and current sensor fault diagnosis method for traction inverters with two current sensors", *International Journal of Electrical Power & Energy Systems*, vol. 144, p. 108 526, Jan. 2023, ISSN: 01420615. DOI: 10.1016/j.ijepes.2022.108526. [Online]. Available: https://linkinghub.elsevier.com/retrieve/pii/S0142061522005282.

[80] A. Dekka, B. Wu, V. Yaramasu, R. L. Fuentes, and N. R. Zargari, "Model Predictive Control of High-Power Modular Multilevel Converters—An Overview", *IEEE Journal of Emerging and Selected Topics in Power Electronics*, vol. 7, no. 1, pp. 168–183, 2019. DOI: 10.1109/JESTPE.2018.2880137.

[81] J.-M. Rodriguez-Bernuz and A. Junyent-Ferré, "Model predictive circulating current regulator for single-phase modular multilevel converter", in *2018 IEEE Energy Conversion Congress and Exposition (ECCE)*, IEEE, 2018, pp. 4824–4830.

[82] J.-M. Rodriguez-Bernuz and A. Junyent-Ferré, "Operating Region Extension of a Modular Multilevel Converter using Model Predictive Control: a Single Phase Analysis", *IEEE Transactions on Power Delivery*, vol. 35, no. 1, pp. 171–182, 2019.

[83] M. Jeong, S. Fuchs, and J. Biela, "When FPGAs Meet Regionless Explicit MPC: An Implementation of Long-horizon Linear MPC for Power Electronic Systems", in *IECON 2020 The 46th Annual Conference of the IEEE Industrial Electronics Society*, IEEE, Oct. 2020, pp. 3085–3092, ISBN: 978-1-7281-5414-5. DOI: 10.1109/IECON43393.2020.9254277. [Online]. Available: https://ieeexplore.ieee.org/document/9254277/.

[84] M. Hassan Fidai, D. Babazadeh, J. Hanning, T. X. Larsson, and L. Nordström, "Real-time Implementation of Optimal Power Flow Calculator for HVDC Grids", in *Cigre*, vol. 2015, 2015, pp. 1–6.

[85] L. Bessegato, L. Harnefors, K. Ilves, and S. Norrga, "A Method for the Calculation of the AC-Side Admittance of a Modular Multilevel Converter", *IEEE Transactions on Power Electronics*, vol. 34, no. 5, pp. 4161–4172, 2019. DOI: 10.1109/TPEL.2018.2862254.

[86] M. Beza, M. Bongiorno, and G. Stamatiou, "Analytical Derivation of the AC-Side Input Admittance of a Modular Multilevel Converter With Open- and Closed-Loop Control Strategies", *IEEE Transactions on Power Delivery*, vol. 33, no. 1, pp. 248–256, 2018. DOI: 10.1109/TPWRD.2017.2701415.

[87] G. Stamatiou, M. Beza, M. Bongiorno, and L. Harnefors, "Analytical derivation of the DC-side input admittance of the direct-voltage controlled modular multilevel converter", *IET Generation, Transmission \& Distribution*, vol. 11, no. 16, pp. 4018–4030, Nov. 2017, ISSN: 1751-8687. [Online]. Available: https://digital-library.theiet.org/content/journals/10.1049/iet-gtd.2017.0278.

[88] O. C. Sakinci and J. Beerten, "Generalized Dynamic Phasor Modeling of the MMC for Small-Signal Stability Analysis", *IEEE Transactions on Power Delivery*, vol. 34, no. 3, pp. 991–1000, 2019. DOI: 10.1109/TPWRD.2019.2898468.

[89] J. Lyu, X. Zhang, X. Cai, and M. Molinas, "Harmonic State-Space Based Small-Signal Impedance Modeling of a Modular Multilevel Converter With Consideration of Internal Harmonic Dynamics", *IEEE Transactions on Power Electronics*, vol. 34, no. 3, pp. 2134–2148, 2019. DOI: 10.1109/TPEL.2018.2842682.

[90] J. Sun and H. Liu, "Sequence Impedance Modeling of Modular Multilevel Converters", *IEEE Journal of Emerging and Selected Topics in Power Electronics*, vol. 5, no. 4, pp. 1427–1443, 2017. DOI: 10.1109/JESTPE.2017.2762408.

[91] P. De Rua, O. C. Sakinci, and J. Beerten, "Comparative Study of Dynamic Phasor and Harmonic State-Space Modeling for Small-Signal Stability Analysis", *Electric Power Systems Research*, vol. 189, 2020.

[92] G. Bergna-Diaz, J. Freytes, X. Guillaud, S. D'Arco, and J. A. Suul, "Generalized Voltage-Based State-Space Modeling of Modular Multilevel Converters With Constant Equilibrium in Steady State", *IEEE Journal of Emerging and Selected Topics in Power Electronics*, vol. 6, no. 2, pp. 707–725, 2018. DOI: 10.1109/JESTPE.2018.2793159.

[93] CIGRE Working Group B4.70, "Guide for electromagnetic transient studies involving VSC converters", Tech. Rep. April, 2021.

[94] WG B4.72, "DC Grid Benchmark Models for System Studies", Tech. Rep. June, 2020, pp. 1–270.

[95] I. Cowan, "D9 . 1 – Real-time models for benchmark DC grid systems", 2020.

[96] M. Wang, W. Leterme, G. Chaffey, J. Beerten, and D. Van Hertem, "Multi-vendor interoperability in HVDC grid protection: State-of-the-art and challenges ahead", *IET Generation, Transmission and Distribution*, vol. 15, no. 15, pp. 2153–2175, 2021, ISSN: 17518695. DOI: 10.1049/gtd2.12165.

[97] BESTPATHS, "BEST PATHS D9.3: Final Recommendations For Interoperability Interoperability of Multivendor HVDC Systems", *Technical Report D9.3*, vol. D9.3, pp. 1–73, 2018.

[98] *READY4DC*. [Online]. Available: https://www.ready4dc.eu/.

[99] J. A. Ansari, C. Liu, and S. A. Khan, "MMC based MTDC grids: A detailed review on issues and challenges for operation, control and protection schemes", *IEEE Access*, vol. 8, pp. 168 154–168 165, 2020, ISSN: 21693536. DOI: 10.1109/ACCESS.2020.3023544.

[100] S. Liu, M. Popov, S. S. Mirhosseini, *et al.*, "Modeling, Experimental Validation, and Application of VARC HVDC Circuit Breakers", *IEEE Transactions on Power Delivery*, vol. 35, no. 3, pp. 1515–1526, 2020, ISSN: 19374208. DOI: 10.1109/TPWRD.2019.2947544.

[101] A. Shetgaonkar, S. Liu, and M. Popov, "Comparative Analysis of a Detailed and an Average VARC DCCB model in MTDC Systems", in *IEEE Power and Energy Society General Meeting*, vol. 2022-July, 2022, ISBN: 9781665408233. DOI: 10.1109/PESGM48719.2022.9916949.

[102] I. Jahn, N. Johannesson, and S. Norrga, "Survey of methods for selective DC fault detection in MTDC grids", *IET Conference Publications*, vol. 2017, no. CP709, pp. 1–7, 2017. DOI: 10.1049/cp.2017.0041.

[103] W. Wang, M. Barnes, O. Marjanovic, and O. Cwikowski, "Impact of DC breaker systems on multiterminal VSC-HVDC stability", *IEEE Transactions on Power Delivery*, vol. 31, no. 2, pp. 769–779, 2016, ISSN: 08858977. DOI: 10.1109/TPWRD.2015.2409132.

[104] S. Yang, W. Xiang, M. Zhou, W. Zuo, and J. Wen, "A Single-End Protection Scheme for Hybrid MMC HVDC Grids Considering the Impacts of the Active Fault Current-Limiting Control", *IEEE Transactions on Power Delivery*, vol. 36, no. 4, pp. 2001–2013, 2021, ISSN: 19374208. DOI: 10.1109/TPWRD.2020.3017895.

[105] J. Xu, X. Zhao, H. Jing, J. Liang, and C. Zhao, "DC Fault Current Clearance at the Source Side of HVDC Grid Using Hybrid MMC", *IEEE Transactions on Power Delivery*, vol. 35, no. 1, pp. 140–149, 2020, ISSN: 19374208. DOI: 10.1109/TPWRD.2019.2927234.

[106] C. Sun, M. Mao, Y. Shi, and Y. Liu, "Comparison of DC Fault Current Suppression by Current-limiting Control Algorithms for Double-Terminal Half-bridge MMC-HVDC System", *5th IEEE Conference on Energy Internet and Energy System Integration: Energy Internet for Carbon Neutrality, EI2 2021*, pp. 4367–4372, 2021. DOI: 10.1109/EI252483.2021.9713078.

[107] X. Zhao, L. Chen, G. Li, J. Xu, and J. Yuan, "Coordination method for DC fault current suppression and clearance in DC grids", *CSEE Journal of Power and Energy Systems*, vol. PP, no. 99, pp. 1438–1447, 2019, ISSN: 20960042. DOI: 10.17775/CSEEJPES.2019.03160.

[108] F. Zerihundejene, M. Abedrabbo, J. Beerten, and D. Vanhertem, "Design of a DC Fault Current Reduction Control for Half-Bridge Modular Multi-Level Converters", *2018 20th European Conference on Power Electronics and Applications, EPE 2018 ECCE Europe*, pp. 1–9, 2018.

[109] T. Zheng, W. Lv, Q. Wu, *et al.*, "An Integrated Control and Protection Scheme Based on FBSM-MMC Active Current Limiting Strategy for DC Distribution Network", *IEEE Journal of Emerging and Selected Topics in Power Electronics*, vol. 9, no. 3, pp. 2632–2642, 2021, ISSN: 21686785. DOI: 10.1109/JESTPE.2020.3014795.

[110] Z. Cai and L. Huang, "Lyapunov-Krasovskii stability analysis of delayed Filippov system: Applications to neural networks with switching control", *International Journal of Robust and Nonlinear Control*, vol. 30, no. 2, pp. 699–718, 2020, ISSN: 10991239. DOI: 10.1002/rnc.4787.

[111] A. Lekic, D. Stipanovic, and N. Petrovic, "Controlling the Ćuk Converter Using Polytopic Lyapunov Functions", *IEEE Transactions on Circuits and Systems II: Express Briefs*, vol. 65, no. 11, pp. 1678–1682, Nov. 2018, ISSN: 1549-7747. DOI: 10.1109/TCSII.2017.2781621.

[112] A. Shetgaonkar, A. Lekic´, L. Liu, M. Popov, and P. Palensky, "Model Predictive Control and Protection of Mmc-Based Mtdc Power Systems", *International Journal of Electrical Power and Energy Systems*, 2022. DOI: 10.2139/ssrn.4127026.

[113] A. Shetgaonkar, A. Lekić, J. L. R. Torres, and P. Palensky, "Microsecond enhanced indirect model predictive control for dynamic power management in mmc units", *Energies*, vol. 14, no. 11, 2021, ISSN: 19961073. DOI: 10.3390/en14113318.

[114] J. Freytes, G. Bergna, J. A. Suul, *et al.*, "Improving Small-Signal Stability of an MMC With CCSC by Control of the Internally Stored Energy", *IEEE Transactions on Power Delivery*, vol. 33, no. 1, pp. 429–439, 2018, ISSN: 08858977. DOI: 10.1109/TPWRD.2017.2725579.

[115] M. Abedrabbo, F. Z. Dejene, W. Leterme, and D. Van Hertem, "HVDC Grid Post-DC Fault Recovery Enhancement", *IEEE Transactions on Power Delivery*, vol. 36, no. 2, pp. 1137–1148, Apr. 2021, ISSN: 0885-8977. DOI: 10.1109/TPWRD.2020.3002717. [Online]. Available: https://ieeexplore.ieee.org/document/9117162/.

[116] J. D. Watson and I. Lestas, "Frequency and voltage regulation in hybrid AC/DC networks", Dec. 2018. [Online]. Available: http://arxiv.org/abs/1812.10189.

[117] M. Enomoto, K. Sano, J. Kanno, and J. Fukushima, "Continuous Operation of Wind Power Plants Under Pole-to-Ground Fault in an HVDC System Consisting of Half-Bridge MMCs and Disconnecting Switches", *IEEE Transactions on Power Electronics*, vol. 38, no. 3, pp. 3812–3823, Mar. 2023, ISSN: 0885-8993. DOI: 10.1109/TPEL.2022.3225209. [Online]. Available: https://ieeexplore.ieee.org/document/9965270/.

[118] P. Ruffing, C. Brantl, and R. Puffer, "Post-Fault Voltage Recovery for Multi-Terminal HVDC Networks Based on Fault Blocking Converters", *Symposium Aalborg*, pp. 1–11, 2019. DOI: null.

[119] Y. Luo, P. Yi, X. Xiaofu, W. Jiang, and S. Yonghui, "DC fault ride-through method for full-bridge MMC-based MTDC systems", *The Journal of Engineering*, vol. 2019, no. 16, pp. 3175–3179, 2019, ISSN: 2051-3305. DOI: 10.1049/joe.2018.8423.

[120] M. Alharbi, S. Isik, F. E. Alfaris, A. Alkuhayli, and S. Bhattacharya, "A Fault Clearance and Restoration Approach for MMC-Based MTDC Grid", *Electronics (Switzerland)*, vol. 11, no. 14, 2022, ISSN: 20799292. DOI: 10.3390/electronics11142127.

[121] E. Kontos, R. T. Pinto, and P. Bauer, "Fast DC fault recovery technique for H-bridge MMC-based HVDC networks", *2015 IEEE Energy Conversion Congress and Exposition, ECCE 2015*, pp. 3351–3358, 2015. DOI: 10.1109/ECCE.2015.7310133.

[122] E. Shahriari, F. Gruson, P. Vermeersch, P. Delarue, F. Colas, and X. Guillaud, "A Novel DC Fault Ride through Control Methodology for Hybrid Modular Multilevel Converters in HVDC Systems", *IEEE Transactions on Power Delivery*, vol. 35, no. 6, pp. 2831–2840, 2020, ISSN: 19374208. DOI: 10.1109/TPWRD.2020.2998535.

[123] J. Zhang, W. Xiang, W. Lin, and J. Wen, "Research on fault protection of DC grid based on hybrid MMC", *The Journal of Engineering*, vol. 2017, no. 13, pp. 822–827, 2017, ISSN: 2051-3305. DOI: 10.1049/joe.2017.0445.

[124] H. Rahman, R. Li, L. Yao, and L. Xu, "Protection and post-fault recovery of large HVDC networks using partitioning and fast acting DC breakers at strategic locations", *Jurnal Engineering*, 2018. DOI: 10.1049/joe.2018.8610.

[125] P. Wang, Z. Li, Z. Li, X.-P. Zhang, R. Zhang, and P. Coventry, "DC fault management for VSC MTDC system using delayed-auto-re-configuration scheme", *null*, 2015. DOI: 10.1049/cp.2015.0102.

[126] M. Abedrabbo, F. Z. Dejene, W. Leterme, and D. V. Hertem, "HVDC Grid Post-DC Fault Recovery Enhancement", *IEEE Transactions on Power Delivery*, 2020. DOI: 10.1109/tpwrd.2020.3002717.

[127] IEC Standard 62501:2009, "Voltage sourced converter (VSC) valves for high-voltage direct current (HVDC) power transmission — Electrical testing", International Electrotechnical Commission, Tech. Rep., 2009, p. 199.

[128] ABB, "Special Report 60 years of HVDC", Tech. Rep. December, 2014, p. 72. [Online]. Available: https://search-ext.abb.com/library/Download.aspx?DocumentID=9AKK106103A8195&LanguageCode=en&DocumentPartId=&Action=Launch.

[129] CIGRE WG B4.37, "VSC Transmission", Tech. Rep., 2005, p. 82.

[130] K. Sharifabadi, L. Harnefors, H. P. Nee, S. Norrga, and R. Teodorescu, *Design, control and application of modular multilevel converters for HVDC transmission systems*. 2016, pp. 1–386, ISBN: 9781118851555. DOI: 10.1002/9781118851555.

[131] O. D. Adeuyi, M. Cheah-Mane, J. Liang, and N. Jenkins, "Fast Frequency Response From Offshore Multiterminal VSC–HVDC Schemes", *IEEE Transactions on Power Delivery*, vol. 32, no. 6, pp. 2442–2452, Dec. 2017, ISSN: 0885-8977. DOI: 10.1109/TPWRD.2016.2632860. [Online]. Available: https://ieeexplore.ieee.org/document/7769201/.

[132] IEC, "IEC 62751-2 - Power losses in voltage sourced converter (VSC) valves for high-voltage direct current (HVDC) systems – Part 2: Modular multilevel converters - Edition 1.1", Tech. Rep., 2019, p. 254.

[133] G. Wu, J. Liang, X. Zhou, *et al.*, "Analysis and design of vector control for VSC-HVDC connected to weak grids", *CSEE Journal of Power and Energy Systems*, vol. 3, no. 2, pp. 115–124, Jul. 2017, ISSN: 20960042. DOI: 10.17775/CSEEJPES.2017.0015. [Online]. Available: https://ieeexplore.ieee.org/stamp/stamp.jsp?tp=&arnumber=7976158.

[134] L. Zhang, L. Harnefors, and H.-P. Nee, "Power-Synchronization Control of Grid-Connected Voltage-Source Converters", *IEEE Transactions on Power Systems*, vol. 25, no. 2, pp. 809–820, May 2010, ISSN: 0885-8950. DOI: 10.1109/TPWRS.2009.2032231. [Online]. Available: http://ieeexplore.ieee.org/document/5308285/.

[135] GE Grid Solutions, "High Voltage Direct Current Systems", Tech. Rep., 2016, pp. 1–12.

[136] Siemens Energy, "HVDC - High-voltage direct current transmission", Tech. Rep., 2021, p. 6.

[137] Hitachi Energy, "HVDC Classic Reference list", Tech. Rep., 2023, p. 24.

[138] Cigre WG B4.52, "HVDC Grid Feasibility Study", Tech. Rep., 2013, p. 189.

[139] V. R. Reddy, Y.-J. Hafner, K. K. Nayak, *et al.*, "Feasibility study of adding a third full bridge VSC-based HVDC terminal on an existing LCC-based HVDC transmission system", in *2022*, 2022, p. 10.

[140] C. W. B4.57, "Guide for the Development of Models for HVDC Converters in a HVDC Grid", *CIGRE Technical Brochure*, no. 604, 2014.

[141] H. Zhou, J. Yuan, F. Chen, and B. Chen, "Inductive Fault Current Limiters in VSC-HVDC Systems: A Review", *IEEE Access*, vol. 8, pp. 38 185–38 197, 2020, ISSN: 2169-3536. DOI: 10.1109/ACCESS.2020.2976116. [Online]. Available: https://ieeexplore.ieee.org/document/9007651/.

[142] C. M. Franck, "HVDC Circuit Breakers: A Review Identifying Future Research Needs", *IEEE Transactions on Power Delivery*, vol. 26, no. 2, pp. 998–1007, Apr. 2011, ISSN: 0885-8977. DOI: 10.1109/TPWRD.2010.2095889. [Online]. Available: http://ieeexplore.ieee.org/document/5686894/.

[143] Cigré JWG B4/B3, "Design,test and application of HVDC circuit breaker", Tech. Rep., 2022, p. 235.

[144] T. Ueda, M. Morita, H. Arita, Y. Kida, Y. Kurosawa, and T. Yamagiwa, "Solid-state current limiter for power distribution system", *IEEE Transactions on Power Delivery*, vol. 8, no. 4, pp. 1796–1801, 1993, ISSN: 08858977. DOI: 10.1109/61.248287. [Online]. Available: http://ieeexplore.ieee.org/document/248287/.

[145] A. Safaei, M. Zolfaghari, M. Gilvanejad, and G. B. Gharehpetian, "A survey on fault current limiters: Development and technical aspects", *International Journal of Electrical Power & Energy Systems*, vol. 118, p. 105 729, Jun. 2020, ISSN: 01420615. DOI: 10.1016/j.ijepes.2019.105729. [Online]. Available: https://linkinghub.elsevier.com/retrieve/pii/S0142061519315005.

[146] J. Magnusson, R. Saers, L. Liljestrand, and G. Engdahl, "Separation of the Energy Absorption and Overvoltage Protection in Solid-State Breakers by the Use of Parallel Varistors", *IEEE Transactions on Power Electronics*, vol. 29, no. 6, pp. 2715–2722, Jun. 2014, ISSN: 0885-8993. DOI: 10.1109/TPEL.2013.2272857. [Online]. Available: http://ieeexplore.ieee.org/document/6557500/.

[147] S. Liu, Z. Liu, J. de Jesus Chavez, and M. Popov, "Mechanical DC circuit breaker model for real time simulations", *International Journal of Electrical Power & Energy Systems*, vol. 107, pp. 110–119, May 2019, ISSN: 01420615. DOI: 10.1016/j.ijepes.2018.11.014. [Online]. Available: https://linkinghub.elsevier.com/retrieve/pii/S0142061518316454.

[148] A. Hassanpoor, J. Hafner, and B. Jacobson, "Technical Assessment of Load Commutation Switch in Hybrid HVDC Breaker", *IEEE Transactions on Power Electronics*, vol. 30, no. 10, pp. 5393–5400, Oct. 2015, ISSN: 0885-8993. DOI: 10.1109/TPEL.2014.2372815. [Online]. Available: http://ieeexplore.ieee.org/document/6963422/.

[149] Y. Murata, M. Sakamaki, K. Abe, *et al.*, "Development of high voltage dc-Xlpe cable system", *SEI Technical Review*, no. 76, pp. 55–62, 2013, ISSN: 13434349.

[150] A. Abbasi, A. Hoang, E. Eriksson, and F. Fälth, "Performance evaluation of 525 kV and 640 kV extruded DC cable systems", *10th International Conference on Insulated Power Cables*, pp. 9–4, 2019.

[151] *321 April 2022 | ELECTRA*. [Online]. Available: https://electra.cigre.org/321-april-2022.html.

[152] Federal Ministry for Economic Affairs and Energy, "Electricity 2030", Tech. Rep., 2017, p. 52. [Online]. Available: https://www.bmwi.de/Redaktion/EN/Publikationen/electricity-2030-concluding-paper.pdf?__blob=publicationFile&v=9.

[153] Cigré JWG B4/B5.59, "Cigre Technical Brochure - Protection and local control of HVDC-grids", Tech. Rep. 739, 2018.

[154] O. E. Oni, I. E. Davidson, and K. N. Mbangula, "A review of LCC-HVDC and VSC-HVDC technologies and applications", in *2016 IEEE 16th International Conference on Environment and Electrical Engineering (EEEIC)*, IEEE, Jun. 2016, pp. 1–7, ISBN: 978-1-5090-2320-2. DOI: 10.1109/EEEIC.2016.7555677. [Online]. Available: http://ieeexplore.ieee.org/document/7555677/.

[155] ENTSO-E, *Line-Commutated Converters - Current Source Converters*, 2023. [Online]. Available: https://www.entsoe.eu/Technopedia/techsheets/line-commutated-converters-current-source-converters.

[156] IEEE Power and Energy Society, "November 2007 PES-TR14 Voltage Sourced Converter (VSC) Applications in Power Transmission", no. November 2007, 2013.

[157] S. Du, A. Dekka, B. Wu, and N. Zargari, *Modular Multilevel Converters: Analysis, Control, and Applications*. Hoboken, NJ, USA: John Wiley & Sons, Inc., Jan. 2017, vol. 40, pp. 116–121, ISBN: 9781119367291. DOI: 10.1002/9781119367291. [Online]. Available: http://doi.wiley.com/10.1002/9781119367291.

[158] J. Freytes, "Small- signal stability analysis of Modular Multilevel Converters and application to MMC – based Multi-Terminal DC grids", Ph.D. dissertation, Ecole Centrale de Lille, 2017. [Online]. Available: https://www.theses.fr/2017ECLI0022.

[159] A. Nabae, I. Takahashi, and H. Akagi, "A New Neutral-Point-Clamped PWM Inverter", *IEEE Transactions on Industry Applications*, vol. IA-17, no. 5, pp. 518–523, 1981, ISSN: 19399367. DOI: 10.1109/TIA.1981.4503992.

[160] CIGRE B4, "Guide for electromagnetic transient studies involving VSC converters", *Technical Brochure 832*, vol. 832, no. April, pp. 3–184, 2021.

[161] J. Svensson, "Synchronisation methods for grid-connected voltage source converters", *IEE Proceedings - Generation, Transmission and Distribution*, vol. 148, no. 3, p. 229, 2001, ISSN: 13502360. DOI: 10.1049/ip-gtd:20010101. [Online]. Available: https://digital-library.theiet.org/content/journals/10.1049/ip-gtd_20010101.

[162] ENTSO-E, "Requirements for Grid Connection Applicable to all Generators", *ENTSOE Standards*, no. October, p. 86, 2013.

[163] Qingrui Tu, Zheng Xu, H. Huang, and Jing Zhang, "Parameter design principle of the arm inductor in modular multilevel converter based HVDC", in *2010 International Conference on Power System Technology*, IEEE, Oct. 2010, pp. 1–6, ISBN: 978-1-4244-5938-4. DOI: 10.1109/POWERCON.2010.5666416. [Online]. Available: http://ieeexplore.ieee.org/document/5666416/.

[164] K. Ilves, A. Antonopoulos, S. Norrga, and H.-P. Nee, "Steady-State Analysis of Interaction Between Harmonic Components of Arm and Line Quantities of Modular Multilevel Converters", *IEEE Transactions on Power Electronics*, vol. 27, no. 1, pp. 57–68, Jan. 2012, ISSN: 0885-8993. DOI: 10.1109/TPEL.2011.2159809. [Online]. Available: http://ieeexplore.ieee.org/document/5887423/.

[165] Q. Tu and Z. Xu, "Impact of Sampling Frequency on Harmonic Distortion for Modular Multilevel Converter", *IEEE Transactions on Power Delivery*, vol. 26, no. 1, pp. 298–306, Jan. 2011, ISSN: 0885-8977. DOI: 10.1109/TPWRD.2010.2078837. [Online]. Available: http://ieeexplore.ieee.org/document/5673482/.

[166] H. Dommel, "Digital Computer Solution of Electromagnetic Transients in Single-and Multiphase Networks", *IEEE Transactions on Power Apparatus and Systems*, vol. PAS-88, no. 4, pp. 388–399, Apr. 1969, ISSN: 0018-9510. DOI: 10.1109/TPAS.1969.292459. [Online]. Available: http://ieeexplore.ieee.org/document/4073845/.

[167] G. Xiong, J. Zhang, and G. He, "FPGA-based resource-aware solutions for sparse matrice in real-time EMT simulation", in *The 16th IET International Conference on AC and DC Power Transmission (ACDC 2020)*, Institution of Engineering and Technology, 2021, pp. 1242–1246, ISBN: 978-1-83953-330-3. DOI: 10.1049/icp.2020.0035. [Online]. Available: https://digital-library.theiet.org/content/conferences/10.1049/icp.2020.0035.

[168] RTDS Technologies, "RSCAD Power System Manual", Tech. Rep., 2023, p. 1200.

[169] T. I. Maguire, B. Warkentin, Y. Chen, and J.-P. Hasler, "Efficient Techniques for Real Time Simulation of MMC Systems", *Proceedings of the International Conference on Power Systems Transients 2013 (IPST 2013)*, no. 3, 2013. [Online]. Available: https://ipst13.elkraft.ntnu.no/openconf/modules/request.php?module=oc_program&action=view.php&id=347.

[170] RTDS Technologies, "MMC generic model manual", Tech. Rep., 2019, p. 41.

[171] Real-Time Digital Simulator, "VSC SMALL TIME-STEP MODELING", RTDS Technologies, Winnipeg, Manitoba, Canada., Tech. Rep. October, 2006, pp. 1–136.

[172] H. Wu and X. Wang, "Dynamic impact of zero-sequence circulating current on modular multilevel converters: Complex-valued AC impedance modeling and analysis", *IEEE Journal of Emerging and Selected Topics in Power Electronics*, vol. 8, no. 2, pp. 1947–1963, 2019.

[173] "Mean Absolute Error", in *Encyclopedia of Machine Learning*, C. Sammut and G. I. Webb, Eds., Boston, MA: Springer US, 2010, p. 652, ISBN: 978-0-387-30164-8. DOI: 10.1007/978-0-387-30164-8{_}525. [Online]. Available: https://doi.org/10.1007/978-0-387-30164-8_525.

[174] CIGRE Working Group B4.72, "DC grid benchmark models for system studies", *CIGRE Technical Brochure*, vol. 804, no. June, p. 270, 2020.

[175] T. B4.76, "DC-DC converters in HVDC grids and for connections to HVDC systems", *CIGRE Technical Brochure*, vol. 827, 2021.

[176] A. Shetgaonkar, A. Lekić, and M. Popov, *HVDC RTDS models*, 2023. [Online]. Available: https://github.com/control-protection-grids-tudelft/HVDC-RTDS-models.

[177] C. W. G. B4.57, "Guide for the Development of Models for HVDC Converters in a HVDC Grid", Tech. Rep. December, 2014, p. 222.

[178] ENTSO-E, "Fault current contribution from PPMS & HVDC", Tech. Rep. November, 2016, p. 15.

[179] C. Electra, "ELECTRA N ° 321 April 2022", no. April 2022, pp. 1–115, 2023.

[180] B. 6. TB, "Connection of Wind Farms to Weak AC networks", *CIGRE Technical Brochure*, vol. 671, 2016.

[181] H. Shariatpanah, R. Fadaeinedjad, and M. Rashidinejad, "A New Model for PMSG-Based Wind Turbine With Yaw Control", *IEEE Transactions on Energy Conversion*, vol. 28, no. 4, pp. 929–937, Dec. 2013, ISSN: 0885-8969. DOI: 10.1109/TEC.2013.2281814.

[182] W. P. 4. P. Project, "Broad comparison of fault clearing strategies for DC grids", Tech. Rep., 2022, p. 252. [Online]. Available: https://cordis.europa.eu/project/id/691714.

[183] J. B. Rawlings and D. Q. Mayne, *Model Predictive Control: Theory and Design*. Nob Hill Pub., 2009, ISBN: 9780975937709. [Online]. Available: https://books.google.nl/books?id=3_rfQQAACAAJ.

[184] H. K. Khalil, *Nonlinear Systems*. Macmillan Publishing Company, 1992, ISBN: 9780023635410. [Online]. Available: https://books.google.nl/books?id=RVHvAAAAMAAJ.

[185] Jiangchao Qin and M. Saeedifard, "Predictive Control of a Modular Multilevel Converter for a Back-to-Back HVDC System", *IEEE Transactions on Power Delivery*, vol. 27, no. 3, pp. 1538–1547, Jul. 2012, ISSN: 0885-8977. DOI: 10.1109/TPWRD.2012.2191577.

[186] D. Zhou, S. Yang, and Y. Tang, "A Voltage-Based Open-Circuit Fault Detection and Isolation Approach for Modular Multilevel Converters With Model-Predictive Control", *IEEE Transactions on Power Electronics*, vol. 33, no. 11, pp. 9866–9874, Nov. 2018, ISSN: 0885-8993. DOI: 10.1109/TPEL.2018.2796584.

[187] J. Bocker, B. Freudenberg, A. The, and S. Dieckerhoff, "Experimental Comparison of Model Predictive Control and Cascaded Control of the Modular Multilevel Converter", *IEEE Transactions on Power Electronics*, vol. 30, no. 1, pp. 422–430, Jan. 2015, ISSN: 0885-8993. DOI: 10.1109/TPEL.2014.2309438.

[188] A. Dekka, B. Wu, and N. R. Zargari, "Minimization of DC-Bus Current Ripple in Modular Multilevel Converter Under Unbalanced Conditions", *IEEE Transactions on Power Electronics*, vol. 32, no. 6, pp. 4125–4131, Jun. 2017, ISSN: 0885-8993. DOI: 10.1109/TPEL.2016.2630921.

[189] M. Vatani, B. Bahrani, M. Saeedifard, and M. Hovd, "Indirect Finite Control Set Model Predictive Control of Modular Multilevel Converters", *IEEE Transactions on Smart Grid*, vol. 6, no. 3, pp. 1520–1529, May 2015, ISSN: 1949-3053. DOI: 10.1109/TSG.2014.2377112.

[190] P. Liu, Y. Wang, W. Cong, and W. Lei, "Grouping-Sorting-Optimized Model Predictive Control for Modular Multilevel Converter With Reduced Computational Load", *IEEE Transactions on Power Electronics*, vol. 31, no. 3, pp. 1896–1907, Mar. 2016, ISSN: 0885-8993. DOI: 10.1109/TPEL.2015.2432767.

[191] J.-W. Moon, J.-S. Gwon, J.-W. Park, D.-W. Kang, and J.-M. Kim, "Model Predictive Control With a Reduced Number of Considered States in a Modular Multilevel Converter for HVDC System", *IEEE Transactions on Power Delivery*, vol. 30, no. 2, pp. 608–617, Apr. 2015, ISSN: 0885-8977. DOI: 10.1109/TPWRD.2014.2303172.

[192] Y. Wang, W. Cong, M. Li, N. Li, M. Cao, and W. Lei, "Model predictive control of modular multilevel converter with reduced computational load", in *2014 IEEE Applied Power Electronics Conference and Exposition - APEC 2014*, IEEE, Mar. 2014, pp. 1776–1779, ISBN: 978-1-4799-2325-0. DOI: 10.1109/APEC.2014.6803546.

[193] J. Huang, B. Yang, F. Guo, *et al.*, "Priority Sorting Approach for Modular Multilevel Converter Based on Simplified Model Predictive Control", *IEEE Transactions on Industrial Electronics*, vol. 65, no. 6, pp. 4819–4830, Jun. 2018, ISSN: 0278-0046. DOI: 10.1109/TIE.2017.2774725.

[194] H. Mahmoudi, M. Aleenejad, and R. Ahmadi, "Modulated Model Predictive Control of Modular Multilevel Converters in VSC-HVDC Systems", *IEEE Transactions on Power Delivery*, vol. 33, no. 5, pp. 2115–2124, Oct. 2018, ISSN: 0885-8977. DOI: 10.1109/TPWRD.2017.2727478.

[195] T. Nowak, M. Suriyah, and T. Leibfried, "Power tracking in a MMC-multi-terminal HVDC system with centralized and decentralized MPC using a black box modeling approach", in *2017 52nd International Universities Power Engineering Conference (UPEC)*, IEEE, Aug. 2017, pp. 1–4, ISBN: 978-1-5386-2344-2. DOI: 10.1109/UPEC.2017.8232017.

[196] J. Zhang, Z. Hu, and X. Tian, "Research on MMC-HVDC multi-objective model predictive control strategy under asymmetric faults", *Energy Reports*, vol. 6, pp. 430–439, Dec. 2020, ISSN: 23524847. DOI: 10.1016/j.egyr.2020.11.218.

[197] S. Pirooz Azad, R. Iravani, and J. E. Tate, "Damping Inter-Area Oscillations Based on a Model Predictive Control (MPC) HVDC Supplementary Controller", *IEEE Transactions on Power Systems*, vol. 28, no. 3, pp. 3174–3183, Aug. 2013, ISSN: 0885-8950. DOI: 10.1109/TPWRS.2013.2247640.

[198] P. Mc Namara, R. R. Negenborn, B. De Schutter, G. Lightbody, and S. McLoone, "Distributed MPC for frequency regulation in multi-terminal HVDC grids", *Control Engineering Practice*, vol. 46, pp. 176–187, Jan. 2016, ISSN: 09670661. DOI: 10.1016/j.conengprac.2015.11.001.

[199] S. Fuchs, M. Jeong, and J. Biela, "Long Horizon, Quadratic Programming Based Model Predictive Control (MPC) for Grid Connected Modular Multilevel Converters (MMC)", in *IECON 2019 - 45th Annual Conference of the IEEE Industrial Electronics Society*, IEEE, Oct. 2019, pp. 1805–1812, ISBN: 978-1-7281-4878-6. DOI: 10.1109/IECON.2019.8927493.

[200] M. Belhaouane, K. Almaksour, L. Papangelis, *et al.*, "Experimental Validation of a Model Predictive Control Strategy on a Three-terminal VSC-HVDC Mock-up", in *15th IET International Conference on AC and DC Power Transmission (ACDC 2019)*, Institution of Engineering and Technology, 2019, 93 (6 pp.)–93 (6 pp.) ISBN: 978-1-83953-007-4. DOI: 10.1049/cp.2019.0093.

[201] A. Zama, A. Benchaib, S. Bacha, D. Frey, and S. Silvant, "High Dynamics Control for MMC Based on Exact Discrete-Time Model With Experimental Validation", *IEEE Transactions on Power Delivery*, vol. 33, no. 1, pp. 477–488, 2018. DOI: 10.1109/TPWRD.2017.2707343.

[202] L. Wang, *Model predictive control system design and implementation using MATLAB®*. Springer Science \& Business Media, 2009.

[203] L. Huang, H. Xin, Z. Wang, *et al.*, "A Virtual Synchronous Control for Voltage-Source Converters Utilizing Dynamics of DC-Link Capacitor to Realize Self-Synchronization", *IEEE Journal of Emerging and Selected Topics in Power Electronics*, vol. 5, no. 4, pp. 1565–1577, Dec. 2017, ISSN: 2168-6777. DOI: 10.1109/JESTPE.2017.2740424. [Online]. Available: http://ieeexplore.ieee.org/document/8011460/.

[204] Z. Zhang, W. Chen, and Z. Zhang, "A New Seamless Transfer Control Strategy of the Microgrid", *The Scientific World Journal*, vol. 2014, Y. Mao, Z. Zhou, J. Zhou, and X. Meng, Eds., p. 391 945, 2014, ISSN: 2356-6140. DOI: 10.1155/2014/391945. [Online]. Available: https://doi.org/10.1155/2014/391945.

[205] W. G. Cigré, "B4. 57."Guide for the Development of Models for HVDC Converters in a HVDC Grid"", *CIGRE Technical Brochure*, vol. 604, 2014.

[206] S. Liu, A. Shetgaonkar, and M. Popov, "Coordinative performance of HVDC circuit breakers in MTDC grids", in *2020 IEEE Power & Energy Society General Meeting (PESGM)*, IEEE, Aug. 2020, pp. 1–5, ISBN: 978-1-7281-5508-1. DOI: 10.1109/PESGM41954.2020.9281921.

[207] N. H. van der Blij, L. M. Ramirez-Elizondo, M. T. J. Spaan, and P. Bauer, "A State-Space Approach to Modelling DC Distribution Systems", *IEEE Transactions on Power Systems*, vol. 33, no. 1, pp. 943–950, Jan. 2018, ISSN: 0885-8950. DOI: 10.1109/TPWRS.2017.2691547.

[208] V. Nougain, S. Mishra, G. S. Misyris, and S. Chatzivasileiadis, "Multiterminal DC Fault Identification for MMC-HVDC Systems Based on Modal Analysis—A Localized Protection Scheme", *IEEE Journal of Emerging and Selected Topics in Power Electronics*, vol. 9, no. 6, pp. 6650–6661, Dec. 2021, ISSN: 2168-6777. DOI: 10.1109/JESTPE.2021.3068800.

[209] V. Nougain, S. Mishra, S. S. Nag, and A. Lekić, "Fault Location Algorithm for Multi-Terminal Radial Medium Voltage DC Microgrid", *IEEE Transactions on Power Delivery*, vol. 38, no. 6, pp. 4476–4488, Dec. 2023, ISSN: 0885-8977. DOI: 10.1109/TPWRD.2023.3318689.

[210] B4.56, "Guidelines for the preparation of "connection agreements" or "Grid Codes" for multi-terminal schemes and DC Grids", Tech. Rep., 2016, p. 64. [Online]. Available: url:%20https://www.e-cigre.org/publications/detail/657-guidelines-for-the-preparation-of-connection-agreements-or-grid-codes-for-multi-terminal-schemes-and-dc-grids.html.

[211] JWG B4/C1.65, "Recommended voltages for HVDC grids", Tech. Rep., 2017, p. 67. [Online]. Available: https://www.e-cigre.org/publications/detail/684-recommended-voltages-for-hvdc-grids.html.

[212] *Weather File*. [Online]. Available: https://weatherfile.com/.

BIOGRAPHY

Ajay Shetgaonkar (Graduate Student Member, IEEE) received a B.E. degree in electrical and electronic engineering from Goa College of Engineering, Goa, India, in 2016. In 2020, he received an M.Sc. degree in electrical power engineering from the Technical University of Delft, The Netherlands (graduated with “cum laude”). He is currently working toward Ph.D. degree at the Technical University of Delft, The Netherlands. His research interests includes future power system dynamics and stability, integration of renewable energy resources, modelling of HVDC breaker and design of advanced protection and control systems for modular multilevel converter-based HVDC systems. He is also student member of CIGRE

List of Publications

Journal Papers

8. **A. Shetgaonkar**, V. Nougain, M. Popov, P. Palensky, A. Lekić, "Predictive DC Fault Ride Through for Offshore MMC-based MT-HVDC Grid," Manuscript under preparation, to be submitted soon.

7. **A. Shetgaonkar**, T. Karmokar, M. Popov, A. Lekić, "Enhanced Real-Time Multi-Terminal HVDC Power System Benchmark Models with Performance Evaluation Strategies," *Cigre Science & Engineering*, vol. 32, February 2024, pp. 29, 2024, Cigre.

6. **A. Shetgaonkar**, M. Popov, P. Palensky, A. Lekić, "Zero-sequence current suppression control for fault current damper based on model predictive control," *Electric Power Systems Research*, vol. 223, pp. 109592, 2023, Elsevier.

5. L. Liu, **A. Shetgaonkar**, A. Lekić, "Interoperability of classical and advanced controllers in MMC based MTDC power system," *International Journal of Electrical Power & Energy Systems*, vol. 148, pp. 108980, 2023, Elsevier.

4. **A. Shetgaonkar**, L. Liu, A. Lekić, M. Popov, P. Palensky, "Model predictive control and protection of MMC-based MTDC power systems," *International Journal of Electrical Power & Energy Systems*, vol. 146, pp. 108710, 2023, Elsevier.

3. J. Stojković, **A. Shetgaonkar**, P. Stefanov, A. Lekić, "Two-layer control structure for enhancing frequency stability of the MTDC system," *International Journal of Electrical Power & Energy Systems*, vol. 145, pp. 108664, 2023, Elsevier.

2. J. Marchand, **A. Shetgaonkar**, J.L. Rueda Torres, A. Lekic, P. Palensky, "EMT real-time simulation model of a 2 GW offshore renewable energy hub integrating electrolysers," *Energies*, vol. 14, no. 24, pp. 8547, 2021, MDPI.

1. **A. Shetgaonkar**, A. Lekić, J.L. Rueda Torres, P. Palensky, "Microsecond enhanced indirect model predictive control for dynamic power management in MMC units," *Energies*, vol. 14, no. 11, pp. 3318, 2021, MDPI.

Conference Papers

4. R.K. Tarcar **A. Shetgaonkar**, M. Popov, A. Lekić, "Large Signal Stability Assessment of MPC-based Control for HVDC Electrical Grid, in *Proc. 2024 IEEE ISGT Europe 2024*, Accepted.

3. R.K. Tarcar, **A. Shetgaonkar**, M. Popov, M. Van Der Meijden, W. Winter, M. Ndreko, R. Dimitrovski, M. Burkhardt, A. Lekić, "Post DC Fault Circulating Current Suppression Control," in *Proc. 2023 IEEE Power & Energy Society General Meeting (PESGM)*, pp. 1–5, 2023, IEEE.

2. **A. Shetgaonkar**, S. Liu, M. Popov, "Comparative Analysis of a Detailed and an Average VARC DCCB model in MTDC Systems," in *Proc. 2022 IEEE Power & Energy Society General Meeting (PESGM)*, pp. 1–5, 2022, IEEE.

1. M. Aghahadi, L. Piegari, A. Lekić, **A. Shetgaonkar**, "Sliding Mode Control of the MMC-based Power System," in *Proc. IECON 2022–48th Annual Conference of the IEEE Industrial Electronics Society*, pp. 1–6, 2022, IEEE.

Repository

1. Shetgaonkar, A., Karmokar, T., Popov, M., & Lekić, A. "Real-time models of the MMC-based Multi-terminal HVDC electrical grids with North Sea ratings," Retrieved March 1, 2024, from https://github.com/control-protection-grids-tudelft/HVDC-RTDS-models

Supervised MSc Student Thesis

2. R. Kamat Tarcar, "Revolutionizing MTDC Networks: Unlocking the Power of FPGA-based MMCs with Grid Forming Control on RSCAD through Model Predictive Control." Available: https://repository.tudelft.nl/record/uuid:7783fc45-acd0-48f0-95f9-f09917f2e337

1. J. Marchand, "EMT model and dynamic power management strategy of an offshore renewable energy hub with local power-to-gas conversion." Available: https://repository.tudelft.nl/record/uuid:96fe177d-539f-43ee-81c0-6ff1bfb4b0aa#metadata

Master Thesis

1. A. Shetgaonkar, "Technical performance of different DC CB technologies for future HVDC Grids," 2020. Available: https://repository.tudelft.nl/record/uuid:4ee00c88-3f7d-4bb0-9433-b237b813e0d3

EU Project Deliverable

1. PROMOTioN, "D6.8: Develop roadmap for VARC DC CB scaling to EHV DC voltage," 2020. [Online]. Available: https://www.promotion-offshore.net/results/deliverables/